



HAL
open science

First Principles Study of the Effect of Chemical Functionalization on Charge Transport in Carbon-Based Systems at the Mesoscopic Scale.

Alejandro Lopez-Bezanilla

► **To cite this version:**

Alejandro Lopez-Bezanilla. First Principles Study of the Effect of Chemical Functionalization on Charge Transport in Carbon-Based Systems at the Mesoscopic Scale.. Condensed Matter [cond-mat]. Université Joseph-Fourier - Grenoble I, 2009. English. NNT: . tel-00438848

HAL Id: tel-00438848

<https://theses.hal.science/tel-00438848>

Submitted on 4 Dec 2009

HAL is a multi-disciplinary open access archive for the deposit and dissemination of scientific research documents, whether they are published or not. The documents may come from teaching and research institutions in France or abroad, or from public or private research centers.

L'archive ouverte pluridisciplinaire **HAL**, est destinée au dépôt et à la diffusion de documents scientifiques de niveau recherche, publiés ou non, émanant des établissements d'enseignement et de recherche français ou étrangers, des laboratoires publics ou privés.

THÈSE

présentée par

Alejandro LÓPEZ BEZANILLA

pour obtenir le grade de
DOCTEUR de l'UNIVERSITÉ JOSEPH FOURIER
(Arrêté ministériel du 30 Mars 1992)

Etude à partir des premiers principes de l'effet de la fonctionnalisation sur le transport de charge dans les systèmes à base de carbone à l'échelle mésoscopique.

Soutenue publiquement le 13 novembre 2009

Composition du jury

MARK CASIDA	Président du Jury
JUAN JOSÉ SAÉNZ GUTIERREZ	Rapporteur
ALAIN ROCHEFORT	Rapporteur
PABLO ORDEJÓN	Examineur
XAVIER BLASE	Examineur
VINCENT DERYCKE	Co-encadrant (Saclay)
PASCALE MALDIVI	Co-encadrante (Grenoble)
STEPHAN ROCHE	Encadrant

Thèse préparée au sein du
CEA – Institut Nanosciences et Cryogénie - Groupe Théorie
GRENOBLE

Cette thèse a été composée en grande partie grâce aux logiciels $\text{T}_{\text{E}}\text{X}$ (Donald E. KNUTH), $\text{L}_{\text{A}}\text{T}_{\text{E}}\text{X}$ (Leslie LAMPORT), $\text{pdfL}_{\text{A}}\text{T}_{\text{E}}\text{X}$ (Sebastian RAHTZ), *these.sty* (Thierry DEUTSCH), Inkscape (<http://www.inkscape.org>) et gnuplot (<http://www.gnuplot.info>) mis gracieusement à la disposition de la communauté scientifique par leurs auteurs.

Composée le 19 novembre 2009

Acknowledgements

Como bien sabe todo aquel que alguna vez lo haya intentado, los agradecimientos sólo pueden darse en la lengua que a uno le enseñaron de pequeño. Por ello me permito escribir estas líneas en la lengua de mis padres y dejo para el lenguaje técnico y prosaico del manuscrito la lengua de otros.

Quede claro que no figuran en estos agradecimientos todos los que por derecho propio lo merecerían. En aras de la concisión, me limito a aquellos amigos, colegas y colaboradores que han jugado un papel decisivo, constante y realmente comprometido en la realización de esta tesis.

Debo comenzar agradeciendo a tantos profesores, y en especial a Juan José Sáenz, el apoyo, la comprensión y, en ocasiones, el exceso de funciones a la hora de considerar mi valía como estudiante y persona. A todos aquellos que en su día accedieron a ayudarme en el camino hacia esta tesis, les doy el mayor de mis agradecimientos.

Como no menos puedo decir de la comisión evaluadora de ChemTronic y sobre todo de Stephan Roche y Robert Baptist, quienes nunca dejaron de confiar en mí, ni siquiera cuando tenían sobradas razones para hacerlo. Muy especialmente quiero destacar a Stephan y su labor como director de tesis. El trabajo que juntos hemos llevado a cabo en estos tres años, a pesar de los problemas y las decepciones siempre llegadas de fuera, modestamente creo que lo hemos sabido hacer muy bien. Ojalá no haya sido ésta la última ocasión de hacer un buen trabajo juntos.

Mi más sincera gratitud a mis compañeros de trabajo. A Rémi Avriller y Luis Foà Torres les debo que me ayudaran con la tesis allá en sus inicios, así como a Mattieu Dubois que aceptara intercambiar conmigo tantas dosis de paciencia.

Pero si a alguien le debo que esta tesis haya podido realizarse es a François Triozon, verdadero "co-encadrant" a lo largo de este proyecto, sin cuya ayuda no hubiera podido llegar tan lejos. Mi consideración hacia mis compañeros de L_Sim, como Martin Persson, Luigi Genovese y, muy especialmente, Thierry Deutsch por compartir sus conocimientos y buen hacer, que tan difíciles me han sido encontrar en ocasiones en otras partes.

No quiero dejar de mencionar a Silvain Latil y Xavier Blase por sus fugaces pero importantes contribuciones a mi formación y producción científica. Así mismo quiero resaltar la colaboración con Jean-Christophe Charlier y Simon Dubois de

Louvain-la-Neuve, quienes nos han mostrado el placer de trabajar juntos en una colaboración científica.

Antes de terminar, quiero mostrar mi agradecimiento a los miembros de mi Jury de Thèse por haberme hecho el honor de aceptar mi invitación a formar parte del mismo.

Por último, agradezco a los responsables europeos la creación y mantenimiento del programa de becas de excelencia Marie Curie que me ha permitido realizar este doctorado. No sin olvidar a mis padres, y a tantos otros de su generación, que supieron hacer lo correcto para que gente como yo pudiéramos hoy ser merecedores del privilegio de formar parte de este proyecto europeo.

Contents

List of Figures	vii
1 Introduction	1
2 Geometrical and Electronic Structure of Carbon-Related Materials	7
2.1 Introduction	9
2.2 Valence Band and Molecular Orbital theories	9
2.3 Hybridization	10
2.4 Carbon	11
2.4.1 Electronic structure of carbon atom	12
2.5 Allotropes of Carbon	12
2.5.1 Diamond	13
2.5.2 Graphite	13
2.5.3 Fullerenes	14
2.5.4 NanoBuds	15
2.5.5 Pyrolytic carbon	16
2.6 Benzene and Aromaticity	16
2.7 Benzene and molecular orbitals	18
2.8 "Functionalizing" the benzene ring	19
2.8.1 Benzene + H	19
2.8.1.1 Nomenclature for aromatic hydrocarbon substitution patterns	20
2.8.2 Benzene + 2H molecule	21
2.8.3 Coronene	22
2.9 Graphene	24
2.9.1 Electronic structure of graphene	26
2.10 Graphene nanoribbons (GNRs)	29
2.10.1 Electronic structure of graphene nanoribbons	29
2.11 Carbon nanotubes (CNTs)	35
2.11.1 Crystal structure of nanotubes	36
2.11.1.1 Electronic structure of carbon nanotubes	38

CONTENTS

2.12	Transport properties of carbon nanotubes, 2D graphene and graphene nanoribbons	43
2.12.1	Ballistic transport regime in pristine CNTs	43
2.12.2	Short-range disorder and elastic mean free path.	45
3	Transport	49
3.1	Introduction	51
3.2	Landauer's idea	52
3.3	Landauer-Büttiker's theory	54
3.4	Green's function	56
3.5	Total density of states (TDoS) and Green's function	58
3.6	Real space renormalization group procedures, also known as decimation	60
3.6.1	Effective Hamiltonians	60
3.6.2	Decimation method	62
3.6.3	Green's functions applied to effective Hamiltonian description	64
3.6.4	Applying Green's functions to the semi-infinite linear chain problem	68
3.6.5	Green's function and diffusion probability	70
3.6.6	Applying Green's function beyond the linear chain problem	71
3.6.7	Renormalization method applied to our case.	73
3.6.7.1	Channel decimation	76
3.6.7.2	Lead computation	79
3.6.7.3	Entire system Green's function	81
3.6.8	Transmission function	84
4	The SIESTA Method and Code	87
4.1	Density Functional Theory	88
4.1.1	Introduction	88
4.1.2	The many-electron Schrödinger equation: Hartree and Hartree-Fock theories	89
4.1.3	DFT	92
4.1.4	The exchange-correlation term: LDA and GGA	95
4.2	SIESTA method	96
4.3	SIESTA code	97
4.3.1	Basis set	98
5	Quantum Transport Study of Chemically Functionalized Carbon Nanotubes	101
5.1	Introduction	102
5.2	Diazonium salts and phenyl groups	104
5.3	Technical details	105
5.4	Breaking the bonds	108
5.5	Metallic armchair carbon nanotubes	108
5.6	Semiconducting zigzag carbon nanotubes	114

5.6.1	Diameter dependent functionalization induced by bond cleaving	114
5.6.2	Quantum transport in functionalized semiconducting nanotubes . . .	116
5.7	Conclusions	120
6	Covalent Attachment of Functional Groups on GNRs and Transport Prop- erties	123
6.1	Introduction	124
6.2	Covalent attachment of functional groups to graphene and GNR	126
6.3	DFT calculations	127
6.4	Transport calculations	130
6.4.1	Short channel	132
6.4.2	Long channel	133
6.5	Conclusions	135
7	Edge Chemical Reactivity of GNRs and Transport Properties	137
7.1	Introduction	138
7.2	Defect description	140
7.3	Ab initio transport study	141
7.4	Tight-binding transport study	145
7.5	Technical details	148
7.6	Conclusions	149
8	Conclusions	151
	Bibliography	155

CONTENTS

List of Figures

1.1	Physisorption and chemisorption of organic molecules on carbon nanotubes. . .	3
1.2	SIESTA and TB_Sim logos	5
2.1	Carbon atom orbitals	12
2.2	C_{60} molecule	15
2.3	Nanobud hybrids and HOPG.	16
2.4	Bonding and antibonding molecular π -orbitals for a C_6H_6 molecule	18
2.5	Species issued from benzene.	21
2.6	Grafting coronene molecule.	23
2.7	Graphene lattice representation	26
2.8	Graphene energy bands.	28
2.9	Making GNRs from CNTs.	30
2.10	N dimers of carbon atoms forming a aGNR unit cell.	32
2.11	N dimers of carbon atoms forming a zGNR unit cell.	34
2.12	Converting graphene sheet in a nanotube.	37
2.13	3-unit cell CNTs	38
2.14	Band folding scheme.	40
2.15	Band structure and DoS.	41
2.16	Experimental layout and results of a typical nanotube-based device for biosensing.	42
2.17	STM image of a nanotube.	42
2.18	Conductance and electrical properties of metallic SWCNTs	44
2.19	Energy mean free path.	45
2.20	Nitrogen-doped nanotube.	47
2.21	Charge mobility in graphene.	48
3.1	Schematic representation of a device	53
3.2	Renormalization of a two-site model	60
3.3	Renormalization of a three-site model	62
3.4	Diagrammatical representation of Dyson's equation.	65
3.5	Diagrammatical representation of Green's function $G_{1,1}$	67
3.6	Network of site decimation	72

LIST OF FIGURES

3.7	Block decimation of a generic channel	77
3.8	Building up of the channel	78
3.9	Example of lead-channel matching	79
3.10	Procedure of lead decimation	80
3.11	Scheme of the final decimated system	82
4.1	Self-consistent loop for Kohn-Sham equations solution.	94
5.1	Grafting process of phenyl groups onto the the sidewall of CNTs.	105
5.2	sp^2 -like and sp^3 -like functionalization	106
5.3	Energy band comparison	109
5.4	Conductance comparison for phenyl and carbene.	110
5.5	Mean free paths	112
5.6	Conductance histograms for functionalized metallic armchair CNT.	113
5.7	The 3 analyzed orientations.	115
5.8	fig1	116
5.9	Conductance comparison in large- and small-gap semiconducting CNTs.	117
5.10	Conductance in large-gap semiconducting CNTs.	118
5.11	fig4	119
6.1	Electrochemical modification of graphene	125
6.2	Geometrical configuration of grafting groups on GNRs	128
6.3	Channel-lead representation	129
6.4	Conductance of small-gap GNRs.	130
6.5	Conductance of narrow GNRs	131
6.6	sp^3 -barrier	133
6.7	Averaged conductance	134
6.8	Mean free path in functionalized GNRs	135
7.1	aGNR edges	139
7.2	Detail of aGNR defects	141
7.3	Conductance profiles of defected edges	142
7.4	Conductance for benzenoid structures.	143
7.5	Tight-binding model.	145
7.6	Micrometer long GNRs conductance within TB scheme	146
7.7	Tight-binding parameterization scheme	148

Chapter 1

Introduction

*“Je suis toujours dans le premier
chapitre du Cohen-Tannoudji.”*

Xavier Blase

Driven by the miniaturization roadmap of the microelectronics industry, the gate length of ultimate silicon-based field effect transistors (MOSFETs) has been downscaled to a few tens of nanometers. This allows for the massive device integration of billions of interconnected transistors, as well as preserving their large current-voltage performances. However, despite the sustained development of silicon-based nanoelectronics, the search for alternative electronics has driven a large scientific community to successively explore the potential of molecular electronics, organic electronics, and carbon nanotubes, or more recently graphene-based nanoelectronics.

The use of carbon nanotubes (CNTs) and graphene nanoribbons (GNRs) as channels in electronic devices has been the focus of genuine efforts of research. Not only in academic environments, but also in industrial laboratories such as IBM, NEC, STMicroelectronics and so forth. However, it turns out that carbon-based nanodevices hardly outperform silicon devices in the field of core microelectronics, so that other types of applications need to be targeted. Among the wealth of possibilities, (bio)sensing at the nanoscale for medicine applications, optical switches, photovoltaic cells or nanoelectromechanical devices (NEMS) seem promising alternatives.

In any case, a deep understanding of the transport properties of carbon-based materials is required. A particular attention to the tuning of transport properties through controlled doping processes or procedures entailing the modification of clean-material physical properties are desirable. Both experimental and theoretical studies have traditionally considered external agents like adsorbed atoms and molecules, substitutional impurities and functional groups as possible candidates to introduce new functionalities in clean systems.

1. INTRODUCTION

For instance, π -conjugated polymers are interesting electroactive systems of which electronic and optical properties can be tuned by appropriate molecular design. Also by modifying the oxidation or protonation states of molecular groups through doping reactions (1), they can adopt several conformations which lead to show different physical properties. Such polymers can form molecular composites with other electroactive components of different composition as with CNTs. The combination of the peculiar properties of these objects with those of the polymers makes such composites potential candidates for a large variety of applications, such as data storage media, photovoltaic cells, etc. Also π -conjugated polymers are known to strongly interact with the carbon nanotube surface through π -stacking interactions to form supramolecular adducts. Such non-covalent functionalization of carbon nanotubes with planar conjugated molecules is found to be of significant interest since it allows for nanotube modification without the introduction of defects. At the same time, this procedure facilitates the molecular mixing of both composite components.

The conjugated π -network associated with the quasi-one-dimensional structure of CNTs and GNRs allows them to exhibit semiconducting and metallic properties, in addition to ballistic transport along micrometer long distances. Their unique electronic transport features may be altered by the presence of external agents which do not necessarily modify their geometries but usually entail an alteration of their unique electronic structures. Doping chemistry, based on both hole and electron introduction, does not change the carbon atom positions in the original systems but is suitable to create localized states and electrostatic fields. These new elements can be used to further creation of conduction gaps or localization phenomena in electronic transport devices.

On the other hand, chemical modification of nanotubes and nanoribbons, through covalent attachment of functional groups on their surface, produces simultaneously geometrical and electronic structure distortion of the initial objects. This perturbs the periodicity of the quasi-1D lattice and eventually destroys the electronic band structure and, hence, their unique transport properties. Moreover, nanotubes and graphene are carbon-based metals and, therefore, they provide an exceptional opportunity to probe the effects of carbon-carbon bond based-functionalization around the Fermi level for a metal.

The experimental achievements in the field of nanotube functionalization have been spectacular. For instance, through the “Click Chemistry” approach, Campidelli and coworkers from CEA-Saclay, succeeded in functionalizing and characterizing CNTs with zinc-phthalocyanine, with the aim of preparing a nanotube-based scaffold, which could make easier the fabrication of more complex functional structures. Actually, the attachment of phthalocyanines to nanotubes and fullerenes has recently emerged as an excellent approach to carbon nanostructure phthalocyanine-based photovoltaic and other electronic devices. Phthalocyanines are planar and electron-rich macrocycles that are characterized by their remarkably high extinction coefficients in the red/near-infrared region (which is an important part of the solar radiation spectrum) and their outstanding photostability and singular physical properties. These features makes of them exceptional building blocks for their incorporation in photovoltaic devices. The theoretical study by means of simulation methods to understand how molecular states of phthalocyanines or other photoactive species mix with carbon nanotubes extended

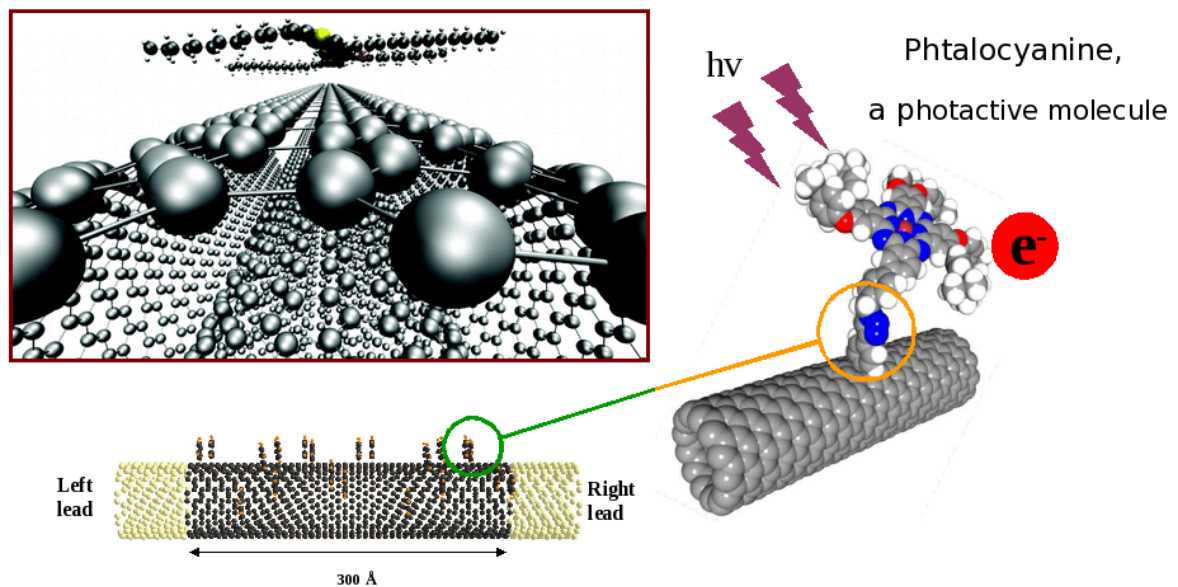


Figure 1.1: Physisorption and chemisorption of organic molecules on carbon nanotubes. - A phthalocyanine is attached to a carbon nanotube with the help of a chain of phenyl groups which act as linker. This chemical attachment allows the nanotube to evacuate the electrons that result from the photoactivation of the phthalocyanine. Modeling the degradation of electron transport abilities of the nanotube upon grafting of the phenyl groups by means of accurate models is one of the main concerns of this thesis. In contrast, physisorption represents a non-invasive fashion of functionalization. The organic molecule sits in the proximity of the nanotube such that chemical bonds are not established and both object electronic structures are only partially affected.

1. INTRODUCTION

states is thus an important objective toward the realization of materials with improved optoelectronic performances.

But some questions regarding the chemical functionalization remain still unsolved when further applications are envisaged: “How the interaction between nanotube and adsorbate affects the physical properties of both objects?” “What is the grafting process that alters the weakest the good transport capabilities of clean nanotubes?” Answering the latest question is the main concern of this work. Two types of functionalizations ¹, in carbon-based systems can be considered with respect to the structural and electronic consequences which entail the modification of the neat system: doping (also called ionic) and covalent functionalization.

The advances on the theoretical side have allowed us to progress in the understanding of some of this physical and chemical issues related to the modification of electronic structure of carbon-based systems. The large computational complexity of calculations involving modified structures does not permit a comparable progress in the field of modelling as in the experimental counterpart. This complexity arises from the need to include a large number of atoms in the computer simulation, as well as from the accuracy required to treat systems in a realistic manner. *Ab initio* tools based on density functional theory (DFT) can fulfill the requirements to obtain a good degree of accuracy when describing the electronic structure of pristine objects. In contrast, to model defected or disordered systems need of large supercells which could contain more atoms than a computer can usually deal with.

Such calculations may give some guidelines to better understand the effects that, for instance, doping cause in the electronic properties of the system under study. Therefore, computer simulation of conductance of doped systems is limited to a small number of impurities, and the behaviour of realistic systems, made up of thousand of atoms, remain unknown as long as new methodologies do not come into play.

An electron which crosses a channel device undergoes multiple scattering events which are at the origin of quantum interferences and localization effects. For the case of channels with defects, these phenomena can only be accounted for exactly for systems containing very few impurities, which suggests that the effect of disorder on large-system transport properties remains beyond the scope of usual first-principles methods. Even when large unit cells are considered, which in principle allows for calculations with a larger amount of impurities, the results only give little statistical approximations. The computational cost of reproducing the many different configurations, that are needed to reproduce the statistical ensemble of the defected system, prevents from performing the calculations.

This problem has been traditionally overcome with the help of less computationally demanding techniques, such as the combination of tight-binding methods and *ab initio* calculations. This type of combination has the advantage of reproducing complex systems with the simplicity of reduced models, in which one can reproduce scattering effects generated by randomly distributed impurities or geometrically modified structures. This is done at the expense of a compromise to accuracy.

¹In this work, we will refer to functionalization as the process of adding new functionalities to a system by means of modifying its intrinsic features.

One of the most popular methods for combining the less expensive, but not always accurate tight-binding technique, with the precise but computationally heavier DFT approach is by fitting the zone-folded tight-binding band structure to that obtained by DFT calculations (2; 3). This strategy involves fitting eigenvalues, which is not unique, since it is dependent on the choice of points of the Brillouin Zone. Rather than band structure fitting or other techniques based on Hamiltonian simplification, here we use an alternative method that relies on *ab initio* evaluations for the optimized geometrical structure of a functionalized system and further use of the resulting Hamiltonian for transport calculations (134).

This methodology presents the advantage of providing a realistic description of the systems under study: geometrical relaxation has been revealed as a necessary step in the description of atomic orbital rearrangement (hybridization) and charge transfer between interacting systems. Indeed, in the case when we resort to the tight-binding approach (Chapter 7) it will be demonstrated that DFT calculations are essential to provide the appropriate values for the parameters of the simplified model. By relating optimal structures with density charge distribution as a general procedure, we obtain appropriate model descriptions and also see in a transparent fashion the effects that functionalization may bring to the physical properties of nanotubes and nanoribbons.



Figure 1.2: SIESTA and TB.Sim logos - Both codes have been intensively used in this PhD. thesis. SIESTA is a Spanish DFT-based method and code for electronic structure and molecular dynamic calculations. TB.Sim is a French code for tight-binding-based calculations initiated and supervised by Y.M. Niquet at CEA. It has been used in this work for the transport calculations.

This thesis work focus on carbon nanotubes and graphene nanoribbons of which external surface has been chemically modified by adsorbed functional groups. Depending on chemical bond of functional addend with the backbone the transport properties of the former can be modified quite significantly. The DFT tool chosen for this work was the SIESTA code. The localized orbital basis set, which constitutes one of the essential features of this code, together with its reliable and fast calculations, are the main advantage of the SIESTA code. The tight-binding-like Hamiltonian obtained from the self-consistent calculation of a electronic structure presents the compactness which is required for transport property studies based on the Green's function formalism.

In what follows, this PhD work is presented. Firstly, a brief introduction to chemistry of aromatic compounds is given, followed by a discussion of the consequence of breaking the π -conjugated network of small-size aromatic molecules. Chapter 2 provides a general overview of most relevant carbon-based materials, with special emphasis in the fundamental electronic

1. INTRODUCTION

and transport properties of carbon nanotubes and graphene nanoribbons. In Chapter 3, the concepts behind the Landauer-Büttiker theory of coherent electronic transport in low dimensional systems are presented, together with a detailed description of the decimation technique, which is further extensively use for the calculation of long disordered systems. Therein, a section is devoted to this technique as it has been implemented in `TB_Sim` code. The results concerning the study of functionalized carbon nanotubes (both metallic and semiconducting) by carbene and phenyl groups, are presented in Chapter 5. Then quantum transport properties of graphene nanoribbons are analyzed, first, in Chapter 6 for the case of functionalized ribbons, and then in Chapter 7 for the ones with edge defects.

The realistic description of defects and chemical addends allows us to explore the various conduction regimes, from quasi-ballistic to diffusive or localized ones. The transition from a metallic to an insulating regime is shown to be strongly driven by the transport dimensionality for a fixed defect density. Our results on functionalized semiconducting nanotubes will permit putting in perspective the real potential of nanotubes materials for sensing applications, as well as the optimization possibilities for enhanced device performances.

Chapter 2

Geometrical and Electronic Structure of Carbon-Related Materials

“No es que Stephan haya trabajado con los popes de los nanotubos, ¡él es uno de los popes de los nanotubos!”

Juan José Sáenz Gutiérrez

Chapter résumé (French version)

Puisque le carbone est le principal élément chimique autour duquel cette thèse est développée, il est approprié de consacrer un chapitre à la description de ses allotropes et de ses propriétés physiques remarquables. Pour remplir cette tâche, nous présentons d’abord les théories de la Bande de Valence et des Orbitales Moléculaires qui nous permettent de comprendre la géométrie et la structure électronique de nos systèmes carbonés à l’aide de considérations d’arrangement des orbitales atomiques et moléculaires (hybridation). Les allotropes du carbone tels que les fullerènes, le diamant et les autres objets carbonés avec des propriétés physiques liées à celles des nanotubes et du graphène sont décrits. Le cas des petites molécules, dont la structure électronique est modifiée par l’ajout d’un atome d’hydrogène, est considéré comme exemple de système chimique réactif. Cela nous donnera une idée de l’importance d’éviter tout électron libre créé par la rupture du réseau π -conjugué des composés aromatiques et l’apparition d’une charge localisée.

2. GEOMETRICAL AND ELECTRONIC STRUCTURE OF CARBON-RELATED MATERIALS

Des sections distinctes sont consacrées aux nanotubes de carbone et aux nanorubans de graphène, où les propriétés électroniques et de transport sont décrites en détail.

Chapter résumé (Spanish version)

Dado que el átomo de carbono es el principal elemento químico alrededor del cual gira este trabajo de tesis, es adecuado dedicar un capítulo a la descripción de sus alótropos así como sus propiedades físicas más importantes. Para ello, en primer lugar se presentan las teorías de Banda de Valencia y Orbitales Moleculares que nos ayudan a comprender la geometría y estructura electrónica de nuestros sistemas a base de carbono a partir de consideraciones basadas en el arreglo de los orbitales atómicos o moleculares (hibridación). Los alótropos del carbono tales como fullerenos, diamante y otros objetos basados en el carbono con propiedades físicas relacionadas con las de nanotubos y el grafeno son descritos. El caso de moléculas de pequeño tamaño cuya estructura electrónica se ve alterada como consecuencia de la adición de un átomo de hidrógeno, es considerado como ejemplo de sistemas químicamente reactivos. Esto nos permitirá hacernos una idea de la importancia de impedir la presencia de electrones libres que se crean a partir de que el sistema aromático deja de ser π -conjugado y se produce la localización de carga en una zona de la molécula.

Secciones especiales son dedicadas a los nanotubos de carbono y “nanoribbons” de grafeno, donde se hace un análisis detallado de sus propiedades electrónicas y de transporte.

Chapter résumé (English version)

Since the carbon atom is the main chemical element around which this doctoral thesis is developed, it is appropriate to devote a chapter to describing its allotropes as well as their most salient physical properties. To cope with this task, we present first the Valence Band and Molecular Orbital theories which help us to rationalize the geometry and electronic structure of our carbon-based systems from the point of view of molecular and atomic orbital (hybridization) arrangement considerations. Carbon allotropes such as fullerenes, diamond and other carbon-based objects with physical properties related to that of nanotubes and graphene are described. The case of small-size molecules, of which the electronic structure is altered upon the addition of a hydrogen atom, is considered as an example of chemically reactive systems. This will allow us to get an idea of the importance of avoiding any free electron in the system which is created as a consequence of the π -conjugated network disruption of aromatic compounds and the appearance of localized charge.

Special sections are devoted to carbon nanotubes and graphene nanoribbons where electronic and transport properties are described in great detail.

2.1 Introduction

Just a few elements from the periodic table are used in this work. The most relevant is carbon (C), the essential component of the materials here studied. Hydrogen (H) is used as a convenient element for passivating the dangling bonds resulting of cutting a graphene sheet when designing a graphene nanoribbon. When oxygen (O) is combined with H becomes a functional group called hydroxyl (OH). These atoms are used along this work as part of the constituents that interact with the carbon-based systems and modify their geometrical and electronic properties.

2.2 Valence Band and Molecular Orbital theories

In our studies, we resort to the theory of hybridization to explain and rationalize the structure of the various systems under study. Hybridization theory is a practical approach to understand the way two or more atoms bond. The resulting covalent bonds have directional properties and impose a particular geometry to the interatomic union. Hybridization is based on the concept of mixing atomic orbitals to form new hybrid orbitals which are appropriated for the qualitative description of molecular orbitals and atomic bonding properties. Carbon has in turn the ability to exist in various molecular and crystalline structures. The nature of these bonds underlies the varied chemical and physical properties of carbon allotropes.¹ Hybridization theory is part of Valence Bond theory (VB) which was developed to explain, in terms of quantum mechanics, orbital interactions and bonding geometries of molecules. It can be complemented with Molecular Orbital theory (MO), in which orbitals are used to describe the whole molecule. In this case, a new molecular orbital set is generated by mixing atomic orbitals from all atoms. The resulting wavefunction is not associated with an electron in a particular bond between atoms, but it is considered to describe the electron as moving under the influence of the nuclei and any remaining charges. We will make extensive use of this approach for the ab initio description of the systems.

Valence Bond theory describes atomic bonding from an atom's point of view. First, valence orbitals of single atoms are mixed to generate the correct orbital geometry, and then molecules are built from the new hybrid orbitals. These hybrid orbitals are constructed by linear superposition of standard atomic orbitals (s,p,d...). Both theories allow for the combination of orbitals to produce bonding and anti-bonding molecular orbitals. The major difference is that VB can be viewed as a "localized" model of bonding, i.e., the bond between two atoms, while MO allows for molecular orbitals to span the entire molecule. The success in VB theory is that it gives a good explanation and prediction of the experimentally observed molecular geometries from their hybridized atomic orbitals. The disadvantage of VB is that

¹In general, atomic orbitals of one-electron atoms are used as a basis for simple schemes of hybridization because they can be "easily" calculated as an analytic solution of the Schrödinger equation. This orbitals are assumed not to be distorted in the case of heavier atoms, like nitrogen or oxygen.

2. GEOMETRICAL AND ELECTRONIC STRUCTURE OF CARBON-RELATED MATERIALS

it does not adequately explain the type of strongly delocalized bonding observed in aromatic compounds.

We will focus on how the atomic orbitals of carbon atoms combine on molecular formation to give individual chemical bonds. By means of atomic orbital overlaps of the participating atoms different bonds can be formed and several geometries can be deduced.

2.3 Hybridization

Depending of the different degree of s and p orbital mixing, three different types of hybridization are distinguished in carbon atom: sp , sp^2 , sp^3 . We give now an algebraic description of the last two hybrid orbitals, which are the ones most used through this manuscript. We shall consider the subspace generated by Schrödinger equation solutions for hydrogen atom that correspond to the second sub-shell, $\epsilon = \epsilon_{2s} \oplus \epsilon_{2p}$. ϵ is spanned by four real orbitals given in state representation by $|s\rangle$, $|2p_x\rangle$, $|2p_y\rangle$, $|2p_z\rangle$. By linear combination of these orbitals other real orbitals, which also form an orthonormal basis set in ϵ , can be constructed. The sp^2 hybridization is obtained with the following linear atomic orbital superposition, involving only 3 orbitals:

$$\begin{aligned} |sp^2\rangle_1 &= \frac{1}{\sqrt{3}}|s\rangle + \frac{2}{\sqrt{3}}|p_x\rangle \\ |sp^2\rangle_2 &= \frac{1}{\sqrt{3}}|s\rangle - \frac{1}{\sqrt{6}}|p_x\rangle + \frac{1}{\sqrt{2}}|p_y\rangle \\ |sp^2\rangle_3 &= \frac{1}{\sqrt{3}}|s\rangle - \frac{1}{\sqrt{6}}|p_x\rangle - \frac{1}{\sqrt{2}}|p_y\rangle \\ |sp^2\rangle_4 &= |p_z\rangle \end{aligned}$$

The forth p orbital is not involved in the generation of the new ones, but it is orthogonal to them. In the case of sp^3 hybridization a linear combination of 4 atomic orbitals gives 4 hybridized orbitals:

$$\begin{aligned} |sp^3\rangle_1 &= \frac{1}{2}|s\rangle + \frac{1}{2}|p_x\rangle + \frac{1}{2}|p_y\rangle + \frac{1}{2}|p_z\rangle \\ |sp^3\rangle_2 &= \frac{1}{2}|s\rangle - \frac{1}{2}|p_x\rangle - \frac{1}{2}|p_y\rangle + \frac{1}{2}|p_z\rangle \\ |sp^3\rangle_3 &= \frac{1}{2}|s\rangle - \frac{1}{2}|p_x\rangle + \frac{1}{2}|p_y\rangle - \frac{1}{2}|p_z\rangle \\ |sp^3\rangle_4 &= \frac{1}{2}|s\rangle + \frac{1}{2}|p_x\rangle - \frac{1}{2}|p_y\rangle - \frac{1}{2}|p_z\rangle \end{aligned}$$

In the rightmost image in Fig 2.1 a hybrid orbital is represented. The complete set of sp^2 and sp^3 hybrid orbitals are obtained by orienting this orbital along the lines that connect the C atom with the vertices of a tetrahedron, for sp^3 hybridization, and with the vertices of an equilateral triangle, for sp^2 hybridization.

Among the carbon-based systems that satisfy this approach of hybrid orbitals, diamond and graphene are two of the most relevant examples. In both cases, sp^2 and sp^3 orbitals perfectly describe their geometry and electrical properties. Graphene is a single layer of carbon atoms arranged in a hexagonal crystal lattice. Each C in the network is bonded to its three first nearest neighbors through sp^2 hybrid orbitals. These σ -orbitals¹ are placed in the plane (say \overline{xy}), with a relative angle 120° . The fourth p_z orbital is perpendicular to this plane. As we will see, the characteristic π -electronic structure of graphene and carbon nanotubes is fundamentally controlled by the network structure of sp^2 carbon, that is to say, the distribution along the material of the high mobility π -electrons. On the other hand, diamond is an extended array of carbon atoms connected between them by a single sp^3 bond with four σ -bands in the electronic structure which makes diamond behave as an insulating material.

In this manuscript we will explore how to model structural disruption of sp^2 nanotube and nanoribbon networks and the corresponding effect in electronic transport properties of these materials. Breaking π -bonds and additional σ -bond production, i.e., transition from sp^2 to sp^3 hybridization, is the main effect of some types of chemisorption on graphene and carbon nanotubes. This disruption acts as an impurity scattering center when transport properties of the material are considered. Before moving to the study of charge transport in systems as CNTs and GNRs, some results concerning the alteration of charge distribution along these systems in presence of impurities are presented. The goal is not to summarize the atom grafting mechanism on pristine molecules, but rather give some practical results that will help to understand the importance of functionalization following certain rules.

2.4 Carbon

Carbon is labelled with symbol C and its atomic number is 6. Following the rules of IUPAC, it is classified as group 14 in the periodic table. As the rest of the elements of this group (Si, Ge, Sn, Pb, Uuq²) C is tetravalent, meaning that four electrons in its outermost shell are available to form chemical bonds. All forms of carbon are highly stable, requiring high temperature to react even with oxygen. The oxidation state of carbon in some inorganic compounds is +4, while +2 is found in carbon monoxide and other transition metal carbonyl

¹In a molecular framework, σ and π are symmetry labels applied to molecular orbitals. π molecular orbitals are antisymmetric with respect to a defining plane containing at least one atom (e.g. benzene) and σ -molecular orbitals symmetric with respect to the same plane. The terms can also be used for localized or two-center orbitals bonds.

²Ununquadium is the temporary name of a radioactive chemical element in the periodic table that has the temporary symbol Uuq and has the atomic number 114.

2. GEOMETRICAL AND ELECTRONIC STRUCTURE OF CARBON-RELATED MATERIALS

complexes. Oxidation state of C in graphene, nanotubes, and diamond is zero. Carbon is the fourth most abundant element in the universe by mass after hydrogen, helium, and oxygen

There are three naturally occurring isotopes, with ^{12}C and ^{13}C being stable, while ^{14}C is radioactive with a half-life of about 5730 years

2.4.1 Electronic structure of carbon atom

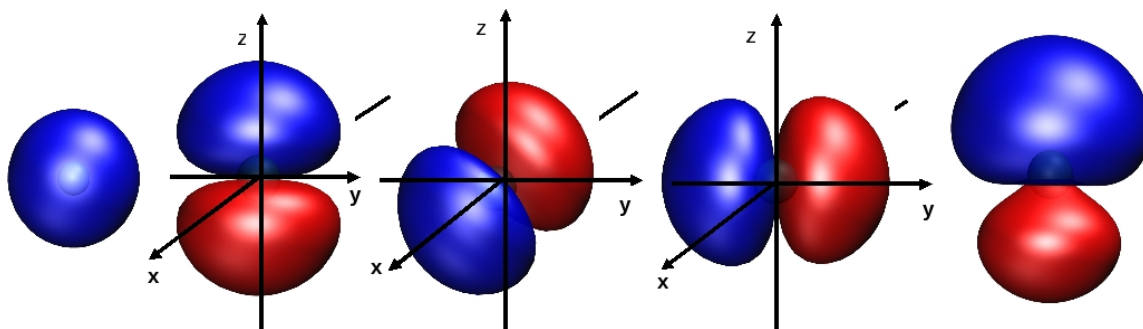


Figure 2.1: Carbon atom orbitals - From left to right: s, p_x, p_y, p_z orbitals of C atom. The fifth figure on the right represents a hybrid orbital resulting of the linear combination of $|2s\rangle$ and $|2p\rangle$ orbitals. The image has been obtained by numerical processing of the data obtained in the calculation of orbitals shown on the left through equations (2).

Carbon atom has six electrons. In its fundamental ground state, 2 of these electrons are in the 1s sub-shell, two in the 2s sub-shell and two in the 2p sub-shell. Only those last two electrons are unpaired which give to carbon the divalent behaviour observed in some compounds. The spatial distribution of electrons in this sub-shell is shown in Fig 2.1.¹ However, carbon is usually found in a quadrivalent form. This is due to the fact that one electron can be promoted to the unoccupied 2p orbital in the free atom. Therefore, in this case there are 4 unpaired electrons. The transition of an electron from the 2s sub-shell to a 2p sub-shell is energetical favorable when the energy needed for this excitation is compensated by the increase in stability due to the hybrid orbital involved in the C-X bonds. In general, X is an atom which also undergoes a hybridization, i.e., another C atom, or simply a H atom.

2.5 Allotropes of Carbon

Carbon is found free in nature in several allotropic forms. Allotropes are different structural forms of the same element which can exhibit different physical properties and chemical

¹Note the real nature of these wavefunctions. Spherical harmonics, which describe the angular of part Schrödinger equation solution, contain a complex exponential dependence and, therefore, atomic orbitals are generally complex functions. A linear combination of the solutions, which correspond to wavefunctions with quantum number $l=1$, allows us to find real orbital wavefunctions that can be represented graphically.

behaviours. An allotrope can change into another by the effect of pressure, temperature or light and its stability depends on particular conditions. In this thesis, we deal with two forms of carbon arrangement, namely, nanotubes and graphene nanoribbons. Two whole sections are devoted to describe their respective structural and electronic properties. In this section, we briefly describe other carbon allotropes.

2.5.1 Diamond

Diamond is an extremely hard, optically isotropic 3D-crystal, with the carbon atoms arranged in a isometric-hexoctahedral crystal lattice. Physical properties of diamond arise from the characteristic of pure covalent C-C sp^3 bonding giving to diamond crystal lattice its exceptional strength. Atoms of nitrogen, boron, hydrogen, phosphorus can be introduced into diamond during the growth at significant concentrations. Note that virtually any element can be also introduced in diamond by ion implantation. These trace impurities substitutionally replacing carbon atoms are responsible for the range of colors observed in diamond. Yellow and brown colors in diamonds are originated by the presence of nitrogen and blue color by boron substitution.

Specialized applications include use as semiconductors: some blue diamonds are natural semiconductors, in contrast to most other diamonds, which are excellent electrical insulators. The conductivity and blue color originate from the boron substitution for carbon atoms in the lattice, donating a hole into the valence band. Substantial conductivity is commonly observed in nominally undoped diamond grown by chemical vapor deposition (13). This conductivity is associated with hydrogen-related species adsorbed at the surface, and it can be removed by annealing or other surface treatments. Diode p-n junctions and UV light emitting diodes (LEDs, at 235 nm) has been produced by sequential deposition of p-type (boron-doped) and n-type (phosphorus-doped) layers (14).

Diamond is an excellent thermal conductor (900 - 2320 W/m K) and has a high refractive index (2.417). Above 1973 K it is converted to graphite, and so the decay of diamond is thermodynamically favorable ($\Delta H = -2$ kJ/mol)

2.5.2 Graphite

The most common and thermodynamically stable form of pure carbon under standard conditions is α -graphite. Unlike diamond, graphite is a reasonably good electrical conductor. It is used in thermochemistry as the standard state (17) for defining the heat of formation of carbon compounds. Graphite may be considered the highest grade of coal, just above anthracite and alternatively called meta-anthracite.

There are three principal types of natural graphite: (1) Flake graphite occurs as isolated, flat, plate-like particles with hexagonal edges if unbroken and, if broken the edges, can be irregular or angular; (2) Amorphous graphite occurs as fine particles and is the result of thermal metamorphism of coal, the last stage of coalification, and is sometimes called meta-anthracite; (3) Lump graphite (also called vein graphite) occurs in fissure veins or fractures

2. GEOMETRICAL AND ELECTRONIC STRUCTURE OF CARBON-RELATED MATERIALS

and appears as massive platy intergrowths of fibrous or acicular crystalline aggregates, and is probably hydrothermal in origin.

Graphite possesses a layer structure in which each carbon is directly bound to three other carbon atoms at a distance of 0.142 nm. Delocalization in the bonding is evident since the C-C distances are equal and shorter than normal C-C single bonds (typically 0.154 nm). The distance between the layers of carbon atoms is 0.335 nm. In most graphite (α -graphite), the layers of atoms are stacked in an ABAB. arrangement while the β -form (rhombohedral) presents a ABCABC stacking, although the distances mentioned above remain the same as in the α -form. The enthalpy difference between α - and β -graphite is less than 1 kJ/mol.

Graphite is a good electrical conductor due to electron delocalization in π orbitals which is responsible of the interaction between carbon layers. These electrons occupy the valence band and are free to move, but only between the plane of the layers. The acoustic and thermal properties of graphite are highly anisotropic, since phonons propagate very quickly along the tightly-bound planes, but are slower travelling from one plane to another. Concerning diamagnetic properties, graphite is, together with bismuth, the elements with the strongest diamagnetism.

2.5.3 Fullerenes

Kroto et al. (26) reported the C_{60} molecule in 1985, found as result of experiments that aimed to understand the mechanisms by which long-chain carbon molecules are formed in interstellar space. In 1990 macroscopic quantities of C_{60} were synthesized through carbon arc vaporization between two graphite electrodes. Fullerene (also called Buckminsterfullerene in the smallest stable version), is a discrete molecular species of 60 C atoms, distributed in a net of 12 pentagons and 20 hexagons folded into a solid that can be inscribed in a sphere. As opposed to other forms of carbon, fullerenes represent well-defined molecules, whereas diamond, graphite, nanotubes, etc., are infinite lattices. In this cluster all the C atoms are equivalent although two types of C-C bonds can be distinguished: bonds at the link of two hexagons which have the character of a double bond, and at the link of a hexagon and a pentagon which have the character of a single bond. In this cluster, C atoms are in sp^2 hybridization leading to the inner and outer surfaces being covered with a sea of π -electrons. A rule to determine whether a fullerene is aromatic is based in the number of π -electrons: if there are $2(n + 1)^2$ π -electrons, then the fullerene would display aromatic properties (27). This follows from the fact that an aromatic fullerene must have full icosahedral symmetry, so the molecular orbitals must be entirely filled. This is possible only if there are exactly $2(n + 1)^2$ electrons, where n is a positive integer. For example, buckminsterfullerene with 60 π -electrons is non-aromatic while the formula does not give a perfect square number. In terms of orbitals, this can also be explained from the fact that the spherical arrangement of the atoms prevents from a full orbital overlap of the fourth atomic orbital. The consequence is that C_{60} is not an aromatic molecule, unlike graphene and carbon nanotubes(31).

Calculations done with the help of Density Functional Theory (DFT) tools predict that C_{60} is able to accept up to 6 electrons. This electron acceptor behaviour is related to its

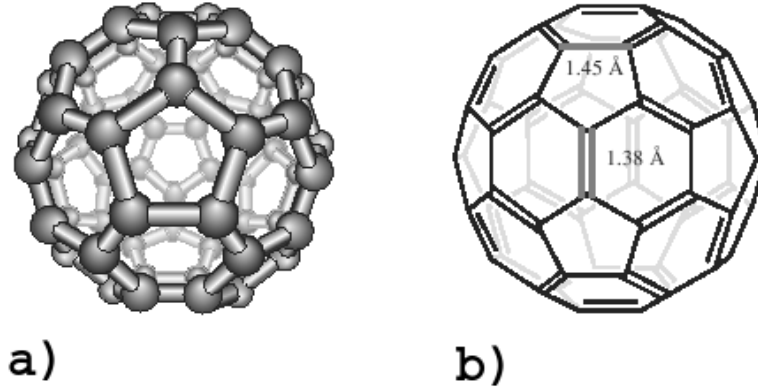


Figure 2.2: C_{60} molecule - a) Structure of C_{60} . b) Illustration of the typical lengths of hexagon-hexagon and hexagon-pentagon bonds associated with a single and double character bond, respectively. (Images from (31))

icosahedral symmetry, which leads to triply degenerate unoccupied molecular orbitals for the ground state (33).

Only fullerenes obeying the isolated pentagon rule are stable. This rule predicts that the fullerene-type structures in which all pentagons are separated from one another by hexagons are more stable than those in which there are two adjacent pentagons. After C_{60} , the second stable fullerene is C_{70} which has an oval profile: at its poles the structure is spherical but it has an equatorial belt made up of a chain of hexagons.

C_{60} diameter is $\sim 7\text{\AA}$, providing an inner cavity which is capable of holding a variety of atoms, such as potassium and other alkali metals to make endohedral structures, denoted as $C_{60}Cs^+$. This gave rise to what was termed the "shrink-wrapping" experiment (28). Fullerenes are extremely stable and resilient to impact and deformation.

2.5.4 NanoBuds

A new carbon hybrid called NanoBudsTM, based on the union of fullerenes and CNTs, has been recently discovered (34). NanoBudsTM consist of (mostly C_{42} and C_{60}) fullerenes attached to the outside surface of CNTs. Scanning tunneling microscopy and spectroscopy measurements of samples deposited on Au demonstrate the covalent nature of fullerene-CNT bonding. As well, DFT calculations showed that systems composed of this two carbon-based systems with single vacancies covalently functionalized can exist. A theoretical study of the electronic transport properties of these compounds using similar techniques to the ones used in this work, has been recently presented (34). It shows the impact of a NanoBud on the transport properties of CNTs when it is attached at different distances of nanotube surface(35).

2. GEOMETRICAL AND ELECTRONIC STRUCTURE OF CARBON-RELATED MATERIALS

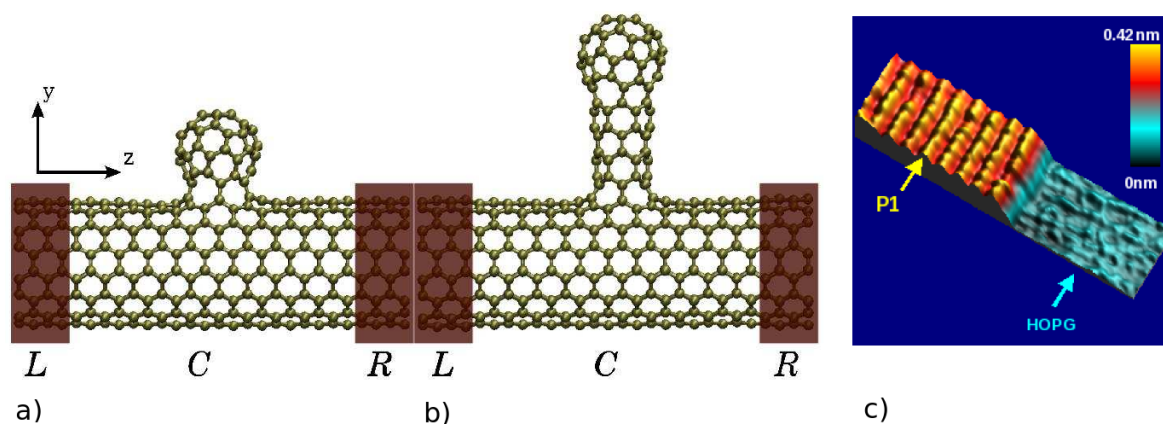


Figure 2.3: Nanobud hybrids and HOPG. - NanoBudsTM are fullerene functionalized carbon nanotubes which form a novel class of hybrid carbon. This nanobud consists of an imperfect C_{60} attached to an armchair (8,8) single-wall nanotube via a neck region, made of a (6,0) nanotube. In a) a zero-unit cell neck is shown while b) presents the case of a two-unit cell neck. (Image from ref.(35)) c) STM image of a single-layer of p3ddt polymer deposited over HOPG (courtesy of B. Grevin)

2.5.5 Pyrolytic carbon

Pyrolytic carbon is a material similar to graphite, but with some covalent bonding between its graphene sheets as a result of imperfections introduced during the fabrication process. It is produced by heating hydrocarbon materials and permitting the graphite to crystallize in a pyrolysis process. Samples of this material usually have a single cleavage plane (23) due to crystallization planar order of graphene sheets (as opposed to graphite) exhibiting several unusual anisotropic properties. It is more thermally conductive along the cleavage plane than graphite, making it one of the best planar thermal conductors existing in nature.

HOPG stands for Highly Oriented Pyrolytic Graphite and is a highly ordered form of pyrolytic graphite with an angular spread of the c axes of less than 1 degree (21). It is commonly used as a calibration tool for probe microscopies, such as Scanning Tunneling Microscopy (STM) or Atomic Force Microscopy (AFM). Commercial HOPG is usually produced by stress annealing at approximately 3300 K (19) and is used as a substrate in many scientific experiments, e.g. (20). It behaves much like a pure metal, being reflective and electrically conductive.

2.6 Benzene and Aromaticity

Benzene C_6H_6 can be thought as the precursor of phenyl ϕ , so that it is frequently denoted as $\phi - H$. In organic chemistry it is classified in the aryl group of compounds. Carbon atoms are arranged in a hexagon ring with a hydrogen atom attached to each of them. The

elucidation of the structure entailed a problem when it was isolated and identified by M. Faraday in 1825. He was the first to identify benzene and determine its composition as containing six carbon atoms and six hydrogen atoms. At that time, it was known that polyunsaturated hydrocarbons would react with hydrogen gas to take up a molecule or more of hydrogen. In 1965, Kekulé conceived a cyclic structure with alternating single and double bonds (37). Using X-ray diffraction, it was discovered that all of the C-C bonds in benzene are of the same length of 1.40 Å. The C-C bond lengths are greater than a double bond (1.35 Å) but shorter than a single bond (1.47 Å). This intermediate distance is explained by electron delocalization: the electrons for C-C bonding are distributed equally between each of the six carbon atoms. It is considered that electrons are free to delocalized around the circular arrangement of carbon atoms, which are alternatively single- and double-bonded to one another. These bonds have identical length, intermediate between that of a single and that of a double bond. One representation of the structure is given as a superposition of so-called resonance structures.¹ This delocalization of electrons is known as aromaticity and gives benzene a great stability. This enhanced stability is the fundamental property of aromatic molecules and compounds (such as carbon nanotubes, graphene, graphene nanoribbons, etc) that differentiates them from molecules that are non-aromatic.

Traditionally, two factors have been required to consider a molecule as aromatic: firstly, a planar (or near planar) cycle of sp^2 hybridized atoms with parallelly oriented π -orbitals. These overlapping p-orbitals generate an array of π -molecular orbitals. Notwithstanding, carbon nanotubes and other non-planar material are considered aromatic despite their curvature. As long as the overlap between p-orbitals is conserved, the system is said to be aromatic, which is not the case of fullerenes. A second traditional requirement, is that these π -orbitals are occupied by $4n+2$ electrons (where n is an integer or zero), which is known as the Hückel Rule. Nowadays it is known that this rule is not valid for many compounds containing more than three fused aromatic nuclei in a cyclic fashion, as coronene, containing 24 conjugated electrons.

In terms of charge distribution, a typical representation of an aromatic compound is that of the circular π -bond in which the electron density is distributed through a π -type bond at both sides of benzene ring. Single bonds are formed with electrons that connect atoms nuclei (σ -bonds) and contribute to keep C atoms in the hexagonal pattern. They are responsible for the electronic density in the inner part of the ring. π -bonds are created by the overlap of the π -atomic orbitals which are perpendicular to the plane formed by the six atoms. Since the energy of electrons placed in p-orbitals is significantly higher than that of electrons in a σ -bond, they can interact with each other and become delocalized around the ring.(8)² These concepts are developed in the next section following an approach based on hybrid orbitals. Afterwards, we will show that a molecular orbital description of benzene provides a general treatment of aromaticity, which can be applied not only to a single hexagon molecule, but also can be generalized to multiple hexagon macromolecules as graphene and

¹Resonance is an averaged electron distribution over two or more contributing structures to produce a hybrid electronic structure.

²The interaction of one p-orbital with another across an intervening σ -bond is called conjugation

2. GEOMETRICAL AND ELECTRONIC STRUCTURE OF CARBON-RELATED MATERIALS

carbon nanotubes. The preservation of aromaticity upon structural modification by means of chemical functionalization is one of the main concern in our studies.

2.7 Benzene and molecular orbitals

Quantum mechanics enables us to interpret the geometrical and electronic structure of benzene molecule. Three out of four valence electrons of a carbon atom (called σ -electrons) are found to have wavefunctions which are symmetrical about three lines making angles of 120 with each other, and defining the directions of the chemical bonds. The overlap of the associated wavefunctions with those of the electrons of neighboring atoms ensures the stability of the C-H bonds and of the C-C bonds. The fourth valence electron (π -electron) has a wavefunction of π symmetry, i.e it is symmetric with regards a line passing through each of them and perpendicular to the plane defined by C and its three neighbouring atoms. The overlap of the wavefunctions of the six π -electrons is maximum and, therefore, the chemical stability of the double bond is greater when all the axes associated with the π -electrons are parallel, that is, when the six atoms of the molecules are in the same plane.

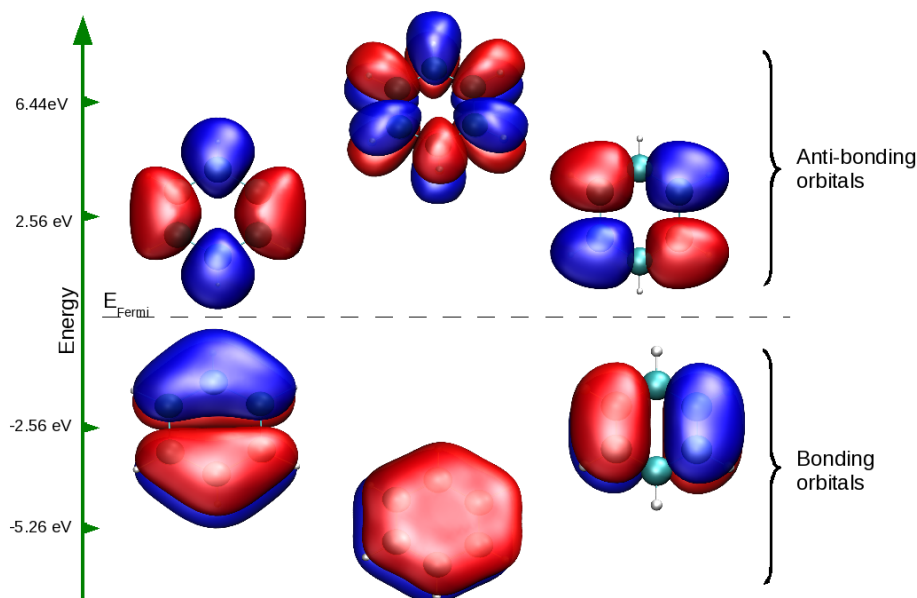


Figure 2.4: Bonding and antibonding molecular π -orbitals for a C_6H_6 molecule -

These overlaps that generate molecular orbitals are graphically represented in Fig. 2.4. The blue and red colors represent opposite phase signs in the wavefunction. When phases correspond, orbitals overlap to generate a common region with the same phase value. Orbitals

having the greatest overlap are the lowest in energy. The remaining carbon valence electrons then occupy the last two molecular orbitals by pairs, resulting in a fully occupied (6 electrons) set of bonding molecular orbitals. In analogy to a filled valence shell octet which confers stability to the inert gases, this completely filled set of bonding orbitals gives to benzene ring its thermodynamic and chemical stability.

The images in Fig.2.4 have been obtained after a SIESTA simulation of the electronic structure of a C_6H_6 molecule. A double- ζ polarized basis set has been used to obtain a set of 60 molecular states. Successively, the 30 electrons coming into play to form the σ - and π -bonds¹ fill up the molecular states. Carbon atoms are cyan and hydrogens atoms are white. The different phases of the molecular orbitals (red and blue colors) are separated by nodes at which electron density is zero. π -orbitals of benzene are formed by overlap of p_z atomic orbitals. The most symmetric π -molecular orbital is the lowest in energy: a single nodal plane parallel to the benzene ring separates the regions of positive and negative wavefunction. An increasing number of nodes shows up when energy increases. Three out of the six orbitals show a node passing through carbon atoms, so the π -electron density at those sites is zero. In the three others, the molecular wavefunction is fully localized on the carbon atoms. The lowest in energy π_1, π_2, π_3 are called bonding molecular orbitals and the three higher ones $\pi_1^*, \pi_2^*, \pi_3^*$, antibonding molecular orbitals.

2.8 "Functionalizing" the benzene ring

Once the benzene ring has been described and the aromaticity explained in the simplest case, the study of a slightly more complicated system is instructive. As studied later on more complicated carbon-based materials, we show now the consequences of altering the aromaticity of benzene ring by adding a single atom to its symmetrical geometry. It will allow us to understand the electron delocalization phenomena that arise upon the chemical functionalization of an aromatic system. Hückel's rule is broken and the molecule has an intrinsic magnetic moment, due to the even number of electrons that remain free in the system.

2.8.1 Benzene + H

The simplest way of disrupting the sp^2 benzene network is approaching a H atom to the planar surface. It interacts in a energetically favourable chemical reaction and the H atom is included in the final geometry of the molecule. The C atom to which it is attached changes its orbital hybridization from sp^2 to sp^3 . Nevertheless, the planar arrangement of the ring remains intact and only two H atoms are out the plane (see Fig.2.5). The number of π -electrons in the new molecule is now equals to five, since one π -electron of the original

¹24 electrons from the 6 C atoms plus 6 electrons from the 6 H atoms occupy by pairs the first 15 molecular states. The 15th state is the HOMO orbital and 16 state the LUMO orbital

2. GEOMETRICAL AND ELECTRONIC STRUCTURE OF CARBON-RELATED MATERIALS

benzene ring is used to establish a σ -bond with the added H. The resulting specimen has a high chemical reactivity associated to its radical nature.

To illustrate the molecular orbital which is created after benzene hydrogenation, we perform a SIESTA simulation to obtain the energy and shape of each molecular orbital. In this case a spin-polarized simulation must be done in order to describe the magnetic moment of the system which arises from the presence of an unpaired electron. In Fig.2.5 the single occupied molecular orbital SOMO¹ state of the C_6H_7 molecule is plotted. Two nodes divide the molecular orbital in three parts. Taking the carbon atom with the two hydrogens as the reference, we observe that positive and negative phases of the wavefunction are centered on each of the H atoms and a part over the C atom. Over the neighbouring C atoms, a part of the molecular orbital is extended and the node passes through the bonds. Finally, an isolated lobe is centered on the opposite C atom. The two other C atoms present a lower density of probability of being activated chemically. The chemical reasons to assess such conclusion involve several factors that are out of this thesis scope but some correlated effects, like the zero-electronic density at those sites for the HOMO state, can be exposed as an argument to confirm the preference of a second H atom to be grafted to an odd-number neighbouring C atom.

We will show this hypothesis by calculating the final states of C_6H_8 systems which are created upon approaching a H atom in the vicinity of a C_6H_7 molecule. Three non-equivalent sites can be considered for the grafting of a hydrogen atom on this molecule. From now on we will follow the IUPAC nomenclature (ortho, meta, para) for referring the adsorption site of a functional group with regards to the position of a previously adsorbed atom or functional group. In the next subsection this nomenclature description is given for the sake of clarity.

2.8.1.1 Nomenclature for aromatic hydrocarbon substitution patterns

It is convenient to devote a short subsection for explaining the terminology that will be used throughout this text concerning the hydrocarbon substitution patterns. When two substituents, other than hydrogen, occupy different positions in an aryl ring, the following nomenclature is commonly used for referring to their relative positions:

1. ortho-substitution (also referred as alpha), indicates a cyclic derivative having two substituents in adjacent carbon positions, occupying positions next to each other.
2. meta-substitution (also referred as beta), refers to a benzene ring in which the carbon atoms with attached groups are separated by one unsubstituted carbon atom.
3. para-substitution, (also referred as gamma), indicates the third of the three possible isomers of benzene in which carbon atoms having attached chemical groups are one in front each other in the ring.

¹From here on, SOMO stands for single occupied molecular orbital, HOMO stands for highest occupied molecular orbital and LUMO stands for lowest occupied molecular orbital

Although this convention is used for the case of substituents groups other than H atoms (electrophilic aromatic substitution), it will be used in the next sections for referring the positions of new H atoms in the various structures. Later on, in the case of nanotubes and nanoribbons it will design the relative position of grafting groups not necessarily H atoms.

2.8.2 Benzene + 2H molecule

Once the benzene molecule has an extra H atom attached to it, "building up" a C_6H_8 molecule can be designed in three different ways. Different final conformations of the molecule can be achieved as a function of the adsorption site of the eighth H atom. Relaxing every system with the same parameters of the previous simulations¹, we can observe three final configurations of a C_6H_8 molecule. The resulting geometries are plotted in Fig.2.5 together with the wavefunctions of the highest occupied molecular state. For meta-configuration, the HOMO image corresponds to spin up configuration. In all cases, the aromaticity of the benzene molecule is not recovered since the number of delocalized π -electrons does not fulfill Hückel's rule.

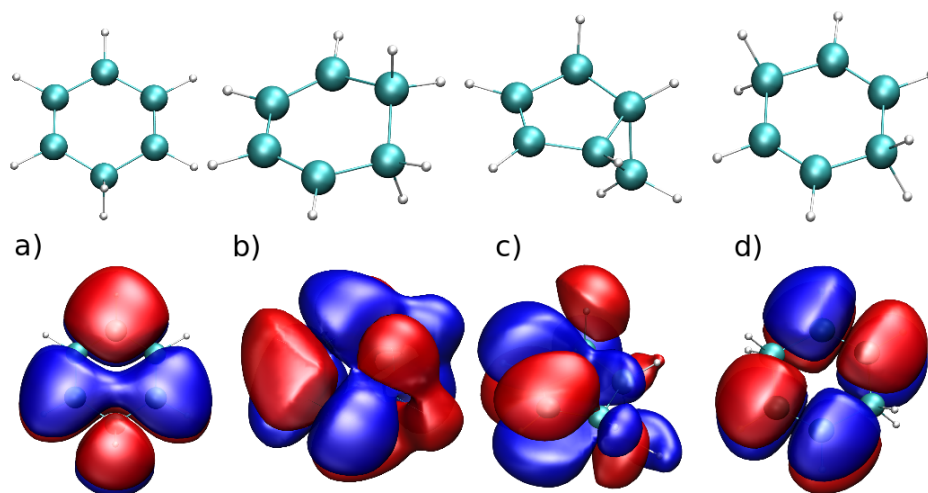


Figure 2.5: Species issued from benzene. - Upper image line: Final relaxed geometries of C_6H_7 and C_6H_8 molecules after addition processes of H atoms to a C_6H_6 molecule. a) Shows a benzene ring with an added H atom in one of its C atoms. b) Represents ortho configuration, c) the distorted result after approaching a H atom in the vicinity of a non-reactive C atom, and d) para configuration. Lower image line: molecular orbital representations of the HOMO state for the geometries shown in the upper image line

¹All calculations have been performed using a DZP basis set, a mesh cutoff of 200 Rydbergs and an energy shift value of 300 meV, which ensures that the radial terms of atomic orbitals are long enough to have mutual interaction. Geometries have been relaxed up to residual forces were smaller than 0.02 eV/Å

2. GEOMETRICAL AND ELECTRONIC STRUCTURE OF CARBON-RELATED MATERIALS

Taking as reference the C atom of the benzene ring to which a H atom has been previously attached, an eighth H atom is brought near to one of the first nearest neighbouring C atoms and the ortho configuration is obtained upon relaxation. It can be observed in Fig.2.5-b) how C atoms that serve as anchor site for the hydrogens do not remain in the original plane and each of them move out in opposite directions. Their orbitals are not anymore in the sp^2 hybridization due to the change into the sp^3 hybridization, as can be deduced by the tetragonal orientation of the bondings that join each of this two C atoms with its nearest neighbours.

In Fig.2.5-c) it can be observed the final geometry obtained upon relaxation of the $C_6H_7 + H$ molecule when the H atom is placed in the vicinity of a second nearest neighbour C atom. As explained above, a HOMO node passes through these C atoms and low reactivity of the molecule in its surroundings is detected. The chemical reaction takes place and changes the hexagonal arrangement of C atoms in C_6H_7 molecule into a pentagonal geometry. The sixth C atom and the two hydrogens attached to it (CH_2 , known as carbene group) sit on one of the C-C bonding.

In Fig.2.5-d) shows the resemblance between the para- C_6H_8 HOMO-shape and one of the antibonding molecular orbitals of the benzene (see Fig. 2.4) and HOMO+1 state of cyclobutadiene (C_4H_4) molecule (not shown here), and this illustrates the effect of removing two π -electrons from the benzene ring.

In this section, the benzene molecule has played the role of the smaller aromatic system to which several H atom can be attached. The molecular orbital resulting from single-H addition allows us to observe the unpaired electron delocalization as a lobe of the MO wavefunction sitting on a single C atom. We have tried to illustrate that the reactivity of odd-number neighbouring C atoms of this new molecule can be roughly deduced by scrutinizing its HOMO state. Those C atoms with an associated node in the HOMO state are shown to be less reactive than those with a wavefunction lobe.

We move on now to bigger systems, such as naphthalene and coronene, that will show the electron delocalization as an effect extended over the whole molecule instead of over a single atom .

2.8.3 Coronene

Benzene rings may be joined together to give larger polycyclic aromatic compounds. Naphthalene ($C_{10}H_8$) is an aromatic hydrocarbon with the structure derived by the fusion of a pair of benzene rings, meaning by fused that rings share two or more atoms. Unlike benzene, the C-C bonds in naphthalene are not of the same length. As shown in Fig.2.6 a), the bonds between C atoms in diagonal orientation in the figure are about 1.37 Å in length, whereas the C-C bonds in vertical are about 1.42 Å long. This result is again consistent within the valence bond model of bonding that involves three resonant structures. The first mentioned bonds are double in two of the structures while the others are double in only one structure.

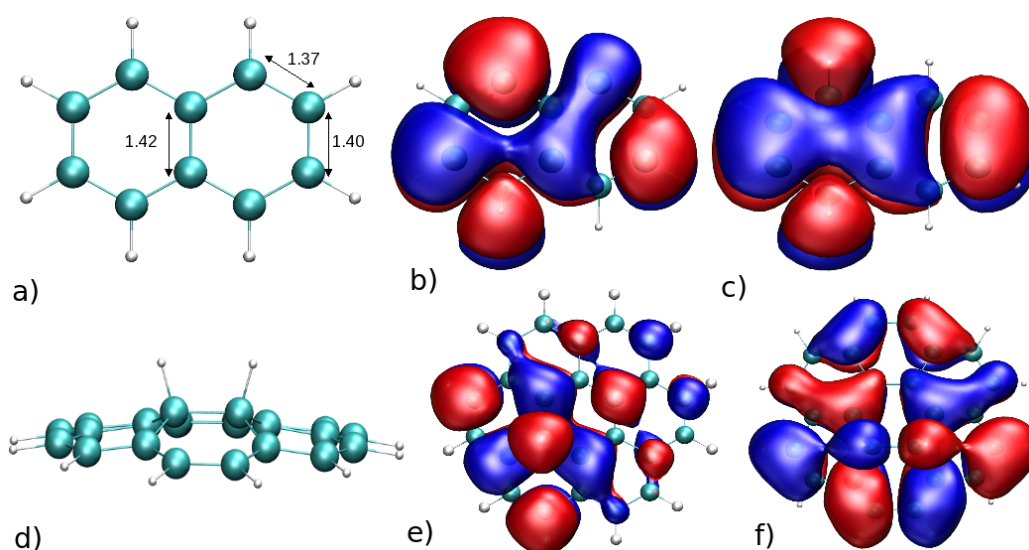


Figure 2.6: Grafting coronene molecule. - a) Atomic structure of naphthalene molecule. Distances in vertical of C-C atoms are greater than distances between C-C in diagonal. b) HOMO state of naphthalene with a H atom attached to it. c) $C_{10}H_{10}$ HOMO state, where all electron are paired. d) Image of the coronene geometry upon two H atom grafting. e) This image show the HOMO state when a single H atom has been grafted to the coronene. Even nearest neighbouring C atom present a node in the HOME state, which disappear upon grafting of the second H atom.

2. GEOMETRICAL AND ELECTRONIC STRUCTURE OF CARBON-RELATED MATERIALS

By extending further the number of fused rings, the symmetrical hexacyclic compound coronene can be constructed. Coronene is a polycyclic aromatic hydrocarbon consisting of seven fused benzene rings and can be described by 20 resonance structures. It has a H/C ratio equal to 1/2, compared with 1 for benzene. Coronene has enhanced aromatic character (higher resonance energy per π -electron) compared to naphthalene and benzene. In the recent years, molecular motifs have been explored to study the magnetic properties of graphene flakes and nanoislands and the convergence to those of graphene (40). Coronene is absolutely flat and, aside from the peripheral hydrogens, reminds a single graphite layer. It has been proposed that coronene can be viewed as a centrosymmetric model substructure of graphite (41).

As these extended aromatic compounds become larger, the ratio of hydrogen to carbon decreases. If we were to imagine fused ring systems of this kind to be further extended in space, the H/C ratio would approach zero, and the resulting compound would be the graphene.

Up to this point the basic chemical properties of aromatic compounds have been explained. We have seen the importance of the atomic orbital hybridization on chemical bonds when describing the structural properties of these finite size molecules. In the next sections, we study aromatic compounds such as graphene, nanoribbons and nanotubes which may be seen as an extension to the infinite of a network made of fused benzene rings. We will focus on the electronic properties of these materials and how they may be implemented in practical applications.

2.9 Graphene

Graphene is basically a single layer of graphite, a hexagonal arrangement of carbon atoms extending to the infinite over two spatial dimensions. Graphite is made of many stacked layers of the same material. The traditional method that chemists used for examining graphene consisted on patches of carbon atoms attached to a surface, but whenever carbon layers were isolated from graphite, they would curve up or stack together. It seemed impossible that planar graphene sheets could be studied in isolation. However, in 2004 A. Geim, K. Novoselov and colleagues at the University of Manchester, UK, announced that they were able to observe individual graphene flakes under an optical microscope by the method of cleaving graphite with sticky tape. This was the starting point of a new era for carbon-based material studies.

The remarkable electronic properties in two-dimensional graphene lattice have been used to demonstrate several predictions of relativistic quantum mechanics. From an experimental approach, it has a practical potential too. An enormous amount of suggested applications include sensors, transistors, terahertz imaging, composites, membranes, energy storage devices, batteries, and thin coatings for solar cells and LCD displays. Hence, graphene may form the basis of a new generation of computer chips which would be smaller and faster than those based on silicon. The pristine quality observed in isolated graphene flakes allows electrons to move through the material for thousands of interatomic distances without scattering

and rapidly dissipate excess heat which converts graphene in a better-quality conductor than silicon. Strong carbon-carbon atom bonds hold the structure intact even at sizes of a few nanometres, where silicon devices decompose.

Scientists have used graphene to test some exotic predictions of quantum electrodynamics in the laboratory. This form of quantum mechanics describes how the movement of an electron is influenced by relativistic effects. An electron moving through an atomic lattice generally behaves as if it were heavier than normal, since it feels the charges on other electrons and atomic nuclei which push and pull it. Electrons in 2D-graphene behave as massless particles which is an astonishing feature derived of graphene electronic structure. Graphene charge carriers respond to electric fields as if they had almost no mass at all and they move through the lattice 300 times slower than the speed of light itself. One of the most exotic effects under investigation in graphene is the Klein paradox, which states that relativistic particles can pass through any potential energy barrier by temporarily pairing up with their antiparticles. In graphene case, this corresponds to electrons and holes passing through electric field barriers.

Graphene benefits from conventional lithography techniques for engineering. In spite of the current progress in these well established techniques for traditional electronics, the main problem is how to create large enough sheets of graphene to be use in industrial applications. Graphene can be made in several ways, the simplest one consists on peeling off a piece of graphite, which is an easy method but poorly controlled.

Another way is to heat up silicon carbide such that silicon leaves the surface and the remaining surface atoms reconstruct into graphene layers. But the graphitic AB-stacking of Si-face graphene causes the band structure of these films to converge to graphite in thin layers. Exfoliated graphene flakes on SiO_2 have been obtained too, but with an important degree of disorder due to impurities and mechanical deformation of the substrate. In contrast, epitaxial graphene grown directly on both $\text{SiC}(0001)$ Si-face and $\text{SiC}(000\bar{1})$ C-face has exceptional film quality. This feature together with epitaxial graphene scalability to integrated circuits makes graphene a good material candidate for BEYOND-CMOS electronics.

Of all forms of graphene (including single exfoliated sheets), only multilayer epitaxial graphene (MEG) grown on the C-face of SiC shows the essential signatures of an isolated graphene sheet like a Berry's phase of π , weak anti-localization and a square root dependence of the Landau's level energies with applied magnetic field (42; 43; 44; 45; 46; 47). Recently, direct measurements of the linear band structure of MEG have been reported. They demonstrate that it is a new material consisting of essentially decoupled graphene layers. These films have long electron relaxation times and present absence of electron-phonon coupling and other distortions related to the Dirac cone, demonstrating that a periodic rotational stacking, other than the 60° associated with graphite, is responsible for MEG's good two-dimensional properties. (48). This special feature make of MEG a promising material for electronic devices.

2. GEOMETRICAL AND ELECTRONIC STRUCTURE OF CARBON-RELATED MATERIALS

2.9.1 Electronic structure of graphene

Graphene is an arrangement of carbon atoms in an infinitely extended two-dimensional hexagonal lattice. In Fig2.7 this lattice is described by the two basis vectors:

$$\vec{a}_1 = -\frac{\sqrt{3}}{2}a_{C-C}\vec{i} + \frac{3}{2}a_{C-C}\vec{j} \quad (2.1)$$

$$\vec{a}_2 = \frac{\sqrt{3}}{2}a_{C-C}\vec{i} + \frac{3}{2}a_{C-C}\vec{j} \quad (2.2)$$

The unit cell contains two inequivalent carbon atoms, each of which is bonded to its first three neighbouring atoms.¹ Two types of bonds are present in the lattice: σ -bonds involving electrons in the $2s, 2p_x, 2p_y$ orbitals of carbon atoms, and π -bonds involving electrons in the $2p_z$ orbitals.

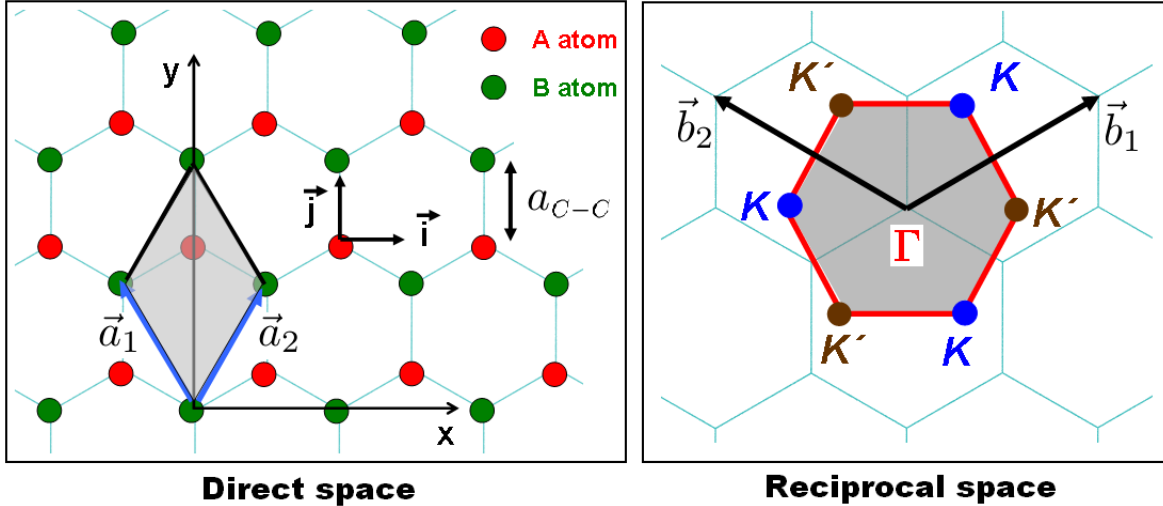


Figure 2.7: Graphene lattice representation - Left: the honeycomb structure of graphene and its Brillouin zone in reciprocal space. Two sites (A and B) per unit cell represent the inequivalent carbon atoms. The hexagonal lattice is generated by linear combination of \vec{a}_1 and \vec{a}_2 which are at 60° against each other. Vector lengths $\|\vec{a}_1\| = \|\vec{a}_2\| = \sqrt{3}a_{C-C} \sim 2.46\text{\AA}$. Right: reciprocal lattice vectors are defined by the orthonormal relation $a_i b_j = \delta_{i,j}$. Brillouin zone of graphene (shaded region) is characterized by the six Dirac points K and K' .

In a first and reliable approximation, electronic band structure of graphene can be calculated using the tight-binding approximation, also known as LCAO method. While localized σ -bonds are committed to have carbon atoms tightly in the hexagonal net, higher energy π -electrons are free to move along the 2D-lattice due to their delocalized character. We can

¹The bond of a carbon atom to the rest of atoms in the lattice is determined by the spatial extension of its wavefunction radial part. The nearest neighbouring atom model, coming from tight-binding models, is extended to further neighbours when some other approach, as DFT models, are considered.

consider only the electrons in the p_z -orbitals which create the π -bands. These energy levels close to graphene Fermi energy account for transport properties of graphene and GNRs.

Due to the periodicity of the lattice, the electronic band structure of graphene can be calculated considering Bloch's functions. Each of the sublattices is described by a function:

$$\Psi_A = \frac{1}{\sqrt{N}} \sum_n^N e^{i\vec{k}\vec{R}_{A_n}} \phi_A(\vec{r} - \vec{R}_{A_n}) \quad (2.3)$$

$$\Psi_B = \frac{1}{\sqrt{N}} \sum_n^N e^{i\vec{k}\vec{R}_{B_n}} \phi_B(\vec{r} - \vec{R}_{B_n}) \quad (2.4)$$

where $\vec{k} = (k_x, k_y)$ is the wavevector, N is the number of arbitrarily large number of unit cells considered, $\phi_A(\vec{r} - \vec{R}_{A_n})$ and $\phi_B(\vec{r} - \vec{R}_{B_n})$ represent the wavefunction of the p_z -orbitals of carbon A and B centered in \vec{R}_{A_n} and \vec{R}_{B_n} n-cell positions, respectively. We assume orthogonality in ϕ_i , i.e., $\langle \phi_A | \phi_B \rangle = \delta_{AB}$. The solution to the electronic structure comes from solving the Schrödinger equation for a wavefunction which is expressed as a linear combination of 2.3 and 2.4:

$$\Psi = a\Psi_A + b\Psi_B \quad (2.5)$$

Let \mathcal{H} be the Hamiltonian describing the motion of an electron in the atomic potential imposed by the rest of charged particles in the graphene lattice. In the tight-binding formalism, the matrix elements are given by $H_{i,j} = \langle \Psi_i | \mathcal{H} | \Psi_j \rangle$ ($i,j=A,B$), which can be obtained from the relations:

$$\langle \phi_A | \mathcal{H} | \phi_A \rangle = \langle \phi_B | \mathcal{H} | \phi_B \rangle = \epsilon_0 \quad (2.6)$$

$$\langle \phi_A | \mathcal{H} | \phi_B \rangle = \langle \phi_B | \mathcal{H} | \phi_A \rangle = \gamma_0 \quad (2.7)$$

Without loss of generality, the on-site energy is shifted to zero, $\epsilon_0 = 0$, which corresponds to a shift in the zero energy. Then \mathcal{H} matrix elements read:

$$H_{AA} = H_{BB} = \langle \Psi_{A(B)} | \mathcal{H} | \Psi_{A(B)} \rangle = 0 \quad (2.8)$$

$$H_{AB} = H_{BA}^* = \langle \Psi_A | \mathcal{H} | \Psi_B \rangle \quad (2.9)$$

The remaining integral can be calculated knowing that the relative positions of the first neighbour atoms of atom A in the unit cell are:

$$\vec{r}_{B1} = \frac{1}{3}(1, 1) \quad (2.10)$$

$$\vec{r}_{B2} = \frac{1}{3}(1, -2) \quad (2.11)$$

$$\vec{r}_{B3} = \frac{1}{3}(-2, 1) \quad (2.12)$$

from which we obtain:

2. GEOMETRICAL AND ELECTRONIC STRUCTURE OF CARBON-RELATED MATERIALS

$$H_{AB} = \gamma_0 \left\{ \exp \left[i\vec{k} \left(\frac{\vec{a}_1 + \vec{a}_2}{3} \right) \right] + \exp \left[i\vec{k} \left(\frac{\vec{a}_1 - 2\vec{a}_2}{3} \right) \right] + \exp \left[i\vec{k} \left(\frac{-2\vec{a}_1 + \vec{a}_2}{3} \right) \right] \right\} \quad (2.13)$$

Once the matrix elements of the Hamiltonian are known, the dispersion relation is obtained by solving the eigenvalue equation:

$$\mathcal{H}(\vec{k})|\Psi\rangle = E(\vec{k})\mathbb{I}|\Psi\rangle \quad (2.14)$$

$$\begin{bmatrix} 0 & H_{AB} \\ H_{BA} & 0 \end{bmatrix} \begin{bmatrix} |\Psi_A\rangle \\ |\Psi_B\rangle \end{bmatrix} = \begin{bmatrix} E(\vec{k}) & 0 \\ 0 & E(\vec{k}) \end{bmatrix} \begin{bmatrix} |\Psi_A\rangle \\ |\Psi_B\rangle \end{bmatrix} \quad (2.15)$$

which has a solution for $E(\vec{k})$ fulfilling:

$$\det [\mathcal{H}(\vec{k}) - E(\vec{k})\mathbb{I}] = 0 \quad (2.16)$$

The solution of this equation is the graphene dispersion relation:

$$E(k_x, k_y) = \pm \gamma_0 \sqrt{1 + 4 \cos \left(\frac{3a_{C-C} k_y}{2} \right) \cos \left(\frac{\sqrt{3}a_{C-C} k_x}{2} \right) + 4 \cos^2 \left(\frac{\sqrt{3}a_{C-C} k_x}{2} \right)} \quad (2.17)$$

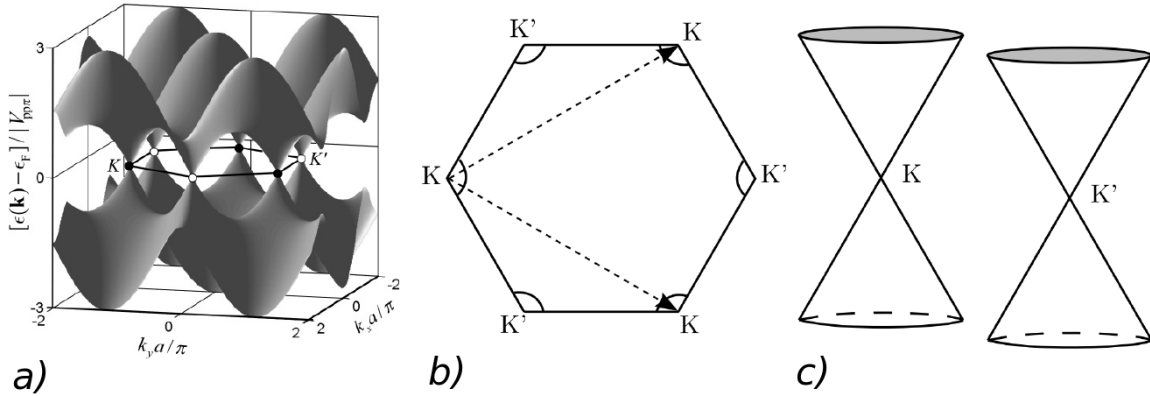


Figure 2.8: Graphene energy bands. - a) The dispersion relation for graphene consists on a full valence band and empty conduction band which touch one another in six points. Center: these points delimits the Brillouin zone and are also indicated in 2.7 by K and K'. (Image obtained from ref.(49)) b) and c) The dispersion relation becomes linear in the surrounding of Dirac's points adopting a conical shape.

Fig.2.8a) shows a plot of this result. Both valence and conduction bands find each other in six points of the reciprocal space called inequivalent Dirac points, labeled as K and K' in Fig.2.8b). In the surrounding of these points, the dispersion relation 2.17 can be linearly

approximated, resulting in the conical-shaped bands depicted Fig.2.8c). Electrons and holes have similar properties due to the specular symmetry of both bands with respect to the Fermi energy plane. Dirac's points form a time-reversal pair, namely, opposite chirality, which along with a Berry's phase of π provides an environment for unconventional two-dimensional electronic properties, such as the absence of backscattering or half-integer quantum Hall effect.

2.10 Graphene nanoribbons (GNRs)

Graphene nanoribbons are unrolled single-walled carbon nanotubes or strips of graphene, cut in a particular pattern. They could be defined as a one-dimensional graphite network confined by a pair of parallel edges at both sides of the structure.

The classification of individual GNRs is similar to the convention followed with CNTs. Depending on edge symmetry, GNRs can either be in a zigzag or armchair configuration. Usually, only achiral GNRs are considered as the shape of the edges plays an important role in the stability. A (N,N) armchair CNT unrolls into a zigzag GNR (zGNR) with a width of $N_z = 2N$ zigzag carbon strips. A (N,0) zigzag CNT unrolls into an armchair GNR (aGNR) with $N_a = 2N$ lines of carbon dimers. Only even values of N_a and N_z refer to symmetric GNRs and can be constructed by unrolling CNTs. Odd values of N_a and N_z correspond to asymmetric GNRs which cannot be constructed by unrolling CNTs.

Interest in GNRs started at the same time as the attraction for the physics of 2D-graphene, since ribbons were considered by theorists as a genuine alternative to CNTs as one-dimensional quantum wires. The challenge lies in obtaining a sharply cut strip from a larger dimensional material. Nanoribbons of graphene must be cut from larger sheets using chemical methods that offer little control over the width of the ribbons. In Fig.2.9 two of the most recent techniques are presented. A simple and more precise alternative has been developed by H Dai's team at Stanford University (55). This technique begins with multi-walled carbon nanotubes made up of up to 20 concentric nanotubes nested inside one another. The tubes are half-submerged in a polymer such that half of each tube is exposed to argon plasma which is used to destroy the exposed side of the tubes. The resulting gutter-shaped graphene sheets can be removed and they are laid flat. With this method ribbons of 10 to 20 nanometres wide and up to several thousand nanometres long can be obtained. Another technique unzip nanotubes by inserting lithium and ammonia in between the concentric layers of a multi-walled carbon nanotube. This forces the tubes to split and open when water is added to react with the lithium (56).

2.10.1 Electronic structure of graphene nanoribbons

Because of its unusual physical properties, graphene is seen as a promising alternative to silicon in future electronic devices. However, graphene is a "zero-gap" material, meaning that there is no energy gap between its conduction and valence bands. In conventional

2. GEOMETRICAL AND ELECTRONIC STRUCTURE OF CARBON-RELATED MATERIALS

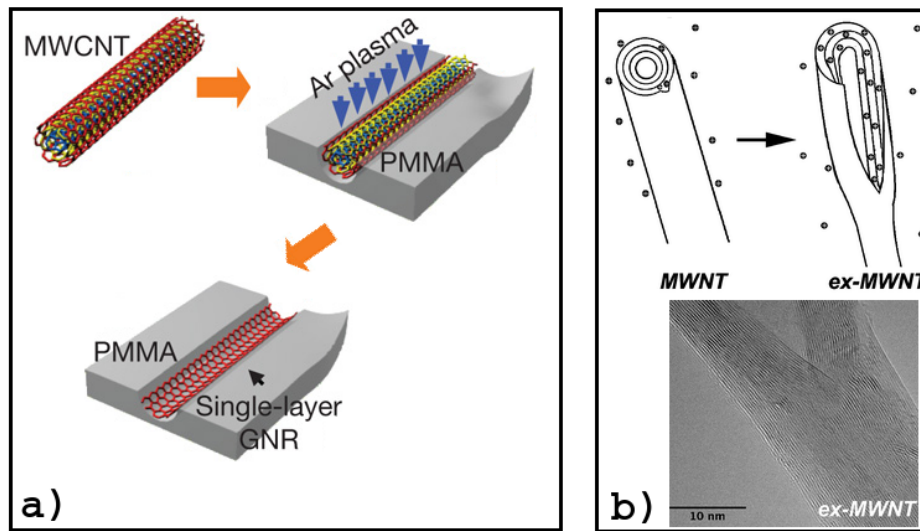


Figure 2.9: Making GNRs from CNTs. - In each presented case, a pristine MWCNT is always used as the starting raw material. a) In Dai's method, the PMMA-MWCNT film is peeled from the Si substrate, turned over and then exposed to an Ar plasma. Multi- or single-layer GNRs are produced after etching for increasing times and, finally, the PMMA is removed to release the GNR. b) Terrones' group approach opens MWCNTs longitudinally by intercalation of lithium and ammonia followed by exfoliation. (Images obtained from Ref.(55) and Ref.(56)).

semiconductors this gap is mandatory to make transistors and other electronic devices. One way of creating energy gaps in graphene is to reduce it into a ultra-thin ($\sim 2-3$ nm) ribbon so that electrons are confined to move in only one dimension. Graphene properties remain when graphene devices scale down to a few benzene rings, which is what one needs for top-down molecular electronics (50). Recently, experimental observation of conductance quantization in graphene nanoribbons has been reported where one-dimensional transport subbands are formed due to the lateral quantum confinement at temperatures of 80 K, channel lengths of $1.7\mu m$ and 30 nm wide (51).

Herein we review the electronic structure of GNRs having armchair and zigzag edges, which are the two basic shapes for graphitic edges. A graphene sheet can be cut along a straight line to obtain the two types of edge shapes with a difference of 30° in the axial direction between the two edge orientations. From now on, we will refer to a N-aGNR or N-zGNR as armchair and zigzag GNR where N denotes the width by indicating the number of armchair and zigzag dimer dimer lines, respectively.

Carbon atoms in the edges are 2-fold coordinates while the inner atoms in the structure are 3-fold coordinated. A common way to passivate the third sp^2 orbital is to attach a hydrogen atom to it, such that the dangling bonds of edge atoms do not contribute to the electronic state near the Fermi level. As in the case of nanotubes, we resort to tight-binding model within the Hückel approximation to calculate the electronic states for the ribbon, which will allows us to extract precious information about the relationship between the π -electronic structure and the edge shape. Indeed, these states are responsible for pristine ribbon transport properties, hence the interest on isolating π -bands and revealing the intrinsic differences originating from the topological nature of both types of edges.

In spite of the difference on the surrounding environment for inner and edge carbon atoms in ribbon structure, all of them are considered to have zero on-site energy. The coupling between first neighbouring carbon atoms is constant and equal to γ_0 . As in graphene, a unit cell of nanoribbon contains two inequivalent types of atoms that will be referred as A and B. The associated wavefunctions can be written as is eq.2.3 and eq.2.4.

In the following, we study separately electronic properties of both aGNRs and zGNRs.

Armchair graphene nanoribbons

An aGNR unit cell contains N A-type atoms and N B-type atoms. Due to translational invariance, the electronic wavefunction can be expressed as a linear combination of Ψ_A and Ψ_B sublattice Bloch's wavefunctions. By applying boundary conditions determined by the quantization rule:

$$q_y = \frac{2\pi}{\sqrt{3}a(N-1)}p \quad \text{where } p \in \mathbb{N} \quad (2.18)$$

for the wavefunction at both edges of the ribbon, the system wavefunction reads:

2. GEOMETRICAL AND ELECTRONIC STRUCTURE OF CARBON-RELATED MATERIALS

$$\Psi = \sqrt{\frac{2}{N_x(N+1)}} \sum_{j=1}^N \sin\left(\frac{\sqrt{3}q_y a j}{2}\right) \left[c_A \sum_{xA} e^{i\vec{k}\vec{R}_{Aj}} \phi_A(\vec{r} - \vec{R}_{Aj}) + c_B \sum_{xB} e^{i\vec{k}\vec{R}_{Bj}} \phi_B(\vec{r} - \vec{R}_{Bj}) \right] \quad (2.19)$$

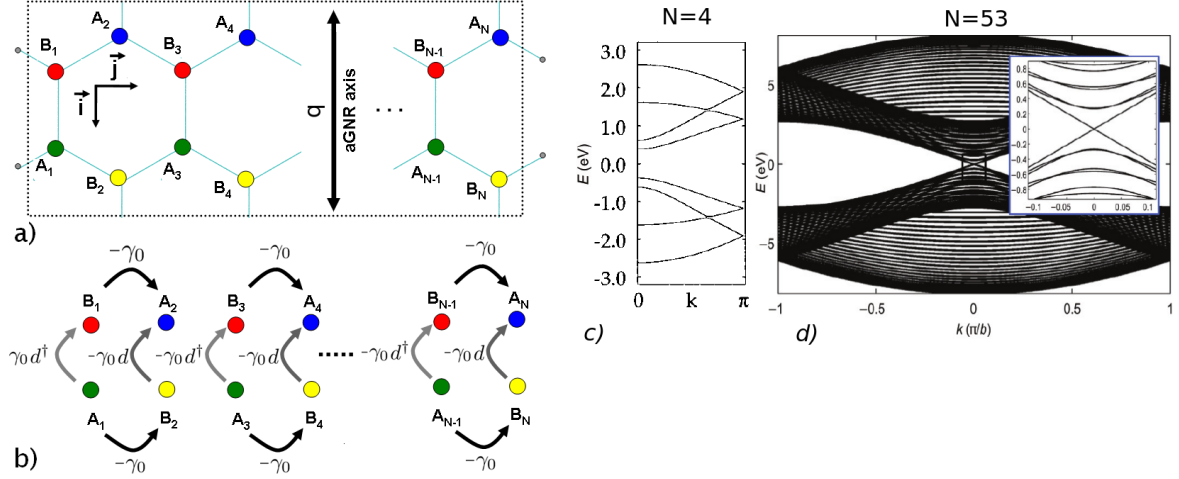


Figure 2.10: N dimers of carbon atoms forming a aGNR unit cell. - a) N A-atoms and N B-atoms in the unit cell (shown in this figure by dashed lines) can be extended along ribbon axis to create an armchair-shaped graphene nanoribbon. Unit cell length is represented by $b = \sqrt{3}a/2$. Little gray circles represent the passivating hydrogen atoms. b) This convenient arrangement of carbon atoms allows us to construct a 4×4 -block Hamiltonian which can be easily decomposed in two linear chains with an interchain coupling given by $\gamma_0 e^{\pm ikb/2}$. The intrachain orbital coupling is γ_0 . c) Energy vs k for an armchair graphene nanoribbon with $N = 4$ (52). d) Calculated energy bands for a metallic ribbon with $N = 53$. In inset, the Dirac-like linear dispersion relation for $k = 0$ (Γ -point) is shown in detail. In both cases, dispersion relations have been computed within the tight-binding framework. (Images of c) and d) obtained from (52) and (53), respectively)

For the two inequivalent atoms in the aGNR unit cell, Schrödinger equation can be written in a 2×2 matrix, from which k -dependent eigenvalues can be found:

$$E(k, q_y) = \pm \gamma_0 |2e^{ika/2} \cos(\sqrt{3}q_y a/2) + e^{-ika}| = \pm |\Gamma^*(k, q_y)| \quad (2.20)$$

This is the dispersion relation for an aGNR which has as eigenfunctions:

$$\Psi(k, q_y) = \frac{1}{\sqrt{2}} \left[\Psi_A \pm \sqrt{\Gamma^*(k, q_y)/\Gamma(k, q_y)} \Psi_B \right] \quad (2.21)$$

By scrutinizing the possible values of $\Gamma^*(k, q_y)$, one can extract information about the electronic behaviour of the ribbon as a function of its width, namely, the number of dimers:

2. GEOMETRICAL AND ELECTRONIC STRUCTURE OF CARBON-RELATED MATERIALS

This result can be obtained by doing $k = 0$ in the Hamiltonian above and diagonalizing. Analytic results can be obtained and, hence, the energy gap of eq.2.22

Zigzag graphene nanoribbons

Fig.2.11-a) shows a N -dimer unit cell of a zigzag GNR. It is evident that all carbon atoms in the left-edge are A-type atoms while the ones in the opposite edge belong to the B-type atom category. Therefore, solving the Dirac's equation implies to assign different boundary conditions to the two sublattices. In particular, the wavefunction of the A-sublattice is required to vanish on the left-side of the ribbon while its counterpart B-sublattice is assumed to behave equally on the right-side of the ribbon. The eigenfunction of Dirac's equation can be separated in two groups, the first of which includes eigenfunctions with wavenumber $k > 1/W$ and the second one includes states with $k < 1/W$, where W is the ribbon width.

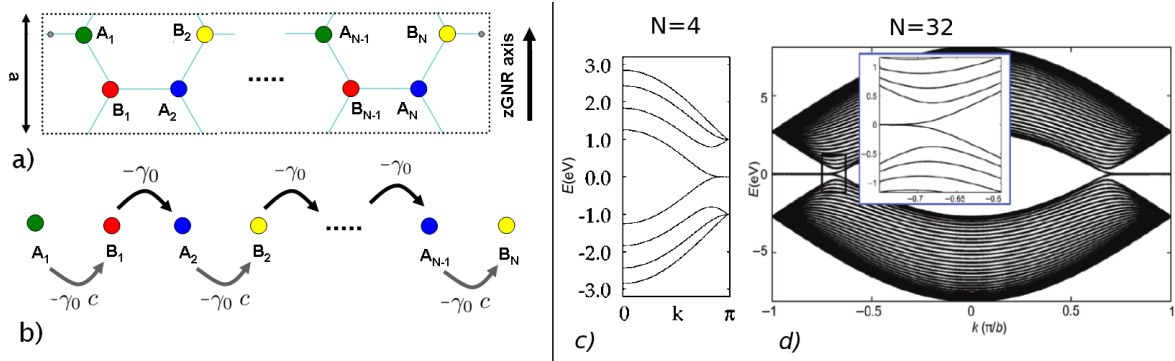


Figure 2.11: N dimers of carbon atoms forming a zGNR unit cell. - a) N A-atoms and N B-atoms in the unit cell (shown by dashed lines) can be extended along ribbon axis to create an armchair-shaped graphene nanoribbon. Little gray circles represent the passivating hydrogen atoms. b) an equivalent system is shown. This particular arrangement of carbon atoms leads to a Hamiltonian which can be interpreted as the energetic description of a single-orbital per site linear chain with an alternating orbital coupling given by γ_0 and $\gamma_0 c$, where $c \equiv c(k) = \cos(ka/2)$. c) Energy vs k for a zigzag graphene nanoribbon with $N = 4$. d) Calculated energy bands for a metallic ribbon with $N = 53$. In inset, the Dirac-like linear dispersion relation for $k = \pm 2\pi/3a$ is shown in detail. In both cases, dispersion relations have been computed within the tight-binding framework. (Images of c) and d) obtained from (52) and (53), respectively)

The first group corresponds to surface states with an exponential decay from the edges of the ribbon while the second group corresponds to confined states with nodes along the transverse section of the ribbon. Tight-binding approximation provides us again a simple and effective model to obtain the shape of these bands. We start by expressing the tight-binding Hamiltonian on the Bloch's sum and within a single-orbital per atom model. The

2. GEOMETRICAL AND ELECTRONIC STRUCTURE OF CARBON-RELATED MATERIALS

filamentary deposit from where he discovered the nanotubes, identifying them as tubular objects with nanometric diameter and micrometric length. Since then, CNTs have been one of the most significant contribution to current research in Nanotechnology.

CNTs, both single- and multi-walled, can be seen as sheets of single or multiple graphene layers rolled into cylinders and capped with half-fullerenes. Nanotubes are considered as macromolecular form of carbon and exhibit unique properties since they manifest properties that are usually associated with molecular species, such as solubility in organic solvents, solution-based chemical transformations, chromatography, and spectroscopy. Furthermore, nanotubes possess some spectacular properties such as high electrical and thermal conductivity, high mechanical strength and high surface area. CNTs provide an example of the special properties inherent at the quantum level because they can act as either semiconductors or metals, depending of the chirality. These properties make nanotubes extremely interesting to industry and researchers.

The same as graphite, CNTs are very resistant in the chemical and mechanical sense. CNTs possible uses in medicine and in engineering are broad and even unexpected, while the health risks they posed need still to be fully analyzed (30).

2.11.1 Crystal structure of nanotubes

One of the most fascinating feature of nanotubes is the possible huge difference between length scales: length ranging from several nanometers up to several micrometers and diameters of nanometric order (typically 1-10 nm), comparable to DNA-helix molecule. Another striking feature of nanotubes is the periodic arrangement of the carbon atoms to form a crystal structure which can be obtained by rolling up a sheet of hexagons as in a graphene structure. Closing the cylinder on the caps requires the distortion of the hexagonal lattice and hence the sp^2 bonds. Structural defects in the form of pentagonal rings are needed to bend the lattice and the distribution of these pentagons convert the tip in a half-fullerene.

To give a complete description of CNTs atomic structure, one must examine the precise way the graphene sheet is rolled up. Fig.2.12 shows the operation of superposing two equivalent hexagons (labeled as A and B) of the lattice and the dependence of the final result with the choice of these hexagons. The diameter of the tube and its chirality are determined by the relative orientation of the chosen rings. The chiral angle or helicity, specifies the direction along which the original lattice is folded and is defined as the angle θ between cylinder axis and a reference direction that could be one of the sides of the hexagon (see Fig.2.12a). Given the symmetry of the hexagonal net, θ can vary between 0 and 30 degrees, and an infinite series of nanotube unit cells can be constructed from this angle. For the sake of simplicity, the set of nanotubes that can be in principle designed by choosing a θ value, is divided in three categories called armchair, zigzag and chiral configurations.

Zigzag and armchair have a chiral angle of 0° and 30° , respectively. These names refer to the shape of the edge obtained upon cutting a nanotube by a plane perpendicular to its axis and they are also known as achiral tubes. In Fig.2.12b) and c) a common feature to both specimens can be observed: two hexagons in the tube facing along the diameter have the

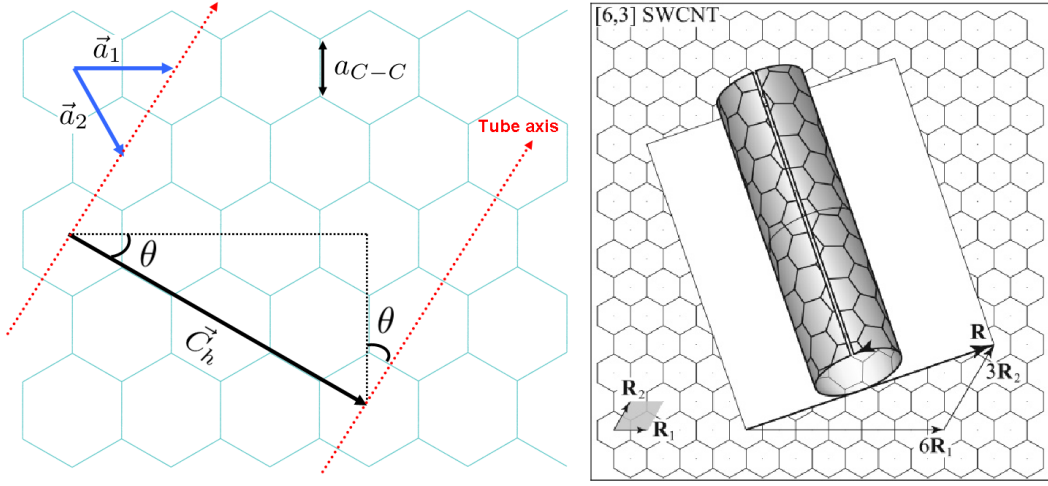


Figure 2.12: Converting graphene sheet in a nanotube. - Left: the two tubes shown in Fig.2.13 result from rolling up the graphene sheet at different angles θ . For $\theta = 30^\circ$ and $\theta = 0^\circ$ armchair and zigzag configurations are obtained, respectively. For any other orientation of \vec{C}_h vector, chiral nanotubes can be constructed. Right: graphical demonstration of (6,3) CNT construction. (Image obtained from ref.(49))

same orientation. This property is not satisfied in tubes with chiral angle ranging between 0° and 30° , which belong to the chiral category. In armchair tubes, carbon atoms are grouped in pairs in each of the perpendicular planes to the tube axis while in zigzag tubes each carbon atom is separated of its nearest neighbour atom the same distance in the same plane. The chiral angle defines the length of nanotube unit cells. In both types of achiral tubes, a unit cell contains the same number of atoms but distributed in a different number of planes: in zigzag tubes, four planes constitute a unit cell while in armchair tubes a unit cell is built up with only two atomic planes.

This can be formally stated by geometry inspection of the graphene sheet from which nanotube geometries are derived. The chiral vector $\vec{C}_h = n\vec{a}_1 + m\vec{a}_2$ (with $n, m \in \mathbb{N}$), which connects two crystallographically equivalent points in the planar lattice. \vec{C}_h is defined as a linear combination of graphene lattice basis vectors a_1 and a_2 which are multiplied by the pair of integer numbers (n,m) . These indices are widely used in the literature to refer to the nanotubes. Chirality and electronic properties of CNTs depend directly on (n,m) indices:

- $(n,0)$ when m index is equals to 0, a metallic or semiconducting zigzag nanotube is obtained depending on n : if $n \bmod 3 \neq 0$ a little gap which depends on nanotube diameter shows up and gives to the tube a quasi metallic-like electronic behaviour. For $n \bmod 3 = 0$ nanotube shows a diameter dependent gap in its structure of bands which provides to the tube a semiconducting character.

2. GEOMETRICAL AND ELECTRONIC STRUCTURE OF CARBON-RELATED MATERIALS

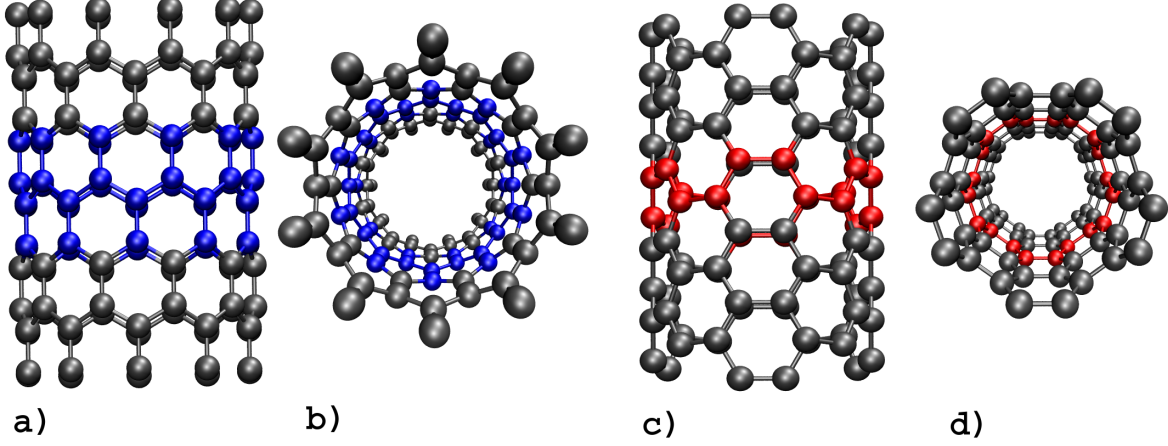


Figure 2.13: 3-unit cell CNTs - a) and c) show zigzag and armchair tubes with one unit cell colored in blue and red, respectively. In both cases, diametrically opposed hexagons are superimposed, a feature which is only found in achiral tubes. b) and d) are images of the same tubes in perspective representation.

- (n,n) if both indices have the same value, nanotube belong to armchair category. A zero gap is always present independently of nanotube diameter size.
- (n,m) for n,m values following a relation other than the above presented, the nanotube is said to be achiral. In general, for any pair of index fulfilling the relation $n - m = 3q$ (q an integer) nanotubes present a metallic character; otherwise, they are semiconducting.

As a matter of fact, (n,m) define all the geometrical properties of defectless carbon nanotubes, such as diameter, chiral angle, unit cell vector (\vec{T}):

- CNT diameter $d_{CNT} = \frac{1}{\pi} \|\vec{C}\| = \frac{\sqrt{3}a_0}{\pi} \sqrt{m^2 + mn + n^2}$
- Chiral angle $\theta = \arctan \frac{\sqrt{3}m}{m+2n}$
- Translation vector $\vec{T} = \frac{2m+n}{d_r} \vec{a}_1 - \frac{2n+m}{d_r} \vec{a}_2$

where:

$$d_r = \begin{cases} \text{cgd}(n, m) & \text{if } m - n \text{ not multiple of } 3 \times \text{gcd}(n, m), \\ 3 \times \text{cgd}(n, m) & \text{if } m - n \text{ multiple of } 3 \times \text{gcd}(n, m) \end{cases} \quad (2.28)$$

and gcd stands for greatest common divisor.

2.11.1.1 Electronic structure of carbon nanotubes

The electronic structure of CNTs can be deduced from that of graphene. A quantization rule is imposed by the periodic boundary conditions:

$$\vec{C} \cdot \vec{k} = 2\pi q \quad , \text{ where } q \in \mathbb{Z} \quad (2.29)$$

Along this work, only armchair and zigzag CNTs are considered. We analyze the electronic properties of each of them separately.

Armchair carbon nanotubes

For a (n,n) tube, $2 \times 2 \times n$ valence electrons are contained in the $2n$ unit cells of corresponding graphene lattice. Regarding the chiral and translational vectors, we have:

$$\vec{C} = n(\vec{a}_1 + \vec{a}_2) \quad (2.30)$$

$$\vec{T} = (\vec{a}_2 - \vec{a}_1) = \sqrt{3}a_{C-C}\vec{i} = a\vec{i} \quad (2.31)$$

The Brillouin zone in an armchair CNT is defined by:

$$-\pi/a < k_x < \pi/a. \quad (2.32)$$

Expressing the chiral vector in terms of the cartesian basis vectors (\vec{i}, \vec{j}) , relation 2.29 shows that the wavevector is quantized as:

$$k_y = \frac{q^2\pi}{3na_{C-C}}, \quad \text{where } q \in \mathbb{Z}, \quad (2.33)$$

This result leads to the dispersion relation:

$$E(k_x, k_y) \equiv E(k_x) = \pm\gamma_0 \sqrt{1 + 4\cos\left(\frac{q\pi}{n}\right)\cos\left(\frac{a}{2}k_x\right) + \cos^2\left(\frac{a}{2}k_x\right)} \quad (2.34)$$

This expression gives us a simple recipe to obtain the electronic band structure of an armchair CNT from a graphene sheet: to cut the hexagonal flat lattice by planes defined by the quantized values of k_y . This is the so-called band folding scheme which is represented in Fig.2.14 for the case of a (5,5) tube, where the cutting planes and the energy bands obtained from Ref. 2.34 are plotted. The $n = 5$ values of q gives rise to n corresponding subbands. The fold over the first BZ gives rise to a $(n + 1)$ th dispersion relation corresponding to $q = 0$. This particular band structure includes 5 subbands for energies greater than Fermi energy and 5 subbands for energies below Fermi energy. Each of these bands is doubly degenerated except the ones corresponding to $q = 0$ and $q = n$, as consequence of the $2n$ graphite unit cells in the nanotube unit cell.

Notice that the two bands at Fermi energy (for $k_x = \pm\frac{2\pi}{3a}$), lead to the metallic features of armchair CNTs, as can be observed on the crossing bands in Fig.2.14c)-left, and the non-zero density of states in Fig.2.14c)-right, at Fermi energy level.

2. GEOMETRICAL AND ELECTRONIC STRUCTURE OF CARBON-RELATED MATERIALS

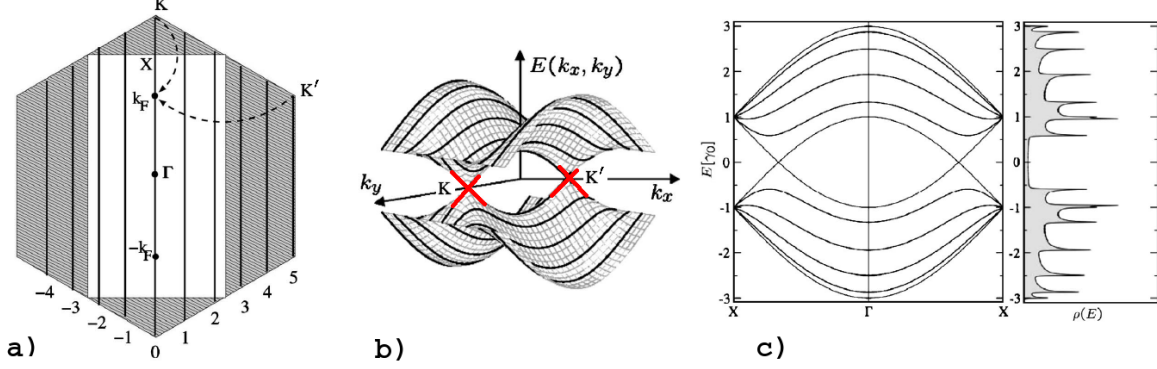


Figure 2.14: Band folding scheme. - a), quantization condition for a (5,5) armchair CNT on the 1st BZ of graphene. b), electronic band structure of the same tube obtained in the band-folding approach, by folding the colored corners onto the rectangular cell and superimposing the graphene energy bands calculated along the thick lines in a). c), band structures and density of states, $\rho(\epsilon)$, for a (5,5) tube (with $\gamma_0 = 2.9eV$). The energy bands are plotted along the $X - \Gamma - X$ direction in the BZ. Images obtained from Ref. (91)

Zigzag carbon nanotubes

For a $(n,0)$ carbon nanotube, chiral and translational vectors are:

$$\vec{C} = n\vec{a}_1 \quad (2.35)$$

$$\vec{T} = (\vec{a}_1 - 2\vec{a}_2) \quad (2.36)$$

In the framework of reference specified in Fig.2.7 and Fig.2.12, the quantization rule applied to zigzag nanotubes leads to:

$$k_x = \frac{2\pi}{\sqrt{3}na_{C-C}}q \quad , \text{ where } q \in \mathbb{Z}, \quad (2.37)$$

As in the case of armchair nanotubes, the electronic band structure folded over the first BZ gives rise to an $(n+1)$ th subband corresponding to $q = 0$. Therefore, this band structure contains $n+1$ subbands with energies above the Fermi level and $n+1$ subbands with negative energies. All the bands except the corresponding to $q = 0, n$, are doubly degenerated. None of the subbands contains a graphene K point and, hence, a forbidden energy gap appears between electron and transport subbands.

In the tight-binding approximation, the electronic band structure of $(3p,0)$ zigzag nanotubes, (where $p \in \mathbb{Z}$) presents a zero gap, as can be appreciated in 2.15 for a $(9,0)$ tube. This is consequence of the presence of a graphene K point in one of the subbands. As it was pointed out above, the $(n,0)$ zigzag carbon nanotubes are metallic only if n is an integer multiple of 3.

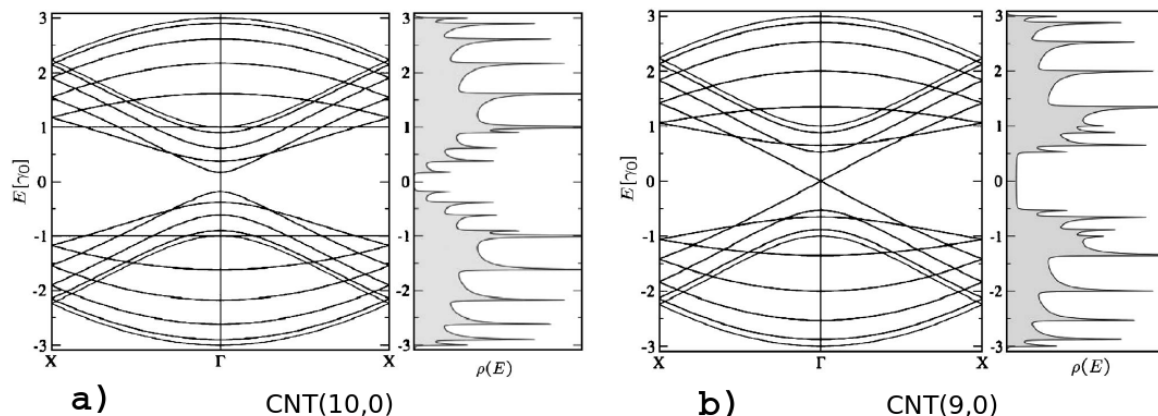


Figure 2.15: Band structure and DoS. - Band structure (a)-left) and density of states (DoS) (a)-right) for a (10,0) zigzag CNT within the zone folding model. At zero energy (Fermi level) electron and conduction bands are separated by a gap and density of states vanishes. Only zigzag CNTs with n-index a multiple of 3 present do not present a gap. (b)-left b)-right) same for a (9,0) zigzag CNT. (Images obtained from Ref.(91))

Within the band-folding picture, the bandgap can be seen to depend inversely on diameter: as the diameter becomes smaller, the spacing between the lines in k-space for which the quantization condition is satisfied becomes larger. For semiconducting nanotubes the result is a bandgap that to first order is given by $E_g = 0.7/d \text{ eV} \cdot \text{nm}^{-1}$, where d is the chirality-independent nanotube diameter. If one takes into account the curvature of the graphene sheet in a nanotube there is an additional contribution to the gap $\sim d^{-2}$, which also means that metallic nanotubes with indices other than (n,n) have a small bandgap.

Nanoscale semiconducting materials such as nanowires and CNTs, show great potential for use as highly sensitive electronic biosensors. SWNTs have been demonstrated to be the ultimate biosensor in this class since they have a remarkably small diameter ($\sim 1\text{nm}$), comparable to the size of biomolecules and to the electrostatic screening length in physiological solutions. Furthermore, the low charge carrier density of SWNTs (73) is directly comparable to the surface charge density of proteins,(74). This makes SWNTs well suited for electronic detection based on electrostatic interactions with analyte biomolecules. Finally, as SWNT consists of one-atom thick surface, every carbon atom is in direct contact with the environment which allows for optimal interaction with environmental biomolecules. Although an important amount of biosensing studies have been made using carbon nanotube as the central part of transistors, the physical mechanism which dominates device sensing capabilities is not completely known yet (75). Previously suggested mechanisms are electrostatic gating, carrier mobility changes, changes in gate coupling, and Schottky barrier effects. Understanding sensing mechanisms and controlling device building techniques will permit further exploitation of these promising nanosensors.

2. GEOMETRICAL AND ELECTRONIC STRUCTURE OF CARBON-RELATED MATERIALS

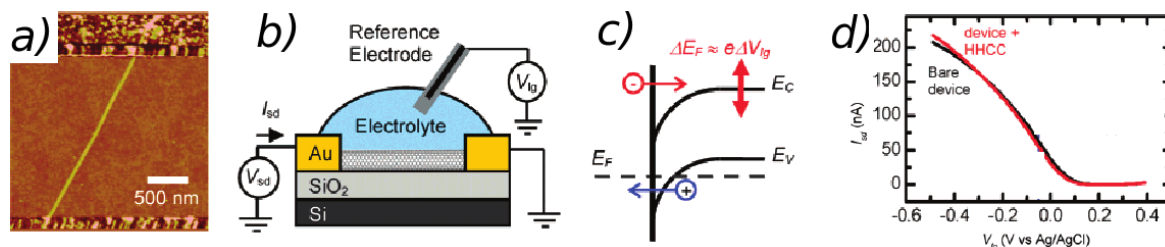


Figure 2.16: Experimental layout and results of a typical nanotube-based device for biosensing. - a) AFM image of a SWNT between Cr/Au contacts on a insulating SiO₂ substrate. b) Measurement setup, where a source-drain bias potential is applied and the device is gated through an Ag/AgCl reference electrode inserted in the electrolyte. c) Band diagram for a hole-doped SWNT showing electron conduction through thermally activated carriers into conductance band and hole conduction through tunneling through the Schottky barrier. E_F is the Fermi energy. E_C and E_V are the energies of SWNT conduction and valence band edges, respectively. The gate potential changes the doping level of the SWNT as indicated by the red arrows. d) as results of a typical biosensing experiment, current vs gate potential curves acquired before (black line) and after (red line) adsorption. Images obtained from ref.(70)

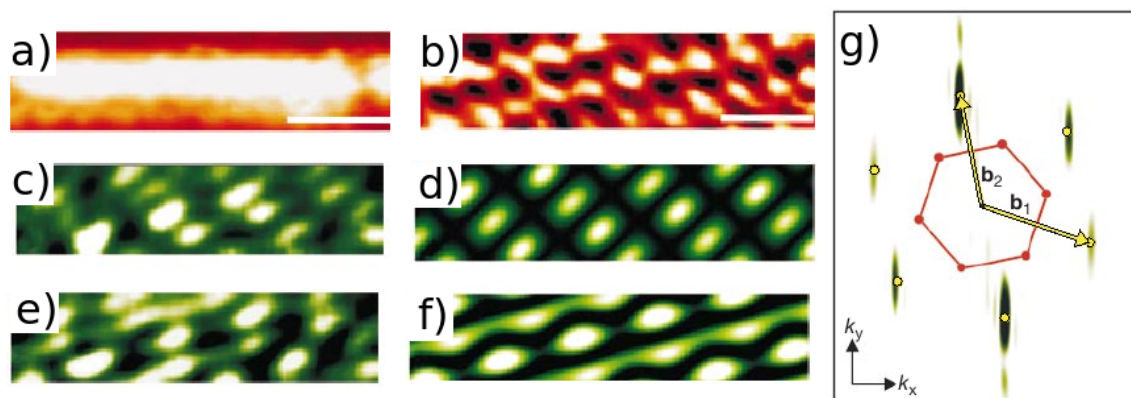


Figure 2.17: STM image of a nanotube. - Energy-resolved images of individual nanotube molecular wavefunctions. a) and b) Constant current topographic image of a chiral metallic SWNT. c) and e) Energy resolved images of the individual states at energies of -96 and 30 eV respectively. d) and f) Calculated spatial maps of the density of states at the energies of c) and e), showing the well reproduced characteristic features of each STM image. g) Two-dimensional Fourier transform of a topographic image of a SWNT atomic lattice. Wavevectors corresponding to reciprocal lattice vectors $\vec{G} = m\vec{b}_1 + n\vec{b}_2$ coincide with the peaks of intensity (yellow circles), where m, n are integers. The red hexagon indicates the border of the first BZ. The experimentally obtained images coincide with the prediction as shown in 2.8. Images obtained from Ref. (76)

2.12 Transport properties of carbon nanotubes, 2D graphene and graphene nanoribbons

Finally, it is worthwhile to mention that near field microscopy methods, like STM, provide excellent correlations between the electronic and structural properties of CNT when compared to theoretical results. In Fig.2.17 it can be observed the good matching between the theoretical model explained above and some experimental results obtained by STM imaging.

2.12 Transport properties of carbon nanotubes, 2D graphene and graphene nanoribbons

Although carbon nanotubes and graphene nanoribbons share similar electronic properties with two-dimensional graphene, the effect of symmetries, defects, edges and dimensionality yield large differences in transport properties. The conduction mechanism ranges from ballistic to diffusive motion, whereas the increasing contribution of quantum interference effects for disordered systems can produce weak or strong localization phenomena, depending on the transport dimensionality. In this section, some theoretical results and experimental observations are briefly reviewed.

2.12.1 Ballistic transport regime in pristine CNTs

Let us first consider the case of ballistic motion and conductance quantization in clean metallic carbon nanotube. For a CNT between metallic contacts reservoirs, the transport regime is ballistic if the measured conductance is independent of the nanotube length, L , and only given as a function of the number of available quantum channels $N_{\perp}(E)$:

$$G(E) = G_0 N_{\perp}(E) \quad (2.38)$$

where $G_0 = \frac{2e^2}{h}$ is the conductance quantum that takes into account the spin degeneracy. This result is valid only in the case of defect-free CNT and good ohmic contacts between the CNT and the metallic leads. In this regime, the energy-dependent conductance spectrum is easily deduced by counting the number of channels at a given energy from band structure calculations. For instance, metallic armchair nanotubes present two quantum channel at the Fermi energy (see Fig.2.14-c)) resulting in $G(E_F) = 2G_0$. At higher energies, the conductance increases as more channels become available to conduction, (see Fig.2.18-a))

However, these values are the uppermost theoretical limits that can be experimentally measured and in practical situations, lower values are found since reflectionless transmission at the interface between the voltage probes and nanotubes is limited by interface mismatch. Additionally, topological and chemical disorder introduce intrinsic backscattering along the tube, which also reduces the transmission capability. These effects are generally accounted by introducing the transmission amplitude for a given channel at a given energy as: $T_n \leq 1$, (63), so that the above equation 2.38 reads now:

$$G(E) = G_0 \sum_{n=1, N_{\perp}} T_n(E) \quad (2.39)$$

2. GEOMETRICAL AND ELECTRONIC STRUCTURE OF CARBON-RELATED MATERIALS

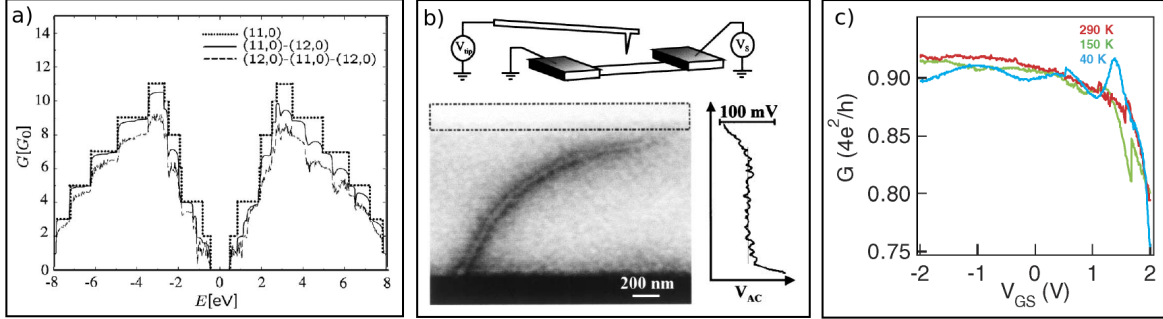


Figure 2.18: Conductance and electrical properties of metallic SWCNTs - a) Conductance spectra for the single (11,0) CNT showing the exact number of conduction channels (dotted line) together with the conductance of the double junctions specified in figure legend. (Image from ref.(91)). In b), images obtained from ref.(77), show first an AFM experimental setup for ac-EFM measurement. The ac-EFM image of a SWCNT and the associated flat signal upon application of 100mV ac-potential. In c) the conductance at low bias $V_{DS}=1\text{mV}$ of ohmically contacted metallic nanotubes is shown when measured at several temperatures for a tube of length $\sim 60\text{nm}$, from ref.(78)

In Fig.2.18-b), some evidences of ballistic conduction were shown by A. Bachtold and coworkers (77) in CNT of diameters $\sim 1\text{nm}$. By using scanning gate microscopy, this study was the first to evidence unambiguous signatures of ballistic transport in metallic SWCNTs contacted to two gold electrodes. When an ac-potential of 100mV is applied to one of the leads, a flat ac-EFM signal is obtained along the SWCNT length¹. As shown in Fig.2.18 the potential drop along the nanotube channel is extracted and it is clearly observed that it occurs at both contacts, whereas potential remains constant along the channel, in agreement with a ballistic motion.

More recently, Jauey et al. (78) related their measured nanotube resistance to a transmission probability using the four-terminal Landauer's formula:

$$R_n = \frac{h}{4e^2} \frac{1 - T_n}{T_n} \quad (2.40)$$

They found that $T_n > 1/2$, namely the majority of electrons traverse the nanotube without scattering. This unequivocally demonstrates that transport in metallic nanotubes is ballistic over lengths of $> 1\mu\text{m}$, even at room temperature (see Fig.2.18-c)).

¹In the ac-EFM approach, the cantilever of an atomic force microscopy, is made to oscillate by an ac-potential that is applied to the sample at the resonant frequency of the cantilever. This produces an ac-force on the cantilever proportional to the ac-potential under the tip. The resulting oscillation amplitude is proportional to this ac-potential.

2.12 Transport properties of carbon nanotubes, 2D graphene and graphene nanoribbons

2.12.2 Short-range disorder and elastic mean free path.

Knowledge of the mean free path in quasi-1D systems is crucial since it allows the identification of the crossover between the ballistic and the diffusive propagation of wavepackets in weakly disordered systems. Assuming that the transport regime remains coherent, a new class of scattering paths will yield an important contribution to the resistance, known as the weak localization correction, which eventually turns the metallic state to an insulating one.

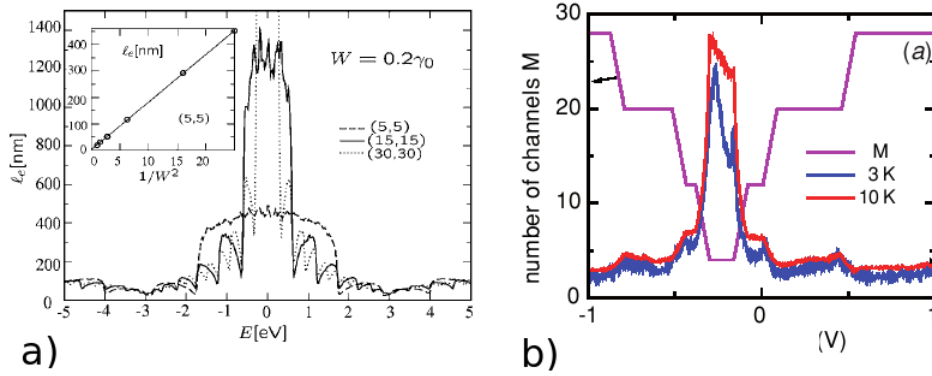


Figure 2.19: Energy mean free path. - a) Energy dependent mean free path as a function of CNT diameter for a given strength of Anderson disorder. Theoretical predictions by Triozon et al. from (79). b) Experimental results obtained for elastic mean free path for 10 K (red) and 3 K (blue). Magenta line shows the number of transport channels per spin direction as a function of gate voltage at zero bias regime.

Elastic mean free path evaluation is fundamental for a better understanding of disorder effects in the presence of short-range disorder. For sufficiently weak disorder, a perturbative treatment can be performed giving access to the elastic mean free path $l_e = v_F \tau$. This result was derived by reducing the band structure to a two-band approximation, as an effective model other two degenerate bands at the charge-neutrality point (Fermi energy) for armchair CNTs. An important result related l_e with a linear diameter scaling for a fixed disorder strength, while at fixed diameter the expected disorder scaling was shown to be $l_e \sim 1/W^2$, where W gives the variation range of the on-site perturbing potential. The analytical derivation this fundamental length scale can be found in ref.(91). Here the transport relaxation rate $1/\tau_e$ at Fermi energy is explicitly indicated as:

$$\frac{1}{\tau_e(E_F)} = \frac{\pi \rho(E_F)}{\hbar} \left(\frac{1}{\sqrt{N_c N_{ring}}} \sum_{N_c N_{ring}} (\epsilon_A^2 + \epsilon_B^2) \right) \quad (2.41)$$

where N_c and N_{ring} are, respectively, the pair of atoms along the circumference and rings taken in the unit cell used for diagonalization, $\rho(E_F)$ the density of states at Fermi energy and $\epsilon_A^2, \epsilon_B^2$ are the on-site energies on inequivalent atoms A and B randomly distributed within

2. GEOMETRICAL AND ELECTRONIC STRUCTURE OF CARBON-RELATED MATERIALS

the interval $[-W/2, W/2]$ following an uniform distribution with probability $P = 1/W$. For this Anderson-type model, the mean free path can be written as:

$$l_e = \frac{18d_{c-c}\gamma_0^2}{W^2} \sqrt{n^2 + m^2 + nm} \quad (2.42)$$

For the armchair (5,5) CNT with disorder $W = 0.2\gamma_0$, by applying eq. 2.42 one obtains $l_e \sim 560nm$ which is much larger than the circumference length. As shown in Fig.2.19-a), numerical studies (79) confirm the above scaling law of l_e . For semiconducting nanotubes, the $1/W^2$ scaling law is still satisfied, but the mean free paths are seen to be much smaller and do not scale with diameter.

One notes that recent experiments have confirmed the large modulation of l_e close to onsets of new subbands as shown in Fig.2.19-b)

Regarding numerical analysis of Landauer conductance in the case of such uniform disorder, Anantram and Govidan were the first to show that the conductance is more sensitive in regions of higher densities of states (like van Hove singularities), whereas it is almost unaffected by moderate disorder close to the Fermi level.

While most works have focused on the effect of a single isolated defect, some studies which combine an *ab initio* calculation with a semiempirical $\pi - \pi^*$ Kubo approach to transport have studied the effect of a random distributions of substitutional or physisorbed dopants at various concentrations for tubes with lengths as long as 1 micrometer. Such studies allow one to extract relevant mesoscopic information such as l_e and conductance of systems with several doping rates.

In Fig.2.20-a) the electronic conductance for long metallic nitrogen-doped armchair CNT is shown as a function of energy and nanotube length (148). The model is based on a $\pi - \pi^*$ model where relevant parameters were obtained from a previous DFT calculation. In the range of energies where electron transport properties are most salient, a tight-binding approximation based on π -orbital on-site energies extracted from a SIESTA calculation, reproduces with good accuracy the transport profiles obtained using the full Hamiltonian. A similar procedure will be presented in Chapter 7 for the tight-binding model used for electronic transport study on defected nanoribbons.

In Fig.2.21-a) (left) the result of a numerical calculation using the Kubo approach is presented. The evolution of μ is shown as a function of the Anderson disorder strength W . The energy-dependence of mobility and mean free path are found to be similar and, in the vicinity of the Dirac's point, the downscaling of μ with W follows the Fermi Golden Rule prediction, while it diverges when approaching to Dirac's point. Fig.2.21-a) (right) shows experimental data from ref.(80) for comparison. Different samples with varying quality present a similar trend although patterns from different samples can substantially differ in shape indicating fluctuations in the disorder characteristics.

By further reducing the dimensionality of the graphene material, charge mobilities can be reduced. Recent transport measurements on nanoribbon-based FET show mobilities in order of $\mu \sim 300cm^2/(V \cdot s)$, which are thus reduced in comparison with the 2D graphene

2.12 Transport properties of carbon nanotubes, 2D graphene and graphene nanoribbons

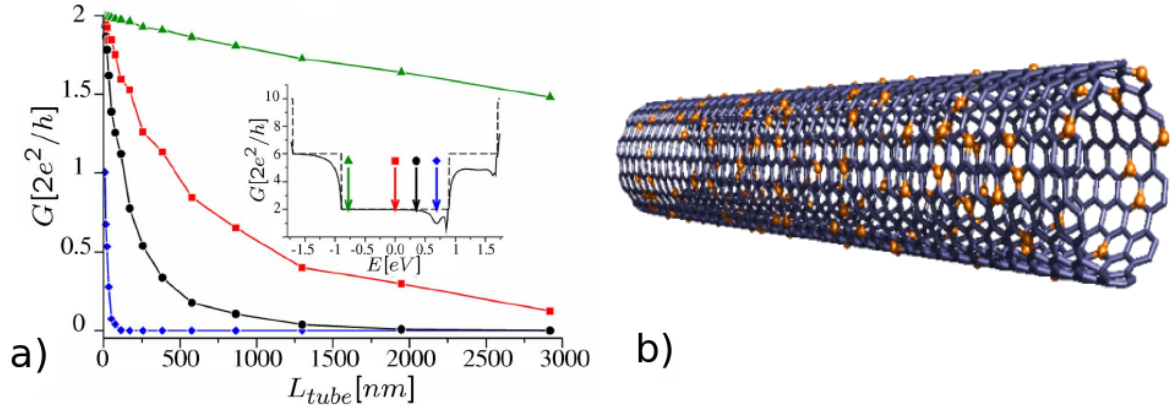


Figure 2.20: Nitrogen-doped nanotube. - a) Conductance length dependence for a disordered (10,10) 0.1% nitrogen-doped CNT at the energies specified in the inset-frame, where conductance versus energy is shown for a perfect tube (dashed line) and a single-impurity case (from (148)). b) Representation of an armchair CNT with boron atoms intercalated between carbon atoms.

measurements. However, the lateral size reduction allows for a larger energy gap, which ensures more efficient field-effect efficiency.

In Fig.2.21-b), the charge mobility in GNRs is seen to increase roughly linearly with the ribbon width. The origin of such behaviour might be due to the scattering effect of edge disorder for larger ribbon width. Additionally, by using the expression of the dispersion relation for GNRs (or semiconducting CNTs) one can define an effective mass that scales linearly with ribbon width (or CNT diameter). This yields to $\mu \sim e\tau R_w$ for quasi-1D nanoribbon, whereas in the very large limit $R \rightarrow \infty$ one recovers the divergence of μ expected for 2D-graphene.

2. GEOMETRICAL AND ELECTRONIC STRUCTURE OF CARBON-RELATED MATERIALS

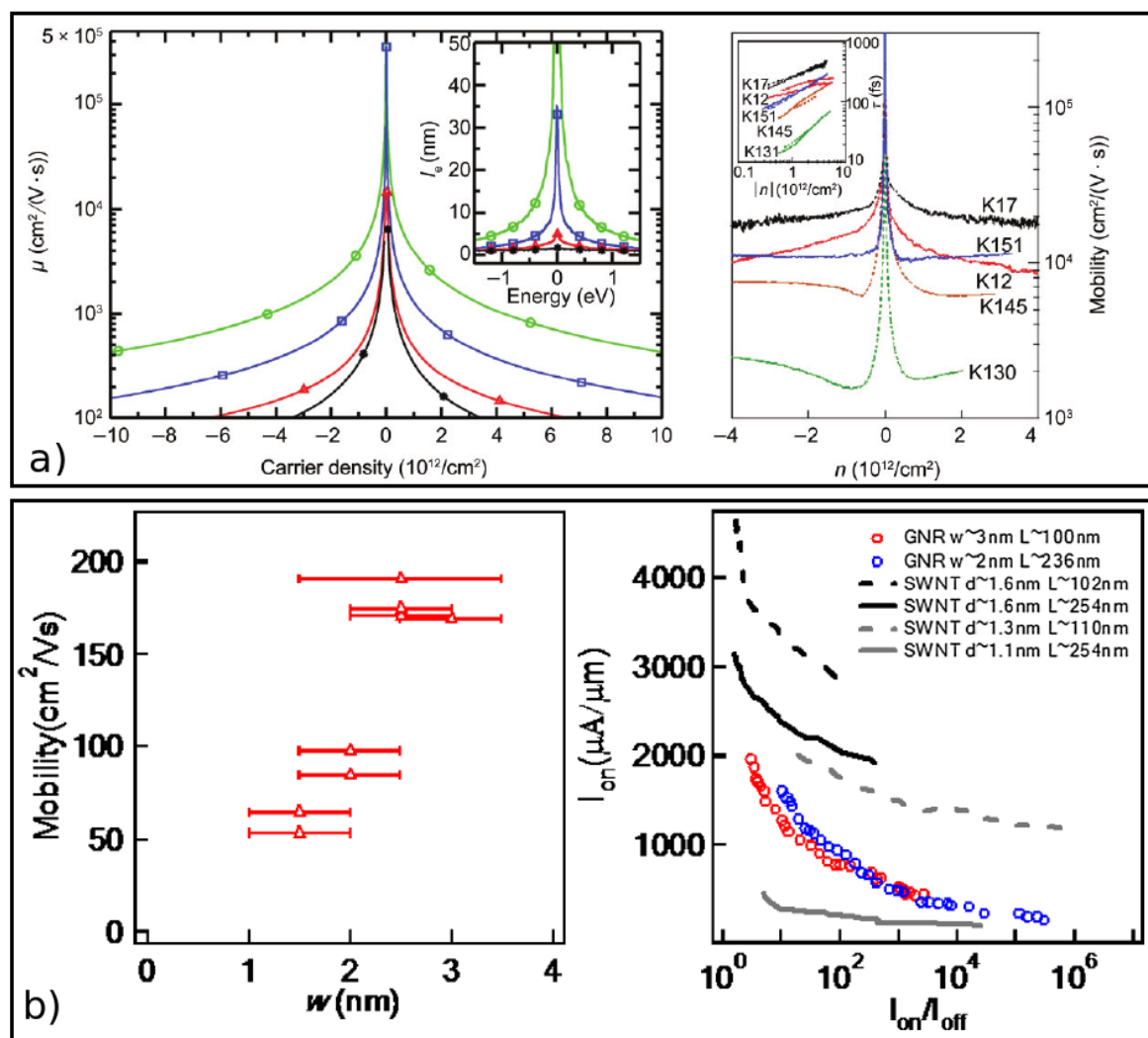


Figure 2.21: Charge mobility in graphene. - The extraordinary high mobility charge μ in graphene is shown in this two figures. In a) μ is represented as function of carrier density for theoretical calculations (left) and experimental results (right), with a divergence at 0. In inset the mean free path for an Anderson disorder of strength $W = 1, 1.5, 2, 2.5$ is shown. (Images obtained from (160)). In b) a performance comparison of mobilities in GNR-FETs and CNT-FETs is presented. On the left, mobility vs ribbon width multi-probe measurements for single-GNR devices. On the right, current density as a function of I_{on}/I_{off} for GNRs and CNTs.

Chapter 3

Transport

*“Si quieres calcular la transmisión es muy fácil:
no tienes más que calcular la resistencia e invertirla.”*
Alejandro Orfila Förster

Chapter résumé (French version)

Cette thèse s'intéresse à la modélisation numérique des spectres de transmission des systèmes carbonés dans l'approche de Landauer-Büttiker (LB) pour les systèmes connectés à deux électrodes. Dans ce chapitre, nous montrons comment ce formalisme nous permet de résoudre le problème de la conductance quantique et comment on peut facilement l'exprimer en termes de fonctions de Green. En combinant des Hamiltoniens des systèmes en bases localisées dans l'espace réel avec des méthodes numériques stables et rapides, la description en fonctions de Green de la diffusion, basée sur le formalisme LB, peut être appliquée pour résoudre le problème de la conductance électronique dans de longues nanostructures.

La méthode d'ordre N dite de décimation nous permet d'étudier les propriétés de transport des systèmes à l'échelle mésoscopique. Le problème des contacts et du couplage canal-électrode est minimisé en considérant les électrodes constituées d'une répétition périodique d'une section parfaite du canal. Les self-énergies des électrodes sont ajoutées au Hamiltonien du canal afin de prendre en compte leur influence sur la formulation du transport. La procédure présentée ici conduit à une évaluation numériquement stable de la transmission dépendant de l'énergie, pour l'analyse des propriétés de transport de CNTs et GNRs très longs avec divers degrés de fonctionnalisation chimique.

3. TRANSPORT

Tout d'abord, les concepts généraux de la théorie de Landauer sont présentés, ce qui constitue une introduction générale au problème du transport électronique. Ensuite, la méthode de renormalisation dans l'espace réel est présentée de manière très détaillée. Enfin, cette technique, telle qu'elle a été implémentée dans le code TB_Sim, est aussi présentée.

Chapter résumé (Spanish version)

La presente tesis trata sobre el la simulación por ordenador del espectro de transmisión de sistemas a base de carbono en la aproximación de Landauer-Büttiker (LB) para sistemas de dos sondas. En este capítulo en concreto se muestra cómo este formalismo nos permite resolver el problema de la conductancia cuántica pudiendo ser expresado fácilmente en términos de funciones de Green. Combinando el Hamiltoniano del sistema en una descripción de un conjunto de funciones base localizadas en el espacio real con métodos computacionales rápidos y estables, el esquema de difusión de funciones de Green basado en el formalismos LB puede ser aplicado para la resolución del problema de la conductancia electrónica en nanoestructuras de gran longitud.

La técnica de decimación de orden N nos permite estudiar las propiedades de transporte en sistemas de escala mesoscópica. El problema derivado del contacto entre canal y electrodos es minimizado considerando que éstos están formados por la repetición periódica de una sección no perturbada del canal. Al Hamiltoniano que describe el canal se le añaden las autonergías de los electrodos de manera que su presencia es considerada en la formulación global del problema de transporte. El procedimiento aquí presentado conduce a una evaluación numéricamente estable de la transmisión electrónica dependiente de la energía para el análisis de las propiedades de transporte de nanotubos de carbono y "nanoribbons" de grapheno de gran longitud y con varios grados de funcionalización química.

En primer lugar, los conceptos generales de la teoría de Landauer son presentados como introducción general al problema de transporte electrónico. A continuación el método para la renormalización del espacio real is presentado con gran detalle. Finalmente, esta técnica, tal como ha sido codificada en el programa TB_Sim es también presentada.

Chapter résumé (English version)

This thesis is concerned with the computational modeling of the transmission spectra of carbon-based systems within the Landauer-Büttiker (LB) two-probe systems approach. In this chapter, we show how this formalism allows us to solve the quantum conductance problem and may be easily expressed in terms of Green's function. By combining system Hamiltonian in a localized real-space basis set with fast and stable computational methods, Green's function scattering-scheme based on LB formalism can be applied to solve electronic conductance problem in long nanostructures.

The $O(N)$ -order decimation technique allows us to study transport properties of systems at the mesoscopic scale. The contact problem derived from channel-electrode coupling is minimized by considering the leads as made of a periodic repetition of a pristine section of the channel. To the channel Hamiltonian, electrode self-energies are added to take into account their influence on the overall transport formulation. The procedure herein presented leads to a numerically stable evaluation of the energy-dependent transmission for the analysis of very long CNTs and GNRs transport properties with various degrees of chemical functionalization.

Firstly, Landauer's theory general concepts are presented as general introduction to the electronic transport problem. Secondly, the method for the renormalization of real-space is presented in great detail. Finally, this technique, such as it has been implemented in `TB.Sim` code, is also presented.

3.1 Introduction

With the progress of miniaturization of electronic devices, the traditional simulation tools for Si based-systems become more and more limited. The increasing of surface/volume ratio in nano-scaled systems complicates the treatment of charge transport since interface properties prevail. Quantum effects become important when the wavelength of the carriers becomes comparable with one of the system dimensions. Therefore, a fully quantum mechanical framework becomes essential to describe the electronic and spin transmission properties of systems at atomic scale. For example, the coherent dynamics of the electrons yield interference phenomena that can only be described if aspects related to the quantum mechanical nature of the particles are taken into account. In chapter 6 it will be shown that the probability for an electron to be backscattered is strongly dependent on the relative distance between defects.

A detailed analysis of the potential profiles introduced by impurity distribution along a device channel becomes essential when considering the motion of charge carriers along a nano-scale conductor. Traditionally, the study of quantum transport properties of materials have been restricted to short-length systems. Even when the physical case of study is understandable within a valid theoretical framework, the analytical or numerical techniques used to solve it could fail if the complexity becomes too high. Thus, numerous works are restricted to the study of the impact of a single impurity on the transport properties of a given system or several impurities constrained in short channels.

This complexity comes from both computational aspects and detailed system description. Simple models represent a great departure for explaining the usual features shown by more realistic systems. Sometimes referred as "academic models", they contain all the richness needed to study the physical properties of systems without requiring to be described in full details.

Then, another kind of complexity could arise: physical laws governing the behaviour of a system are known but some useful quantities are required for a detailed description of it. In this thesis, we deal with electronic transport in CNTs and GNRs at the mesoscopic scale. Electron behaviour when moving along these systems is well known and simple models based in the so-called p_z orbitals are usually enough to explain coherent electronic transport

3. TRANSPORT

properties. Physicists have resorted to a single orbital per atom model to describe with a good degree of accuracy the impressive conduction capabilities of metallic and semiconducting nanotubes. The question to address now is: “Does this model fail when other atoms, alien to original pristine carbon-based structure, alter it?”. “May these changes be described accurately?”. The original structure can be altered either by substitutional element modification (doping) or by close interaction of both objects. DFT approaches constitute a powerful tool to obtain accurate descriptions of electronic properties of pristine and chemically modified systems. Therefore, transport properties that are derived from these descriptions, can be explored with greater precision. We will see that a model that takes into account more orbitals per atom than the mentioned p_z -orbital model is mandatory in order to get a proper description of electron behavior in CNTs and GNRs, which have been locally modified by the presence of grafted functional groups or original carbon-network distortions.

Coupling the electronic structure calculated by means of a DFT code with transport properties analysis of long system constitutes the heart of this work. At this point, a second kind of complexity arises: how a system at the mesoscopic scale can be treated if current state of the art first-principles approaches can only deal with a few hundred atoms? If we are able to give a description of the electronic structure of a system made of, let’s say, up to one thousand atoms, is there a way to extend this information to build up a system of hundreds of thousands of atoms? The answer comes from intensive use of $O(N)$ approaches implementation.

In the next sections, the $O(N)$ techniques developed for the study of transport properties of systems at the mesoscopic scale will be explained. Firstly, a reminder of the Landauer-Büttiker’s formalism, which constitutes the central theory for transport calculations, will be given. Basic notions of Green’s function are outlined for a better understanding of Green’s function formalism applied to transport. Finally, the technique as it is implemented in TB_Sim code (93) is described.

3.2 Landauer’s idea

In 1957, R. Landauer was the first to realize that contacts play an important role in transport description. In addition to the molecule or device resistance, there exists the intrinsic resistance of the whole system due to the fact that the channel is coupled to electrodes. Landauer’s formulation for quantum mechanical problem of electronic transport consists, basically, in establishing a relation between the conductance of a one dimensional conductor and the probability of an electron to pass through it without being reflected.

We define a device as some region or material where charge carriers spend a certain amount of time during their propagation. It is characterized by a cross section and a longitudinal length, along which the wavepackets propagate quantum mechanically. The sample is connected to left (L) and right (R) one-dimensional semi-infinite leads which are also in thermal equilibrium with electron reservoirs. Landauer’s approach makes intensive use of the classical concepts such as scattering. An incoming electron has a certain probability to be backscattered or transmitted when it flows along the material due to the presence of

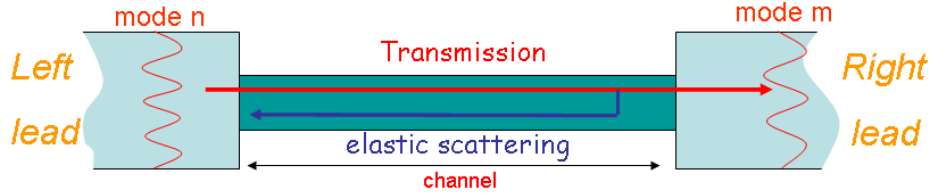


Figure 3.1: Schematic representation of a device - An electron with a given energy enters into the channel from the left lead. In Landauer's model the incoming wavepacket in the n -mode has a certain probability to be elastically backscattered and a probability of reaching the left lead. This probability is called channel transmission.

impurities. Material impurities are seen by charges as potential barriers or wells and the mutual interaction are responsible for the various material conductance regimes. This transport model treats electron interferences from a quantum point of view that arise from the coherent dynamics.

Landauer's model deals with strictly one-dimensional systems, the conductance of which can be expressed by

$$G_L = \frac{e^2}{h} T \quad (3.1)$$

where T and R are the transmission and reflexion probabilities, respectively. In the following, a schematic deduction of this expression is given.

Let us consider a one-dimensional conductor as a serie of quantum barriers randomly distributed along a distance L . An electron which is initially in the left reservoir flows along the left lead and gets into the channel. Only in reservoirs inelastic processes occur while in the channel only elastic scattering processes are considered. μ_L and μ_R are the chemical potentials of left and right electrodes respectively. Due to a small difference in the chemical potentials, a net flux electronic current is established between both leads. If $\mu_L > \mu_R$ the density of charge carriers will be $1+R$ at the left side of a barrier, where 1 is the total incoming electron flow and R is fraction of electrons that are reflected. At the right side of last barrier the charge density will be $T=1-R$, namely, the fraction of particles that went through the barriers without undergoing a reflexion. Averaging the number of particles per unit of length (as if the system were homogeneous), this gradient would be:

$$\nabla n = \frac{(1 - R) - (1 + R)}{L} = -\frac{2R}{L} \quad (3.2)$$

This density current can be evaluated with two expressions:

$$j = nv \quad (3.3)$$

where j is the current of the $n=1-R$ particles and v the velocity. From the expression $j = -D\nabla n$ that relates the current density with the diffusion coefficient, D , this value can be

3. TRANSPORT

obtained by substituting 3.2 in this equation and making equal to 3.3. The result is

$$D = \frac{VL T}{2 R} \quad (3.4)$$

By means of Einstein formula that relates conductivity σ with D:

$$\sigma = \frac{e^2 D}{\left(\frac{\delta\mu}{\delta n}\right)_T} \quad (3.5)$$

Landauer's equation 3.1 can be obtained if $\left(\frac{\delta\mu}{\delta n}\right)_T$ is substituted by the expression for the free electron case.

3.3 Landauer-Büttiker's theory

Equation 3.1 has a limitation: if $T=1$, which is the case of a perfect conductor, the conductance of the device becomes infinite. This result yielded a lot of controversy at the time of Landauer's publication since it was obvious that no channel has an infinite capacity for electron transmission and dissipation was lacking in the case of a clean model. Büttiker's work definitely put an end to the controversy by further providing an extended theoretical framework that takes into account the contribution of several transmission channels.

Landauer-Büttiker's approach states that, in a two-probe system, conductance is

$$G = \frac{e^2}{h} T \quad (3.6)$$

where T is the transmission coefficient for a given channel. In this formula, several assumptions are made: there is no electron-electron interaction and each charge propagates coherently through the conductor with only possible elastic scattering events, since all the inelastic processes take place in the reservoirs. The final expression that takes into account all channel contributions, in addition to spin degeneracy, reads,

$$G = \frac{2e^2}{h} \sum_{n=1}^N T_n \quad (3.7)$$

where the sum runs over all the different conducting channels at a given Fermi energy. This is the two probe conductance formula.

Let us consider two electron reservoirs at equilibrium and connected between themselves by means of a short and narrow conductor, of which longitudinal and transversal dimensions are much smaller than electron MFP. An electron current flow can be initiated by increasing one chemical potential with respect to the other and allowing the charges to leave the reservoir. If no scattering process takes place during the propagation from one lead to the other, the quantum regime is said to be ballistic.

Each reservoir releases electrons with an energy which is determined by the local Fermi-Dirac (FD) distribution function

3.3 Landauer-Büttiker's theory

$$f_{L(R)}(\epsilon) = \frac{1}{e^{(\epsilon - \mu_{L(R)})/k_B T} + 1} \quad (3.8)$$

where ϵ is the energy of the incident electron and $\mu_{L(R)} = \mu_0 + \delta$ is the left (right) chemical potential after being displaced by quantity δ from the equilibrium value μ_0 . The density of states of these electrons is $\frac{1}{2}N_{(L)R}(\epsilon)$ and v_i their velocity. Thus, taking the left (L) lead as a reference and assuming that $T_{R,L} > 0$ gives the current flowing through the channel from L to R, the net current is expressed as a function of the number and velocities of electrons available in both leads as:

$$I_L = e \int [T_{R,L}(\epsilon)v_L \frac{1}{2}N_L(\epsilon)f_L(\epsilon) - T_{L,R}(\epsilon)v_R \frac{1}{2}N_R(\epsilon)f_R(\epsilon)]d\epsilon \quad (3.9)$$

This equation represents a balance of charges flowing from left to right leads, and vice versa, in the one-dimensional conductor. The first term in the integral gives the net outgoing charges while the second one is the net incoming charge contribution. One of most important of Landauer's contributions was to consider the density of states in a propagating mode as inversely proportional to its group velocity:

$$N_{L(R)} = \frac{2}{h} \frac{1}{v_{L(R)}} \quad (3.10)$$

This allows the velocity to be cancelled within the integral, meaning that all modes contribute equally to the current. The formula is then simplified to:

$$I_L = \frac{2e}{h} \int [T_{R,L}(\epsilon)f_L(\epsilon) - T_{L,R}(\epsilon)f_R(\epsilon)]d\epsilon \quad (3.11)$$

by imposing a weak bias at both sides of the conductor, i.e., $(\delta\mu_L - \delta\mu_R) = eV$, distributions fulfill $f_{R(\epsilon)} = f_L(\epsilon - eV)$. In the linear response regime ($\delta\mu_{L(R)} = \mu_{L(R)} - \epsilon_F$) the integral can be evaluated at the Fermi energy: ¹.

$$f_R(\epsilon) - f_L(\epsilon) = f_R(\epsilon) - f_R(\epsilon - eV) \quad (3.12)$$

$$= f_R(\epsilon) - f_R(\epsilon) - \frac{\delta f_R}{\delta E} eV = \quad (3.13)$$

$$= -\frac{\delta f_R}{\delta E} eV \quad (3.14)$$

Assuming time reversal symmetry for transmittances $T_{R,L} = T_{L,R}$ and the step function as a convenient approximation for FD distribution (low temperature limit) this formula can be simplified to:

$$I_L = -\frac{2e^2}{h} V \int \frac{\delta f_R}{\delta E} T_{R,L}(\epsilon) d\epsilon \quad (3.15)$$

¹It is worth to notice at this point that all relevant electronic transport properties take place at energies close to Fermi energy

3. TRANSPORT

In the limit of $T=0$ (zero Kelvin):

$$\left(-\frac{\delta f_R}{\delta E}\right)_{T=0} = \delta(\epsilon - \epsilon_F) \quad (3.16)$$

The two-probe conductance $G=I/V$ is then,

$$G_{R,L}(\epsilon_F) = G_0 T_{R,L}(\epsilon_F) \quad (3.17)$$

where $G_0 = \frac{e^2}{h}$ is the quantum of conductance. This formula asserts that the conductance of a one-dimensional conductor is proportional to the transmission probability.

The difference with Landauer's original formula 3.1 is the finite conductance of 3.17: in a perfect one-dimensional conductor $T_{R,L} = 1$ and G_0 gives the maximum value of conductance and, reciprocally,

$$R = 1/G_0 = \frac{h}{e^2} = 25.812 K\Omega \quad (3.18)$$

is the quantum of resistance.

It is worthwhile to notice that Landauer's original formula represents an attempt to measure the voltage drop along the conductor: in addition to the leads that inject and drain charges from the system, two other (in principle) non-invasive probes are weakly connected to the channel, so that an electric field gradient along the channel can be estimated. The difference of the inverse of both conductances at Fermi energy:

$$R^{2contacts} = \frac{h}{2e^2} + \frac{h}{2e^2} \frac{1-T}{T} = \frac{h}{2e^2} \frac{1}{T} \quad (3.19)$$

can be interpreted as a lead-channel interface resistance.

From Kirchoff's law, the more general expression 3.7 can be obtained using Landauer's conductances:

$$I_i = \frac{e}{h} \sum_j \int [T_{j,i}(\epsilon) f_j(\epsilon) - T_{i,j}(\epsilon) f_i(\epsilon)] d\epsilon \quad (3.20)$$

This expression gives a general (N-channel) case at finite temperatures. $T_{i,j}$ can be read as the probability of a left-lead outgoing electron from j-channel be transmitted to i-channel in right-lead. The sum runs over all open channels i,j (those which fulfill the condition $\epsilon_i < \epsilon_{Fermi}$) and the transmission coefficients depend on external parameters, such as voltages. Therefore, it accounts for the non-linear response regime.

3.4 Green's function

In this section, some useful reminder about Green's function is given. In this work, we attempt to solve transport problems of a single-particle problem, the energetics of which is

described by a density functional Hamiltonian, H , such as that appearing in the Schrödinger equation:

$$H\psi_i = \epsilon_i\psi_i \implies \left[-\frac{1}{2}\nabla^2 + V(\mathbf{r}) - \epsilon_i \right] \psi_i(\mathbf{r}) = 0 \quad (3.21)$$

where $V(\mathbf{r})$ is the potential energy of the electron and ϵ_i are the eigenvalues associated to the eigenfunctions $\psi_i(\mathbf{r})$. The wavefunctions of this equation can be expressed by an expansion in a finite set of basis functions $\{\phi_\nu(\mathbf{r})\}_\nu$:

$$\psi_i(\mathbf{r}) = \sum_{\nu=1}^N c_{i\nu}\phi_\nu(\mathbf{r}) \quad (3.22)$$

A sufficient large number of basis functions can reduce the imprecision which is consequence of the finiteness of the basis set $\{\phi_\nu(\mathbf{r})\}_\nu$. We define the Hamiltonian matrix elements of H as:

$$H_{\nu\nu'} \equiv \int d^3r \phi_\nu^*(\mathbf{r}) \left[-\frac{1}{2}\nabla^2 + V(\mathbf{r}) \right] \phi_{\nu'}(\mathbf{r}) \quad (3.23)$$

and the overlap matrix element of two functions as:

$$S_{\nu\nu'} \equiv \int d^3r \phi_\nu^*(\mathbf{r}) \phi_{\nu'}(\mathbf{r}) \quad (3.24)$$

Inserting expression 3.22 into 3.21 we obtain a generalized eigenvalue problem:

$$\sum_{\nu'} H_{\nu\nu'} c_{i\nu'} = \epsilon_i \sum_{\nu'} S_{\nu\nu'} c_{i\nu'} \quad \forall \nu \quad (3.25)$$

From the previous definitions, the Green's function $G(\epsilon)$ (also called resolvent) is defined by:

$$\sum_{\nu''} (\epsilon S_{\nu\nu''} - H_{\nu\nu''}) G_{\nu''\nu'}(\epsilon) \equiv \delta_{\nu\nu'} \quad (3.26)$$

This expression shows the powerfulness of expressing Green's functions in the matrix form, since it does not depend on the operator $-\frac{1}{2}\nabla^2 + V(\mathbf{r})$, but on the inverse of the matrix $\epsilon S_{\nu\nu'} - H_{\nu\nu'}$. Within a tight-binding framework, the basis set can be formed by a set of orbital wavefunctions centered on each atom of the system which confers to the matrix a compact form. Inverting the matrix for a given value of ϵ is, in principle, all one needs to calculate the Green's function of the electronic system. In this work, the Hamiltonian and overlap matrices are provided by a DFT calculation of a system composed by more than 500 atoms. Since SIESTA code implements a basis set of atomic-like orbitals, the Hamiltonian matrix that results from a simulation fits exactly with the requirements of size and compactness for computational Green's function calculation. An appropriate choice of basis set size allows us to deal with relatively compact matrices within LCAO model.

Problems arise when the size of the matrix is too large to be inverted by regular computational tools as in the case of systems with more than thousand of atoms. Therefore, a reduction of the basis function space is mandatory when the Green's function needs to

3. TRANSPORT

be calculated with limited computational resources. In section 3.6, a method of real space normalization is described as an effective pathway to reduce the computational complexity of a problem when calculating its Green's function. Before, some notes about the calculation of the density of states of a system with the help of the Green's function are given.

3.5 Total density of states (TDoS) and Green's function

Let $\{\phi_n\}$ be an orthonormal complete basis function set and \hat{H} the Hamiltonian operator of a system. An example of this Hamiltonian (in matrix form) is given in eq.3.113. Let $\{\Psi_n\}$ and $\{E_n\}$ be the finite set of normalized eigenfunctions and eigenvalues that can be obtained upon diagonalization of \hat{H} :

$$\det[\hat{H} - IE_n] = 0 \quad (3.27)$$

The total density of states of such a system is defined as:

$$D(\epsilon) = \sum_n \delta(\epsilon - E_n) \quad (3.28)$$

Integration of TDoS over an interval of energy $\Delta E = E_2 - E_1$:

$$N_{\Delta E} = \int_{E_1}^{E_2} D(\epsilon) dE \quad (3.29)$$

provides the number of states with energies within the limits of this interval. It is obvious that if E_1 is the lowest occupied state and E_2 the highest occupied state, the integral gives the total number of states in the system.

The projected or local density of states (LDoS) over a particular orbital $|\phi_i\rangle$ is defined as:

$$n_i(\epsilon) = \sum_n |\langle \phi_i | \Psi_n \rangle|^2 \delta(\epsilon - E_n) \quad (3.30)$$

LDoS describes the density of states, but space-resolved, providing information about the energy interval of interest for the orbital $|\phi_i\rangle$. If this orbital is normalized then $\int n_i(\epsilon) d(\epsilon) = 1$. The sum of the LDoS on any complete orthonormal set of $|\phi_i\rangle$ gives the TDoS.

The retarded (advanced) Green's function of the Hamiltonian operator H is defined as:

$$G^{r(a)}(\epsilon) = \lim_{\eta \rightarrow 0^+} \frac{1}{(\epsilon \pm i\eta)\mathbf{I} - \hat{H}} \quad (3.31)$$

where the energy is defined in the complex plane by adding to the real part an infinitely small quantity η . In the case of a non-orthogonal basis set, the overlap matrix would replace the identity matrix in eq.3.31. Let's consider a diagonal matrix element of $G^{r(a)}$ as the projection of Green's function over a given orbital $|\phi_i\rangle$:

$$G_{i,i}^{r(a)}(\epsilon) = \lim_{\eta \rightarrow 0^+} \langle \phi_i | \frac{1}{\epsilon + i\eta - \hat{H}} | \phi_i \rangle \quad (3.32)$$

3.5 Total density of states (TDoS) and Green's function

Inserting the unit operator $\hat{I} = \sum_n |\Psi_n\rangle\langle\Psi_n|$ we obtain:

$$G_{i,i}^{r(a)}(\epsilon) = \lim_{\eta \rightarrow 0^+} \langle \phi_i | \frac{1}{\epsilon \pm i\eta - \hat{H}} \left[\sum_n |\Psi_n\rangle\langle\Psi_n| \right] | \phi_i \rangle \quad (3.33)$$

$$= \lim_{\eta \rightarrow 0^+} \langle \phi_i | \left[\sum_n \frac{1}{\epsilon \pm i\eta - E_n} |\Psi_n\rangle\langle\Psi_n| \right] | \phi_i \rangle \quad (3.34)$$

$$= \lim_{\eta \rightarrow 0^+} \sum_n | \langle \phi_i | \Psi_n \rangle |^2 \frac{1}{\epsilon \pm i\eta - E_n} \quad (3.35)$$

$$= \lim_{\eta \rightarrow 0^+} \sum_n \frac{| \langle \phi_i | \Psi_n \rangle |^2}{(\epsilon - E_n)^2 + \eta^2} (\epsilon - E_n \pm i\eta) \quad (3.36)$$

It can be verified from 3.36 that $G_{i,i}^{r(a)}(\epsilon)$ is an analytic function. The real part of $G_{i,i}^{r(a)}(\epsilon)$ exhibits poles in the real axis at the eigenvalues of \hat{H} while the imaginary part exhibits δ -singularities:

$$\frac{1}{\pi} \text{Im}[G_{i,i}^{r(a)}(\epsilon)] = \mp \lim_{\eta \rightarrow 0^+} \frac{1}{\pi} \sum_n \frac{\eta}{(\epsilon - E_n)^2 + \eta^2} | \langle \phi_i | \Psi_n \rangle |^2 \quad (3.37)$$

$$= \mp \sum_n | \langle \phi_i | \Psi_n \rangle |^2 \delta(\epsilon - E_n) \quad (3.38)$$

Comparing this equation with 3.30, the standard spectral theorem is obtained:

$$n_i(\epsilon) = -\frac{1}{\pi} \text{Im}[G_{i,i}^r(\epsilon)] \quad (3.39)$$

The sum of all diagonal elements of the Green's function expressed on any chosen complete orthonormal set, gives the TDoS of the system:

$$D(\epsilon) = -\frac{1}{\pi} \text{Im}[\text{tr}\{G^r(\epsilon)\}] \quad (3.40)$$

In this procedure for Green's function calculation of a Hamiltonian operator, we resort to the diagonalization of the Hamiltonian matrix expressed in some orthonormal basis set. As it was pointed out in the previous section, when the investigated system is composed of hundred of atoms and the basis set is chosen to have several orbitals centered on each atom, the Hamiltonian might become computationally intractable. A reduction of matrix size is then mandatory. In the next section a real space renormalization group procedure is presented as a computationally stable and efficient method that allows to systems with sparse matrix Hamiltonian representation to have an alternative representation based in a reduction of its basis space.

3.6 Real space renormalization group procedures, also known as decimation

After the presentation of the basic concepts related to quantum transport within the Landauer-Büttiker approach we now give an overview of the technique that will be used to compute the Green's function of a system and, as a last resort, transmission coefficients $T_{R,L}$.

The renormalization method allows us to describe the properties of systems for which a large number of basis functions is required but needs to be reduced in order to make it tractable. It consists on reducing progressively the dimension of the space of the basis functions without information loss. In the LCAO model considered in this work, the number of orbitals per atom multiplied by the total number of atoms create a matrix Hamiltonian which is out of reach for any computer operation. The solution comes from a reduction of the original matrix to a smaller one that could be inverted by regular algorithms in order to find the Green's function at a certain energy.

The main references for this section are (94; 95; 96; 97; 98; 99; 100; 101)

Before getting into the details of the renormalization method applied to large systems, let's see how the method works in the case of several orbital systems.

3.6.1 Effective Hamiltonians

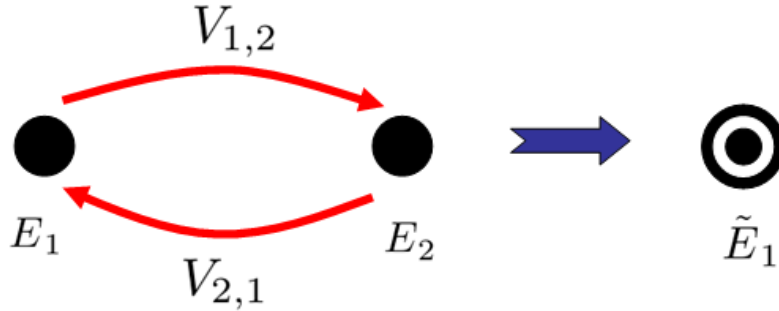


Figure 3.2: Renormalization of a two-site model - The single-orbital two-site model is reduced to an effective single-orbital one-site model

The simplest case of two interacting particles that can be conceived is the one depicted in Fig.3.2. The Hamiltonian (\mathbf{H}) and the system wavefunction Ψ read:

$$\mathbf{H} = \begin{pmatrix} E_1 & V_{1,2} \\ V_{2,1} & E_2 \end{pmatrix} \quad (3.41)$$

$$|\Psi\rangle = \begin{pmatrix} a \\ b \end{pmatrix} \quad (3.42)$$

3.6 Real space renormalization group procedures, also known as decimation

a and b are real factors that combine linearly the two orbitals centered on each atom, of energies E_1 and E_2 to give the system wavefunction. The degree of coupling between both orbitals is given by the hopping terms $V_{1,2}$ and $V_{2,1}$. To a certain extent, $V_{1,2}$ can be rationalized as the probability of an electron in site 1 to jump to site 2, and similarly for $V_{2,1}$. Therefore, in most cases, both coupling terms are taken as exactly equal. Then, the eigenvalue problem can be expressed as:

$$\begin{pmatrix} E_1 & V_{1,2} \\ V_{2,1} & E_2 \end{pmatrix} \begin{pmatrix} a \\ b \end{pmatrix} - \epsilon \begin{pmatrix} a \\ b \end{pmatrix} = 0 \quad (3.43)$$

The energy spectrum of this two-site problem is obtained from the secular equation:

$$\det[\mathbf{H} - \epsilon \mathbf{I}] = 0 \quad (3.44)$$

with eigenvalues:

$$\epsilon_{1,2} = \left(\frac{E_1 + E_2}{2} \right) \pm \sqrt{\left(\frac{E_1 - E_2}{2} \right)^2 + V_{1,2}V_{2,1}} \quad (3.45)$$

Due to the simplicity of 3.43, we can afford to solve the equation in an alternative form. Breaking up the matrix notation and writing the linear equation down explicitly:

$$E_1 a + V_{1,2} b = \epsilon a \quad (3.46)$$

$$V_{2,1} a + E_2 b = \epsilon b \quad (3.47)$$

Solving out for b in the second equation:

$$b = V_{2,1} \frac{1}{\epsilon - E_2} a \quad (3.48)$$

and substituting in the first one, we obtain:

$$\left(E_1 + V_{1,2} \frac{1}{\epsilon - E_2} V_{2,1} \right) a = \epsilon a \quad (3.49)$$

ϵ is straightforwardly obtained from the former expression

$$\epsilon = E_1 + \Sigma_1(\epsilon) \quad (3.50)$$

where $\Sigma_1(\epsilon) = |V_{1,2}|^2/(\epsilon - E_2)$ is called self-energy and can be interpreted as an effective potential that corrects the non-interacting on-site energy E_1 as:

$$\tilde{E}_1 = E_1 + \Sigma_1(\epsilon) \quad (3.51)$$

The eigenvalues $\epsilon_{1,2}$ already obtained in 3.45 could also be obtained from this equation.

This simple example shows that an initial two-site problem can be reduced to a one-site problem by a simple mathematical operation that involves a multiplication and an inversion.

3. TRANSPORT

The resulting single orbital system has its original on-site energy plus a term that takes into account the influence of the former orbital. An effective Hamiltonian with the same properties than the two-orbital model is obtained for each energy ϵ value.

3.6.2 Decimation method

In the preceding section, the basic ideas of decimation we presented by showing that the two-site model can be reduced to an equivalent one-site model in which energy is shifted by a quantity that depends on the energy of the second site and the coupling between boths. Before generalizing the procedure, let's take a look to a slightly more difficult problem: the three-site problem. By adding a one-orbital new site which is coupled to both of the previous

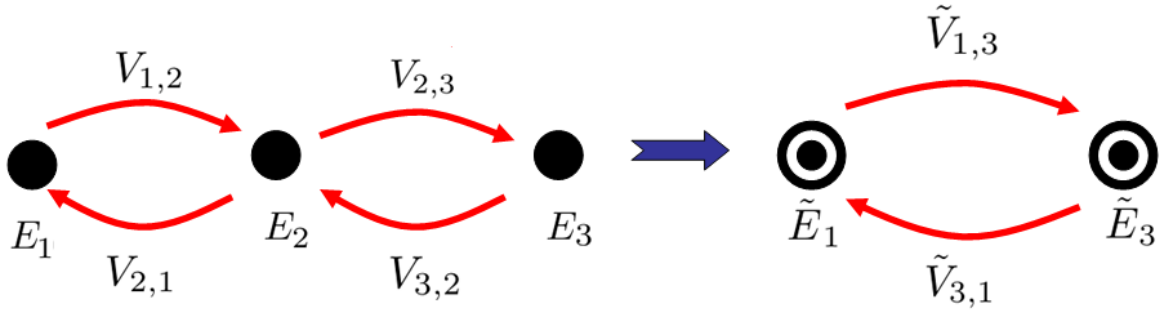


Figure 3.3: Renormalization of a three-site model - Representation of a two-site effective Hamiltonian construction from an initial model of three sites.

sites, a new three-site Hamiltonian can be built up:

$$\begin{pmatrix} E_1 & V_{1,2} & 0 \\ V_{2,1} & E_2 & V_{2,3} \\ 0 & V_{3,2} & E_3 \end{pmatrix} \begin{pmatrix} a \\ b \\ c \end{pmatrix} = \epsilon \begin{pmatrix} a \\ b \\ c \end{pmatrix} \quad (3.52)$$

To reduce the dimension of this system several procedures can be applied. One of the sites on the extremes could be eliminated as described before and then, the obtained two-site effective model could be reduced again to a single site. Instead of that, we remove the central site and obtain an equivalent expression of the original problem. See Fig. 3.3 for a schematic representation of this procedure. Writing the linear equations down and working out coefficient b of the wavefunction linear expansion

$$b = V_{2,1} \frac{1}{\epsilon - E_2} a + V_{2,3} \frac{1}{\epsilon - E_2} c \quad (3.53)$$

which can be substituted in the rest of the equations to obtain the two coupled non-linear equations:

$$\begin{pmatrix} \tilde{E}_1 & \tilde{V}_{1,3} \\ \tilde{V}_{3,1} & \tilde{E}_3 \end{pmatrix} \begin{pmatrix} a \\ c \end{pmatrix} = \epsilon \begin{pmatrix} a \\ c \end{pmatrix} \quad (3.54)$$

3.6 Real space renormalization group procedures, also known as decimation

where

$$\tilde{E}_1(\epsilon) = E_1 + V_{1,2} \frac{1}{\epsilon - E_2} V_{2,1} \quad (3.55)$$

$$\tilde{E}_3(\epsilon) = E_3 + V_{3,2} \frac{1}{\epsilon - E_2} V_{2,3} \quad (3.56)$$

$$\tilde{V}_{1,3}(\epsilon) = V_{1,2} \frac{1}{\epsilon - E_2} V_{2,3} \quad (3.57)$$

$$\tilde{V}_{3,1}(\epsilon) = V_{3,2} \frac{1}{\epsilon - E_2} V_{2,1} \quad (3.58)$$

The energies of the original sites have been replaced by new values which depend on the properties of the eliminated orbital, and the coupling term between them is shifted by a quantity that depends on the previous couplings. Whatever the initial number of orbitals, the same procedure can thus be applied iteratively until an effective two-site model, with renormalized on-site energies and hoppings is obtained.

This general operating method provides a recursive way to reduce the dimension of the Hamiltonian basis function space down to the minimum amount of degrees of freedom, at the cost of transforming a linear equation into a non-linear one.

Extending the method to a N-site problem, some general formulas can be derived. The recursion formulas which give the correction to the on-site energies and coupling terms of single-orbital extreme sites of a linear chain are as follows:

$$H_{1(n)}^+(\epsilon) = H_{1(n-1)}^+ + \tilde{V}_{1,n} \frac{1}{\epsilon - E_n - H_n^-} \tilde{V}_{n,1} \quad (3.59)$$

$$H_{n+1}^-(\epsilon) = V_{n+1,n} \frac{1}{\epsilon - E_n - H_n^-} V_{n,n+1} \quad (3.60)$$

$$\tilde{V}_{1,n+1}(\epsilon) = \tilde{V}_{1,n} \frac{1}{\epsilon - E_n - H_n^-} V_{n,n+1} \quad (3.61)$$

$$\tilde{V}_{n+1,1}(\epsilon) = V_{n+1,n} \frac{1}{\epsilon - E_n - H_n^-} \tilde{V}_{n,1} \quad (3.62)$$

where:

$H_{1(n)}^+$ is the energy that must be added to first atom on-site energy when all sites (to the right, +) up to atom n (inclusive) have been eliminated.

H_{n+1}^- is the energy that must be added to n+1 atom on-site energy when all sites (at the left, -) up to atom next to 1 have been eliminated.

$\tilde{V}_{1,n+1}(\epsilon)$ is the effective coupling term between the two remaining layers, from number 1 to number n+1.

$\tilde{V}_{n+1,1}(\epsilon)$ is the effective coupling term between the two remaining layers, from n+1 to 1.

3. TRANSPORT

These recursion formulas can suitably be applied to systems of arbitrary length. The method involves replacing the original 1-D chain by an effective one of two extreme atoms which interact through energy-dependent effective terms 3.61 and 3.62.

After considering the one-dimensional chain within the model of single-orbital centered in each particle, the general case of a Hamiltonian described in terms of an arbitrary number of localized orbitals is given. Moreover, the Green's function formalism, which provides a framework to treat the solutions of the Schrödinger equation, is also introduced. We will see how it can be connected to transport problems.

3.6.3 Green's functions applied to effective Hamiltonian description

Once the procedure for obtaining the effective Hamiltonian by means of the decimation method has been established, the connection with Green's function formalism can be treated as illustrated in this section for the simple case of finite atomic chain with a single orbital per atom.

We recall that the retarded (advanced) Green's function matrix is defined in the upper (lower) complex plane by:

$$\mathbf{G}^{r(a)}(\epsilon) = \frac{1}{E\mathbf{I} - \mathbf{H}} \quad (3.63)$$

where \mathbf{H} is the system Hamiltonian and the energy $E = \epsilon + i\eta$ ($-\eta$ for the advanced (a) case) is a complex variable which give a physical meaning to the zeros of the real Green's function. \mathbf{H} can be thought as the sum of the Hamiltonian of the isolated system \mathbf{H}_0 and a perturbation term \mathbf{W} :

$$\mathbf{H} = \mathbf{H}_0 + \mathbf{W} \quad (3.64)$$

The question is how to determine the eigenvalues and eigenfunctions of \mathbf{H} , assuming that for \mathbf{H}_0 the spectrum is known. Let's consider the following identity:

$$E\mathbf{I} - \mathbf{H}_0 = (E\mathbf{I} - \mathbf{H}_0 - \mathbf{W}) + \mathbf{W} \quad (3.65)$$

and multiply both members of the equation by $1/(E\mathbf{I} - \mathbf{H}_0)$ and by $1/(E\mathbf{I} - \mathbf{H}_0 - \mathbf{W})$ to obtain:

$$\frac{1}{E\mathbf{I} - \mathbf{H}_0 - \mathbf{W}} = \frac{1}{E\mathbf{I} - \mathbf{H}_0} + \frac{1}{E\mathbf{I} - \mathbf{H}_0} \mathbf{W} \frac{1}{E\mathbf{I} - \mathbf{H}_0 - \mathbf{W}} \quad (3.66)$$

Indicating with $\mathbf{g}(E)$ the Green's function of unperturbed Hamiltonian \mathbf{H}_0 and with $\mathbf{G}(E)$ the Green's function of \mathbf{H} , we get:

$$\mathbf{G}(E) = \mathbf{g}(E) + \mathbf{g}(E) \cdot \mathbf{W} \cdot \mathbf{G}(E) \quad (3.67)$$

This is the Dyson's equation that relates the isolated (\mathbf{H}_0) and perturbed (\mathbf{H}) Hamiltonian matrices when a perturbation (\mathbf{W}) is switched on. In Fig.3.4, this equation is diagrammatically derived with the help of Feynman diagrams.

3.6 Real space renormalization group procedures, also known as decimation

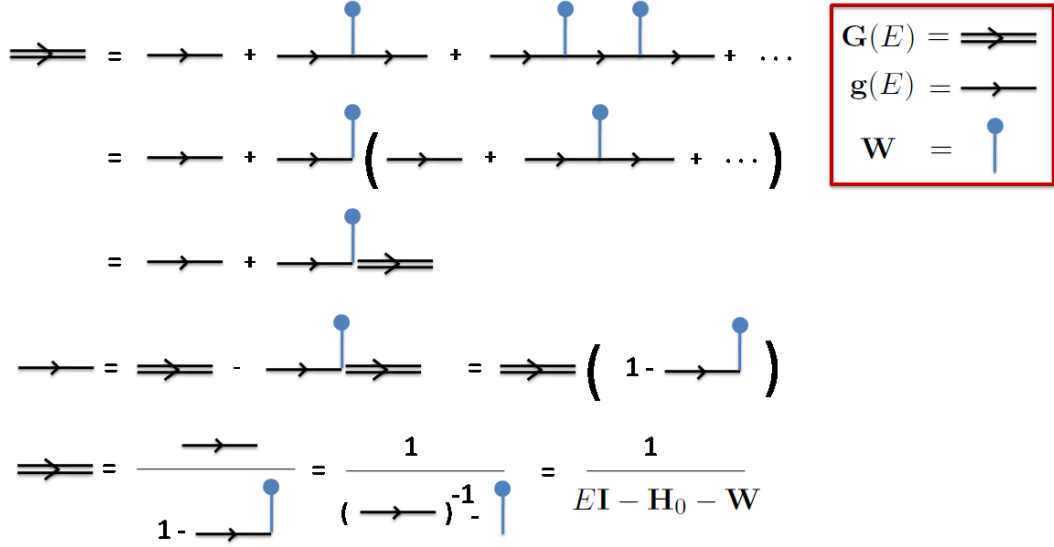


Figure 3.4: Diagrammatical representation of Dyson's equation. - Using Feynman diagrams Dyson's equation can be derived. The perturbed Green's function $G(E)$ is defined by a doubled-line which is decomposed in a perturbation series. Single lines represent the Green's function $g(E)$ of the isolated system which is calculated from the unperturbed Hamiltonian H_0 . Finally, $G(E)$ is deduced from the series expansion.

This equation stands for all operators represented in a given orthonormal set. Let \mathbf{H} be now the two-site matrix Hamiltonian given in 3.41, the simplest case that has been considered. E_1 is the energy of the one-dimensional subspace spanned by the single orbital centered on the first atom, and similarly for E_2 . The Hamiltonian can be separated into the unperturbed part and a perturbation term, according to equation 3.64, as:

$$\mathbf{H} = \begin{pmatrix} E_1 & 0 \\ 0 & E_2 \end{pmatrix} + \begin{pmatrix} 0 & V_{1,2} \\ V_{2,1} & 0 \end{pmatrix} \quad (3.68)$$

Applying Dyson's equation we obtain:

$$\begin{pmatrix} G_{1,1} & G_{1,2} \\ G_{2,1} & G_{2,2} \end{pmatrix} = \begin{pmatrix} g_{1,1} & 0 \\ 0 & g_{2,2} \end{pmatrix} + \begin{pmatrix} g_{1,1} & 0 \\ 0 & g_{2,2} \end{pmatrix} \begin{pmatrix} 0 & V_{1,2} \\ V_{2,1} & 0 \end{pmatrix} \begin{pmatrix} G_{1,1} & G_{1,2} \\ G_{2,1} & G_{2,2} \end{pmatrix} \quad (3.69)$$

where $g_{1,1}(E) = (E - E_1)^{-1}$ and $g_{2,2}(E) = (E - E_2)^{-1}$. Performing the matrix operations of the above equation, the following expressions are obtained:

$$G_{1,1}(E) = g_{1,1}(E) + g_{1,1}(E) \cdot V_{1,2} \cdot G_{2,1}(E) \quad (3.70)$$

$$G_{2,1}(E) = g_{2,2}(E) \cdot V_{2,1} \cdot G_{1,1}(E) \quad (3.71)$$

Similar expressions are obtained by exchanging the subscripts 1 and 2. After using matrix multiplication properties and indicating explicitly the imaginary part of the energy E , a final

3. TRANSPORT

expression for $G_{1,1}^{r(a)}(\epsilon)$ is reached:

$$G_{1,1}^{r(a)}(\epsilon) = \frac{1}{\epsilon \pm i\eta - E_1 - V_{1,2} \frac{1}{\epsilon \pm i\eta - E_2} V_{2,1}} \quad (3.72)$$

$$= \frac{1}{\epsilon \pm i\eta - \tilde{E}_1} \quad (3.73)$$

where

$$\tilde{E}_1 = E_1 + \underbrace{V_{1,2} \frac{1}{\epsilon \pm i\eta - E_2} V_{2,1}}_{\Sigma_1 = \Delta_1 - i\Gamma_1} \quad (3.74)$$

is the renormalized on-site energy of the first single-orbital site. $G_{1,1}^{r(a)}(\epsilon)$ is the retarded (advanced) Green's function of site 1 and it is determined by the renormalized energy 3.74.

With this simple case, it has been shown that Green's function formalism provides us a suited framework to find eigenvalues and eigenfunctions of a physical system in which the unperturbed description can be easily determined and the perturbation term is known. First, the Green's function $\mathbf{g}(E)$ associated with the isolated system \mathbf{H}_0 is found, then the Green's function $\mathbf{G}(E)$ associated with the total Hamiltonian \mathbf{H} is expressed in terms of $\mathbf{g}(E)$ and \mathbf{W} and, finally, the eigenvalues and eigenvectors of \mathbf{H} are obtained from $\mathbf{G}(E)$.

The development of Green's function formalism in terms of perturbative calculations can also be done in terms of Feynman's diagrams. Although an exhaustive review of diagrammatical representations is out of this work scope, it is worth to show the former results with the help of Feynman's diagrams, as can be done after the following operations. Taking up again the final form for $G(\epsilon)_{1,1}^R$ in 3.72, and expressing the denominator in a series expansion, Dyson's equation for this matrix element can be found:

$$G_{1,1}^R(\epsilon) = \frac{1}{\epsilon + i\eta - E_1 - V_{1,2} \frac{1}{\epsilon + i\eta - E_2} V_{2,1}} \quad (3.75)$$

$$= \frac{1}{[G_{1,1}^{(o)R}(\epsilon)]^{-1} - V_{1,2} G_{2,2}^{(o)R}(\epsilon) V_{2,1}} \quad (3.76)$$

$$= G_{1,1}^{(o)R}(\epsilon) \left[1 - \sum_{n=0}^{\infty} (V_{1,2} G_{2,2}^{(o)R}(\epsilon) V_{2,1})^n \right] \quad (3.77)$$

$$= G_{1,1}^{(o)R}(\epsilon) + G_{1,1}^{(o)R}(\epsilon) V_{1,2} G_{2,2}^{(o)R}(\epsilon) V_{2,1} G_{1,1}^{(o)R}(\epsilon) + \dots \quad (3.78)$$

$$= G_{1,1}^{(o)R}(\epsilon) + G_{1,1}^{(o)R}(\epsilon) \Sigma_{1,1}(\epsilon) G_{1,1}^R(\epsilon) \quad (3.79)$$

In systems with a finite number of sites N , $G_{i,j}(\epsilon)$ is a well behaved complex function except at the N poles. In this case, $\Sigma(\epsilon) = \Delta(\epsilon) - i\Gamma(\epsilon)$ fulfills the condition $\Gamma(\epsilon) = 0$ and $\Sigma(\epsilon) = \Delta(\epsilon)$. The super-indices for retarded and advanced Green's function distinction are no longer necessary.

The serie expansion of Dyson's equation 3.79 is represented diagrammatically in Fig.3.5. The total Green's function $G_{1,1}$ is represented by the double line. It can be decomposed

3.6 Real space renormalization group procedures, also known as decimation

$$\begin{aligned}
 \overline{\overline{1 \rightarrow 1}} &= 1 \rightarrow 1 + \cancel{1 \rightarrow \overset{\bullet}{1} \rightarrow \overset{\bullet}{1} \rightarrow 1} + 1 \rightarrow \overset{\bullet}{1} \rightarrow \overset{\bullet}{2} \rightarrow \overset{\bullet}{2} \rightarrow \overset{\bullet}{1} \rightarrow 1 + \dots \\
 &= 1 \rightarrow 1 + 1 \rightarrow \overset{\bullet}{1} \rightarrow \overset{\bullet}{2} \rightarrow \overset{\bullet}{2} \left(1 \rightarrow 1 + 1 \rightarrow \overset{\bullet}{1} \rightarrow \overset{\bullet}{2} \rightarrow \overset{\bullet}{2} \rightarrow \overset{\bullet}{1} \rightarrow 1 + \dots \right) \\
 &= 1 \rightarrow 1 + 1 \rightarrow \overset{\bullet}{1} \rightarrow \overset{\bullet}{2} \rightarrow \overset{\bullet}{2} \overline{\overline{1 \rightarrow 1}}
 \end{aligned}$$

For $\Sigma_{1,1} = \overset{\bullet}{2} \rightarrow \overset{\bullet}{2} = V_{1,2} G_{2,2}^{(o)R}(\epsilon) V_{2,1}$

$$\overline{\overline{1 \rightarrow 1}} = 1 \rightarrow 1 + 1 \rightarrow 1 \Sigma_{1,1} \overline{\overline{1 \rightarrow 1}}$$

$$G_{1,1}(\epsilon) = G_{1,1}^{(o)}(\epsilon) + G_{1,1}^{(o)}(\epsilon) \Sigma_{1,1}(\epsilon) G_{1,1}(\epsilon)$$

$$\tilde{E}_1 = E_1 + \Sigma_1(\epsilon)$$

Figure 3.5: Diagrammatical representation of Green's function $G_{1,1}$. - Feynman diagrams allow us to obtain the expression for the amplitude of probability for a particle to be transmitted from site 1 to site 2 when an interaction $V_{1,2}$ couples them (see Fig.3.2). The embedding self-energy $\Sigma_{1,1}$ can be easily deduced from the diagrammatical development of Dyson's equation removing the non-allowed terms. In this figure, the second term in the series expansion has been removed since a propagation from site 1 to itself through an internal interaction has not been defined. As claimed in (96), "the interpretation of $G_{1,1}(\epsilon)$ is immediate" and the corresponding renormalized energy \tilde{E}_1 in eq.3.51 has a "self-explanatory physical meaning": besides E_1 , it contains the effect of an excursion from A to B, a propagation within B, and an excursion back to A.

3. TRANSPORT

into an infinity sum of terms that represent the unperturbed Green's function (single line) and a recursive succession of hopping interactions (blue line & sphere) which modify Green's function indices. The blue dots, which are connected with blue lines to the expansion, relate two conjugated hopping interactions.

As it was done previously in eq.3.59 for the renormalized effective potential to on-site energies some recursion formulas can be obtained. In a system composed of states numbered from 0 to N+1, the effective hopping between first and last sites is given by:

$$\tilde{V}_{0,N+1} = \tilde{V}_{0,N} \frac{1}{\epsilon - \tilde{E}_N} V_{N,N+1} \quad (3.80)$$

$$= V_{0,1} \{G_{1,N-1} V_{N-1,N} [\epsilon - E_N - H_N^-]^{-1}\} V_{N,N+1} \quad (3.81)$$

$$= V_{0,1} G_{1,N} V_{N,N+1} \quad (3.82)$$

The correction to on-site energies from sites at right and at left are, respectively:

$$H_{0(N)}^+(\epsilon) = V_{0,1} G_{1,1} V_{1,0} \quad (3.83)$$

$$H_{N+1(N)}^-(\epsilon) = V_{N,N+1} G_{N,N} V_{N,N+1} \quad (3.84)$$

Notice that effective hoppings are always related to non-diagonal terms of Green's function matrix. As the system grows, additional non-diagonal Green's function can be calculated by iteration. Identifying $G_{1,N}$ as the term between braces in 3.81, a Green's function recursion formula for the additional site is easily deduced:

$$G_{1,N+1}^{(N+1)} = G_{1,N}^{(N)} V_{N,N+1} G_{N+1,N+1}^{(N+1)} \quad (3.85)$$

which can be used in conjunction with:

$$G_{N+1,N+1}^{(N+1)} = \left[\epsilon I - E_{N+1} - V_{N+1,N} G_{N,N}^{(N)} V_{N,N+1} \right]^{-1} \quad (3.86)$$

the continued fraction expansion of the diagonal Greens's function.

3.6.4 Applying Green's functions to the semi-infinite linear chain problem

Before moving on to more general systems than single-orbital per site models, the ending of this section is devoted to the case of a linear chain which is infinitely long in one direction. It has been shown that the discrete set of eigenvalues of a finite Hamiltonian represented by a finite size matrix can be solved through the decimation method. When the linear chain is extended to the infinity by adding an infinite number of sites at one of the extremities, discrete states no longer exist and a continuum spectrum appears instead. It will be demonstrated that the self-energy operator $\Sigma(\epsilon)$ has an imaginary part which encodes some physical meaning.

To simulate the semi-infinite linear chain, we consider the same hopping values between two nearest neighbouring orbitals, $V_{n,n+1} = V$, and the same on-site energy value, $E_n = 0$,

3.6 Real space renormalization group procedures, also known as decimation

for every site n in the system. The Hamiltonian reads:

$$\mathbf{H} = \begin{pmatrix} E_0 & V & 0 & \dots \\ V^\dagger & E_0 & V & \dots \\ 0 & V^\dagger & E_0 & \dots \\ \vdots & \vdots & \vdots & \ddots \end{pmatrix} \quad (3.87)$$

The goal is to calculate the self-energy of the first site $\Sigma_{1,1}$ due to the presence of the rest of the sites. Let's start the analysis by reducing the system again to a three-site problem, assuming that $V^\dagger = V$. As it has been shown previously, the three-site problem can be reduced to a two-site problem by renormalizing the energy of the second site to $\tilde{E}_2 = E_0 + V[\epsilon - E_0]^{-1}V$ and a hopping parameter of V . Finally the self-energy of the first site due to the presence of the other two is:

$$\Sigma_{1,1}(\epsilon) = \frac{V^2}{\epsilon - E_0 - \frac{V^2}{\epsilon - E_0}} \quad (3.88)$$

If one further extends the continued fraction for the self-energy for the first site one gets: ¹

$$\Sigma_{1,1}(\epsilon) = \frac{V^2}{\epsilon - E_0 - \left(\frac{V^2}{\epsilon - E_0 - \frac{V^2}{\epsilon - E_0 - \dots}} \right)} \quad (3.90)$$

Identifying the term in brackets as $\Sigma_{1,1}(\epsilon) = \Sigma(\epsilon)$, the following relation is obtained:

$$\Sigma(\epsilon) = \frac{V^2}{\epsilon - E_0 - \Sigma(\epsilon)} \implies \Sigma(\epsilon)^2 + (E_0 - \epsilon)\Sigma(\epsilon) + V^2 = 0 \quad (3.91)$$

The solutions to this second order equation are:

$$\Sigma(\epsilon) = \frac{\epsilon - E_0}{2} \pm \sqrt{\left(\frac{\epsilon - E_0}{2}\right)^2 - V^2} \quad (3.92)$$

Notice that even when ϵ only takes real values, the self-energy can be complex. Expressing $\Sigma(\epsilon)$ along as a complex function:

$$\Sigma(\epsilon) = H(\epsilon) \mp i\Gamma(\epsilon) \quad (3.93)$$

we have:

$$H(\epsilon) = \begin{cases} \frac{\epsilon - E_0}{2} - \sqrt{\left(\frac{\epsilon - E_0}{2}\right)^2 - V^2} & \text{if } \epsilon - E_0 > 2|V| \\ \frac{\epsilon - E_0}{2} & \text{if } \epsilon - E_0 \leq 2|V| \\ \frac{\epsilon - E_0}{2} + \sqrt{\left(\frac{\epsilon - E_0}{2}\right)^2 - V^2} & \text{if } \epsilon - E_0 < -2|V| \end{cases} \quad (3.94)$$

¹This approximation can be also justified in terms of Dyson's equation by writing:

$$\Sigma_n(\epsilon) = \frac{V^2}{\epsilon - E_0 - \Sigma_{n+1}(\epsilon)} \quad (3.89)$$

and assuming the fact that every site has to (say) right an infinite chain. Therefore $\Sigma_n = \Sigma$ for every n .

3. TRANSPORT

for $H(\epsilon) = \text{Re}[\Sigma(\epsilon)]$, and

$$\Gamma(\epsilon) = \begin{cases} 0 & \text{if } |\epsilon - E_0| > 2|V| \\ \sqrt{V^2 - \left(\frac{\epsilon - E_0}{2}\right)^2} & \text{if } |\epsilon - E_0| \leq 2|V| \end{cases} \quad (3.95)$$

for $\Gamma(\epsilon) = \text{Im}[\Sigma(\epsilon)]$. Both real and imaginary parts have a meaningful physical interpretation: $H(\epsilon)$ is the energy correction to the on-site energy of first single-orbital site as a consequence of its interaction with the rest of the chain at (say) left, and corresponds to the self-energy term that has been calculated in the above finite size systems.

It is worth noticing that the allowed Bloch solutions to the problem of the infinite linear chain are limited to the range of energies in which

$$\epsilon \equiv \epsilon_k = E_0 - 2V \cos(ka), \quad (3.96)$$

the region where the spectrum is continuous.¹ In such a situation, $\Gamma(\epsilon) \neq 0$

3.6.5 Green's function and diffusion probability

It has been shown that for a certain range of energy values, the self-energy of a system can be expressed with a complex function of energy. We demonstrate the relation between the imaginary part and the time spent by an electron on the extreme site before leaving the system (the mean lifetime), showing that $\Gamma(\epsilon)$ is related to possibility of an electron to escape to the infinite through the linear chain.

The Green's function of the semi-infinite linear chain is given by

$$G(\epsilon) = \frac{1}{\epsilon - E_0 - \Sigma(\epsilon)} \quad (3.97)$$

where $\Sigma(\epsilon)$ is the self-energy of the chain as expressed in 3.93. If the density of states is given by:

$$D(\epsilon) = \mp \frac{1}{\pi} \text{Im} \{ \text{tr}[G(\epsilon)] \} \quad (3.98)$$

the density of states of the single orbital centered in the edge atom of the semi-infinite linear chain is:

$$D(\epsilon) = \frac{1}{\pi V} \sqrt{1 - \left(\frac{\epsilon - E_0}{2V}\right)^2} \quad (3.99)$$

Performing the Fourier's transform of the Green's function we can calculate the probability amplitude of a state in site 0 to evolve in time and to go back to its initial state:

¹In this case a is the inter-site separation along the straight line defining the semi-infinite chain, and k is the wavevector

3.6 Real space renormalization group procedures, also known as decimation

$$P_{0,0}(t) = |\langle 0 | \exp[-iHt/\hbar] | 0 \rangle|^2 \quad (3.100)$$

$$= \left| \int G_{0,0}(\epsilon) \exp[-i\epsilon t/\hbar] d\epsilon \right|^2 \quad (3.101)$$

$$= \left| J_1(2Vt/\hbar) \frac{\hbar}{Vt} \right|^2 \quad (3.102)$$

$$\sim \frac{1}{\pi} \left[\frac{\hbar}{Vt} \right]^3 \quad (3.103)$$

where J_1 is the Bessel's function of first order. For $t \rightarrow \infty$ the probability of a particle (an electron) to be back at the initial state decays to zero. The imaginary part only appears in the case of an infinite system and is related to the possibility of no return diffusion.

In the case of an infinite linear chain, the Green's function is expressed as in eq.3.97 but with self-energy multiplied by 2, which accounts for the two semi-infinite chains extended at both sides of reference site. Now the density of states of this orbital is:

$$D(\epsilon) = \frac{1}{\pi V} \sqrt{1 - \left(\frac{\epsilon - E_0}{2V} \right)^2} \quad (3.104)$$

The probability of return to the remaining site after decimation is given by:

$$P_{0,0}(t) = |\langle 0 | \exp[-iHt/\hbar] | 0 \rangle|^2 \quad (3.105)$$

$$= |J_0(Vt/\hbar)|^2 \quad (3.106)$$

$$\sim \frac{1}{\pi} \frac{\hbar}{Vt} \quad (3.107)$$

This represents a substantial change with respect to the classical problem of random walk in an infinite linear chain. Within the quantum approach, there exists a certain probability for the particle to be diffused to the infinite, in contrast with the exponential and diffusive laws of empirical descriptions or the finite case.

3.6.6 Applying Green's function beyond the linear chain problem

The techniques described in this section aim to obtain effective Hamiltonians by means of the so-called decimation method, consisting on reducing the dimension of the basis function space down to a one-dimensional effective system with the same electronic features as the original one. The advantage of decimation techniques is that they provide a procedure which works in real space, directly on the lattice description. On the other hand, Dyson's equation allows us to calculate the Green's function of a system which Hamiltonian can be decoupled into an isolated term and a coupling term. Up to now, the renormalization method has been presented in the simplified framework of the linear chain with a single orbital centered

3. TRANSPORT

on each atom. It was established that the two-dimensional Hamiltonian 3.54 representing two renormalized sites is equivalent to the whole original linear chain as long as they are connected by the effective coupling terms 3.57 and 3.58. Then, the linear chain was extended in one direction to the infinite to obtain a semi-infinite chain and, finally, in both directions to obtain an infinite linear chain.

Herein it is shown that the decimation scheme can be generalized to higher dimensions if the same procedure of elimination is preserved. We will now reformulate the decimation technique with the help of layer concept. The problem of solving the conventional linear chain of equations from the matrix elements of a $N \times N$ -dimensional Hamiltonian, (where N is the total number of orbitals), will be replaced by a more generic one, in which the single orbital linear chain is changed by a multi-orbital linear chain. Moreover, each atom is replaced by atomic planes which are periodically repeated in one direction of the space. The interaction with the nearest neighbour orbitals is substituted by a complete description of interacting orbitals between layers. The atomic plane with only neighbouring atoms at one side is then considered as the bulk surface. Therefore, the single orbital representation is now replaced by a multi-orbital matrix representation. The decimation scheme can be then generalized to a problem of larger dimensions as long as the elimination procedure is performed layer by layer.

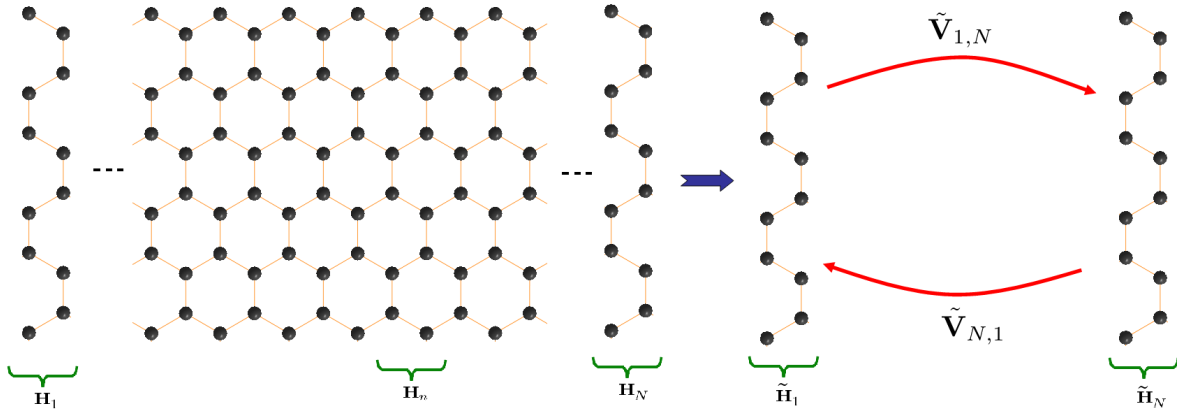


Figure 3.6: Network of site decimation - A one-dimension hexagonal lattice of N unit cells is decimated to an effective system of two unit cells (sites within dashed green line) represented by effective Hamiltonians \tilde{H}_1 and \tilde{H}_N which are connected by coupling matrices $\tilde{V}_{1,N}$ and $\tilde{V}_{N,1}$

Every site in the above procedure becomes now an $N \times N$ -matrix, where N is the size of the layer. Fig.3.6 shows a piece of a finite strip of atoms constructed by a periodic repetition of a hexagonal unit cell. The number of orbitals per atom does not need to be constrained to one and a general model with several orbitals centered on each atom could be taken into account. Moreover, the tight-binding model can go beyond the nearest neighbour problem. We proceed now to decimate the finite strip ($Im[\Sigma(\epsilon)] \equiv \Gamma(\epsilon) = 0$), and write down the general equations for the real self-energies by successive elimination of intermediate layers

3.6 Real space renormalization group procedures, also known as decimation

from the 2nd to the (N-1)th. Bold notation is now adopted to indicate the matrix nature of the self-energies which are evaluated following the iterative procedure. The recursion formulas are:

$$\mathbf{H}_{1(n)}^+(\epsilon) = \mathbf{H}_{1(n-1)}^+ + \tilde{\mathbf{V}}_{1,n} \frac{1}{\epsilon \mathbf{I} - \mathbf{H}_n^0 - \mathbf{H}_n^-} \tilde{\mathbf{V}}_{n,1} \quad (3.108)$$

$$\mathbf{H}_{n+1}^-(\epsilon) = \mathbf{V}_{n+1,n} \frac{1}{\epsilon \mathbf{I} - \mathbf{H}_n^0 - \mathbf{H}_n^-} \mathbf{V}_{n,n+1} \quad (3.109)$$

$$\tilde{\mathbf{V}}_{1,n+1}(\epsilon) = \tilde{\mathbf{V}}_{1,n} \frac{1}{\epsilon \mathbf{I} - \mathbf{H}_n^0 - \mathbf{H}_n^-} \mathbf{V}_{n,n+1} \quad (3.110)$$

$$\tilde{\mathbf{V}}_{n+1,1}(\epsilon) = \mathbf{V}_{n+1,n} \frac{1}{\epsilon \mathbf{I} - \mathbf{H}_n^0 - \mathbf{H}_n^-} \tilde{\mathbf{V}}_{n,1} \quad (3.111)$$

where:

\mathbf{H}_n^0 is the nth layer on-site matrix Hamiltonian. The diagonal elements of the matrix account for the on-site energy of each of the orbitals contained in the current layer. Non-diagonal elements account for the intra-layer hopping values between each pair of orbitals.

$\mathbf{H}_{1(n)}^+(\epsilon)$ is the self-energy correction to the first layer when all layer to the right have been eliminated.

$\mathbf{H}_{n+1}^-(\epsilon)$ is the self-energy correction to layer (n+1) when all layer to the left have been eliminated.

$\tilde{\mathbf{V}}_{1(n+1)}$ is the effective coupling term between the two remaining layers.

The initial values are: $\mathbf{H}_1^{+(1)}(\epsilon) = 0$, $\mathbf{H}_2^-(\epsilon) = 0$ and $\tilde{\mathbf{V}}_{1,2}(\epsilon) = \mathbf{V}_{1,2}(\epsilon)$. Intra-layer interactions are contained in \mathbf{H} and elimination of strip intermediate layers is reflected in effective interactions among the orbitals between the not decimated layers. ¹

3.6.7 Renormalization method applied to our case.

Green's function formalism provides us a suitable framework for transport calculations. The goal is to find the Green's function $\mathbf{G}(\epsilon)$ in the matrix form of a system composed of two semi-infinite leads in contact with a region called channel, through which electrons can flow with a certain probability to be backscattered. The usual approach to determine $\mathbf{G}(\epsilon)$ consists on inverting the matrix:

$$\mathbf{G}(\epsilon) = \frac{1}{(\epsilon + i\eta)\mathbf{I} - \mathbf{H}} \quad (3.112)$$

¹The layer division model considered in this work groups interacting atomic planes in principal layers, in such a way that interactions between vecinal layers are restricted to nearest neighbours.

3. TRANSPORT

where \mathbf{H} is the Hamiltonian matrix of the whole system, usually expressed in a tight-binding form. The main problem is that one has to deal with the inversion of an infinite dimensional matrix. This problem arises from the fact that the channel is an open system connected to infinite leads, which allow us to study charge carriers propagation in a one-dimensional conductor with no reflecting boundaries. The main concern when dealing with numerical transport problems is then how to "collapse" the infinite matrices representing the leads into finite and more easy-to-use matrices.

In the previous sections, an efficient and computationally stable procedure for basis space reduction of systems have been presented. The decimation of systems made up of an arbitrary large (even infinite) number of sites with a single orbital centered on each was presented. Recursion formulas 3.59 allow us to reduce the size of the system and 3.108 formulas extend the from single-orbital model to a multi-orbital model, in which matrices play the role of on-site energies and coupling terms. It has been shown that this reduction of the entire system to an effective system maintains the electronic properties of the original one, and allows us to calculate the Green's function with a reasonable amount of effort. A system of λ layers containing n orbitals each would be represented by a Hamiltonian of size $\lambda \times n$. By performing λ times a set of algebraic operations (matrix inversion plus multiplication) an effective Hamiltonian of size n may be obtained. The original system Hamiltonian becomes thus computationally tractable for n sufficiently small.

In this section, the renormalization method as implemented in our code is presented. The approach is basically the same than the one presented above, only the way it is implemented changes with respect to the recursion formulas 3.108. A technique that uses the numerical data computed for channel description to define the electrodes is presented as well.

In the charge transport problem through a device channel, the electron is assumed to come far from one of the leads and leave the system (if not backscattered) from the opposited lead. In order to simulate the electrodes to which the channel is connected, a computational efficient implementation of the decimation procedure for finding the self-energy matrices of long one-dimensional leads must be done. In this way, perfect CNTs and GNRs with length of micrometers are reproduced in an efficient fashion which avoids the repetition of the same algebraic operations thousand of times.

Later on, the connection between Green's function and transport formalism will be detailed. The self-energy of the electrodes and the Green's function of the channel are needed for transmission coefficient calculation. The goal now is to compute the Green's function of the entire device by dividing it into a finite-size channel plus two semi-infinite leads.

In the case of electrodes, the decimation procedure is implemented in `TB.Sim` program that simultaneously eliminates all equivalent sites in a very long lead. The decimation process replaces original on-site Hamiltonians and coupling terms between layers by renormalized new matrices. This replacement is performed iteratively until residual interactions between effective layers are small enough to consider that they are no coupled anymore. The semi-infinite lead is then approximated by an on-site renormalized Hamiltonian which is weakly coupled to a very far similar Hamiltonian. The electrode is then completely characterized by

3.6 Real space renormalization group procedures, also known as decimation

a reduced effective on-site matrix plus a self-energy term that effectively takes into account the previously existing layers.

Regarding the central part of the device, we consider a channel as a structure with a potential distribution which differs from that of the leads. This potential is responsible of the probability of an electron to be backscattered when traversing the channel. In our approach, the original electronic structure alteration of the pristine channel comes from the quantum barriers and potential wells created around the carbon atom to which a functional group is attached¹. All the unit cells treated in this work are supposed to achieve a condition when they are created: the original geometric and electronic structure properties of the layers where periodic conditions are applied must be unaltered after the perturbation is introduced.

The starting point for our decimation procedure is the tight-binding Hamiltonian of a given system. This system is called “building block” (BB) and is further repeated and combined with similar BB along one direction of the space (say z-coordinate) to create the device channel. Without entering into the details of the Hamiltonian origin, we assume that it takes into account periodic boundary conditions applied on the building block borders. We will see later that this approach is the most convenient description when the Hamiltonian comes from a DFT SIESTA calculation. In general a model of several orbitals per atom is considered.

Once the system has been divided into N first neighbouring interacting layers, the Hamiltonian \mathcal{H} of a BB has a sparse representation, namely block-tridiagonal representation, plus corner elements which take into account boundary conditions:

$$\mathcal{H} = \begin{pmatrix} \mathbf{H}_1 & \mathbf{V}_1 & & & \mathbf{V}_N \\ \mathbf{V}_1^\dagger & \mathbf{H}_2 & \mathbf{V}_2 & & \\ & \mathbf{V}_2^\dagger & \ddots & \ddots & \\ & & \ddots & \mathbf{H}_{N-1} & \mathbf{V}_{N-1} \\ \mathbf{V}_N^\dagger & & & \mathbf{V}_{N-1}^\dagger & \mathbf{H}_N \end{pmatrix} \quad (3.113)$$

\mathbf{H}_i ($i = 1\dots N$) are the on-site energy diagonal submatrices of the layers in which the system is divided. Diagonal terms contain the on-site energy of the orbitals within the layer and the non-diagonal terms describe the intra-layer orbital-orbital coupling. \mathbf{V}_j ($j = 1\dots N - 1$) submatrices contain all the information related to coupling between nearest neighbouring layers. \mathbf{V}_i couples orbitals of i -layer to orbitals of $i + 1$ -layer, and \mathbf{V}_i^\dagger couples orbitals of $i + 1$ -layer to orbitals of i -layer. Corner submatrices \mathbf{V}_N and \mathbf{V}_N^\dagger describe the interactions between adjacent layers in the periodic images of the supercell.

In addition to the Hamiltonian matrix, we also consider an overlap matrix \mathcal{S} coming from the fact that the chosen basis set is non-orthogonal. This matrix takes the same block-tridiagonal form than the Hamiltonian matrix:

¹In one case (edge defects in GNRs) the perturbation will come from the new density of states upon one or several carbon atoms are removed from the original structure

3. TRANSPORT

$$\mathcal{S} = \begin{pmatrix} \mathbf{S}_1 & \mathbf{U}_1 & & & \mathbf{U}_N \\ \mathbf{U}_1^\dagger & \mathbf{S}_2 & \mathbf{U}_2 & & \\ & \mathbf{U}_2^\dagger & \ddots & \ddots & \\ & & \ddots & \mathbf{S}_{N-1} & \mathbf{U}_{N-1} \\ \mathbf{U}_N^\dagger & & & \mathbf{U}_{N-1}^\dagger & \mathbf{S}_N \end{pmatrix} \quad (3.114)$$

In the following, the contribution of \mathcal{S} matrix will be explicitly included in decimation formulas.

3.6.7.1 Channel decimation

A long functionalized channel suitable for transport studies can be built up by random assembling of elementary building blocks. Introducing segments of non perturbed building blocks, a defected channel with longitudinal disorder can be easily built. In this way, a channel as long as desired can be constructed from the previous calculations of a finite set of defected and pristine building blocks. The Hamiltonian associated to such a system is intractable if the decimation method is not applied, which avoids the task of direct inversion of the large matrix $[E\mathbf{S} - \mathbf{H}_{channel}]$. We introduce for the first time the overlap matrix which takes into account the non-orthogonal nature of the basis set.¹ With the renormalization method the Green's function of a reduced two-layered system described by two effective Hamiltonians and an effective coupling between both layers can be easily computed. The procedure is similar to the one described with eq. 3.55 but here scalar on-site energies need to be substituted by on-site energy matrices:

$$\mathbf{H}_{1(l)}^+(\epsilon) = \mathbf{H}_{1(l-1)}^+ + \tilde{\mathbf{V}}_{1,l} \frac{1}{\epsilon \mathbf{S}_l - \mathbf{H}_l^0 - \mathbf{H}_l^-} \tilde{\mathbf{V}}_{l,1} \quad (3.115)$$

$$\mathbf{H}_{l+1}^-(\epsilon) = (\mathbf{V}_l^\dagger - E\mathbf{U}_l^\dagger) \frac{1}{\epsilon \mathbf{S}_l - \mathbf{H}_l^0 - \mathbf{H}_l^-} (\mathbf{V}_l - E\mathbf{U}_l) \quad (3.116)$$

$$\tilde{\mathbf{V}}_{1,l+1}(\epsilon) = \tilde{\mathbf{V}}_{1,l} \frac{1}{\epsilon \mathbf{S}_l - \mathbf{H}_l^0 - \mathbf{H}_l^-} (\mathbf{V}_l - E\mathbf{U}_l) \quad (3.117)$$

$$\tilde{\mathbf{V}}_l(\epsilon) = (\mathbf{V}_l^\dagger - E\mathbf{U}_l^\dagger) \frac{1}{\epsilon \mathbf{S}_l - \mathbf{H}_l^0 - \mathbf{H}_l^-} \tilde{\mathbf{V}}_{l,1} \quad (3.118)$$

By iterative elimination of intermediate layers, the final system is equivalent to the original one if \mathbf{H}_1 submatrix of the first building block and \mathbf{H}_N submatrix of the last one are connected by the effective coupling terms $\mathbf{V}_{1,N}$ and $\mathbf{V}_{N,1}$ (tilde symbol, $\tilde{}$, stands for "renormalized"). An important remark must be made: the corner-block matrices which connect layers in the extremities through an external coupling do not play a role in this process.

¹Introducing the overlap matrix in the calculation of the Green's function is mandatory if no previous orthonormalization procedure is applied to the Hamiltonian. Working with this matrix instead of an orthonormalized Hamiltonian has the advantage of shorter coupling distances between distant orbitals.

3.6 Real space renormalization group procedures, also known as decimation

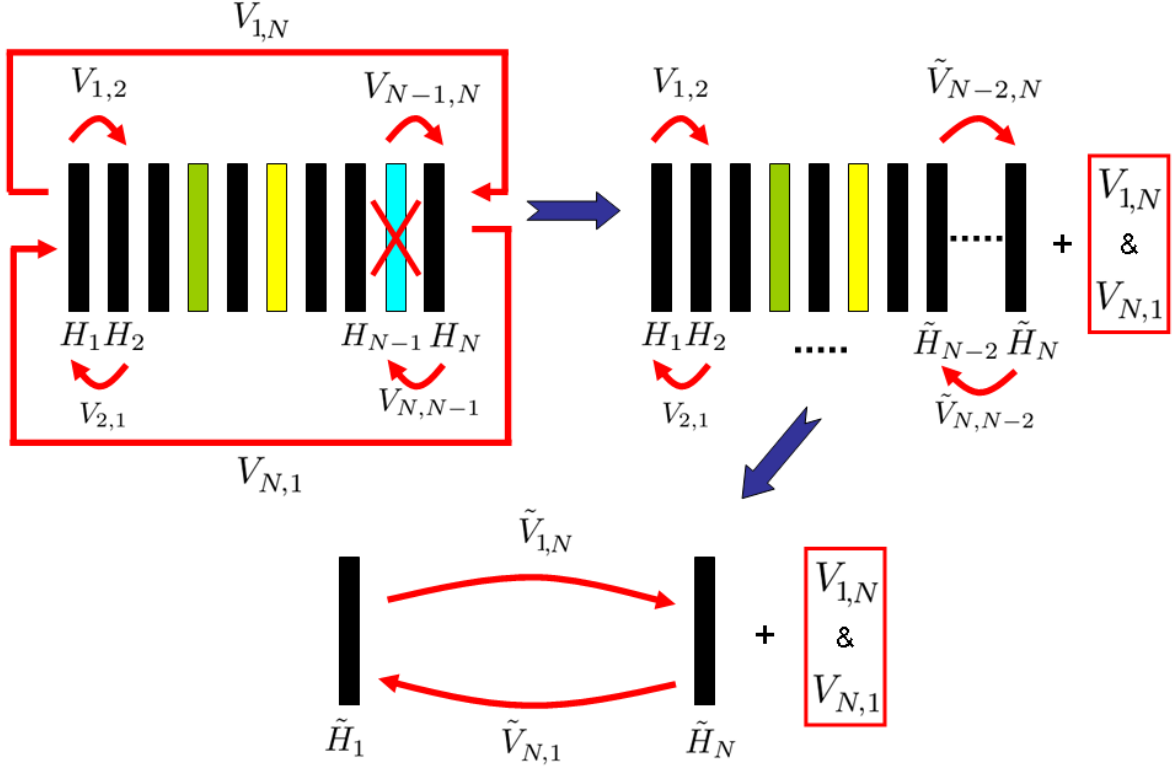


Figure 3.7: Block decimation of a generic channel - The first design represents graphically the Hamiltonian 3.113 of the initial system. The system is partitioned into different layers of various compositions (colors), numerically represented by Hamiltonian matrices \mathbf{H}_n . Intra- and inter-cell coupling between layers are denoted by \mathbf{V}_n matrices. The decimation process starts on $N-1$ layer and successively eliminates intermediate block matrices down to the second one. At each step, the computed self-energy that accounts for the eliminated system is added to next block and effective coupling terms $\tilde{\mathbf{V}}_{l,N}$, $\tilde{\mathbf{V}}_{N,l}$ are also calculated. At the end of the process only two effective layers \mathbf{H}_1 and \mathbf{H}_N remain. The corner-block matrices in the original Hamiltonian are left apart in this process since the coupling of edge layers with external system has not been considered yet. Therefore, one should not confuse the effective intra-layer coupling $\tilde{\mathbf{V}}_{1,N}$, $\tilde{\mathbf{V}}_{N,1}$ with the block matrix external coupling $\mathbf{V}_{1,N}$, $\mathbf{V}_{N,1}$.

3. TRANSPORT

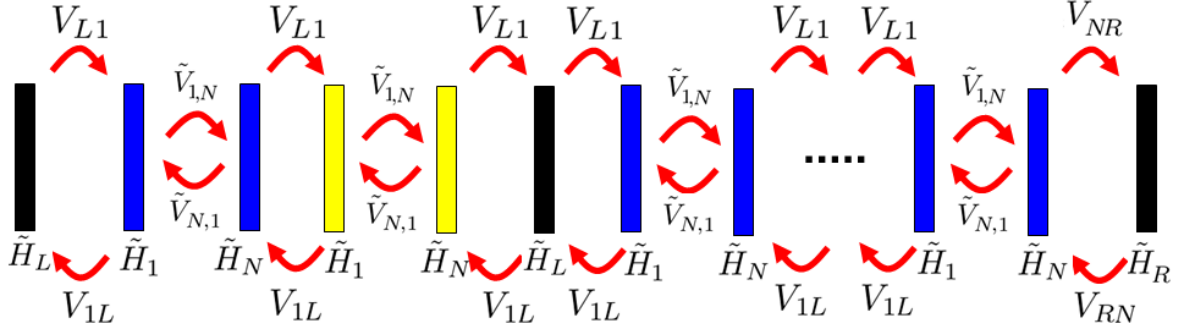


Figure 3.8: Building up of the channel - A generic channel is composed of different building blocks (different colors) which have been previously decimated. This assembling procedure is a N-order method which allows us to construct extremely long channels with a reasonable amount of computational effort.

Figure 3.7 schematizes the decimation process of a building block from its initial Hamiltonian representation down to the final effective system. From left to right, every intermediate layer is successively eliminated and the external coupling $\mathbf{V}_{1,N}$ and $\mathbf{V}_{N,1}$ are left besides, since they only account for the coupling with outer layers of the neighbouring periodic cells. In principle, each layer could contain a variable amount of sites as well as be composed of different types of atoms with varying number of orbitals. The main concern is to divide the system in grouped atomic planes in such a way that interlayer interactions are restricted to nearest neighbours. Notwithstanding, in our procedure effective last matrix layers \mathbf{H}_1 and \mathbf{H}_N have always the same size. The final renormalized Hamiltonian reads:

$$\tilde{\mathbf{H}} = \begin{pmatrix} \tilde{\mathbf{H}}_1 & \tilde{\mathbf{V}}_{1,N} \\ \tilde{\mathbf{V}}_{N,1} & \tilde{\mathbf{H}}_N \end{pmatrix} \quad (3.119)$$

The entire channel decimation can be efficiently performed if the different types of building blocks forming the channel have been all previously decimated. Once the building blocks have been decimated down to two effective layers, the channel made up of effective building blocks is recursively decimated from the second layer in one extreme to the last but one layer of the opposite building block in the linear structure. Pristine sections of channel can be then included in the final channel structure in a convenient way, as explained below (see Fig.3.8 and Fig.3.11).

The building block Hamiltonian creation process consists of introducing a geometrical defect which breaks pristine channel symmetries and introduces a perturbative potential in its electronic structure. The length of the building block is chosen such that these induced perturbations vanish at the edges where periodic boundary conditions are applied. This constraint results in a numerical equivalence of \mathbf{H}_1 and \mathbf{H}_N submatrices of eq.3.113 to the unit cell of a pristine channel section. Since corner-block matrices describe the coupling to these pristine external layers in the periodic repetition of the unit cell, they can be used for coupling

3.6 Real space renormalization group procedures, also known as decimation

pristine segments to defected building blocks or to other pristine sections. In other words, main diagonal corner-block matrices in eq.3.113 represent on-site matrix energies of pristine sections of the channel and secondary-diagonal corner-block matrices in the Hamiltonian represent the coupling between them. Therefore, assembling of successive building blocks can be done with the help of the corner-block coupling matrices without creating artificial mismatches in the joint region. In conclusion, this methodology represents a way to define pristine sections and electrodes from the *ab initio* Hamiltonian of a defected section.

3.6.7.2 Lead computation

The technique described above for building blocks matching can be used again for building up the electrodes. In our simulations, a lead is seen as an extension to the infinity of the non pertubated structure of the channel. This allows us to consider the simplest case for the lead-channel contact problem. In this way no charge reflection takes place in the regions where channel and semi-infinite electrodes match. Far from reality of experiments, this is a convenient way of determining the transmission probability of an electron when flowing through a pertubated channel without considering contact effects. In an experimental set-up, charge carriers are supplied to the channel through metallic contacts, as shown in Fig3.9. This shows an example of a palladium nanowire-CNT interface at which a Schottky barrier develops and strongly influences charge transmission and device characteristics. The nature of metal/CNT contact imposes an effective potential across the junction which makes it difficult to describe just the backscatting phenomena within the channel.

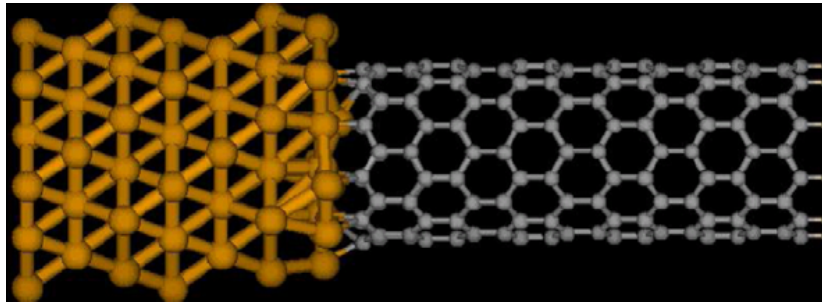


Figure 3.9: Example of lead-channel matching - Carbon nanotube structure is deformed upon matching with "ABC" stacking palladium nanowire acting as a lead. The interface between both materials entail additional backscattering effects when electrons flow from lead to channel due to the electronic and geometrical rearrangement. (Image obtained from (102))

The approach that has been followed here consists in connecting the functionalized channel to two semi-infinite electrodes which have the same geometry and electronic structure than the channel before being pertubated. The four corner block matrices of eq.3.113 contain all the information needed to build up the leads. Fig3.10 shows schematically this procedure. Outermost layers of the building block are assumed to have the geometry and electronic

3. TRANSPORT

structure of a pristine system since they are far from the perturbation induced by the impurity. Therefore, Hamiltonian on-site submatrices \mathbf{H}_1 and \mathbf{H}_N are roughly equal and represent the electronic parametrization of pristine electrode and unit layer-cell. By periodic repetition of \mathbf{H}_1 long electrodes can be reproduced reusing the information already calculated for building block description. The coupling matrices describing the interaction of unit cells are the secondary diagonal block matrices $\mathbf{H}_{1,N}$ and $\mathbf{H}_{N,1}$

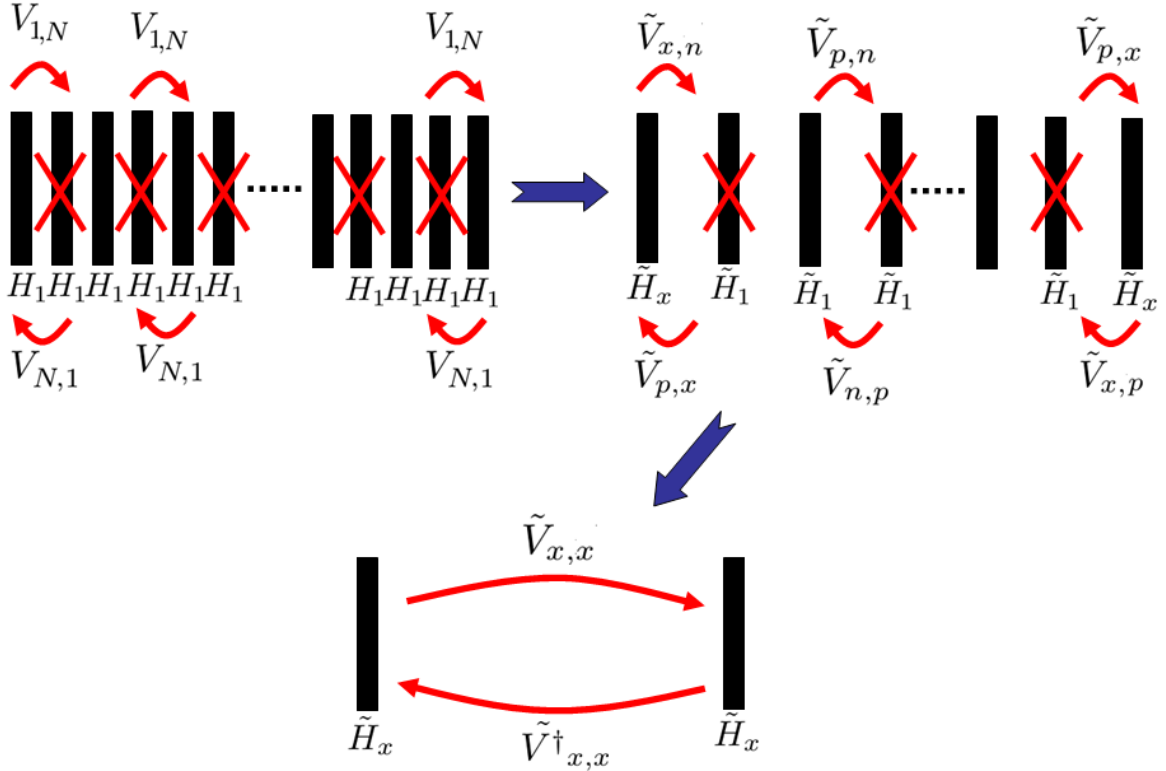


Figure 3.10: Procedure of lead decimation - .

Following ref.(95), TB_Sim program has been coded in an efficient way so that at each step all equivalent sites are simultaneously eliminated. Suppose an electrode composed of layers numbered from 1 to N , for N an odd number. Let block matrices \mathbf{H}_1 and \mathbf{H}_N in eq.3.113 be both renamed to \mathbf{H}_P when representing internal layers of the lead and keep the same notation only for extremity layers. Also block matrices are renamed: $V_N \equiv V_P$. In a first step all even-numbered sites from 2 to $N - 1$ are simultaneously eliminated and the corresponding self-energies are added to the remaining sites. Therefore, $(N - 1)/2$ layers are removed at once. \mathbf{H}_1 and \mathbf{H}_N are different from the bulk layers since they are coupled to the system at only one side. A simple generalization of eq.3.115 yields to the convenient expressions:

3.6 Real space renormalization group procedures, also known as decimation

$$\tilde{\mathbf{H}}_1 = \mathbf{H}_1 + \mathbf{V}_U^1 \frac{1}{E\mathbf{S}_P - \mathbf{H}_P} \mathbf{V}_U^2 \quad (3.120)$$

$$\tilde{\mathbf{H}}_N = \mathbf{H}_N + \mathbf{V}_U^2 \frac{1}{E\mathbf{S}_P - \mathbf{H}_P} \mathbf{V}_U^1 \quad (3.121)$$

for layers on lead extremities, where

$$\mathbf{V}_U^1 \equiv \mathbf{V}_P - E\mathbf{U}_P \quad (3.122)$$

$$\mathbf{V}_U^2 \equiv \mathbf{V}_P^\dagger - E\mathbf{U}_P^\dagger \quad (3.123)$$

and:

$$\tilde{\mathbf{H}}_P = \mathbf{H}_P + \mathbf{V}_U^1 \frac{1}{E\mathbf{S}_P - \mathbf{H}_P} \mathbf{V}_U^2 + \mathbf{V}_U^2 \frac{1}{E\mathbf{S}_P - \mathbf{H}_P} \mathbf{V}_U^1 \quad (3.124)$$

$$\tilde{\mathbf{V}}_P^1 = \mathbf{V}_U^1 \frac{1}{E\mathbf{S}_P - \mathbf{H}_P} \mathbf{V}_U^1 \quad (3.125)$$

$$\tilde{\mathbf{V}}_P^2 = \mathbf{V}_U^2 \frac{1}{E\mathbf{S}_P - \mathbf{H}_P} \mathbf{V}_U^2 \quad (3.126)$$

for internal odd-layers. Most of these sites are equivalent and the two only inequivalent sites at the extremities are stored apart. In a second step, again all even-numbered equivalent sites are removed from the system and the inequivalent ones are recorded. This decimation procedure is repeated until no equivalent intermediate layer remain in the system and only the two outermost ones remain. An effective coupling connects both distant extremity layers.

The Hamiltonian which results of the decimation process yields the Green's function matrix upon inversion. For an electrode composed of N layers, the number of renormalizations to be performed to obtain the Green's function at a given energy is of the order of $2\log_2(N)$. Therefore, this iterative scheme allows for effective Hamiltonian calculation of an extremely long lead with very quick convergence and reasonable computation effort. After n steps 2^n layers are taken into account instead of the N layers one would have included with the method based on the recursion formulas 3.108. The convergence can be considered reached when the coupling elements between the two far distant effective layers are small enough to consider that they are not coupled anymore. Usually, no more than 25 iterations suffice to get a converged result. Then the unit cell that will be connected to the channel contain an energetic description which is equivalent to the semi-infinite lead.

3.6.7.3 Entire system Green's function

In the previous sections, the presented methodology was based, firstly, on reducing channel Hamiltonian size, and then, on removing the infinite size problem related to ideal leads. The main question to address now is how the effective Hamiltonian descriptions of the divided

3. TRANSPORT

device can be put together. We resort again to the concept of self-energy to make possible the description of the whole device starting from channel and electrode Green's functions, which are obtained from these Hamiltonians.

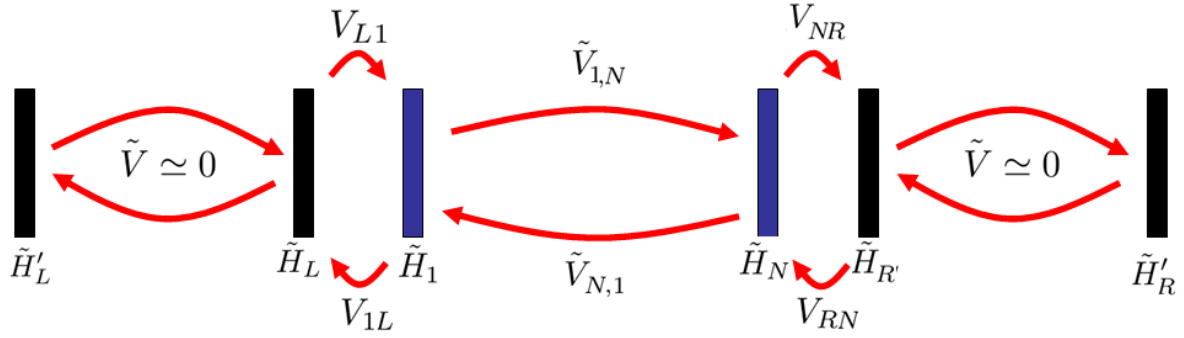


Figure 3.11: Scheme of the final decimated system - Once right and left lead along with the channel have been decimated separately, the system Green's function can be calculated. \tilde{H}'_L and \tilde{H}'_R and the matrix Hamiltonians of the far distant effective on-site terms of left and right lead, respectively. Assuming that they weakly coupled ($\tilde{V} \simeq 0$) to their counterpart \tilde{H}_L and \tilde{H}_R which remain coupled to the effective on-site channel matrices \tilde{H}_1 and \tilde{H}_N , the system can be considered to be describe by these four effective on-site matrices plus the three coupling matrix terms (and their conjugated complex)

We finally arrive at a lead-channel system like the one showed in Fig.3.11. The left-lead is described by \tilde{H}_L , the rightmost decimated renormalized layer which is coupled to leftmost renormalized channel layer \tilde{H}_1 through the coupling matrix V_{L1} (and its complex conjugate V_{1L}). Due to the weak coupling to the rest of the system, the leftmost distant part of the lead decimated Hamiltonian is considered to be isolated and, hence, further neglected on the calculations. Similar reasoning is applied to the right-lead. The simplified system Hamiltonian now reads:

$$\mathcal{H} = \begin{bmatrix} \tilde{H}_L & V_{1L} & & & \\ V_{L1} & \tilde{H}_1 & \tilde{V}_{N1} & & \\ & \tilde{V}_{1N} & \tilde{H}_N & V_{RN} & \\ & & V_{NR} & \tilde{H}_R & \\ & & & & \end{bmatrix} \quad (3.127)$$

and overlap matrix,

$$\mathcal{S} = \begin{bmatrix} \tilde{S}_L & U_{1L} & & & \\ U_{L1} & \tilde{S}_1 & \tilde{U}_{N1} & & \\ & \tilde{U}_{1N} & \tilde{S}_N & U_{RN} & \\ & & U_{NR} & \tilde{S}_R & \end{bmatrix} \quad (3.128)$$

Focusing in the subsystem composed of left-lead, leftmost on-site matrix channel and the coupling terms, we can calculate its associated Green's function shown in eq.3.112 partitioning

3.6 Real space renormalization group procedures, also known as decimation

the matrix in:

$$\mathbf{G} = \begin{bmatrix} \mathbf{G}_L & \mathbf{G}_{L1} \\ \mathbf{G}_{1L} & \mathbf{G}_1 \end{bmatrix} \quad (3.129)$$

where the two submatrices \mathbf{G}_L and \mathbf{G}_1 represent lead and conductor subspaces, respectively. Green's function fulfills the equation ¹:

$$\begin{bmatrix} \mathbf{G}_L & \mathbf{G}_{L1} \\ \mathbf{G}_{1L} & \mathbf{G}_1 \end{bmatrix} \begin{bmatrix} (\epsilon + i\eta)\mathbf{S}_L - \tilde{\mathbf{H}}_L & (\epsilon + i\eta)\mathbf{U}_{L1} - \mathbf{V}_{L1} \\ (\epsilon + i\eta)\mathbf{U}_{1L} - \mathbf{V}_{1L} & (\epsilon + i\eta)\mathbf{S}_1 - \tilde{\mathbf{H}}_1 \end{bmatrix} = \begin{bmatrix} 1 & 0 \\ 0 & 1 \end{bmatrix} \quad (3.130)$$

where $[(\epsilon + i\eta)\mathbf{S}_L - \tilde{\mathbf{H}}_L]$ is the effective Hamiltonian matrix representing the isolated lead, and $[(\epsilon + i\eta)\mathbf{S}_1 - \tilde{\mathbf{H}}_1]$ is the renormalized channel Hamiltonian. Performing the algebraic matrix operations on the above equation, the following expressions are obtained:

$$\left[(\epsilon + i\eta)\mathbf{S}_L - \tilde{\mathbf{H}}_L \right] \mathbf{G}_{L1} + (\mathbf{V}_{L1} - (\epsilon + i\eta)\mathbf{S}_{L1}) - \mathbf{G}_1 = 0 \quad (3.131)$$

$$\left[(\mathbf{V}_{1L} - (\epsilon + i\eta)\mathbf{S}_{1L}) - \tilde{\mathbf{H}}_1 \right] \mathbf{G}_1 + (\mathbf{V}_{1L} - (\epsilon + i\eta)\mathbf{S}_{1L})\mathbf{G}_{L1} = 1 \quad (3.132)$$

From eq.3.131 we obtain:

$$\mathbf{G}_{L1} = \mathbf{g}_L^{r(a)} (\mathbf{V}_{L1} - (\epsilon + i\eta)\mathbf{S}_{L1})\mathbf{G}_1 \quad (3.133)$$

where

$$\mathbf{g}_L^{r(a)} = \left[(\epsilon \pm i\eta)\mathbf{S}_L - \tilde{\mathbf{H}}_L \right]^{-1} \quad (3.134)$$

is the retarded (advanced) Green's function of the isolated semi-infinite lead which can be calculated by inversion of the effective Hamiltonian $\tilde{\mathbf{H}}_L$. Substituting 3.133 into 3.132, and considering as well the presence the right-lead (by following a similar reasoning), a final expression for the retarded (advanced) channel Green's function upon renormalization by electrodes is obtained: ²

$$\mathbf{G}_1^{r(a)} = \frac{1}{(\epsilon \pm i\eta)\mathbf{S}_1 - \tilde{\mathbf{H}}_1 - \Sigma^{r(a)}} \quad (3.135)$$

where $\Sigma^{r(a)} = \Sigma_{Left}^{r(a)} + \Sigma_{Right}^{r(a)}$, and:

$$\Sigma_{Left}^{r(a)} = (\mathbf{V}_{1L} - (\epsilon \pm i\eta)\mathbf{S}_{1L})\mathbf{g}_L^{r(a)}(\mathbf{V}_{L1} - (\epsilon \pm i\eta)\mathbf{S}_{L1}) \quad (3.136)$$

$$\Sigma_{Right}^{r(a)} = (\mathbf{V}_{cR} - (\epsilon \pm i\eta)\mathbf{S}_{cR})\mathbf{g}_R^{r(a)}(\mathbf{V}_{Rc} - (\epsilon \pm i\eta)\mathbf{S}_{Rc}) \quad (3.137)$$

are the retarded (advanced) self-energies due to the left and right leads, respectively. $\Sigma \equiv \Sigma(\epsilon)$ represents the probability amplitude for an electron to propagate between two points

¹Here, only retarded Green's function of the lead is considered

²Note that including \pm symbol, the more general expression for retarded (R) and advanced (A) Green's functions is now explicitly written

3. TRANSPORT

inside the conductor taking the effect of the leads into account. \mathbf{G}_1 has the dimension of the finite decimated submatrix $\tilde{\mathbf{H}}_1$

It is worth to remind that semi-infinite self-energy is a quantity which can be expressed as a complex function. When added to channel Hamiltonian, $Re[\Sigma]$ entails a global shift in energy, and $Im[\Sigma]$ gives an electron lifetime at the edge of the channel.

3.6.8 Transmission function

Now that the Green's function of the channel has been determined, the Fisher-Lee relation can be used to calculate the transmission function. Herein, we limit ourselves to show how transmission function can be expressed in terms of device Green's functions, $\mathbf{G}_1^{r(a)}(\epsilon)$. In its compact form, transmission between right and left lead $T_{RL}(\epsilon)$ or simply $T(\epsilon)$ reads:

$$T(\epsilon) = tr [\mathbf{\Gamma}_R(\epsilon)\mathbf{G}_c^r(\epsilon)\mathbf{\Gamma}_L(\epsilon)\mathbf{G}_c^a(\epsilon)] \quad (3.138)$$

where contact terms, $\mathbf{\Gamma}$, for left (L) and right (R) electrodes have been rewritten with the new expressions:

$$\mathbf{\Gamma}_{R(L)}(\epsilon) = i \left[\Sigma_{R(L)}^r(\epsilon) - \Sigma_{R(L)}^a(\epsilon) \right] \quad (3.139)$$

By means of the Landauer-Büttiker formula in the low bias limit the conductance $\mathcal{G}(\epsilon)$ of a quantum system with static disorder is related to its transmission by the simple relation:

$$\mathcal{G}(\epsilon) = \mathcal{G}_0 T(\epsilon) \quad (3.140)$$

where $\mathcal{G}_0 = \frac{2e^2}{h}$ is the quantum of conductance.

In the coherent transport regime, the transmission function obtained as solution to the problem of a particle diffusion through a conductor connected to semi-infinite perfect leads is proportional to its conductance. In the transmission function calculation both channel Green's function and lead self-energies are involved.

To allow numerical calculations of these expressions, the Hamiltonian of the system and electrodes must be expressed in terms of a tight-binding expression expanded within a basis of orbitals, $\{|\phi_\alpha\rangle\}_\alpha$. The trace formula can then be expressed as:

$$\mathcal{G}(\epsilon) = \frac{2e^2}{h} \sum_{\alpha\beta\alpha'\beta'} \langle \beta | \mathbf{\Gamma}_R | \alpha \rangle \langle \alpha | \mathbf{G}^r | \alpha' \rangle \langle \alpha' | \mathbf{\Gamma}_L | \beta' \rangle \langle \beta' | \mathbf{G}^a | \beta \rangle \quad (3.141)$$

The interface localized states α, β run over the left-lead orbitals, and α', β' run over right-lead orbitals. The main task is to evaluate the retarded Green's function elements

$$\mathbf{G}_{\alpha,\alpha'}^r = \langle \alpha | \mathbf{G}^r | \alpha' \rangle \quad (3.142)$$

which propagates an electron from an orbital α' in the right side to an orbital in the left side α of the system. Note that the advanced Green's function matrix elements of the above

3.6 Real space renormalization group procedures, also known as decimation

equation does not need to be calculated from a new matrix inversion, they can be deduced from the relation:

$$\langle \beta' | \mathbf{G}^a | \beta \rangle = (\langle \beta | \mathbf{G}^r | \beta' \rangle)^\dagger \quad (3.143)$$

In the following chapter, **SIESTA** code and method are presented. DFT calculations in localized atomic-like orbital basis set in the key of our studies. In the accuracy and compactness of the Hamiltonian matrix which describes the building blocks of interest lies the powerfulness of our method, since it combines the well established formalism hereafter presented with the precision of the DFT.

3. TRANSPORT

Chapter 4

The SIESTA Method and Code

*“Je ne veux pas bosser avec la DFT,
c’est trop ennuyeux de travailler
avec les états fondamentals.”*

Rémi Avriller

Chapter résumé (French version)

Ce chapitre résume le cadre théorique ab initio supportant les calculs sur lesquels cette thèse est basée. Les techniques ab initio, telles que la méthode SIESTA, tentent de résoudre les équations de la mécanique quantique pour des systèmes contenant jusqu’à plusieurs milliers d’atomes. En pratique, la solution exacte de ces équations est un problème analytique insoluble et plusieurs approximations doivent être faites. Ces approximations sont décrites et justifiées dans la description de la méthode SIESTA et implémentées dans le code SIESTA.

Chapter résumé (Spanish version)

Este capítulo resume el marco de trabajo teórico en el que se han efectuado los cálculos ab initio en los que se ha basado esta tesis. Técnicas ab initio tales como el método SIESTA, son una alternativa a la solución de las ecuaciones mecánico cuánticas que describen el comportamiento de sistemas formados por miles de átomos. En la práctica, la solución exacta de estas ecuaciones es un problema analíticamente irresoluble y diversas aproximaciones deben ser efectuadas. Estas son descritas y analizadas en la descripción del método SIESTA y aplicadas en el código SIESTA.

4. THE SIESTA METHOD AND CODE

Chapter résumé (English version)

This chapter outlines the theoretical *ab initio* framework underlying the calculations on which this thesis is based. *Ab initio* techniques, such as the SIESTA method, attempt to solve the quantum mechanical equations of systems composed of up to thousand of atoms. In practice, the exact solution of these equations is an unsolvable analytic problem and a several approximations must be made. These approximations are described and justified in the description of SIESTA method and implemented in SIESTA code.

Plane wave density functional electronic structure calculations do not satisfy the requirement of locality needed to implement the Landauer's formula efficiently. This chapter describes the *ab initio* technique used to obtain a complete description of the electronic structure of the system in terms of localized atomic orbital basis set. The results obtained from these calculations will be then used as input in the treatment of electronic transport problems within a quantum mechanical approach.

4.1 Density Functional Theory

4.1.1 Introduction

DFT is one of the most powerful and sophisticated methods of the computational chemistry for electronic structure calculations. This quantum mechanical approach to solving molecular structure allows the calculation of molecular properties including geometry, stability, bond strengths, thermochemical properties, etc. Specifically, the term *ab initio* indicates that the calculation is derived from first principles and does not depend on any empirical data. It is often related to the quantum mechanical framework of Hartree-Fock and related methods for molecular electronic structure elucidation. A variety of *ab initio* methods exist and although these calculations are computationally expensive, they allow to chemists to make predictions of molecular properties of existing and probable compounds.

DFT (abbreviation of "Density Functional Theory") is also used to investigate the electronic structure of many-body systems, principally their ground state. With this theory, the properties of a many-electron system can be determined by using functionals, namely functions of another function, which in this case is the spatially dependent electron density. Hence DFT is characterized by the use of functionals of the electron density and is among the most popular and versatile methods available in condensed-matter physics. In this thesis DFT method constitutes one of the main tools that have been used for quantum transport properties study at the atomic- and nano-scale due to its reliability, efficiency and accuracy to describe the systems of interest.

Understanding of electron transport through nanostructures becomes important with the advancement of fabrication process to construct atomic-scale devices. Due to the drastic change of transport properties by contact conditions to electrodes in local electric fields, first-principles calculation approaches are essential to understand and characterize the transport properties of nanometer-scale molecular devices. Empirical and semi-empirical models need of

parameters derived of data fitting coming from experimental data. The range of applicability of this fitted data varies from model to model and nothing guarantees the generality of a specific model results. The advantage of DFT calculations with respect to empirical methods is that approximations do not rely on the specific nature of the system under investigation, namely, the system under study does not require a model of the interactions between the atoms. Instead of that, the quantum mechanical equations which govern the behaviour of a system can be solved by providing the geometry and nature of chemical elements of the system under study and only a certain amount of approximations based on general physical principles must be made. Therefore, problems related to the assumptions of the model are minimized and results have a better degree of confidence. This makes of DFT techniques a good tool for predictive calculations of material properties, offering at the same time reliability and performance. Nevertheless, due to the limitations imposed in some cases by system size and computational cost of DFT calculations, empirical methods can play an important role in answering questions on larger scale systems.

In this work an efficient technique allows us to couple DFT with transport calculations, thanks to the tight-binding-like compact form of SIESTA DFT code. In a first stage, we resort to full DFT calculations for solving the problem of electronic and geometrical structure. Then, the problem of electronic transport is solved with the help of Landauer's formula within the framework of Green's function formalism as presented in the previous chapter. This mixing of techniques allows us to reach an accurate and computational cost balanced methodology for quantum transport property studies of nano-size systems.

4.1.2 The many-electron Schödinger equation: Hartree and Hartree-Fock theories

Describing completely the quantum mechanical behaviour of electrons in solids means to calculate the many-electron wavefunction Ψ for the system. This is done by finding the solution to the many-body Schrödinger equation for the system under study. The fundamental equation governing a quantum system is the time-dependent Schödinger equation:

$$i\hbar \frac{d\Psi(\mathbf{r}_i, t)}{dt} = \hat{H}\Psi \quad (4.1)$$

where $\Psi(\mathbf{r}_i, t)$ is the many-electron spinless wavefunction which is antisymmetric in spatial coordinates \mathbf{r}_i . The eigenstates of this equation are

$$\Psi(\mathbf{r}_i, t) = \Psi(\mathbf{r}_i) \exp(-iEt/\hbar) \quad (4.2)$$

where E is the total energy.

By means of Born-Oppenheimer approximation the total wavefunction can be decoupled in two parts, one concerning the electrons $\Psi_{electrons}$ of the system and a second one Ψ_{nuclei} that deals merely with nuclei description:

$$\Psi_{system} = \Psi_{electrons} \otimes \Psi_{nuclei} \quad (4.3)$$

4. THE SIESTA METHOD AND CODE

This approximation follows from the small inertia of electrons that can be neglected when compared to the velocity of the atoms to which they are bound. In a first stage, electronic Schrödinger equation is solved independent of time, yielding to a wavefunction $\Psi_{electrons}$ which only depends on electron variables. Along the solution of this problem, nuclei are fixed in a certain configuration, very often close to the one of equilibrium.

For a given nuclear spin and spatial distribution, the total energy of interest is that of the ground state of electrons and ions in that configuration. The equation to be solved is therefore,

$$\hat{H}\Psi(\mathbf{r}_i) = E\Psi(\mathbf{r}_i) \quad (4.4)$$

The non-spin dependent Hamiltonian can be expressed by:

$$\hat{H} = -\sum_i \frac{\hbar^2}{2m_e} \nabla_{\mathbf{r}_i}^2 + \sum_{j>i} \frac{e^2}{|\mathbf{r}_i - \mathbf{r}_j|} + \sum_{i,I} \frac{Z_I e^2}{|\mathbf{r}_i - \mathbf{r}_I|} \quad (4.5)$$

The first term represents the kinetic energy of electrons and the next term is the Coulomb interaction between each pair of electrons expressed in the Hartree form. The last term in this Hamiltonian expression is the electron-nuclei interaction.

Hartree was one of the first scientist who attempted to solve this problem by simplifying the problem by making an assumption: the form of the N -electron wavefunction is just the product of a set of N single-electron wavefunctions which would take the form of simple plane waves in a homogeneous system. Once this assumption is set it would make possible to solve the problem using the variational principle (VP) and assuming that the system can be described by a set of parameters. VP states that the set of parameter values which most correctly describes the ground state of the system is the set of values which minimizes the total energy:

$$\delta \frac{\langle \Psi | \hat{H} | \Psi \rangle}{\langle \Psi | \Psi \rangle} \equiv \delta E[\Psi] = 0, \quad (4.6)$$

so that :

$$E[\Psi_0] = E_0 = \min_{\Psi} E[\Psi], \quad (4.7)$$

namely full minimization of the functional $E[\Psi]$ with respect to all the allowed N -electron wavefunctions will give the true ground state Ψ_0 of energy E_0 . But in practice the potential that each electron experiences is imposed by the behaviour of all the other electrons in the solid. To solve the Schrödinger equation for all the electrons would then need to solve a system of $\sim 10^{23}$ simultaneous differential equations and this operation scales factorially with the number of electrons in the system. Such a calculation is beyond the capabilities of any nowadays computer.

Hartree found by using the variational method that the equations which dictate the motion of the electrons in the system depended only on the time-averaged electron distribution of the system instead of the coupled individual motions of all the other electrons. This fact allows the treatment of each electron separately as a single-particle. Consequently, the Hartree approximation allows us to calculate approximate single-particle wavefunctions for electrons

in uniform solids, and hence calculate other related properties. Unfortunately, the Hartree approximation does not give particularly good results since, for example, it predicts that in a neutral uniform system there will be no binding energy holding the electrons in the solid.

Hartree approach fails due to the initial assumption of a product wavefunction. Pauli's exclusion principle states that it is not possible for two electrons to exist with the same spatial coordinates and with the same set of quantum numbers. This principle leads to an effective repulsion between any pair of identical electrons possessing the same set of quantum numbers. Pauli's exclusion principle ensures that the wavefunction of a set of electrons in a crystal is antisymmetric under exchange of any pair of particles. The Hartree product wavefunction is symmetric rather than antisymmetric, so Hartree's approach implicitly does not take into account Pauli's exclusion principle and hence the lack of physical coherence.

An improvement over the Hartree's framework is the Hartree-Fock's (HF) approach in that the N -electron wavefunction is constructed from the single-electron wavefunctions is required to be antisymmetric. The wavefunction becomes much more complicated than the Hartree's product wavefunction since it involves the solution of the so-called Slater determinant:

$$\Psi_{HF} = \frac{1}{\sqrt{N!}} \det[\Psi_1 \Psi_2 \dots \Psi_N] \quad (4.8)$$

where Ψ_i are the single-electron wavefunctions.

Thanks to this new assumption the Hamiltonian equation for the system can be deduced through the variational principle:

$$E_{HF} = \langle \Psi_{HF} | \hat{H} | \Psi_{HF} \rangle = \sum_{i,j=1}^N H_i + \frac{1}{2} (J_{ij} - K_{ij}) \quad (4.9)$$

where H_i is the single particle Hamiltonian, J_{ij} are the Hartree potential integrals and K_{ij} are the exchange integrals. These integrals are real and $J_{ij} \geq K_{ij} \geq 0$ (81).

In this approximation, in addition to the Hartree potential (which described the direct Coulomb interaction between an electron and the average electron distribution) a second type of integral operator influencing the electrons arises: the so-called exchange potential. The exchange potential is a direct consequence of Pauli's exclusion principle inclusion in problem formulation through the use of an antisymmetrized wavefunction. This potential corrects one of the failures of Hartree's approach by contributing to the binding energy for electrons in a neutral uniform system. However, HF approach fails in calculating many other properties becoming even worse than the Hartree's approach. Hartree-Fock's theory includes the exchange effect but does not take into account the electrostatic correlation of electrons.

Notwithstanding, HF approach gives good results for small molecules due to the fact that the number of electrons involved are lower than in a solid, so that correlation effects are small compared to exchange effects. Although neither the Hartree nor the HF method succeeds in solving the many-body problem for electrons in crystals they bring to light some relevant physical problems that need to be described: exchange and correlation. Electronic structure theory field had a breakthrough in 1964 with the advent of a new approach, the

4. THE SIESTA METHOD AND CODE

Density Functional Theory (DFT). This is a theory that allows one to replace the N-electron wavefunction Ψ and the associated Schrödinger equation by the much simpler electron density $\rho(\mathbf{r})$ and its associated calculation scheme.

4.1.3 DFT

Hartree's and HF methods above describe were based in the VP. VP and its success depends on a good parametric description of the problem and a good choice of the starting wavefunctions. It was shown that both models fail not because of a bad description of the parameters but because of not having good enough approximate forms of the initial wavefunctions. In 1964, Hohenberg and Kohn suggested that the problem for finding the fundamental state of a many-electron system lay in considering the system wavefunction as the fundamental variable which leads to a complicated entity to deal with in the variational approach.

Density Functional Theory (DFT) is based on the notion that the description of the ground state an interacting system of electrons can be done with the help of its electronic density instead of its many-body wavefunction. DFT is based in the Hohenberg-Kohn (HK) theorem which states that there exists a bijective (one-to-one) relation between the ground state of a system $\Psi_0(\mathbf{r})$ and its electronic density $n_0(\mathbf{r})$: given the ground state density $n_0(\mathbf{r})$ of a system it is possible, in principle, to calculate the corresponding ground state wavefunction $\Psi_0(\mathbf{r})$, and vice versa. If the wavefunction Ψ_0 can be calculated from $n_0(\mathbf{r})$, both functions are equivalent and contain the same information. Since all properties (kinetic energy, etc.) are uniquely determined for a given density $n(\mathbf{r})$, then each such property may be viewed as a functional of $n(\mathbf{r})$:

$$E_{HK}[n] = F_{HK}[n] + E_I + \int n(\mathbf{r})V_{ext}(\mathbf{r})d^3\mathbf{r} \quad (4.10)$$

where E_I is the interaction energy of the nuclei and V_{ext} is an external potential. The functional $F_{HK}[n] = T[n] + E_{int}[n]$ includes the internal kinetic and potential energies of the interacting electron system and is universal.

If we consider a system with a ground state density n_0 corresponding to an external potential $V_{ext,0}$, the HK functional is equals to the expectation value of the Hamiltonian in the unique ground state with wavefunction Ψ_0 :

$$E_0 = E_{HK}[n_0] = \langle \Psi_0 | \hat{H} | \Psi_0 \rangle \quad (4.11)$$

For a different wavefunction Ψ_1 , there is a different density n_1 associated to it and, hence, the energy E_1 of this state is necessarily greater than E_0 , since:

$$E_0 = \langle \Psi_0 | \hat{H} | \Psi_0 \rangle < \langle \Psi_1 | \hat{H} | \Psi_1 \rangle = E_1 \quad (4.12)$$

Thus the energy given by 4.10 is terms of the E_{HK} functional evaluated for the correct ground density, $n_0(\mathbf{r})$, is lower than the value of this expression for any other density, $n(\mathbf{r})$.

The properties of this HK energy functional can be summarized as follows: the energy functional, which exists and is unique, is minimal at the exact ground-state density, and its minimum gives the exact ground-state energy of the many-body electron system for a given external potential.

This exact result means that the electron density and, therefore its energy, can be found through a variational minimization over $n(\mathbf{r})$. HK theorem demonstrates the existence of a ground state but does not give any guidance for constructing $F[n(\mathbf{r})]$ and no exact functionals are known for any system of more than one electron. The ansatz proposed by Kohn and Sham made possible the development of DFT beyond such limitation. It provides a way to make approximate ground state functionals for many-electrons systems, replacing the many-electron interacting problem with an independent-particle problem in which all the many-body effects are included in an exchange-correlation functional. Thus all many-body effects of exchange and correlation are grouped into the exchange-correlation energy E_{XC} . Kohn-Sham theorem claims that a functional could be:

$$F[n] = -\frac{\hbar^2}{2m_e} \sum_i \int \Psi_i^* \nabla^2 \Psi_i d^3\mathbf{r} + \frac{e^2}{2} \int \int \frac{n(\mathbf{r})n(\mathbf{r}')}{|\mathbf{r} - \mathbf{r}'|} d^3\mathbf{r} d^3\mathbf{r}' + E_{XC}[n(\mathbf{r})] \quad (4.13)$$

where the first term represents the kinetic energy of a non-interacting electron system and the second term is the Hartree electron-electron interaction. $E_{XC}[n]$ is the exchange-correlation energy.

Resorting to the variational principle and the Lagrange multiplier method for handling constraints (the constant number of electrons in the system can be considered as a constraint), $E[n]$ can be minimized with respect to $n(\mathbf{r})$ to obtain the Kohn-Sham Schrödinger-like equations:

$$H_{KS}\Psi_i(\mathbf{r}) = \epsilon_i\Psi_i(\mathbf{r}) \quad (4.14)$$

where ϵ_i are the eigenvalues and H_{KS} the effective Hamiltonian:

$$H_{KS} = -\frac{\hbar^2}{2m_e} \nabla^2 + V_{KS}(\mathbf{r}) \quad (4.15)$$

with $V_{KS}(\mathbf{r})$ the Kohn-Sham potential:

$$V_{KS}(\mathbf{r}) = V_{ext}(\mathbf{r}) + V_{Hartree}(\mathbf{r}) + V_{XC}(\mathbf{r}) \quad (4.16)$$

where

$$V_{XC}(\mathbf{r}) = \frac{\delta E_{XC}[n(\mathbf{r})]}{\delta n(\mathbf{r})} \quad (4.17)$$

With these equations the interacting many-body system has been translated onto a non-interacting electron problem where charges move in an effective potential that must be found self-consistently with the resulting density. These equations would lead to the exact ground state density and energy for the interacting system if this functional were known. From Hohenberg-Kohn theorems it can be deduced that the ground state density only determines

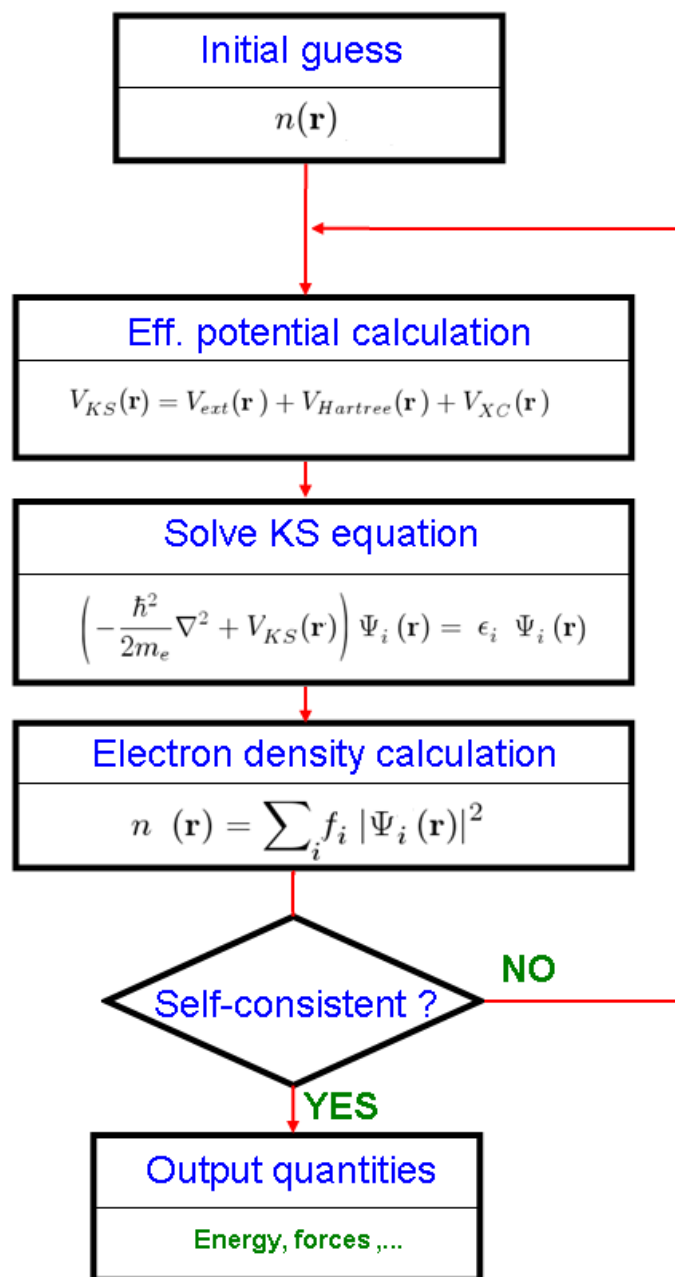


Figure 4.1: Self-consistent loop for Kohn-Sham equations solution. - An initial guess for both up and down spin densities is evaluated in the effective potential equation. It is then introduced in the KS equations for electron density computation. When self-consistency is reached some useful quantities may be extracted from the density $n(\mathbf{r})$ as ground state energy, eigenvalues, forces between atom, etc.

the potential at the minimum, so that a unique Kohn-Sham potential is associated with any given interacting electron system: $V_{eff}(\mathbf{r})|_{min} \equiv V_{KS}(\mathbf{r})$.

Kohn-Sham equations solving procedure is summarized in the flow chart of Fig.4.1. They must be solved subject to the condition that both the effective potential and the density are consistent. Once the self-consistency is reached, the loop is over and one has access to the useful quantities that can be obtained from the ground state of the system: forces between atoms, energies, densities, etc.

However, it has to be noticed that conceptually the Kohn-Sham equations determine exactly the electron density and the electronic energy of the ground state, by the orbital energies ϵ_i appearing in eq.4.14 are purely formal Lagrange multipliers, without physical meaning. However, we have access to other meaningful quantities through the electron density. Any identification of ϵ_i with one-particle energies is to be justified at each specific situation and the total energy of the system is not the sum of KS eigenvalues: $E_{KS} \neq \sum_i^N \epsilon_i$.

4.1.4 The exchange-correlation term: LDA and GGA

The Kohn-Sham approach is based on the introduction of the exchange-correlation energy, which is expressed as a functional of the energy:

$$E_{XC}[n] = \int n(\mathbf{r})\epsilon_{xc}([n], \mathbf{r})d\mathbf{r} \quad (4.18)$$

where $\epsilon_{xc}([n], \mathbf{r})$ is an energy per electron at position \mathbf{r} which depends only upon the electronic density $n(\mathbf{r})$ in the vicinity of \mathbf{r} . From an analysis of the exchange correlation hole the following expression can be derived for $\epsilon_{xc}([n], \mathbf{r})$ from the energy density:

$$\epsilon_{xc}([n], \mathbf{r}) = \frac{1}{2} \int \frac{\bar{n}_{xc}(\mathbf{r}, \mathbf{r}')}{|\mathbf{r} - \mathbf{r}'|}, \quad (4.19)$$

where $\bar{n}_{xc}(\mathbf{r}, \mathbf{r}') = \int_0^1 n_{xc}^\lambda(\mathbf{r}, \mathbf{r}')d\lambda$ is the coupling constant-averaged hole.

The above mentioned ansatz makes possible to obtain independent-particle equations that reduce the complexity of the many-body problem. Although the $E_{XC}[n]$ functional is in general very complex, some approximations can be made. The local density approximation (LDA) and general gradient approximation (GGA) are two of the most relevant functionals.

LDA is based on the local character of exchange and correlation effects when the charge is distributed as a homogeneous electron gas. Exchange-correlation energy is assumed to be an integral over the entire space with the exchange-correlation energy density assumed to be the same as in a homogeneous electron gas with the same density since it respects sum rules. Although a crude approximation, LDA has been found to give good results in a wide range of solid state systems.

Generalized Gradient Approximations (GGA) are also local but takes into account the gradient of the density at the same point \mathbf{r} : $\epsilon_{xc} \equiv \epsilon_{xc}(n(\mathbf{r}), \vec{\nabla}n, (\mathbf{r}))$. Although GGA does offer a consistent improvement over LDA in all kind of systems, they have been shown to improve on the LDA for calculations of molecular structures and in representing weak inter-molecular

4. THE SIESTA METHOD AND CODE

bonds. Potentially more accurate than the GGA functionals are meta-GGA functions which include a further term in the expansion, depending on the density, the gradient of the density and the Laplacian (second derivative) of the density.

Experience shows that the calculations performed within one version or another of the exchange-correlation form tend to underestimate the energy band gap in semiconductor and insulators however, the general trend of the dispersion curves of valence and conduction bands is often represented to reasonable accuracy.

4.2 SIESTA method

As computing power increases and new methods based on DFT theory are developed, the range of problems which may be solved by DFT methods is everyday expanding. At present, systems containing hundreds of atoms may be modelled on parallel supercomputers and it is foreseen in the next future the simulation of materials containing thousands of atoms. However, the cornerstone of *ab initio* calculation is the cube-scaling algorithms that are still used in most of the codes. The use of the so-called order N algorithms ($O(N)$) becomes then important, allowing for the computing time and memory to scale linearly with the size of the system. A great effort in the field of density functional theory is devoted to find the Kohn-Sham Hamiltonian by means of linear scaling operations for solving Schrödinger equation (82)(83), and efficient method development is mandatory.

SIESTA (Spanish Initiative for Electronic Simulations with Thousands of Atoms) is a first-principles molecular dynamics simulation and electronic structure code for molecules and solids. Wavefunctions are represented in a basis of atomic-like orbitals which, in opposition to plane wave basis sets, provides a natural way for the interpretation of solid state physics problem results. The Kohn-Sham equations are solved self-consistently in a linear combination of atomic orbitals (LCAO) basis set and they restricted to periodic boundary conditions. This framework leads to very accurate and fast simulations using a reduced number of orbitals in the basis set with complete multiple-zeta and polarized bases, depending on the required accuracy. SIESTA method is implemented in an efficient code which fulfills the desired $O(N)$ scaling. (87)(88)

SIESTA method was proposed in the mid-nineties as a combination of two existing ideas: Sankey's finite atomic orbitals (84) for basis set description, and 3D real-space grid representation of the electronic density and the basis functions. The coupling of this approach to a linear scaling solver was the origin of the code. SIESTA method presents some advantage as described by its authors in ref.(85): "*Kohn-Sham based DFT, as opposed to the so-called orbital-free DFT, which computes the total energy directly from the electron density with approximations to the kinetic energy functional in addition to exchange and correlation. This approach is linear-scaling, extremely efficient and best suited for metals*".

SIESTA method is based in periodic boundaries conditions in all directions of the space, namely, every system is described in a 3D supercell. Therefore, molecules are treated in supercell scheme and enough empty space between neighbouring images must be left in order to avoid any artificial interaction. This approach, which is widely used within plane wave

based frameworks, guarantees that boundary condition effects are small and can be neglected. For high precision calculations in periodic systems an integration over the Brillouin zone must be performed. In the code, this integration is replaced by converged sums over a set of k-points.

4.3 SIESTA code

SIESTA method is based in periodic boundaries conditions in all directions of the space, namely, every system is described in a 3D supercell. Therefore, molecules are treated in supercell scheme and enough empty space between neighbouring images must be left in order to avoid any artificial interaction. This approach, which is widely used within plane wave based frameworks, guarantees that boundary condition effects are small and can be neglected. Bloch's functions provide the adequate framework for solving problems in which periodic boundary conditions are applied. The wavefunction of the system can then be written as:

$$\Psi_{n\mathbf{k}}(\mathbf{r}) = u_{n\mathbf{k}}(\mathbf{r})e^{i\mathbf{k}\cdot\mathbf{r}}, \quad (4.20)$$

where $u_{n\mathbf{k}}(\mathbf{r})$ is a function with same periodicity than the supercell, \mathbf{k} is the wavevector in the 1st BZ and n is the band index. Thanks to Bloch's theorem, KS equations can be solved for each k-point in the reciprocal space. That is why for high precision calculations in periodic systems an integration over the Brillouin zone must be performed. In the code, this integration is replaced by a sum over a set of k-points, and the expectation value of a given operator \hat{O} is found as:

$$\langle \hat{O} \rangle \approx \frac{1}{V_{BZ}} \sum_{\mathbf{k}} w_{\mathbf{k}} O(\mathbf{k}), \quad (4.21)$$

where V_{BZ} is the BZ volume and $w_{\mathbf{k}}$ represents a weight for each value of $O(\mathbf{k})$. By the inversely proportional relationship between direct and reciprocal space, the larger the supercell the smaller the BZ is. For large enough supercells or calculations with no relevant boundary conditions, the number of k-points can be reduced to just one, the so-called Γ -point.

If all the electrons in a system were explicitly included when performing a calculation and $V_{ext}(\mathbf{r})$ were calculated from the nuclei Coulomb potential, the computational cost would be prohibitive still using a atomic-like orbital basis set. The rapid oscillations of the wavefunctions near to the nucleus, due to the very strong potential in the region mean that a very large cut-off energy and basis set would be necessary. But Nature is generous with physicists and allows us to treat the core electrons on different atoms as almost independent of the environment surrounding the atom, such that interactions between atoms may be described only with valence electron participation. Thus, core electron states are assumed to be fixed and a pseudopotential is constructed for each atomic species. Effects related to the nucleus and core electrons are thus taken into account.

In SIESTA code, core electrons are replaced by norm-conserving pseudopotentials in their fully separable form (90). It constitutes an efficient approximation to the charge density of

4. THE SIESTA METHOD AND CODE

core electrons that has to be represented in the real space grid. Typically (as done in this thesis) the pseudopotential that one uses in a **SIESTA** calculation is of the Troullier-Martin's type.

The treatment of the exchange and correlation is done within Kohn-Sham formalism, and both the local (spin) density approximation (L(S)DA) and general gradient approximation (GGA) are implemented.

The Born-Oppenheimer approximation is implemented which allows to nuclear and electronic motions to be decoupled and treated separately. **SIESTA** code allows for molecular dynamic simulations based on the nuclear motion by calculating forces between nuclei. Therefore, the electronic wavefunction computation is repeated for different nuclear configurations up to an optional degree of structural relaxation is achieved.

4.3.1 Basis set

A lot of methods have traditionally used plane wave basis sets for electronic structure calculations and to represent the electronic eigenstates of a system. Plane waves present the advantage to form a complete basis set and then a good control of the convergence, but fail when describing local atomic properties due to the extended nature of the basis states. For analyzing *ab initio* calculation results, it is useful to have a measure of local atomic properties such as inter-nuclei distances and ionic charges. Using ionic charges and bond populations allows us to measure the ionicity and covalency of atom-atom bond. These local properties may be calculated with the help of methods as quantum mechanical eigenstates projection onto a localized atomic basis set.

These conceptual and technical difficulties are overcome in the **SIESTA** approach with the help of strictly confined basis orbitals, i.e. orbitals that are zero beyond a certain radius. Within the **SIESTA** DFT-technique, the Kohn-Sham orbitals are expanded into localized orbitals, which allows to the present method to cope with some of the order-N method requirements.

As already mentioned, the numerical solution of the KS equations is based in a linear expansion of the wavefunctions in terms of an atomic-like basis set:

$$\Psi_n(\mathbf{r}) = \sum_m \mathbf{c}_{nm} \phi_m(\mathbf{r}) \quad (4.22)$$

where $\{\phi_m(\mathbf{r})\}$ is the set atomic orbitals which adopt the form of real functions centered on the atoms. In the case of a complete set of functions this development would lead to the exact representation of the system wavefunction. One of the main limiting features of **SIESTA** approach is the impossibility of improving result accuracy by just increasing the number of functions in the basis set. Therefore, the main advantage of atomic orbitals is their efficiency and the main disadvantage is the lack of systematicity in the basis set for a good convergence. This limitation is partially overcome by adjusting the simulation parameters until an adequate convergence is reached. For an atom sitting at point $\mathbf{R}_I = \mathbf{r} - \mathbf{r}_I$ in the real space, the set of orbitals would be:

$$\phi_{I,nlm}(\mathbf{r}) = \phi_{nl}(|\mathbf{r} - \mathbf{r}_I|)Y_{lm}(\theta_I, \varphi_I) \quad (4.23)$$

where $\phi_{nl}(|\mathbf{r} - \mathbf{r}_I|)$ and $Y_{lm}(\theta_I, \varphi_I)$ are the radial part and the spherical harmonics of the atomic orbital wavefunction, respectively. Radial and angular dependence are thus split in two different functions with associated quantum numbers: n is the principal quantum number and l, m label the angular momentum numbers. It is common to denote as "multiple-zeta" to multiple radial functions with the same l, m , i.e. single- ζ (also SZ), double- ζ (also DZ), for 1 or 2 radial functions. Some guidelines for the choice of optimal radial basis functions say that in a molecule or a solid the localized orbitals typically are best described by those with shorter range and larger amplitude at the nucleus than in the isolated atom. This is a consequence of the fact that the binding force of solids lowers the total energy by keeping the electrons closer to the nuclei without paying as much cost in kinetic energy, compared to electrons in isolated atoms. Moreover, the long-range decaying tails of the atomic orbitals leads to irrelevant results in regions that overlap other atoms. In addition to these standard arguments, in this thesis short radial tails have been preferred because of Hamiltonian compactness. In a tight-binding-like model a compact description of the Hamiltonian matrix is highly desirable since it saves us having to deal with large matrix computational operations. Generally, orbital extensions up to no more than third-nearest neighbouring atoms have been considered.

Regarding the angular part of the orbital wavefunctions, as the environment of an atom in the solid is not in general spherical, basis requires higher angular momenta than the minimal basis in the atom. In SIESTA method, polarization functions incorporate in their definition a spacial orientation which comes basically from the local distortion of the pseudoatom orbital in the presence of a small electric field. A shell with angular momentum $l + 1$ (or more shells with higher l) is usually added to polarize the most extended atomic valence orbitals (l), giving angular freedom to the valence electrons.

It has been found in general that double- ζ , singly polarized (DZP) bases give precisions within the accuracy of LDA and GGA functionals for geometries and energetics properties. We will see that in this thesis systems are treated with both DZ and DZP bases depending on the complexity, size and type of calculation, which can consists on geometrical optimization or Hamiltonian calculation for transport study.

Once the basis set has been chosen, Hamiltonian and overlap matrices adopt a tight-binding form as:

$$\mathbf{H}_{\mu,\nu} = \langle \phi_\mu | \hat{H}_{KS} | \phi_\nu \rangle = \int \left[\phi_\mu^*(\mathbf{r}) \left(-\frac{1}{2} \nabla^2 + V_{eff}[n_0] \right) \phi_\nu(\mathbf{r}) \right] d\mathbf{r} \quad (4.24)$$

$$\mathbf{S}_{\mu,\nu} = \langle \phi_\mu | \phi_\nu \rangle = \int \phi_\mu^*(\mathbf{r}) \phi_\nu(\mathbf{r}) d\mathbf{r} \quad (4.25)$$

where μ, ν indices run over all system orbitals. This leads to the non-orthogonal matrix eigenvalue equation:

$$\mathbf{H} \cdot \mathbf{c}_n = \epsilon_n \mathbf{S} \cdot \mathbf{c}_n \quad (4.26)$$

4. THE SIESTA METHOD AND CODE

As mentioned at the end of section 4.1.3, these eigenvalues have in principle no physical meaning, since they do not represent the energy levels of the interacting N-electron system. The Hamiltonian \mathbf{H} corresponds to the mean field theory approximation and not to the energetic description of many-electron interacting system given in eq.4.5. Assuming this limitation, we take \mathbf{H} (and \mathbf{S}) as the matrix that gives a complete energetic description of electron motion in our systems.

Chapter 5

Quantum Transport Study of Chemically Functionalized Carbon Nanotubes

*“Tú no eres un teórico,
eres un experimental virtual.”*

Silvano De Franceschi

Chapter résumé (French version)

Ce chapitre traite des calculs de premiers principes du transport quantique dans des nanotubes de carbone métalliques et semi-conducteurs fonctionnalisés chimiquement, avec des longueurs atteignant l'échelle du micromètre et une distribution aléatoire de groupes fonctionnels. Deux cas typiques sont examinés, à savoir une liaison de type sp^2 entre des groupes carbène (CH_2) et les parois du nanotube, et une liaison de type sp^3 des nanotubes avec des groupes phényl. Il est montré que pour des densités similaires de groupes fonctionnels, le transport de charge va d'un régime quasi-balistique à un régime diffusif voire localisé, avec des libres parcours moyens correspondants variant de plusieurs ordres de grandeur, selon la nature de la liaison chimique.

5. QUANTUM TRANSPORT STUDY OF CHEMICALLY FUNCTIONALIZED CARBON NANOTUBES

Chapter résumé (Spanish version)

Este capítulo trata sobre el transporte cuántico basado en cálculos de primeros principios en nanotubos de carbono, tanto metálicos como semiconductores, de longitudes micrométricas y cuyas superficies externas han sido modificadas químicamente mediante adición en posiciones aleatorias de grupos funcionales. Dependiendo del tipo de hibridación de los orbitales de los átomos de carbono del nanotubo a los cuales el grupo funcional queda unido, dos tipos de funcionalización son analizadas: por una parte, la que tiene lugar al crearse una configuración híbrida de tipo sp^3 debido al enlace químico con un grupo de tipo bencénico y, por otra la funcionalización que preserva el carácter original de hibridación sp^2 característica de los átomos de carbono del nanotubo cuando el grupo funcional es un carbeno (CH_2). Se muestra que para una misma densidad de grupos añadidos, el transporte de carga varía desde el régimen cuasibalístico a los regímenes difusivos y localizados, con la consiguiente variación de los recorridos libre medio en varios órdenes de magnitud, dependiendo de la naturaleza del enlace químico.

Chapter résumé (English version)

This chapter deals with first-principles calculations of quantum transport in chemically functionalized metallic and semiconducting carbon nanotubes with lengths reaching the micron scale and random distribution of functional groups. Two typical cases are investigated, namely an sp^2 -type bonding between carbene groups (CH_2) and the nanotube sidewalls, and an sp^3 -type bonding of nanotubes with phenyl groups. It is shown that for similar functional group coverage density, charge transport is found to range from a quasiballistic-like to a diffusive or localized regime, with corresponding mean free paths changing by orders of magnitude depending on the nature of chemical bonding.

5.1 Introduction

Owing to their unique physical properties (103; 112; 113; 114), carbon nanotubes (CNTs) stand as exceptional materials for the exploration of new quantum phenomena in low dimensionality or to envision innovative applications. In particular, the (bio)-chemical sensing capability of carbon nanotubes or nanowires based devices has been the focus of many recent studies with possible applications in the field of nanobioelectronics (115; 116; 117; 118). This engineering of CNTs sidewall chemical functionalization has opened much perspectives in the development of innovative systems such as chemical sensors (104), optically modulated conductors (105), or novel switching devices and molecular memories (106). However, many difficulties remain to be overcome in order to benefit from the large diversity of organic chemistry reactions that can be performed on a tube wall together with the exceptional transport properties of pristine CNTs.

We cannot fully understand the functionality of carbon nanotubes without analyzing the structure from a microscopic view, i.e., the structure as a network of sp^2 carbon fragments.

Studies on fullerene molecules tell us that the topological structure of an sp^2 carbon network critically controls its electronic structure and functionality as a material. In the closed cages of fullerene molecules, the relative arrangement of the 12 pentagonal rings, which act as pentagonal defects in the graphite network, generates a variety of electronic states. Carbon nanotubes further demonstrate that the chiral vector critically controls whether the electronic state is metallic or semiconducting.

These studies on electron networks of nanometer dimensions show that the characteristic electronic structure of carbon materials is essentially controlled by the network structure of sp^2 carbon, namely the topology of the mobile and high energy electrons which creates the π -bondings. An eventual question arises when we investigate chemically modified CNTs by attachment of functional groups: does this attachment entail the modification of the sp^2 network? How this modification affects the electron conductance ability of the nanotube?

The modifications of carbon nanotubes transport properties can indeed result from molecular adsorption events onto the tube sidewalls (119; 120; 121). In turn, nanotube functionalization has become a genuine way for tailoring CNTs electronic properties, or giving the device a novel functionality. For instance, by grafting photoactive molecules onto the nanotube sidewalls, the resulting nanotube-based devices could be optically controlled (122; 123). Two types of chemical functionalization are traditionally investigated, namely physisorption and chemisorption. Both functionalization methods provide effective pathways for modifying the intrinsic properties of electric transport along CNTs. However, it is not clear at the moment which method allows the best compromise between a weak degradation of intrinsic nanotube properties upon tube functionalization and the required efficient monitoring of the added nanotube functionality (121).

As demonstrated by Latil and coworkers (124) for physisorption, the scattering efficiency that results from molecule deposition over the nanotube surface is expected to be low due to the weak amount of charge exchanged between both systems. Non-covalent adsorption has, therefore, the advantage of enabling CNTs functionalization while preserving their electronic structure, since the original sp^2 hybridized bonds and conjugation remain unaltered (125). In contrast, covalent functionalization of CNT involves the creation of saturated sp^3 -bonds which break the p_z -orbital repartition symmetry in the nanotube surface (126; 127). The consequence is a dramatic loss in quantum transport quality due to its extended π -conjugation dependent characteristics. Rehybridization introduces resonant states in the electronic structure of the pristine CNT which act as scattering centers. This particular differences on the electrochemical nature of the bondings turn out to be critical for the preservation of good transport properties over large distances.

The impact of covalent functionalization on tube conductance can however be significantly reduced by a suitable choice of the addends. Commonly used functionalization processes, such as the diazonium addition, (107) produce a number of sp^3 -like defects which dramatically disrupt the CNTs π -conjugated network, severely damaging their conductance (108; 109). To circumvent such a problem, [2 + 1] cycloaddition reactions have been proposed (110). This functionalization is driven by grafted carbene (or nitrene) groups that induce bond cleaving

5. QUANTUM TRANSPORT STUDY OF CHEMICALLY FUNCTIONALIZED CARBON NANOTUBES

between adjacent sidewall carbon atoms, maintaining the sp^2 hybridization and providing sites for further attachment of more complex molecules and related functionalities (111).

A transport study based in a non-orthogonal tight-binding Hamiltonian by Park and coworkers (128) first reported strong differences between monovalent and divalent additions in short length nanotubes. Using *ab initio* calculations, Lee and Marzari (129; 130) further demonstrated that cycloaddition reactions leading to the grafting of *e.g.*, dichlorocarbene groups (CCl_2) could preserve most of the conductance of a (5,5) CNT metallic nanotubes, in contrast to phenyl-type functionalization that would result in strong damping of conduction ability. These calculations were however limited to short nanotube segment with length below 50 nanometers. To date, the relative impact of covalent sp^3 versus sp^2 -type functionalization on realistically long nanotubes remains to be explored in-depth. In particular the clarification of the transport regime and extraction of transport length scales is highly suitable for a quantitative understanding of experiments (131). Since standard devices such as field effect transistors exclusively rely on the use of semiconducting tubes, it is also crucial to clarify the effect of functionalization on semiconducting objects.

5.2 Diazonium salts and phenyl groups

Diazonium salts are a group of organic compounds sharing a common functional group with the characteristic structure of $R-N_2^+X^-$ where R can be any organic residue such alkyl or aryl and X is an anion such as a halogen (8). Phenyl group (denoted with the formula C_6H_5 and sometimes abbreviated as Φ) is the aryl component of diazonium salts which is widely used in chemistry to functionalized carbon nanotubes to form nanotubes composites.

Among the rich group of covalent reactions for nanotube functionalization that has been described in specialized literature, those ones involving diazonium coupling have become very popular thanks to its simplicity and versatility. Diazonium salts have the advantage of providing a selective chemical reaction that favors the covalent attachment to metallic CNTs, utilizing the difference of population of electrons having energies near the Fermi level (9). This selectivity is used for manipulation of nanotubes of different chiralities and enables the separation of semiconducting from metallic nanotubes as well as the direct fabrication of devices of a particular electronic type.

Strano et al. (10) found that water-soluble diazonium salts which have been shown to react with carbon nanotubes can extract electrons from nanotubes in the formation of a covalent aryl bond and, thereby, demonstrate highly chemical selective reactions with metallic tubes. In the grafting process, the aryl diazonium cation gets one electron from the substrate and subsequently becomes an aryl radical by losing a N_2 molecule.

The attachment of a phenyl group onto the sidewall of nanotubes makes of it an interesting candidate to be the molecule that serves of anchorage point to more complex molecules with specific functionalities (11). Due the sp^3 rehybridization induced in the C atom to which phenyl group is attached, this functional group strongly alters local features of the carbon-based systems. This orbital rearrangement involved in the covalent bond constitutes

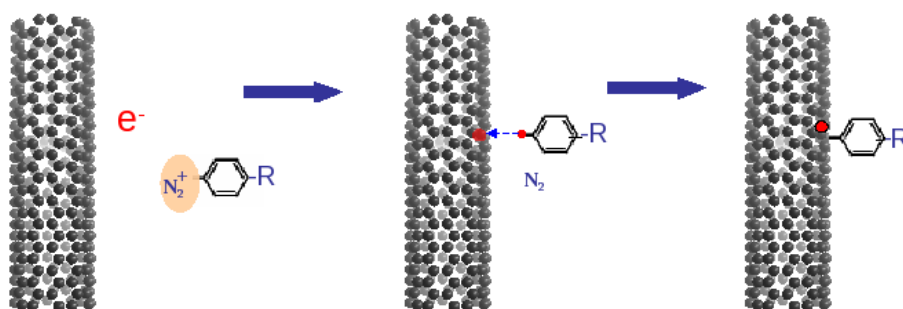


Figure 5.1: Grafting process of phenyl groups onto the the sidewall of CNTs. - First, an electron is extracted from the nanotube by means of the reaction with diazonium reagents. A N_2 molecule is formed and the aryl group gets chemically attached to the nanotube. The result is the creation of a stable C-C covalent bond and a radical which is further passivated by another aryl group in a similar process.

an obstacle to preserve the exceptional electronic transport properties of nanotubes and nanoribbons, which is our object of study.

We start our analysis of transport properties on chemically modified CNTs by giving the technical details of the DFT calculations.

5.3 Technical details

In this study, a first-principles computational study of charge transport in metallic single-walled CNTs with random distribution of phenyl and carbene functional groups bonded to the tube sidewalls is first presented. The disorder introduced by the grafted groups breaks both translational and rotational symmetries, and the study is performed for long nanotubes from a few hundreds of nanometers to the micron scale. The conductance changes and related conduction regimes (from quasiballistic to diffusive) are investigated as a function of both incident electron energy and functional groups coverage density. This first-principles mesoscopic transport study on disordered nanotubes allows to go beyond prior works on short nanotubes (129; 130), and shows that carbene cycloaddition preserves ballistic conduction up the micron scale, whereas the grafting of phenyl groups yields mean free path in the nanometer scale, leading to strong localization regime for commonly studied nanotube length.

The computational approach is based on the already explained strategy, and a large set of first principles calculations are first performed to obtain the *ab initio* Hamiltonian and overlap matrix associated with small tube sections functionalized by single groups. Such a set of building blocks Hamiltonian further allows to reconstruct a micrometer long tube Hamiltonian formed by a random succession of functionalized sections and pristine tube portions to reproduce rotational and translational disorder (see Fig.5.2 for illustration). A detailed analysis of

5. QUANTUM TRANSPORT STUDY OF CHEMICALLY FUNCTIONALIZED CARBON NANOTUBES

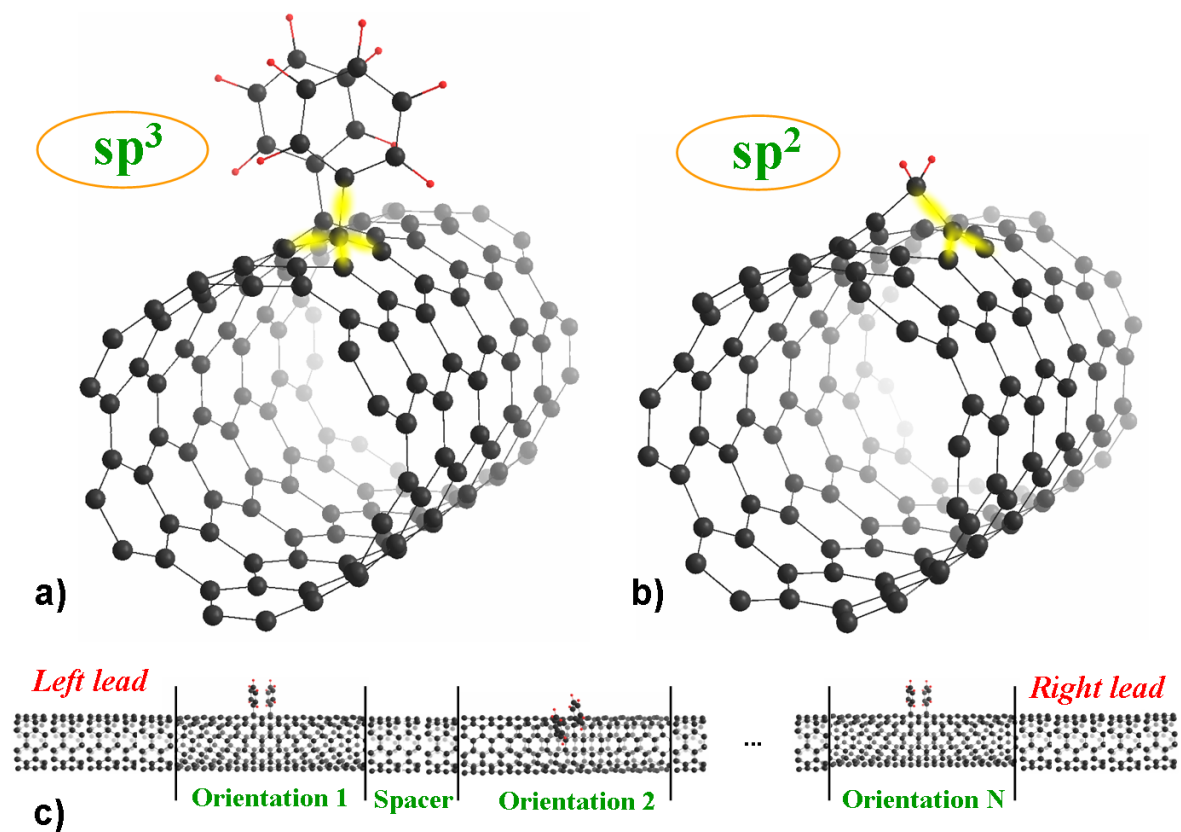


Figure 5.2: sp^2 -like and sp^3 -like functionalization - Top panel: atomic structures of the building blocks which are the starting point for the study of longer structures for both kind of grafting methods: a) sp^3 -like functionalization with phenyl groups and b) sp^2 -like functionalization through divalent addition by carbene groups. c) represents a CNT with phenyl functionalization obtained by assembling individual sections. Translational and rotational disorders, as well as external leads (pristine semi-infinite nanotubes), are included.

the CNT electronic structure is instructive for understanding the interplay between functional groups and the nanotube backbone. To that end, following (140), self-consistent electronic structure calculations and functionalization-induced atomic relaxations are performed using the SIESTA code. The calculations are performed using the local density approximation for the exchange-correlation term with Perdew and Zunger (141) parametrization. Standard norm-conserving Troullier-Martins pseudopotentials (142) are used to describe the interaction between ionic cores and localized pseudo-atomic orbitals.

The description of the hybridized bondings needs to be done with a model that takes into account the contribution of several orbitals at each atom. Split-valence double- ζ polarized (DZP) basis set contains 13 orbitals per carbon and oxygen atoms while split-valence double- ζ (DZ) basis set defines 8 centered orbitals in the same atoms. 5 and 2 orbitals are defined for hydrogen atoms for DZP and DZ, respectively. The basis chosen for the *ab initio* relaxation of the building block consists of two sets of s and p orbitals in the DZ case and an extra set of d orbitals in the DZP case. No basis set engineering is performed in any case and the number of orbitals associated to each atom is kept constant with respect to the standard definition of basis set as implemented in SIESTA code.

A combined strategy is used regarding the basis set size depending on geometric relaxation or transport calculations. Atomic relaxations of nanotubes in interaction with functional groups are done by means of a DZP basis set in all cases. When calculating the Hamiltonian for transport studies, and only for large diameter nanotubes, the polarized component can be removed with no loss of accuracy and essential gain of computational efficiency. The DZ electronic structure parametrization is performed from the atomic positions obtained from the DZP calculation without geometric relaxation, which ensures computational convergence with respect to the number of orbitals, as it can be appreciated by comparing transmission profiles for large and reduced basis sets.

When building the small block Hamiltonian associated with one scattering center, periodic boundary conditions are used with one functional group per unit cell. The length of the building block is chosen such that geometric and energetic perturbations induced by functional groups vanish as we reach its edges. Atomic positions are relaxed up to residual atomic forces are smaller than 0.02 eV/\AA . Once the Hamiltonian (H) and overlap (S) matrices have been calculated, we obtain an energetic description parametrized by a Hamiltonian where the orbitals of higher energy, close to the Fermi level, contribute substantially to the electronic transport. The renormalization procedure used in this study takes advantage of the locality of this orbital basis set, allowing us to consider the system as formed by nearest-neighbors interacting sections. As depicted in Fig.5.2 (bottom panel), an armchair CNT is divided in segments, so that H is partitioned in on-site energy diagonal blocks and nearest-neighbors coupling blocks. By coupling in a random way functionalized and pristine building blocks, we are able to build up CNTs as long as desired. The present approach is limited to the low bias regime but allows us to study systems of realistic lengths as usually investigated in the experiments (131).

5. QUANTUM TRANSPORT STUDY OF CHEMICALLY FUNCTIONALIZED CARBON NANOTUBES

5.4 Breaking the bonds

Before moving on to the analysis of the case of multiple functional groups attached to long nanotubes, it is worth examining the case of a single functional group. In order to check the effect of a pair of phenyl rings and a carbene group on the electronic structure of an armchair CNT, we plot the band energy diagram of the hybrids and compare them with pristine tube band energy diagram. Fig.5.3-a) shows the unaltered band structure of a (10,10) upon functionalization with a carbene group. The bond between neighbouring circumferential carbon atoms is broken and new bonds between carbene carbon atom and two nanotube carbon atoms are formed. Fig.5.3-c) and Fig.5.2-b) show a CNT with a carbene group covalently attached in an orientation that favors a stable configuration. The system CNT-CH₂ reaches its minimum of configuration energy by displacing the carbon atoms that serves of anchorage site to the carbene, which entails a rupture of the original C-C bond of nanotube atoms. If we restrict ourselves to a nearest neighbour scheme, it can be observed that every C atom in the tube is now bonded to three C atoms which allows for the preservation of the original network of π -orbitals. In Fig.5.3-d), the preserved π -orbitals centered in the altered nanotube carbon atoms are shown in a representation based in Wannier functions approach(132).

As we will see below, carbene bond orientation on the nanotube plays a fundamental role in electronic transport properties. The orientations shown in Fig.5.3-c) and -d) are the most stable configurations for zigzag and armchair CNT, respectively.

In contrast, covalent functionalization of CNTs involves the formation of saturated sp^3 -orbitals which break the p_z network symmetry of the nanotube surface. As we will see, the consequence is a dramatic loss in charge transport ability. Rehybridization introduces resonant states in the electronic structure of the pristine CNT which act as scattering centers and reduce critically its good transport properties over distances ranging from nanometers to micrometers. As it can be observed in Fig.5.3-b), two flat bands (red lines) at energy values that coincide with the conductance dips in Fig.5.4-a) (red line) show up in the energy band diagram. This points out the presence of molecular states which localized the system wavefunction around the phenyl groups, as observed in Fig.5.3-f) where the LDOS is plotted for the state at energy -0.6 eV. It can be observed that, at this energy, the largest contribution to the density of states comes from the orbitals associated to the functional groups, i.e system wavefunction is localized over the molecules, unlike e) where the wavefunction is homogeneously spread along the system.

5.5 Metallic armchair carbon nanotubes

We focus on the case of a metallic armchair (10,10) CNT tube. As shown in earlier works (130), the diameter of such a tube is close to the limit separating the area of stability for closed carbene configurations (larger tubes) and opened geometries (smaller tubes). Closed configurations introduce significant backscattering and the advantage of cycloaddition

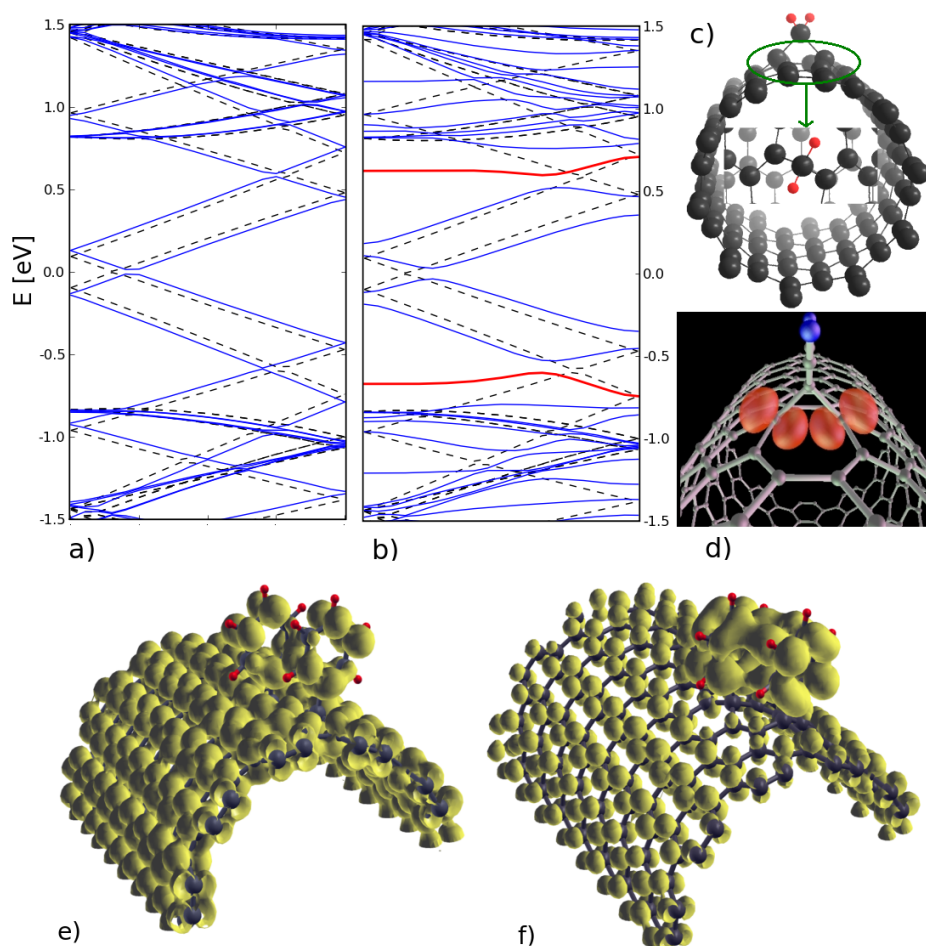


Figure 5.3: Energy band comparison - Energy bands near the Fermi level of functionalized armchair CNTs. The effect of mono- and divalent sidewall cycloaddition on the electronic structure of nanotubes can be observed by comparing the pristine (dashed lines) vs functionalized case (blue lines) of a 12-cell (10,10) CNT. In left panel: a carbene group with the orientation shown in d), is shown not to introduce any modification in the electronic structure of the tube. On the contrary, a pair of phenyl rings disrupt the p_z -conjugated network and introduce new states in the diagram, as shown in the right panel with red lines. These non-dispersive bands correspond to localized states which cause the drop of conductance as shown in Fig.5.4-a) (red line) by two dips at the same energy. In c), a carbene group is grafted on the surface of a semiconducting nanotube in a skewed orientation, which provokes a partial break of the nanotube C-C atom bond. d) This image is taken from (133) and shows the π -orbital preservation upon carbene functionalization when the C-C bond is perpendicular to nanotube axis. e) and f) show the localized density of states of the hybrid CNT-pair of phenyl at two energies: in e) the density of states has been projected over an interval of energy close to Fermi energy; in f) the projection is over the localized state at -0.6 eV.

5. QUANTUM TRANSPORT STUDY OF CHEMICALLY FUNCTIONALIZED CARBON NANOTUBES

is therefore lost for larger diameter tubes. Further, it was shown on the basis of activation energy calculations for desorption that carbene is not thermally stable on large tube diameter and graphene. Due the planar-like geometry of large CNTs, graphene groups do not induce the displacement of C atoms from the original structure (as in the case of small diameter armchair nanotubes) and they spontaneously desorb at room temperature (144).

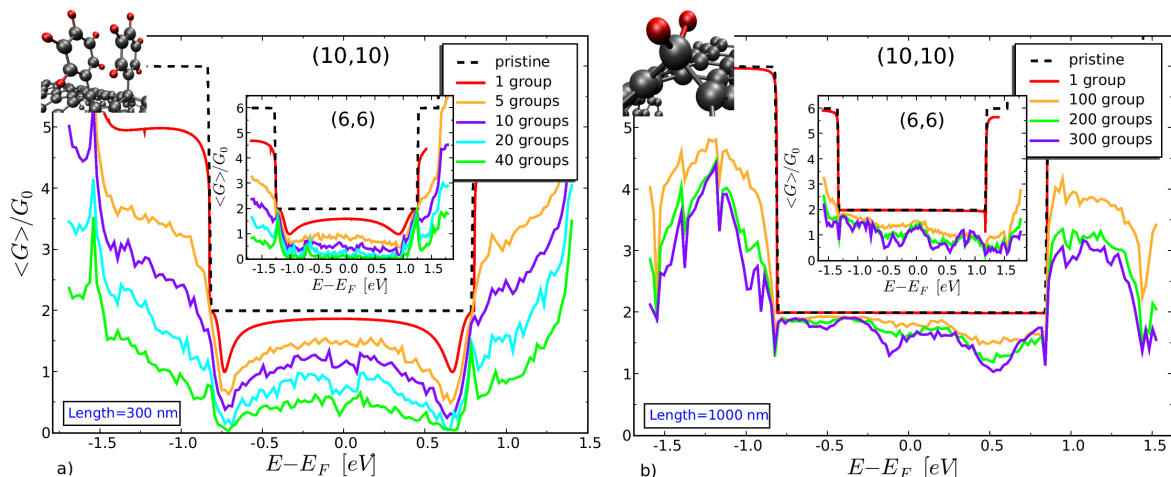


Figure 5.4: Conductance comparison for phenyl and carbene. - Left panel: Conductance (in units of G_0) of a 300 nm long (10,10) CNT nanotube functionalized with phenyl groups. The conductance has been averaged over 40 different random configurations. Together with the case of pristine nanotube (dashed lines), the averaged conductance is shown for an increasing number of grafted groups to the surface. Right panel: Same as in left panel, but for a 1000 nm long nanotube functionalized with divalent addition of carbene groups. All insets give the same information but for the (6,6) nanotubes.

Concerning the phenyl moieties, we study paired configuration in the 1,4-geometry (para) where two phenyls are grafted as third-nearest neighbors, keeping intact the conjugation properties of the CNT. Several arguments suggest that such a configuration is the most likely to occur on nanotubes: (a) the grafting of a first radical is known to enhance the reactivity of a carbon atom at an odd-number of bonds away from it (145), (b) the 1,4-configuration is slightly more stable than the 1,2-configuration (ortho), and (c) isolated phenyls have been shown to spontaneously diffuse or desorb at room temperature on standard diameter tubes (144). These considerations are consistent with the experimental observation based on a careful RMN analysis (147) that, in the case of nanotube alkylation, the 1,4-addition (para configuration) appears to be more common than the 1,2-addition (ortho configuration).

In Fig.5.4 (right and left panels), the impact of an increasing number of grafted phenyl groups is shown for 300 nanometer long (6,6) and (10,10) nanotubes. It is first interesting to note the effect of a single group on the otherwise clean nanotube (dashed curves). The sp^3 bond between such a single phenyl and the tube surface induces a decay of conductance in

the whole spectrum with the occurrence of two symmetric peaks (in the first plateau) that are related with the suppression of one conduction channel. The increase of the coverage density results in stronger damping of the conductance pattern, which however roughly follows the initial single group signature. For a fixed molecule density, the effect is found to be further enhanced with reducing nanotube diameter, which is expected because of lower transport dimensionality. As shown in Fig.5.4 (left panel), the conductance decay at the charge neutrality point appears roughly inversely proportional to the coverage density. By using a conventional phenomenological law the disorder average transmission coefficient can be related to the elastic mean free path as

$$\bar{T} = \langle G \rangle / G_0 = N_{\perp} \left(1 + \frac{L}{\ell_e}\right)^{-1} \quad (\text{where } G_0 = \frac{2e^2}{h}), \quad (5.1)$$

which allows us to give some approximated range and scaling behavior of the mean free path (Fig.5.4 left panel inset). This formula gives the correct asymptotic limits $\bar{T} \approx N_{\perp}$ for $L \ll \ell_e$ and $\bar{T} \approx N_{\perp} \ell_e / L$ for $L \gg \ell_e$, but is only approximative within 3% of error in the intermediate regime $L \approx \ell_e$ (148).

With more simple disorder models (such as Anderson-type onsite disorder), analytical forms and scaling behavior of elastic mean free paths were derived for both carbon nanotubes (149) or graphene nanoribbons (150) (see also section 2.12). In particular, ℓ_e was shown to upscale linearly with tube diameter for a fixed disorder strength. For our computed 300 nm long (6,6) nanotube, the mean free path quickly decreases with coverage density to reach $\ell_e \sim 15$ nm when 40 groups are attached to the sidewalls. The same number of functional groups on a larger diameter nanotube (10,10) will however yield $\ell_e \sim 100$ nm. The calculated mean free path thus also shows some upscaling with nanotube diameter, although the scaling behavior can not be extracted in detail. As evidenced by these results, sp^3 bonds are clearly not in favor of good conduction efficiency of hybrid nanotubes, which therefore advice against their use for any applications.

In contrast, the cycloaddition of carbene groups yields a small downscaling of the conductance in the first plateau, respect to the coverage density. (see Fig.5.4). Differently to the case of phenyl groups, an asymmetry of the conductance decay is already observed for the single molecule case. This is seen as a small dip in the conductance just before the transition to the first higher subband (red curve). The much weaker change of conductance indicates a quasiballistic regime, and by using the phenomenological formula eq.5.1, a rough estimate of the corresponding elastic mean free path is achieved, after computing the average conductance at the charge neutrality point (Fig.5.5-a, main panel). The values of ℓ_e are reported in the inset of Fig.5.5-right panel, and are in the range of $\sim 2 - 9 \mu\text{m}$ depending on coverage density and nanotube diameter. In this case a rough linear scaling of ℓ_e is observed with tube diameter. One also notes that for the chosen parameters, the coverage density in the case of carbene groups is larger than for phenyl case. This demonstrates the weak effect of such kind of functionalization on transport properties of pristine nanotubes, which is crucial for further envisioning the use of long hybrid nanotubes.

5. QUANTUM TRANSPORT STUDY OF CHEMICALLY FUNCTIONALIZED CARBON NANOTUBES

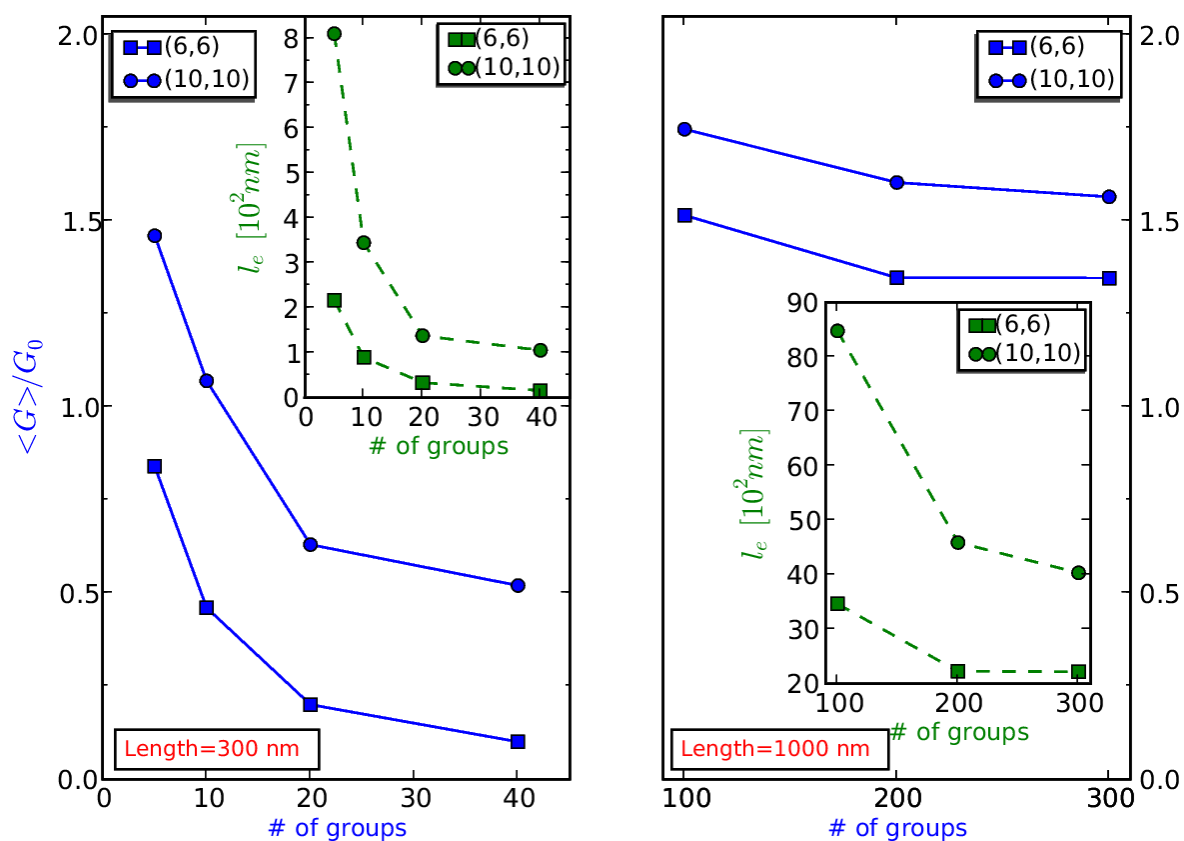


Figure 5.5: Mean free paths - Left panel: Disorder average conductance at the charge neutrality point (main panel) and estimated elastic mean free path (inset) as a function of grafted phenyl groups density for a nanotube 300 nanometer long. Right panel: same as in left panel but for grafted carbene groups and for a nanotube length of $1\mu\text{m}$.

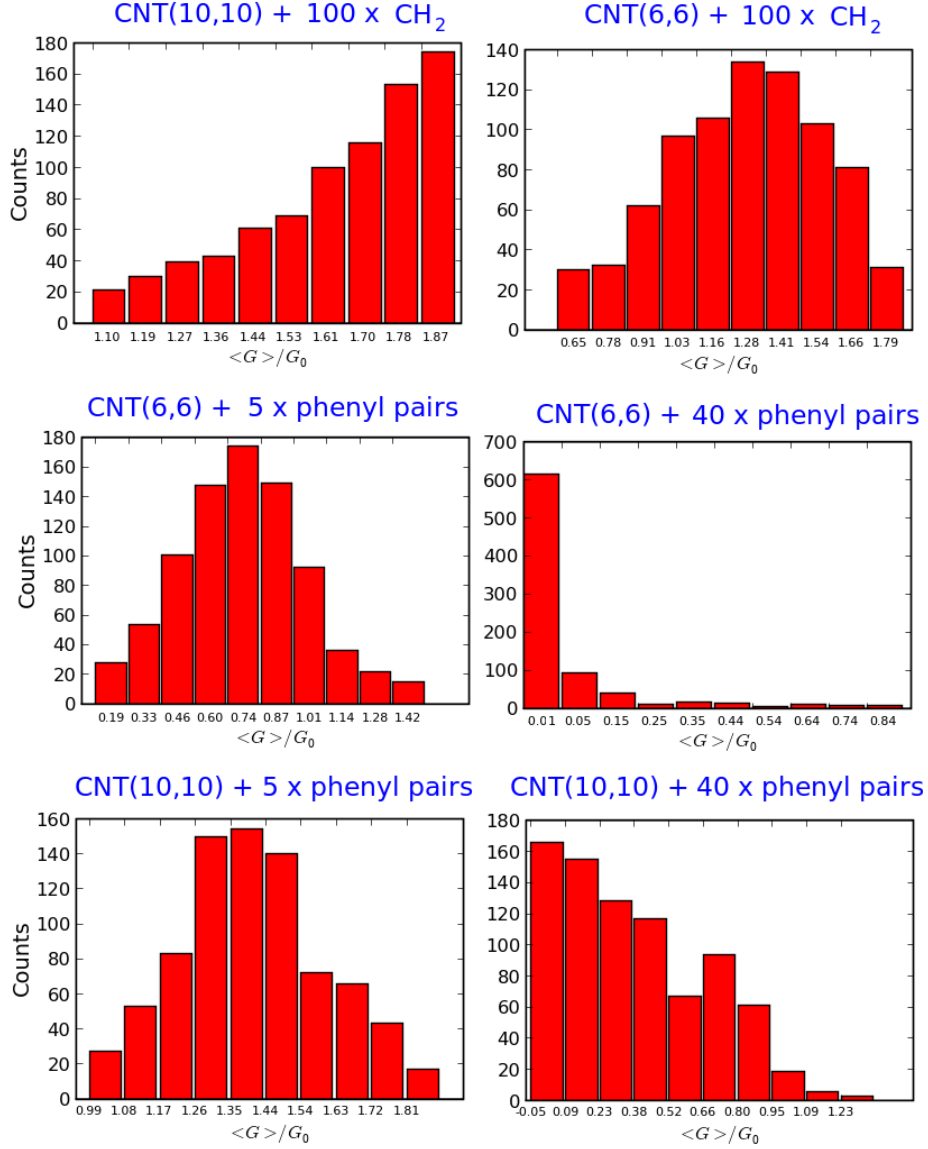


Figure 5.6: Conductance histograms for functionalized metallic armchair CNT. - This histograms account for the number of conductance values obtained at Fermi energy for each conductance interval. The two upper panels show a predominance of values close to the pristine nanotube (more clear in the large diameter tube), indicating that electronic transport takes place in the quasi-ballistic regime. The two middle panels show conductance behaviour of small diameter armchair nanotube for both low and high grafting rates. The same as in the lower panel, diffusive conductance is observed with regards to the rate of functionalization. In all cases, conductance has been measured at the neutrality charge point (Fermi energy level), for nanotubes of $0.3\mu\text{m}$ (carbene) and $1\mu\text{m}$ (phenyl).

5. QUANTUM TRANSPORT STUDY OF CHEMICALLY FUNCTIONALIZED CARBON NANOTUBES

Finally, transport regimes can be also characterized with the help of histograms. For a given distribution δ of grafting groups in the nanotube, the normalized conductance $T(\delta) = G(\delta)/G_0$ will depend on the particular chosen distribution. The conductance then becomes a random variable of which first moments are its mean value $\bar{T} = \frac{1}{\delta} \sum_{\delta} T(\delta)$ and its mean square deviation $\Delta T = \sqrt{\overline{T^2} - \bar{T}^2}$, where equiprobability for each configuration of disorder is assumed.

The histograms shown in Fig.5.6 corroborate the differences between the two types of functionalization when analyzing transport properties. Carbene-based functionalization hardly affects the properties of the pristine CNTs and a big amount of conductance values are obtained in the vicinity of $G = 1.8G_0$, revealing quasi-ballistic transport. For nanotubes with phenyl functional groups, nearly zero conductance values are obtained when 40 groups are grafted in 300 nm long (6,6) tube, with low dispersion ΔT associated to the conductance. In this case, the system is found in the localized regime. In a (10,10) tube, for only 5 phenyl grafted groups a similar behaviour of the conductance is observed than in the former case. However, for a higher grafting rate a decreasing of the conductance as the inverse of group number is observed, with a trend to saturation around $\langle G \rangle = 0$.

5.6 Semiconducting zigzag carbon nanotubes

In this section, we report on a first principles computational study of the effect of CH_2 carbene grafting on the charge transport properties of micrometer long semiconducting carbon nanotubes. The evolution of conductance as a function of tube diameter and with a random distributions of up to one hundred functional groups is explored. It is shown that for zigzag tubes, the transition from a quasi-ballistic to a strongly diffusive regime occurs at a much smaller tube diameter as compared to armchair metallic tubes. This is related to an earlier transition from the “open” to “closed” configuration for the nanotube C-C bond bridged by the carbene molecule. As a result, above 1.2-1.4 nm tube diameter, the conductance of functionalized semiconducting tubes is found to decay rapidly with increasing number of grafted groups, in great contrast with armchair tubes of equivalent diameter.

Interactions between addends and their replica in the periodic one-dimensional cells are avoided by considering six-unit CNT-cells (25.55 Å) which guarantees a convergence to pristine CNT in the borders of the supercell.

5.6.1 Diameter dependent functionalization induced by bond cleaving

In the case of zigzag CNTs, there are two types of C-C bond orientations onto which a CH_2 can be grafted, namely parallel (||) or skewed (\) with respect to the tube axis. These bond orientations are depicted in Fig. 1 (inset) and Fig. 2 (left inset) respectively, where the bridged tube C-C bonds upon carbene adsorption have been outlined (yellow links). This is

5.6 Semiconducting zigzag carbon nanotubes

at odds with the case of metallic armchair tubes for which (a) the parallel configuration does not exist, and (b) bonds perpendicular to the tube axis offer preferential addition sites (130). In each case, the equilibrium position is reached when the carbon atom of CH_2 is located on top of the C-C tube bond forming a bridge-like structure. The calculations shows that the (\backslash) conformation is always more stable than the (\parallel) one. This is consistent with the result of Chen *et al.* (111) in the case of a small (8,0) finite-size cluster. It is further consistent with the study by Lee and Marzari of metallic armchair tubes showing that bonds orthogonal to the tube axis are preferentially grafted (130; 153). As a rule of thumb summarizing all these results, bonds with largest angle with respect to the tube axis are more active towards adsorption, since they experience most of the tube curvature.

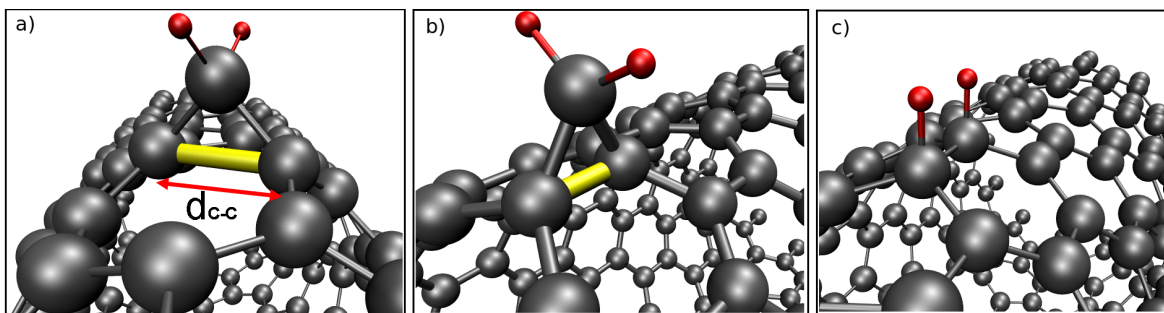


Figure 5.7: The 3 analyzed orientations. - A ball-and-stick model illustrates the a) skewed (\backslash) and b) parallel (\parallel) conformations for carbene group (CH_2) bonded to the CNT. In c) 2 hydrogen atoms are bonded to the zigzag nanotube in ortho configuration.

We therefore focus on the skewed configurations and show in Fig.5.8 the evolutions of the sidewall bond distance ($d_{\text{C-C}}$) between the two carbon atoms anchoring the carbene molecule as a function of zigzag CNT index, for both large and small gap CNTs (154). As observed in the case of armchair tubes for the most stable orthogonal configuration (130; 153), there is a transition from an "open-skewed" configuration at small diameter, with $d_{\text{C-C}} = 2.1 \text{ \AA}$ for the (8,0) CNT, to a closed one, with $d_{\text{C-C}} = 1.65 \text{ \AA}$ for the (22,0) tube. The transition occurs for the (15,0) tube with a diameter of 11.7 \AA , at much smaller a diameter than for armchair tubes for which the transition occurs for the (18,0) tube (diameter = 24.5 \AA).

Such results can be rationalized by remarking that bonds along the circumferential direction undergo the largest tensile stress induced by curvature and are thus more prone to open. As a matter of fact, we find that bonds parallel to the tube axis, which do not feel the effect of curvature, always exhibit the closed configuration. An interesting observation is that large gap zigzag tubes exhibit a transition to the closed configuration at a larger diameter than small gap ones. This transition to closed configurations at rather small diameters for semiconducting tubes bears important consequences on transport, as explained hereafter.

5. QUANTUM TRANSPORT STUDY OF CHEMICALLY FUNCTIONALIZED CARBON NANOTUBES

5.6.2 Quantum transport in functionalized semiconducting nanotubes

Following the well established computational strategy as discussed in previous chapters, from the first principles calculations of long tube sections functionalized by single groups, *ab initio* Hamiltonian and overlap matrices are obtained. Such a set of initial “building blocks” is then used to construct micrometer long nanotubes composed by a random series of functionalized and pristine tube sections, introducing rotational and translational disorder. First-principles transport calculations of complex and disordered systems with several thousands of atoms can therefore be achieved.

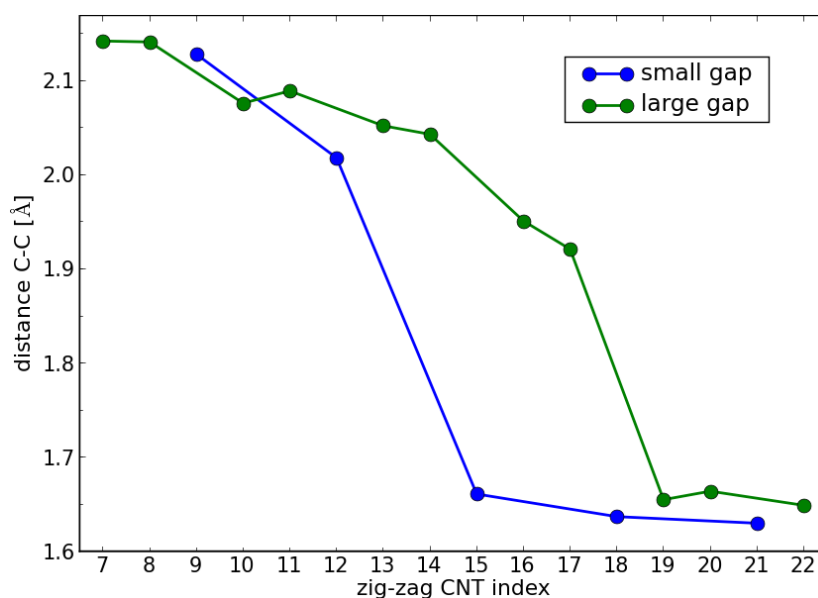


Figure 5.8: fig1 - Sidewall equilibrium distance for C-C bond anchoring the carbene group, as a function of the tube (n,0) index, for both types of zigzag tubes: small gap ($n=3m$) and large gap ($n=3m+1$) CNTs, for m an integer.

We first discuss the effect of a single functional group. In Fig.5.10-left the energy-resolved conductance for a (19,0) CNT (main panel) and a (12,0) CNT (inset) is shown. These tubes are on both sides of the “open-to-closed” C-C bond distance transition for the skewed (\backslash) configuration (see Fig.5.8). In the case of the small gap (12,0) CNT, the grafted molecule in the (\backslash) configuration, with open C-C bond, has hardly any effect on the conductance as shown in the inset (blue curve). On the contrary, the parallel ($||$) bonding geometry, with closed C-C bond, yields a dramatic drop of conductance at nearly all energies (red curve inset). Such a behavior can be rationalized by observing that in the open geometry, the carbon atoms remain 3-fold coordinated preserving thus the conjugated character of the sp^2 pristine tube network. (130; 152) Differently, in the closed geometry, the bridged carbon atoms are 4-fold coordinated, destroying the local the conjugated character of the π -network and thus reinforcing backscattering probability. Such a transition to a local sp^3 character

5.6 Semiconducting zigzag carbon nanotubes

can be strikingly evidenced by comparing our data with the conductance profile generated by two hydrogen atoms bonded to neighbouring C atoms on a (\parallel) bond (see Fig.5.10-left). Clearly, the two kinds of functionalization lead to very similar conductance profiles with up to one full conducting channel (one G_0) quenched at selected energies on the first plateaus on each side of the gap.

Assuming that the functionalization process follows the thermodynamic limit, with all addends in the skewed configuration, one may possibly conclude that the conductance of the small gap (12,0) tube can be preserved up to very large coverages. It was shown in the case of a standard (10,10) armchair tubes that up to several hundreds of carbene groups could be grafted while preserving nearly 75% of the conductance at all energies. However, as shown above, the open-to-close transition in zigzag tubes occurs at much smaller diameter when compared to armchair tubes, so that basically all zigzag tubes with a diameter larger than ~ 1.2 -1.5 nanometers will exhibit closed grafting configurations, even for the most stable skewed bonds. As a result, and as shown in Fig.5.10-left for the (19,0) tube, even an isolated carbene group grafted on a skewed bond induces severe backscattering close to band edges (onsets of plateaus). Even though the effect is less pronounced than that induced by a carbene or two hydrogens on a parallel bond (red and dashed green lines), the consequences are now shown to become rapidly dramatic for a few tens of attached molecules.

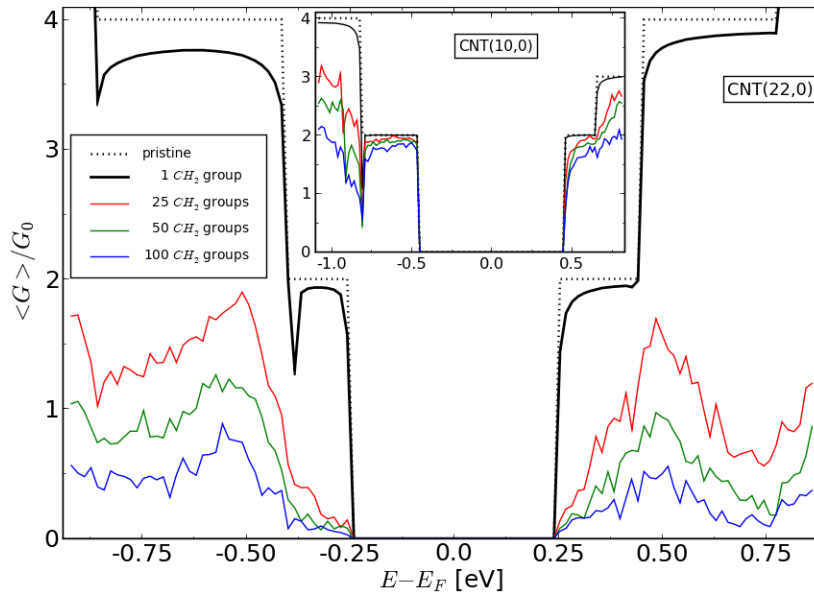


Figure 5.9: Conductance comparison in large- and small-gap semiconducting CNTs.

- Conductance for pristine (22,0) nanotube (dotted line), with a single grafted carbene in the conformation (solid line), and for averaged configurations with varying addends density (25, 50 or 100 CH_2 groups distributed at random along one μm). Inset: same as in main panel but for the small diameter (10,0) semiconducting tube.

5. QUANTUM TRANSPORT STUDY OF CHEMICALLY FUNCTIONALIZED CARBON NANOTUBES

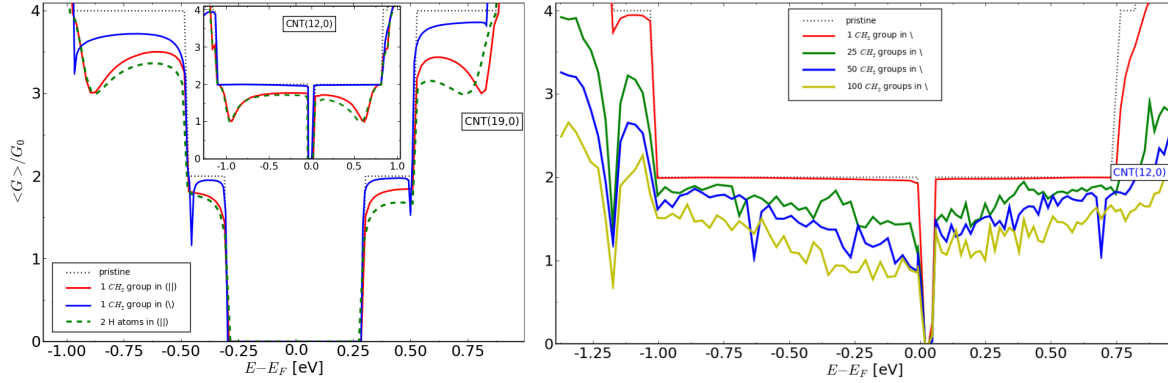


Figure 5.10: Conductance in large-gap semiconducting CNTs. - Left panel, main panel: conductance in G_0 units of pristine (19,0) tube (dotted line) and with a carbene grafted in the parallel (\parallel) (red line) and skewed (\backslash) (blue line) configuration. Carbene in the \parallel conformation shows similar conductance profile than two grafted hydrogens (green dashed). Inset: same as in main panel but for a small gap (12,0) tube. Right panel: conductance averaged over 20 configurations of an increasing number of functional carbene groups randomly distributed over 1 micrometer long small-gap (12,0) CNT in skewed configuration. This grafting mode is the less invasive method to functionalized a zigzag nanotube.

To further explore the transport properties of long and chemically modified semiconducting nanotubes, we have performed a mesoscopic study for several tubes with a length of 1 μm and random grafting of an increasing number of carbene molecules. Conductances were averaged over up to 20 configurations of disorder for a given tube and number of molecules. As a representative case, Fig.5.9 shows a comparison between the (10,0) and the (22,0) tubes for a single grafted carbene and for an increasing number of groups (25, 50 and 100) in (\backslash) conformation. For a single grafted molecule, we recover the results of Fig.5.10-left established for the (12,0) and (19,0) tubes: the backscattering is negligible for very small tubes, but becomes significant for tubes such as the (22,0) with a diameter beyond the open-close bond transition value ($\sim 1.2\text{-}1.4$ nm). This initial difference is then amplified when adding a much larger number of addends, which enhances disorder effects and allows quantum interferences between scattering centers to set in. As a result, for the same number of grafted groups, their impact on transport in both semiconducting tubes becomes markedly different. While the (10,0) manifests a weak reduction of conductance on the first plateau (which remains close to $2G_0$ even for the largest number of addends), a strong decay is observed for the (22,0) with an almost fully suppressed conductance even for the lower studied density (25 groups randomly distributed over 1 μm). Fig.5.10-right panel shows in detail the evolution of conductance with an increasing number of functional carbene in skewed orientation. Among all the cases here analyzed, this conformation for a functional group is shown to be the weakest perturbing way of chemical attachment.

5.6 Semiconducting zigzag carbon nanotubes

To characterize the related conduction regimes, we report in left panel of Fig.5.11, the average conductance for (12,0) and (19,0) CH_2 -functionalized CNTs as a function of the number of attached carbene. Both (\backslash) and (\parallel) bonding configurations of CH_2 are considered, together with two-hydrogen atoms in the parallel configuration. The average is performed over 20 configurations of disorder and at the selected energy $E - E_F = 0.35eV$, that is roughly at the center of the first electron subband. For the (\backslash) bonding in the (12,0) tube, a weak conductance decay evidences a quasiballistic regime for the considered addends density. In contrast, for the (\parallel) bonding configuration, the conductance decrease is roughly inversely proportional to the number of grafted groups, indicating a diffusive regime. This results in a conductance reduction by one order of magnitude for only 40 groups distributed over $1\mu m$, showing the large impact of such bonding type. The increase in diameter further degrades the conductance properties. In the (19,0) case, even the more favourable (\backslash) bonding leads now to a quick drop of conductance with increasing grafted molecules.

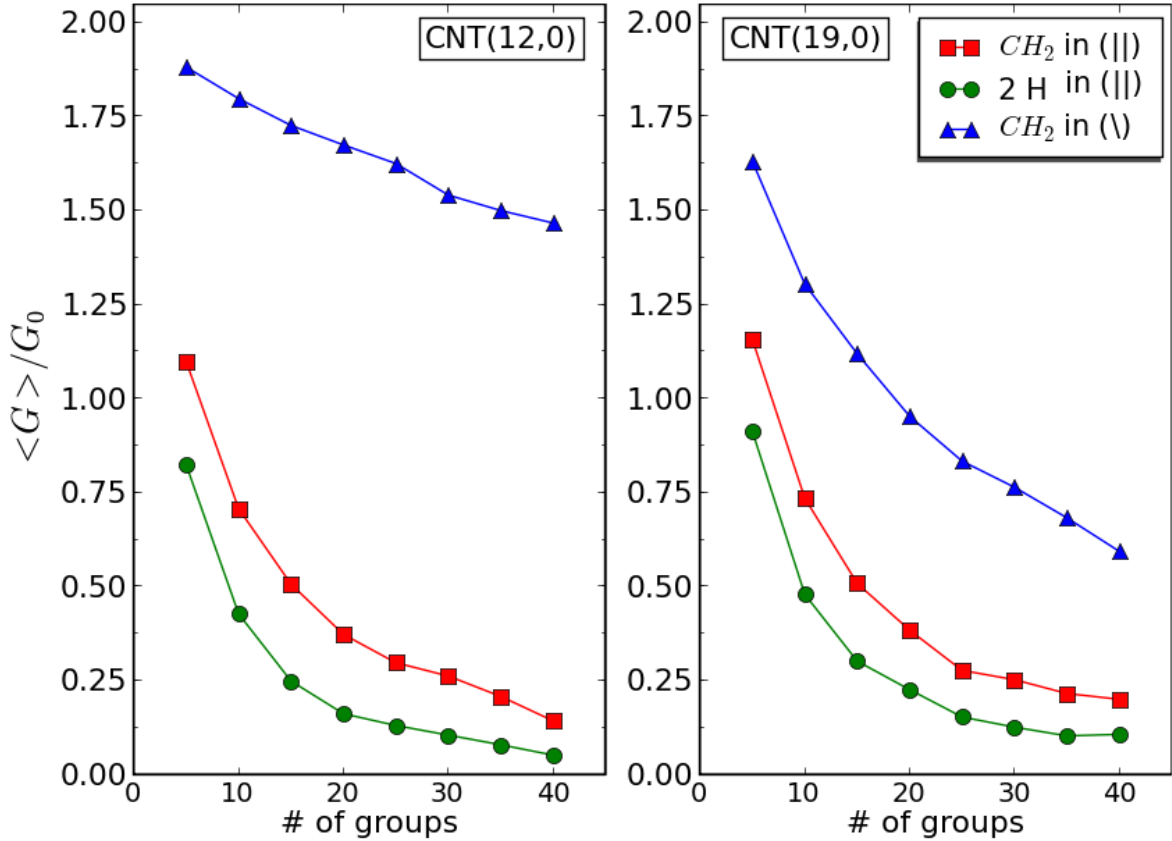


Figure 5.11: fig4 - Average conductances versus number of attached carbene groups for the (12,0) and (19,0) nanotubes, and different conformations of molecule bonding.

The early transition from the open to closed configuration for carbene grafted onto zigzag nanotubes, with a critical diameter of about 1.2 nm, represents a serious drawback for the use

5. QUANTUM TRANSPORT STUDY OF CHEMICALLY FUNCTIONALIZED CARBON NANOTUBES

of such functional groups in the case of semiconducting nanotubes. While smaller diameter tubes can always be synthesized, mass produced CNTs exhibit a mean diameter which does not go below such a critical value. As demonstrated above, for standard semiconducting tubes, carbene functionalization is thus expected to lead to a drastic reduction of conductance with a few functional groups. Besides, it was shown that carbene desorbs easily at room temperature from graphene, that is in the closed C-C bond configuration (144). Namely, the desorption barrier (a few tenths of an eV (144)) can be easily overcome in ambient conditions. It is therefore not even clear that, beyond the transition diameter, carbene grafting can be a viable way for functionalizing zigzag nanotubes.

5.7 Conclusions

By using a fully *ab initio* transport approach, we have explored the transport regimes in chemically functionalized metallic and semiconducting carbon nanotubes. By comparing two different and important types of chemical bonding we have assessed the true potential of cycloaddition reactions as a precursor for further enhancement of devices functionalities. For metallic nanotubes, the results evidence good conduction ability in the case of carbene cycloadditions, whereas phenyl addends were found to yield a strongly diffusive regime, with estimated mean free path ranging from a few tens to the nanometer scale, depending on the coverage density and incident electron energy.

In the case of semiconducting CNTs, small diameter functionalized tubes have been shown to preserve good conduction ability, whereas a strongly diffusive regime was obtained for larger diameter tubes, similarly to the effect of a low dihydrogenation density. This effect was explained by the orbital rehybridization of the atoms to which functional groups are attached. Our study quantifies the severe limits of divalent additions in large diameter semiconducting nanotubes, and suggest that smaller diameter sizes nanotubes should be targeted to engineer efficient novel device functionalities.

This demonstrates the non-invasive character of carbene functionalization when compared with phenyl and sp^3 -like functionalization, which preserves good conduction capability of underlying nanotubes, and suggests this type of functionalization as a better option for adding new functionalities to the nanotube-based devices.

Notwithstanding, it must be highlighted the limitations of the study here presented. Typically, scaling analysis are performed with the length of the system L as a variable which is modified. In this way, some useful quantities as the mean free path l_e and localization length ξ can be related to the averaged conductance of a system with a constant impurity rate. Given l_e , ξ different transport regimes can be defined depending on L . In this study, however, the approach has been the opposite: the system length has been fixed to a constant value ($1\mu\text{m}$ for carbene functionalization and $0.3\mu\text{m}$ for phenyl functionalization) and the impurity rate has been varied. This allows us to extract some useful information about the functionalization possibilities of nanotubes with regard the conservation of their electronic conduction abilities. Although such a system are not completely characterized in terms of

5.7 Conclusions

relevant quantum transport quantities, these results may be considered of interest interest for a broad scientific community ranging from chemist to engineering.

5. QUANTUM TRANSPORT STUDY OF CHEMICALLY FUNCTIONALIZED CARBON NANOTUBES

Chapter 6

Covalent Attachment of Functional Groups on GNRs and Transport Properties

‘Computer simulations, as meteorology, do not give anything but approximate forecasts.’

Ivana Savić

Chapter résumé (French version)

Ce chapitre traite de l'étude des propriétés de transport électronique des GNRs avec des modifications de surface introduites via le greffage chimique de groupes fonctionnels hydroxyle (OH) et hydrogène (H). Des détails sont donnés ici en complément de ceux déjà publiés dans l'article "Chemical Functionalization Effects on Armchair Graphene Nanoribbons Transport", dans la revue Nano Letters.

Chapter résumé (Spanish version)

Este capítulo trata sobre el estudio de las propiedades de transporte electrónico de GNRs cuya superficie ha sido modificada mediante funcionalización química con grupos funcionales hidroxil e hidrógeno. Aquí se exponen los resultados y detalles del estudio previamente publicado en el artículo "Chemical Functionalization Effects on Armchair Graphene Nanoribbons Transport", aparecido en la revista especializada Nano Letters.

6. COVALENT ATTACHMENT OF FUNCTIONAL GROUPS ON GNRs AND TRANSPORT PROPERTIES

Chapter résumé (English version)

This chapter deals with the study of electronic transport properties of GNRs with surface modification introduced via chemical attachment of hydroxyl (OH) and hydrogen (H) functional groups. Herein details are given in addition to the those already published in the article "Chemical Functionalization Effects on Armchair Graphene Nanoribbons Transport", in Nano Letters review.

Results are obtained with the full first-principles transport computational methodology developed in chapter 3 which allows us to tackle simultaneously chemical complexity at the nanoscale and the resulting effect on charge transport of graphene nanoribbons. In this work it is clarified at a quantitative level, how conduction properties in chemically modified GNRs with lengths relevant for experiments (from few hundreds of nanometers to the micron scale) can be tuned by chemical addends. The nature of chemical bonding is shown to be similar to an sp^3 -type defect, whereas transport length scales (elastic mean free paths) are estimated from the obtained diffusive regime. These estimates are the first reported in the literature, and will be surely of interest for experimental groups that are currently working on such different types of functionalization of graphene based materials and devices.

6.1 Introduction

The fabrication of a single graphene layer, either through exfoliation of graphite (158), or using epitaxial growth (159), has raised a huge amount of activities given the possibility to explore low dimensional transport in a material with spectacular electronic properties (91; 160), and owing to the perspective for carbon-based nanoelectronics (159; 161). Reported charge mobilities in graphene layers can be as large as $\sim 2 \text{ m}^2\text{V}^{-1}\text{s}^{-1}$ close to the Dirac point (162; 163). Notwithstanding, as a peculiar two-dimensional system, a single graphene layer behaves as a zero gap semiconductor, with poor field effect capability. As a matter of fact, the charge current modulations (tuned by electrostatic gating) in undoped graphene layers hardly change by more than one order of magnitude (162). To enable its use for designing active electronic devices, two strategies are proposed. The first one is based on the fabrication of graphene strips with reduced lateral size, i.e. graphene nanoribbons (164)) and larger energy bandgap. GNRs with width from several tens of nanometers down to 2 nm have been fabricated either by plasma etching (165) or by means of chemical treatment of graphite (166). Band-gap engineering of GNRs has been demonstrated (167), and GNRs-based field effect transistors with good performances have been reported (168).

Alternatively, chemical functionalization of graphene-based materials is a promising strategy to reversibly tune 2D graphene electronic properties such as channel resistivity in field effect devices, without requiring aggressive ribbon width downsizing. By strong chemical modification of a graphene substrate, the design of reversible electrochemical switches, and their use for nonvolatile memory applications have been reported by Echtermeyer et al. in

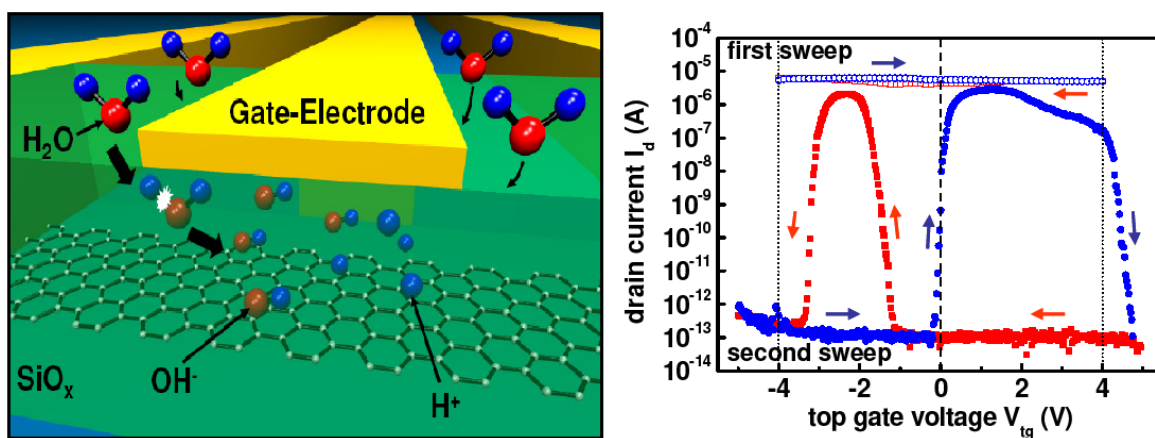


Figure 6.1: Electrochemical modification of graphene - Water from the environment is attracted inside the capacitor formed by the top gate, silicon-oxide and graphene. Inside the porous oxide layer water molecules are broken into H^+ and OH^- by the electric field. Depending on field polarity, ions diffuse towards graphene and transform it. This transformation is established when carbon atom orbitals of the graphene substrate hybridize to sp^3 and creates a chemical bond with an oxygen atom or a hydrogen atom. Two new insulating species can thus be created: graphane (graphene + H) or graphene oxide (graphene + OH). As a consequence of this modification graphene conductance switches between "ON-state" and "OFF-state" states (as shown on the right image). The top open-circle lines show the typical top-gate transfer characteristics for ref.(157) FED at a drain-source voltage $V_{ds} = 50mV$. In the second sweep, by using higher top-gate voltages, the drain current can be switched between both states, which creates a bipolar behaviour for the two sweep directions.

6. COVALENT ATTACHMENT OF FUNCTIONAL GROUPS ON GNRS AND TRANSPORT PROPERTIES

ref.(157). In this experiment, the water molecule from the ambient or at the SiO₂ graphene interface splits into H⁺ and OH⁻ groups, which are further assumed to attach to the graphene surface and open a large band gap. The conductance in the field-effect device (FED) is switched between a conductive "ON-state" and an insulating "OFF-state" which yields a difference in the conductance of more than six orders of magnitude. A chemical modification takes place to form insulating graphene derivatives, such as graphane (graphene+H) and graphene oxide, when a critical value is reached upon application of an electric field to the FED. The effect can be reversed when the electrical field gets opposite polarity to recover the initial state and desorbing attached molecules. If these reversible switches are massively implemented, different device construction like nonvolatile memories can be engineered.

Additionally, beyond a reversible control of the current intensity, the possibility to induce chemical doping would enable the fabrication of either *p*-doped or *n*-doped graphene-based transistors, as shown for carbon nanotubes (180). The experimental work by Farmer and coworkers (181) suggests that covalent chemical functionalization can induce significant doping of graphene-based devices, although in this experiment contact effects prevail. Finally, functionalization also allows the development of new applications such as chemical sensors (182; 183). In this context, the understanding of the impact of covalent functionalization on charge transport in graphene-based material stands as a challenging issue.

6.2 Covalent attachment of functional groups to graphene and GNR

Covalent functionalization of graphene materials triggers the formation of saturated *sp*³-bonds which break the *p*_z-network symmetry (126; 169; 170). Obviously this should induce a severe disruption of the otherwise good conducting properties of clean graphene, even yielding the possibility to grow graphene oxide, in case of massive coverage (171). As well, a strong increase of the resistance of nitrophenyl functionalized graphene sheet has been recently reported (174).

After graphene discovery, several studies have been devoted to the hydrogenation of the graphite single-layer to unravel its modified physical and chemical properties. In ref.(175) the chemisorption of a single H atom was treated in details, as well as the induced magnetic moment interaction as a consequence of grafting several atoms in the same sublattice. The creation of unpaired electrons leads in this case to a ferromagnetic graphene-addends interaction. Afterwards, it was shown that the most energetically stable configuration is reached when the pair of atoms sit in different sublattices, leading to a non-magnetic hybrid. This non-magnetic graphene state is lost again when a third atom H sits on a third C atom.

More ambitious grafting processes were studied by Sofo et al. (176) by considering a graphene sheet completely covered by H atoms, distributed at both sides of the layer. The resulting diamond-like layer presents all the C atoms in *sp*³-orbital hybridization instead of the original *sp*² + *p*_z orbital conformation. This transformation of *π*- and *π*^{*}-orbitals to *σ*- and *σ*^{*}-orbitals results in opening a gap of ~ 3 eV in graphene band energy. A cohesive

energy of 0.4 eV/(H atom) allows to make the hydrogenation process reversible. In ref.(177), the most stable configuration of one-side hydrogenated graphene was found when H atoms are bonded at first neighbouring C atoms.

Graphene is an aromatic material, meaning that it finds a minimum of configuration energy when π -electrons of C atoms are completely delocalized and all conjugated chemical bonds are equivalent. This symmetry disappears when a functional group is grafted onto graphene surface and breaks a π -bond, inducing an sp^2 to sp^3 rehybridization. In the bonding formation, a π -electron is used to establish the link graphene-addend and the second electron that was participating in the $\pi - \pi$ -bond, remain unpaired in the vicinity of the new σ -bond. This electron is smeared in one of the sublattices and forms a magnetic moment. The spin density is localized ~ 1 nm around the graphene-addend bond, which is correlated with the crystal lattice distortion (178). However, this situation is not stable: as soon as a second atom is chemisorbed on the graphene, the unpaired electron is used in the second sp^3 hybridization and the magnetic moment vanishes.

Some studies reveal that the most stable configuration for grafting two hydrogen atoms is reached when they sit at first neighbour carbon atoms but at different sides of the sheet, due to the minimal additional distortion upon second atom grafting. If only one side is available for the chemisorption the most favorable configuration of two addends is the bonding with carbon atoms in opposite corners of the hexagon (1,4 or para-position)(179).

In this work, this principles of graphene hydrogenation have been applied as a general procedure when considering any kind of functional group that covalently bonds to the graphene layer. We deal with the case of H and OH functional groups attached on GNRs by pairs and always in opposite C atoms in a hexagonal graphene ring. In the experiment previously described, the authors claim that the increase of drain current for different polarities depends on the predominance of a functional group (H over OH, or viceversa) on the device surface. Here we consider the case of both groups attached by pairs such that two bond with different charge density are introduced at the same time in the system. The oxygen atom of OH group is known to be a good acceptor of electrons and, when located in the vicinity of a C atom, H atom behaves as donor. The case of two equivalent bonds is also treated by considering two phenyls as shown in Fig.6.2

In the following, we will refer to an armchair GNR composed of P dimer lines as *aPGNR* (185). Armchair ribbons are all semiconductors with typical sizes of energy bandgaps. The two first studied ribbons (a17GNR and a35GNR) belong to the GNRs class with small energy bandgaps (185; 186). Their widths range between 2.3 and 4.2 nm, which is within the reach of experiments (166). Two other GNRs (a16GNR and a34GNR) with much larger energy bandgaps will be also investigated (185; 186).

6.3 DFT calculations

Our first principles calculations are performed using localized atomic-like basis set in the local density approximation (LDA) (SIESTA code (87; 88)), with a double- ζ basis for each atom. In each case, the whole structure has been relaxed until residual forces were

6. COVALENT ATTACHMENT OF FUNCTIONAL GROUPS ON GNRs AND TRANSPORT PROPERTIES

smaller than 0.04 eV/\AA . To avoid any artificial backscattering effect in the coupling region, the supercell is chosen such that the influence of the grafting groups becomes negligible in the borders where periodic conditions are applied. To cope with this constraint, large supercells containing up to 600 atoms are considered. In all cases, they are formed by 8 unit cells for armchair GNRs, with a total number of 560 C atoms for the a35GNR (544 C atoms for the a34GNR) and 272 C atoms for the a17GNR (256 C atoms for the a16GNR).

The dangling σ -bonds of edge C atoms are passivated by 32 H atoms following (185). Each supercell contains from one to three OH and H grafted groups that have been placed at different positions along the ribbon width. It is observed that the length of the C-C bond near the edges is slightly shortened with regards to the central region of the ribbon. Indeed, after molecular dynamics relaxation, one observes that the anchorage C-atom sites are pulled a bit out ($\sim 0.7 \text{ \AA}$) of the graphene plane, which in turn alters the coupling between such C atoms and their three neighboring C atoms, almost yielding an sp^3 defect conformation. Finally, one also notes that the bond length between the hydroxyl group and the anchorage C atom site in the substrate is always larger when compared to the H counterpart bond, in agreement with prior energetics studies (171; 184).

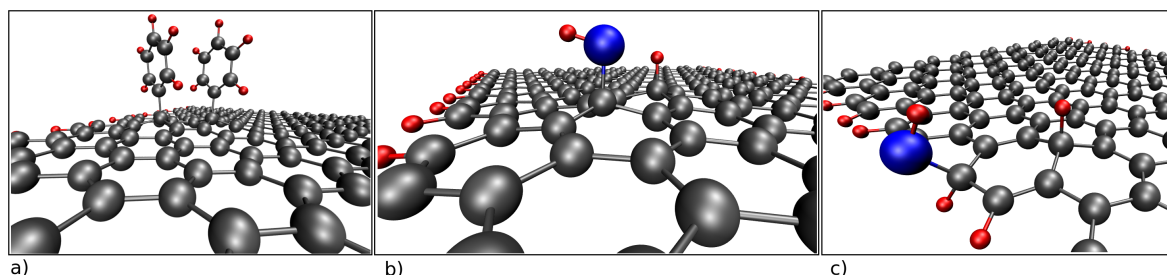


Figure 6.2: Geometrical configuration of grafting groups on GNRs - Graphical representations of the configurations of phenyls (left) and OH/H (center) when attached to an armchair graphene nanoribbon. The special case of a hydroxyl attached to an edge C atom is shown on the right

As previously indicated, the chosen configuration in every case consists in groups bonded to the GNR by third nearest neighboring carbon atoms which leads to the absence of local magnetic moments and dangling bonds. This configuration also is associated to a gain of system energy. The grafting groups sit in the middle of the GNRs such that they are not seen by the ones in the virtual images. With the couple of groups at different distances of the ribbon edge, the whole structure is fully relaxed. The angle between the C-O bond and O-H bond is about 100° , in the optimized GNR-OH system. The three p-orbitals of O atom are perpendicular to each other when the atom is isolated. Orbitals undergo a hybridization when an oxygen p-orbital bonds the hydrogen s-orbital to form an sp -orbital which is, in principle, perpendicular to the C-O bond. Due to the interaction of this hybrid orbital with the carbon-oxygen p-p orbital bond, the final angle is tilted, as shown in Fig.6.2-b)

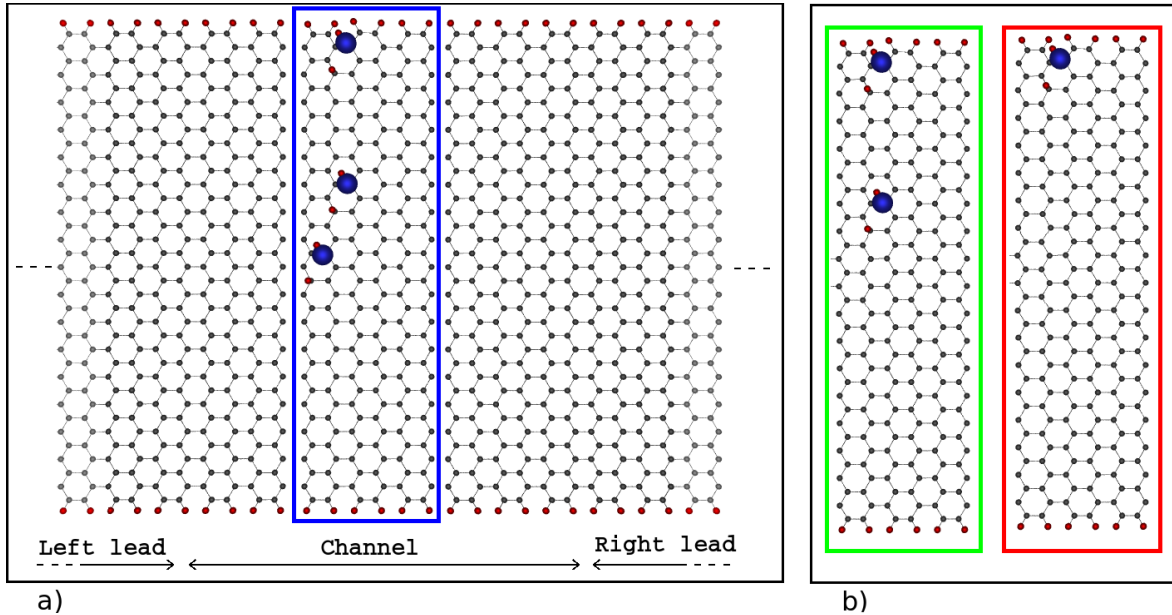


Figure 6.3: Channel-lead representation - Representation of the nanoribbon-based structure used for the conductance calculation. The color of the rectangles corresponds with the conductance curve color plotted in 6.4.

Several groups can be attached at the same time as shown in Fig.6.3, which allows us to compare conductance and structural changes relative to the position of the addends. The particular configuration of nanoribbon with functionalization at the edge is also analyzed due to the special feature of the electronic structure already reported in ref.(193). In this latter case, no localized states are introduced by the functional group at energies close to the Fermi level and, therefore, the conductance ability of the ribbon is not affected. In Fig.6.2-right, the sp^3 structure can be appreciated: The functional group reorients the four orbitals of the C atom to which it is attached to the typical tetrahedral conformation of sp^3 orbital hybridization, as in the methane molecule. The sp^2 hybridization is locally destroyed and a $pp\sigma$ bond is formed between C and O atoms.

Similarly, the attachment of a H atom to the nanoribbon surface induces a similar rehybridization of C atomic orbitals and the subsequent geometric and p_z network distortion. These modifications in GNR physical properties lead to the differences in the electronic properties of the functionalized and pristine nanoribbons, which have serious consequences in their electronic transport abilities.

6. COVALENT ATTACHMENT OF FUNCTIONAL GROUPS ON GNRS AND TRANSPORT PROPERTIES

6.4 Transport calculations

Once the set of *ab initio* calculations have been performed to obtain the Hamiltonian and overlap matrices associated with short functionalized nanoribbon sections, we can build up the complete disordered system by randomly assembling such elementary parts containing a single or a few defects (as explained in chapter 3). Sections of pristine nanoribbons are also assembled such that translational disorder is introduced. This allows us to study transport through very long GNRS by using standard decimation techniques for the calculation of Green's function and transmission probabilities.

To compute the conductance of clean and defected GNRS, the multichannel Landauer-Büttiker technique as described in chapter 3 is extensively used. The channel is defined between two perfect GNR-based right (left) leads (see Fig.6.3) which impose chemical potentials μ_1 (μ_2) and minimize the contact effects. The transmission coefficient $T(\epsilon)$ is obtained by solving the quantum mechanical problem of a single electron scattered within the channel. At zero temperature and in the low bias limit ($\mu_1 - \mu_2 = eV \rightarrow 0$), the conductance is given by $G = G_0 T(\epsilon)$, where $G_0 = 2e^2/h$ is the quantum conductance while ϵ denotes the energy of the incident charge carrier. Experimentally, the energy dependence of the conductance can be modulated through a capacitive coupling between the ribbon channel and a gate electrode. The transmission is calculated by evaluating channel Green's function and electrode self-energies.

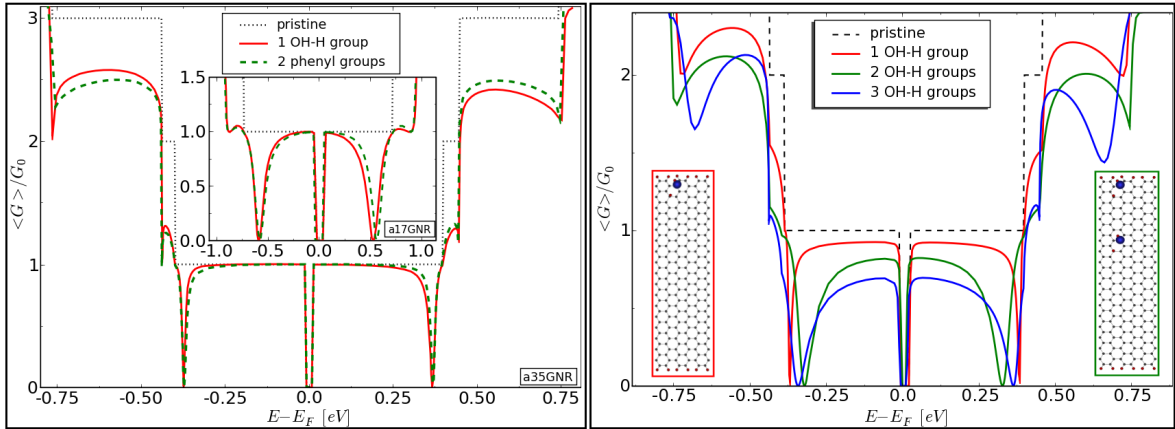


Figure 6.4: Conductance of small-gap GNRS. - Left panel: Conductance of the a35GNR (main frame) and the a17GNR (inset) for the pristine case (dotted lines) and for the single pair defect (C-OH, C-H) case (solid line). The case for a pair of phenyl groups is also given for comparison (dashed lines). The associated geometries are shown in Fig.6.2-a) and b). Right panel: Conductance of a35GNR with 1, 2 or 3 defects in a short ribbon channel (from top curve to bottom curve) corresponding to the configurations shown in Fig. 6.3

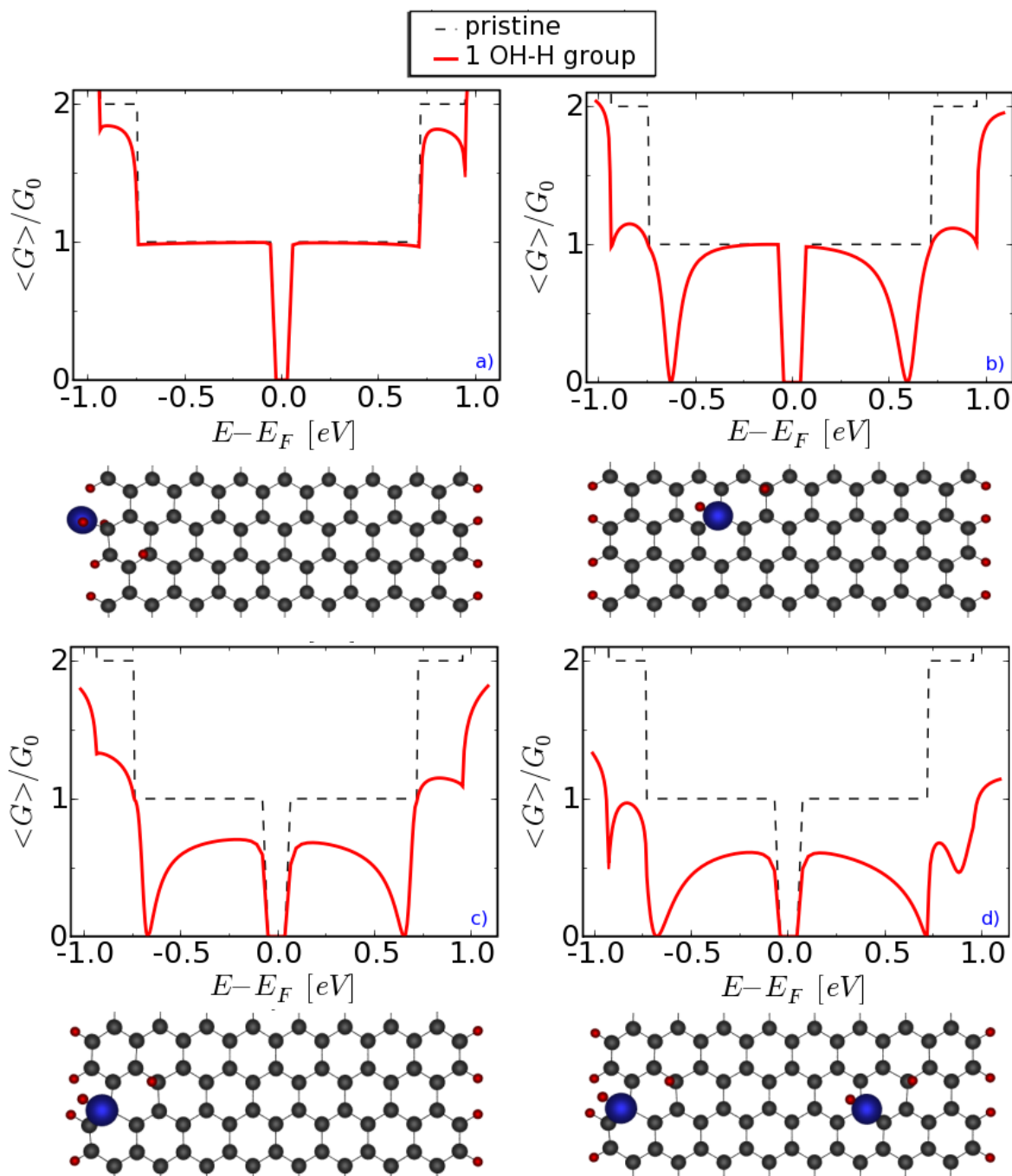


Figure 6.5: Conductance of narrow GNRs - Conductance of a17GNR as a function of defect position. The locations of the defects for a), b), c) and d) are illustrated at bottom. Case d) shows the conductance in case of two defects.

6. COVALENT ATTACHMENT OF FUNCTIONAL GROUPS ON GNRS AND TRANSPORT PROPERTIES

6.4.1 Short channel

For pristine ribbons, the electronic conductance is quantized $G = N_{\perp} G_0$, where N_{\perp} is the number of active transverse modes available at the considered energy. Close to charge neutrality point, a single degenerated band is found in the first conductance plateau ($N_{\perp} = 1$).

Spin polarized calculations within LSDA were also performed to check the multiplicity of the ground state. For the a17GNR the triplet state ($S=1$) is found to be 240 meV above the singlet state ($S=0$), meaning that the presence of structural defects does not introduce higher multiplicity. Fig.6.4 (inset) and Fig.6.5 show the effect of a single pair of hydroxyl (OH) and hydrogen (H) groups on the conductance of the a17GNR at different positions along the nanoribbon width. The main effect of the defect is to induce zero conductance dips at two energies at both sides of the charge neutrality point. This is a clear signature of the sp^3 nature of the bonding as evidenced by the comparison with the phenyl signature on the same system (see Fig.6.4 dashed lines).

A small electron-hole transport asymmetry is observed for the case of hydroxyl-hydrogen pair. It is likely to result from the asymmetric charge distribution around the new bonds between the grafted groups and the GNR substrate, while for the case of two phenyl groups no such asymmetry is observed, as both bonds are equivalent. Note that our calculations on phenyl interaction with GNRS show that there is no direct doping from the phenyl groups to the graphene material, which support the interpretation in (181) of a contact-induced doping effect driven by functionalization. For higher energy subbands, the impact of the single defect is enhanced due to the increase of backscattering probability, as also found for less realistic disorder potentials (192). One also notes that the influence of the asymmetry on backscattering is slightly more pronounced at higher energies.

The dependence of the a17GNR conductance as a function of the defect position is illustrated in Fig.6.5 for a set of typical configurations. If the C-OH bond is located at the GNR edge, a full suppression of backscattering is obtained in the first plateau (Fig.6.5-a), although some weak backscattering is seen for higher energy subbands. As discussed in ref.(193) for NH_2 , edge functionalization does not alter the electronic properties of the aGNR in the first subband since the impurity states are located far away from the Fermi level. In contrast, when the C-OH bond is shifted out of the edge line, the conductance is typically disturbed as shown in Fig.6.5-b or in Fig.6.5-c. Fig.6.5-b (see also Fig.6.4) shows similarity with the situation for pair of grafted phenyls, whereas other locations (Fig.6.5-c) exhibit a larger suppression of conductance in the first plateau, although higher energy subbands remain similarly affected. Such peculiar behavior of conductance depending on the OH/H pair location stems from the variation of screening effects that profile the precise scattering potential.

Fig.6.4-right shows how the conductance is suppressed as the number of defects is increased along the width of a short ribbon channel. In this case, the blue line corresponds to 3 OH/H pairs. This result is in agreement with the general statement of the Quantum Mechanics about the ondulatory nature of electron. The conductance decay is driven by backscattering on individual functional groups together with quantum interferences that occur due to the proximity of the defects.

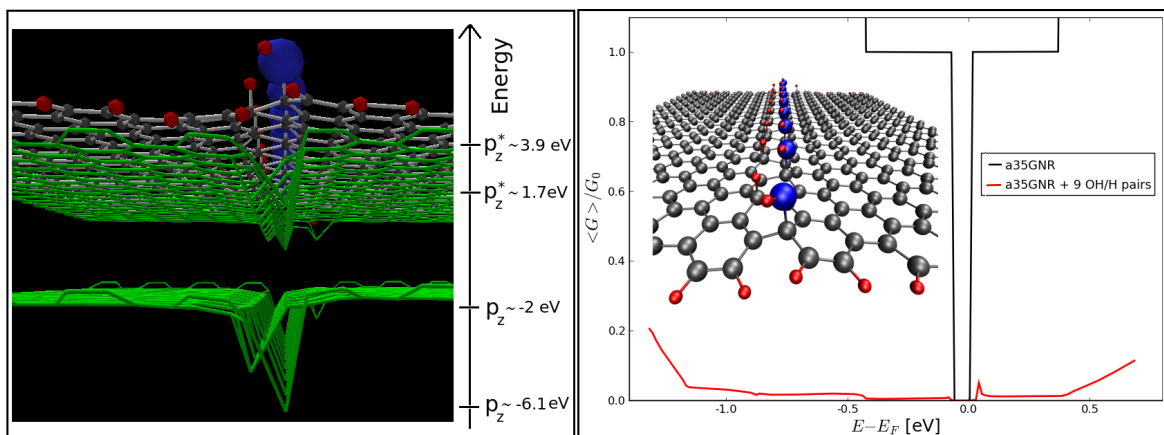


Figure 6.6: sp^3 -barrier - In left panel, the onsite energies of carbon atom p_z and p_z^* orbitals extracted from a SIESTA simulation are plotted. A potential well is created along the line where functional groups are grafted to the nanoribbon, leading to a conductance drop for the range of energies shown in right panel. The lowest values for the onsite energies of p_z and p_z^* orbitals indicated on the left panel correspond to the carbon atoms to which OH group are grafted. The highest ones correspond to unperturbed carbon atoms.

As example of the effect of covalent bonding of functional groups in transmission capabilities of GNRs, we show the ideal case of a line of OH/H pairs grafted along a nanoribbon width. By attaching 9 OH/H pairs as shown in Fig.6.6 the conductance of the ribbon is fully suppressed up to high energy. No single p_z -orbital is available along the line for regular coherent electron conduction and the contribution to the transmission through the potential barrier is based on tunneling effect. This shows that a single defect-line is enough to transform the ribbon to an insulating material.

6.4.2 Long channel

We further explore the conduction regime in long and disordered chemically functionalized aGNRs by computing configuration averaged conductance for aGNRs with varying defect density, length and width. No more than one grafted OH/H pair along the same line perpendicular to the nanoribbon axis. As randomness is introduced in the defect distribution, both backscattering and quantum interferences are strongly enhanced, and ultimately lead to strong localization of states and full suppression of conductance.

The results obtained for the small-gaps a17GNR and a35GNR (6.7 left panel) are here compared with the other types of semiconducting GNRs (a16GNR and a34GNR) which display initially larger energy bandgaps (6.7 right panel). Fig.6.7 (left) shows how the average conductance of a17GNR and a35GNR decays, when doubling the defect density (from 25 to 50 groups for a 200 nm long ribbon), or when increasing the length at a fixed density (from 200 to 600 nm). One notices a larger robustness of the conductance in the first plateau

6. COVALENT ATTACHMENT OF FUNCTIONAL GROUPS ON GNRS AND TRANSPORT PROPERTIES

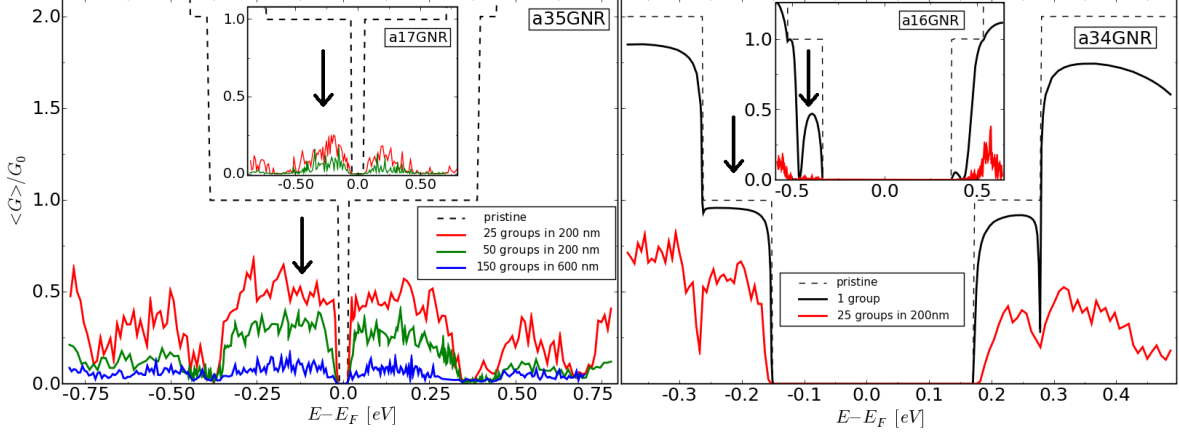


Figure 6.7: Averaged conductance - Left panel: averaged conductance of the a35GNR and the a17GNR (inset) (in G_0 units) for different numbers of grafted groups and ribbon lengths. Right panel: same information for a34GNR and a16GNR (inset). Dashed lines give the conductance for the pristine cases.

when compared with higher energy subbands, similarly to the single defect case (Fig.6.4,6.5), but more pronounced for long disordered systems. This feature has been already observed for model disorder (192), and stems from the linear dispersion of excitations and pseudospin symmetry. This is clearly not the case for semiconducting armchair graphene ribbons a16GNR and a34GNR. As illustrated in 6.7 (right-panel), the difference of the quantum transmission observed for a single OH-H defect between the a16GNR and the a35GNR, further develops as the number of attached molecules is increased. This results in a superimposed transport gap that widens the initial electronic bandgap. This phenomenon has been already discussed for edge defects (194; 195; 196) and is related to the enhanced contribution of quantum interferences that yield localization of states and insulating regime. This transport gap widens as the ribbon is further narrowed (for a fixed number of grafted groups) as shown in Fig.6.7 (right panel-inset).

To further contrast transport properties of different ribbons, the conductance scaling behavior is analyzed at a fixed energy (marked with arrows in Fig.6.7) in Fig.6.8. By using the formula $\langle G \rangle / G_0 = N_{\perp} (1 + \frac{L}{\ell_e})^{-1}$ (where $\langle G \rangle$ denotes the average over 200 random defect configurations), one can infer the corresponding elastic mean free path (ℓ_e) that drives the scaling behavior. For the a35GNR, ℓ_e downscals from $\sim 1 \mu\text{m}$ to $\sim 200 \text{ nm}$, as the number of attached groups varies from 25 to 100. Since $\ell_e \geq L$ (L the channel length = 200 nm), the conduction mechanism is consistent with a quasiballistic regime. Similar behavior is found for the a34GNR for which ℓ_e decays from 850 nm to 260 nm for the same change in defect density. In contrast, for the a17GNR (resp. the a16GNR), ℓ_e decreases from 275 nm to 35 nm (resp. 20 to 10 nm), such that $\ell_e \ll L$, outlining that the electronic states are strongly localized along the ribbon channel. This is further confirmed by an exponential decay of the

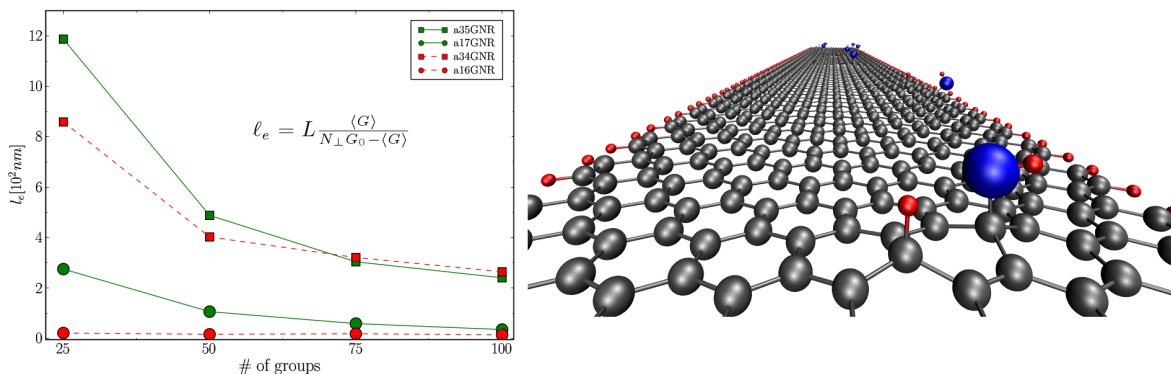


Figure 6.8: Mean free path in functionalized GNRs - Left: elastic mean free path as a function of number of attached pair OH-H defects for various graphene nanoribbons. The inset shows the formula that gives the mean free path from the conductance average. Right: picture of a given disorder configuration. The ribbon channel length is here $L = 200$ nm

conductance versus ribbon length (not shown here).

6.5 Conclusions

In conclusion, by using a fully ab initio approach, we have analyzed the sensitivity of charge transport with respect to OH-H and phenyl pair defects attached to a graphene nanoribbon surface. The joint attachment of hydroxyl and hydrogen groups induces atomic orbital rearrangement from sp^2 to sp^3 hybridization. The bonding nature of these defects onto graphene gives rise to strongly energy-dependent backscattering phenomena, with conductance pattern that are dependent on the functionalization sites. Results show a rapid decay of the conduction ability of armchair GNRs with increasing defect density and when reducing transport dimensionality. For armchair GNRs with initial large energy gaps, a superimposed functionalization-induced transport gap develops close to the band edges and, at a fixed coverage density, widens with decreasing ribbon width or increasing ribbon length. The possible presence of intrinsic defects on the GNRs such as vacancies, edge defects, etc. would also impact on the hydrogenation and functionalization processes with obvious consequences on the transport mechanisms.

6. COVALENT ATTACHMENT OF FUNCTIONAL GROUPS ON GNRS AND TRANSPORT PROPERTIES

Chapter 7

Edge Chemical Reactivity of GNRs and Transport Properties

*“Si querés que te dé una respuesta coherente
debés formularme una pregunta con sentido.”*

Luis Foà Torres

Chapter résumé (French version)

Ce chapitre présente la première étude ab initio du transport électronique dans des rubans de graphène avec des profils de bords reconstruits (et donc réalistes), prenant en compte différents degrés de passivation à l'hydrogène des bords hautement réactifs chimiquement. Notre méthodologie numérique habituelle, basée sur les premiers principes et sur techniques d'ordre N pour la structure électronique et le calcul du transport, est combinée ici avec un modèle de liaisons fortes reparamétrisé, ce qui nous permet d'explorer les propriétés de transport au niveau mésoscopique (pour des systèmes de longueur micrométrique).

Chapter résumé (Spanish version)

Este capítulo trata sobre el estudio ab initio de transporte electrónico de nanoribbons de grafeno con reconstrucción de bordes, tomando en cuenta diferentes grados de pasivación por hidrógeno de bordes con reactividad química alta. Nuestra habitual metodología computacional basada en técnicas de primeros principios y métodos de orden N para la determinación de la estructura electrónica y cálculos de transporte, es combinada ahora con un modelo tight-binding

7. EDGE CHEMICAL REACTIVITY OF GNRS AND TRANSPORT PROPERTIES

reparametrizado, lo que nos permite explorar propiedades de transporte a escala mesoscópica, esto es, sistemas con longitudes superiores al microméetro.

Chapter résumé (English version)

This chapter presents the first *ab initio* electron transport study of graphene ribbons with reconstructed edge profiles, taking into account different degrees of hydrogen passivation of highly chemically reactive edges. Our usual computational tools based on first principles and N-order method techniques for electronic structure and transport calculation, is here combined with a reparameterized tight-binding model, which allows us to explore transport properties at the mesoscopic level (for micrometer long systems).

Our results bring a significant advance in the field of quantum transport on nanoribbons by highlighting the deep influence that edge reconstructions might have on their electronic and transport properties. This should also affect the performances graphene based transistors and applications.

7.1 Introduction

When a sheet of graphene is cut along a given direction, the resulting structure is named graphene nanoribbon, which can exhibit several edge shapes (200). Unlike carbon nanotubes, graphene nanoribbons present a flat hexagon network featured with the presence of open edges with mainly two well-defined and stable geometries: zigzag and armchair. A recent high resolution transmission electron microscope measurement has confirmed the complexity of graphene edge geometries (197), whereas first principles calculations have discussed the edge defects stability and specific topologies (198). To date, the understanding of the consequences of such structural imperfections on charge transport remains to be established. In this work, we show the impact of irregular geometries on charge transport in long armchair nanoribbons and for different degrees of defect hydrogenation.

As illustrated in Chapter 2, graphene nanoribbons (GNRs) are strips of graphene with widths varying from a few to several hundreds of nanometers (201), presenting a particular interest for the development of carbon-based nanoelectronics (202; 203). Notwithstanding, in contrast to carbon nanotubes, GNRs exhibit a high degree of edge chemical reactivity, which, for instance, prevents the existence of truly metallic nanoribbons (204). Additionally, the discrepancy between the theoretical electronic confinement gap and the experimentally measured transport gap (202) has been attributed to localized states induced by edge disorder (205).

So far, most transport studies of edge disordered GNRs have assumed simplified defect topologies (205). However, recent *ab initio* calculations have unveiled a much larger complexity of edge reconstructions and edge chemistry (206). Several experimental studies have also reported the characterization of individual edge defects by means of Raman, scanning tunneling and transmission electron microscopies (209). Finally, the control of monoatomic hydrogen deposition on graphene surface has revealed the possibility to tune a metal-insulator

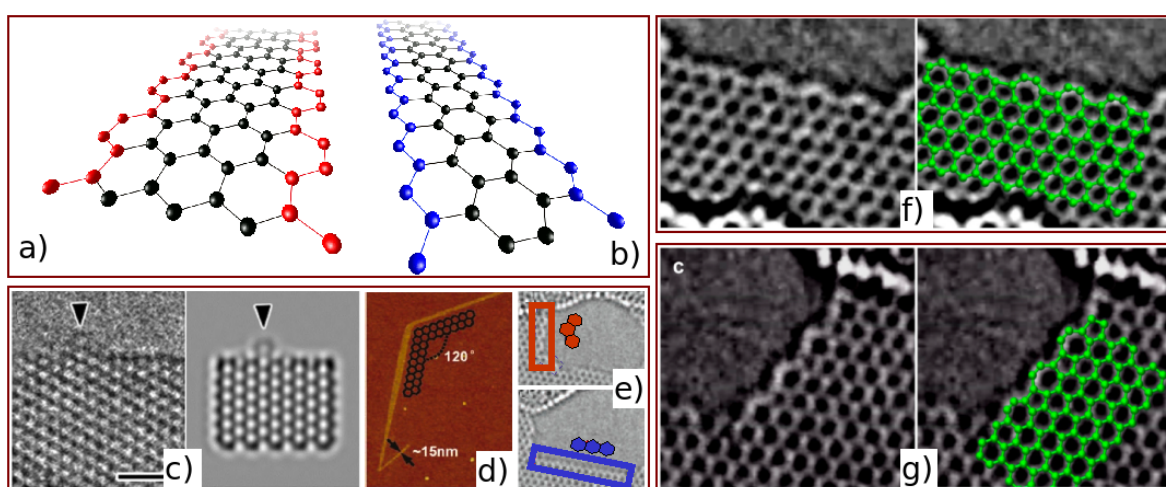


Figure 7.1: aGNR edges - Representation of two non hydrogenated armchair (a) and zigzag (b) GNRs. Red and blue atoms show off the characteristic armchair-shaped and zigzag-shape, respectively. c) High resolution transmission electron microscope image of an aGNRs with an isolated benzenoid-type defect in the edge (from Ref. (197)). This edge-defect reconstruction and transport properties of the ribbon have been simulated, as shown in 7.4-c) and -d), for the hydrogenated case. In d), an AFM image shows a long zigzag-shaped GNR (from (207)). In e) an aberration-corrected image of nanographene with armchair and zigzag defected structures (from (208)). In f) and in g), non-hydrogenated heptagon-type defects are shown in zigzag-shaped nanographene.

7. EDGE CHEMICAL REACTIVITY OF GNRS AND TRANSPORT PROPERTIES

transition (210). Accordingly, it is of great importance to investigate the impact of realistic edge defect topologies and the role of hydrogenation on charge transport properties of long and disordered GNRs.

Here we focus on charge transport properties in armchair GNRs (aGNRs). It turns out that these properties strongly depend on the geometry of the reconstructed edge profile and local defect chemical reactivity. Indeed, depending on edge reconstruction type, the effect of single edge defects is found to range from a suppression of either hole or electron conduction to a vanishing contribution to backscattering.

Additionally, based on the derivation of a suited tight-binding model, mesoscopic transport calculations of disordered ribbons with lengths up to several microns are achieved, and conduction is found to change from metallic to insulating regime depending on the geometry and density of edge defects.

This chapter describes in details the work presented in the paper *Quantum Transport in Graphene Nanoribbons : Effects of Edge Reconstruction and Chemical Reactivity*. It was carried out in close collaboration with the group of Professor Jean-Christophe Charlier from the University of Louvain-La-Neuve (Belgium). *ab initio* calculations on nanoribbons with a single defects were mostly performed at Louvain, whereas the mesoscopic transport study (both at a first principles level and tight-binding level) was conducted at CEA-Grenoble.

7.2 Defect description

Following the nomenclature detailed in the previous chapter, we refer to an aGNR made up by N dimers lines as an N -aGNR. We have focused on the 35-aGNR, with a width of 4.2 nm, but our conclusions remain valid for wider aGNRs. 3 nm long supercells have been considered in order to limit the spurious interaction between defects introduced by periodic boundary conditions.

In Fig.7.2 the defects which are treated in this study are shown in detail. D1-defect is the pentagonal-type defect resulting from a single carbon atom removal from the original hexagonal network and subsequent geometrical optimization. D2-defect represent a heptagon-type defect obtained upon inclusion of an extra carbon atom in the pristine aGNR. The creation of two heptagons in D3-defect involves four extra carbon atoms and the formation of an inner-pentagon to the ribbon. D4-defect is created by removing two-edge carbon atom from the original structure.

D1H and D2H are obtained following the same procedure than for D1 and D2 but with 2 hydrogen atoms passivating the radical which appears after pentagon-type or heptagon-type defect creation.

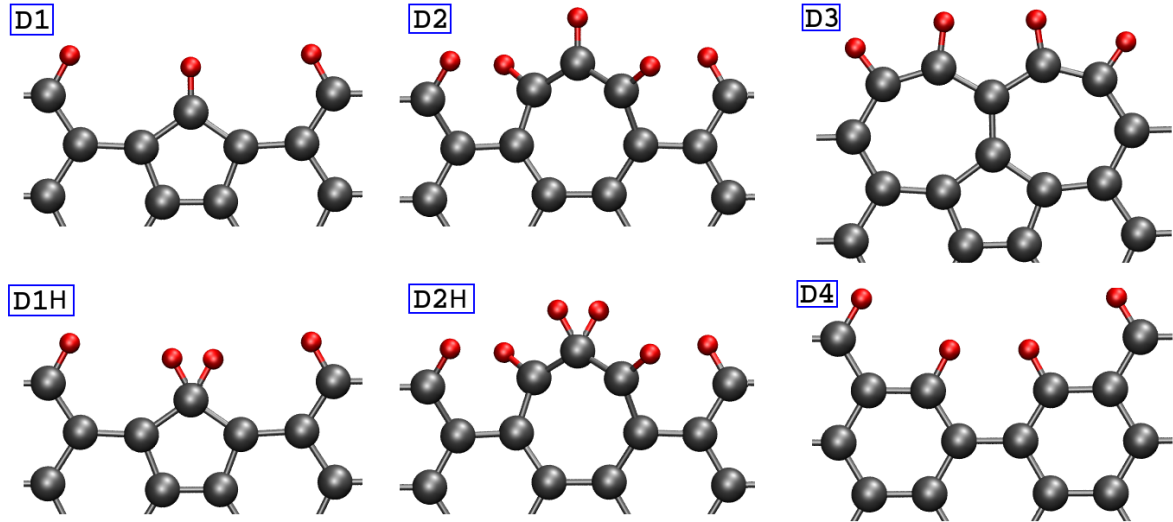


Figure 7.2: Detail of aGNR defects - A detailed representation of the armchair graphene nanoribbon defects studied in this work is given. The doubly-hydrogenated carbon atoms in heptagon-type and pentagon-type defects are obtained from the single-hydrogenation defect to passivate the radical which is created upon GNR pristine structure modification.

7.3 Ab initio transport study

The presence of (mono-hydrogenated) edge defects produces backscattering of propagating electrons, which is reflected in a reduced transmission coefficient. Among all the different studied defects, the reconstructed geometries that preserve the benzenoid structure turn out to weakly impact on the transmission, as exemplified in the conductance profile of the D4 defect (see Fig.7.3-e)). The conductance remains very close to its maximum quantized value as found in the pristine (clean) case, with weak backscattering mainly observed in higher subbands. Slightly different is the case of the double heptagon-type plus single pentagon-type defect (D3) exhibits two conductance suppression dips, as shown in Fig.7.3-d), symmetric with respect to the charge neutrality point, thus reminding the conductance drops observed in the case of functionalized nanoribbons (see Fig.6.4 in chapter 6). Other topologies preserving the benzenoid structure (see Fig.7.4) yield very similar results to those of the pristine nanoribbons. Only for higher subbands a conductance drop is observed while for energies close to the charge neutrality point the transmission remains unaltered.

However, in large contrast, edge defects containing odd-membered rings convey much stronger backscattering efficiency. Conductance fingerprints for single reconstructed pentagon-type and heptagon-type defects are shown in Fig.7.3-a) and -b), respectively. Interestingly, a marked acceptor (donor) character develops for the pentagon-type (heptagon-type) defect, as evidenced by the strong electron-hole conductance asymmetry. Such an effect, already observed in nanotubes junctions (212), is clearly due to the charge transfer taking place in

7. EDGE CHEMICAL REACTIVITY OF GNRS AND TRANSPORT PROPERTIES

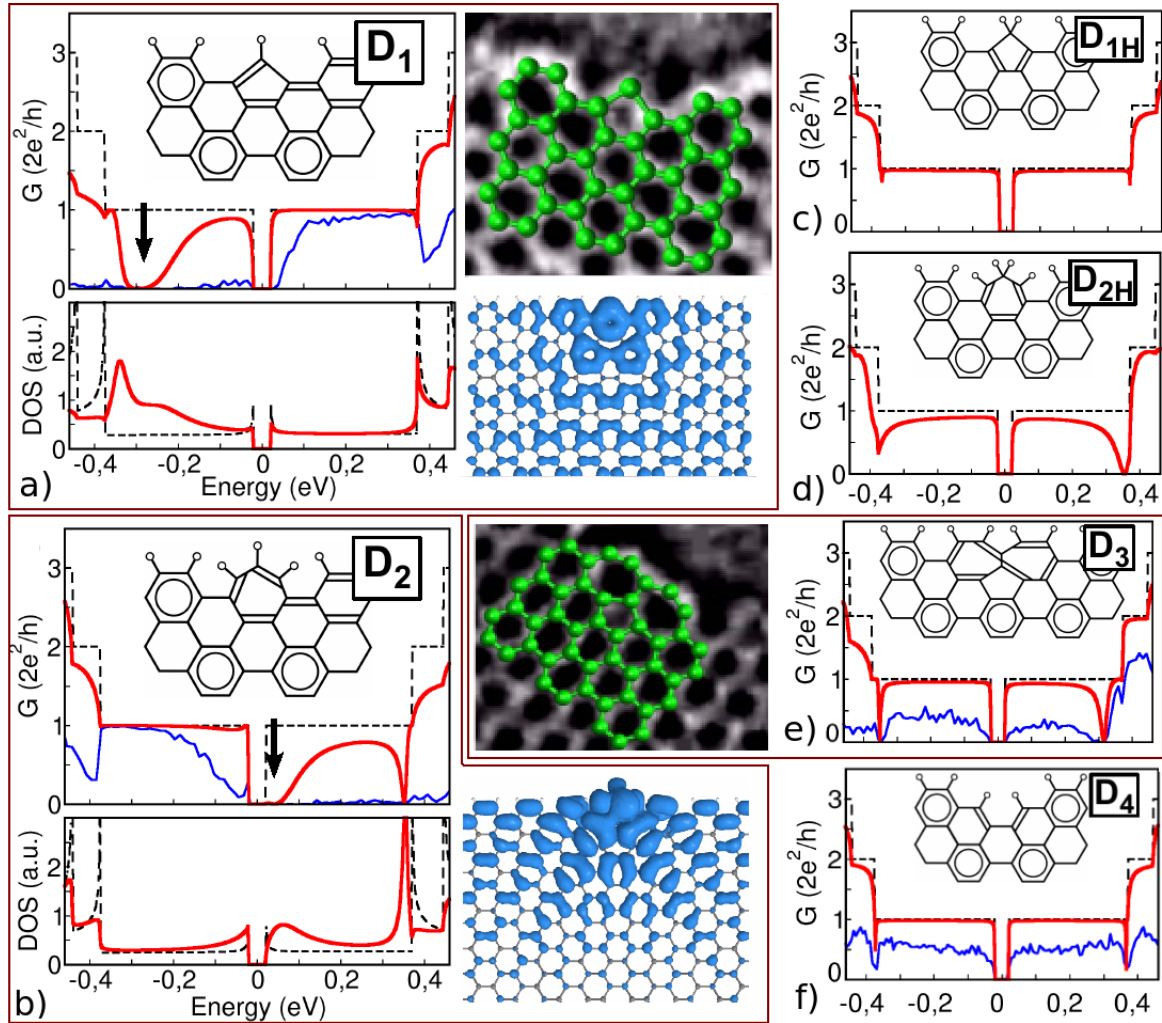


Figure 7.3: Conductance profiles of defected edges - Conductance profiles of 35-aGNR for six different edge geometries: pristine ribbon (dashed black lines), single defect (red lines), and average conductance for 500 nm long aGNRs containing 30 defects (blue lines). Total DoS for pristine (dashed lines), and D1 and D2 are also shown in lower-left figures in a) and b). In c) and d) it is shown that radical passivation by means of pentagon- and heptagon-type defects di-hydrogenation, re-establish conductance profile in the former case and partially in the last one. D1H and D2H denote the di-hydrogenated pentagon and heptagon, respectively. Edge defect topologies containing odd-membered rings are also shown in a) for a single pentagon defect, D1, and e) 2 heptagons and 1 pentagon defect, D3. (from (206)) f) panel shows the small-hole defect due to a dimer extraction, D4. In a) and e), spatial representation of the transmission eigenchannel is plotted at the energy marked by an arrow in their respective conductance profile figures. In all cases, Clar's sextet representation for each edge geometry.

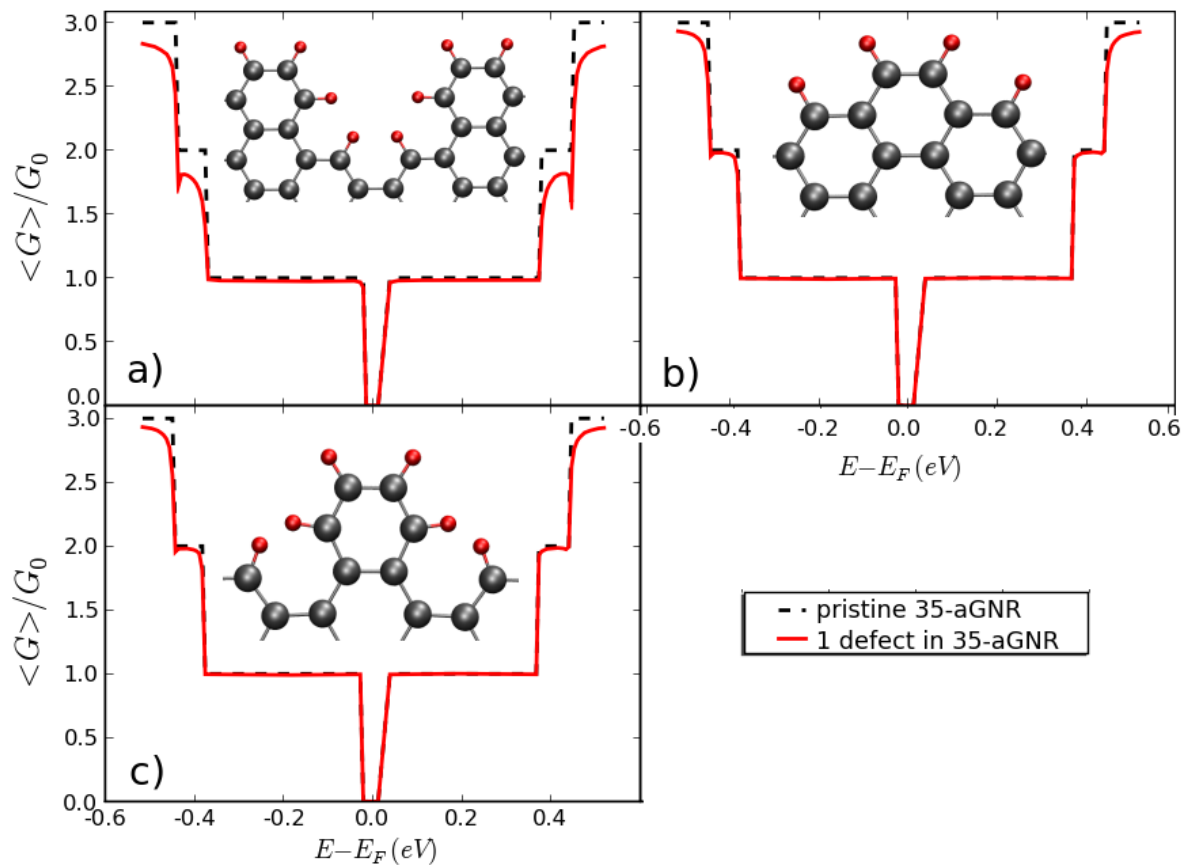


Figure 7.4: Conductance for benzenoid structures. - For configurations of armchair nanoribbons in which the original hexagonal structure is preserved upon addition or removal of an even-number carbon atoms, no conductance perturbation is observed. These four cases correspond to a slightly lateral widening (b,c) or narrowing of the ribbon (a). Notice that c) configuration coincide with HR-TEM observed geometry in (197), as shown in Fig.7.1

7. EDGE CHEMICAL REACTIVITY OF GNRS AND TRANSPORT PROPERTIES

the $\pi - \pi^*$ bands when odd-membered rings are embedded in a perfect hexagonal network. A slight excess of π -electrons is found on the pentagonal ring and a small electron deficit on the heptagon ring. For both cases, the total and local densities of states have been computed (shown for D1 and D2 in Fig.7.3), and reveal the energy position of quasibound states which are responsible for the conductance drops (214). The charge density contour plot shows the electronic state incident from the left and totally reflected by the quasibound state at the energy indicated by an arrow in Fig.7.3-b). While the reported charge transfer in the presence of pentagon-type and heptagon-type defects is a general mechanism, the broadening of conductance dips due to quasibound states is expected to narrow with increase of the ribbon width. We thus forecast the intensity of the observed electron-hole conductance asymmetry to depend on the actual ribbon size.

Summarizing, five-membered rings (D1) are attractive (acceptor character), seven-membered rings (D2) are repulsive of electrons (donor character) (213), and even-membered rings (D3, D4) are predicted to be neutral in a planar hexagonal network. In the odd-membered ring, the intrinsic doping effect can be attributed to the presence of a radical, i.e. delocalized electron, which alters the π -conjugation equilibrium of the original lattice and favors the predicted electron backscattering phenomena. It is logical to ask, “Would the conductance be re-established if this unpaired electron is further passivated by a hydrogen atom”?

The high chemical reactivity of defects such as D1 and D2 is further explored by assuming a dihydrogenation of the carbon atom sitting at the edge. Resulting conductance profiles for the new defects D1H (Fig.7.3-e)) and D2H (Fig.7.3-f)) strongly differ from the mono-hydrogenated cases, D1 and D2. Indeed, in the presence of additional passivation, the conductance is fully restored for D1H whereas the signature for D2H becomes similar to that of D3. In both cases, the initial strong reduction of electron or hole conductance is markedly suppressed. This clearly suggests a possibility to tune the transport properties from a metallic to a truly insulating state, or vice versa, upon varying the coverage of monoatomic hydrogen, as recently discussed experimentally for 2D graphene (210).

The Clar’s sextet representation (215) (Fig.7.3-insets) provides a pictorial scheme to understand the impact of edge defects (216) on the transport properties. Indeed, for the defects D1 and D2, the bonding at the edge of aGNRs can be seen as the superposition of two mirroring Kekulé structures that partially destroy the benzenoid character of the aGNRs (Figs.7.3-a) and 7.3-b). By increasing the localization of π -electrons in carbon-carbon double bonds, such defects destroy the local conjugation at the ribbon edge and are thus expected to have a large effect on the π - π^* conduction channels. On the contrary, the dihydrogenation of defects D1 and D2 restores the complete benzenoid character of the ribbon as illustrated by Clar’s sextet representations (Figs.7.3-e) and 7.3-f).

To further substantiate the effect of these topological defects on the mesoscopic transport properties, one needs to explore the behavior of long disordered aGNRs with random distribution of edge defects.

In Fig.7.3, the conductance of the 500 nm long disordered aGNRs containing 30 defects (blue lines) are superimposed to the single defect results (red lines). Computed conductances are averaged over 20 different disorder configurations. The original conductance fingerprints

of the considered defects are further exacerbated when longitudinal disorder is introduced, resulting for D1 (D2) in an almost fully suppressed hole (electron) conduction for low defect density.

7.4 Tight-binding transport study

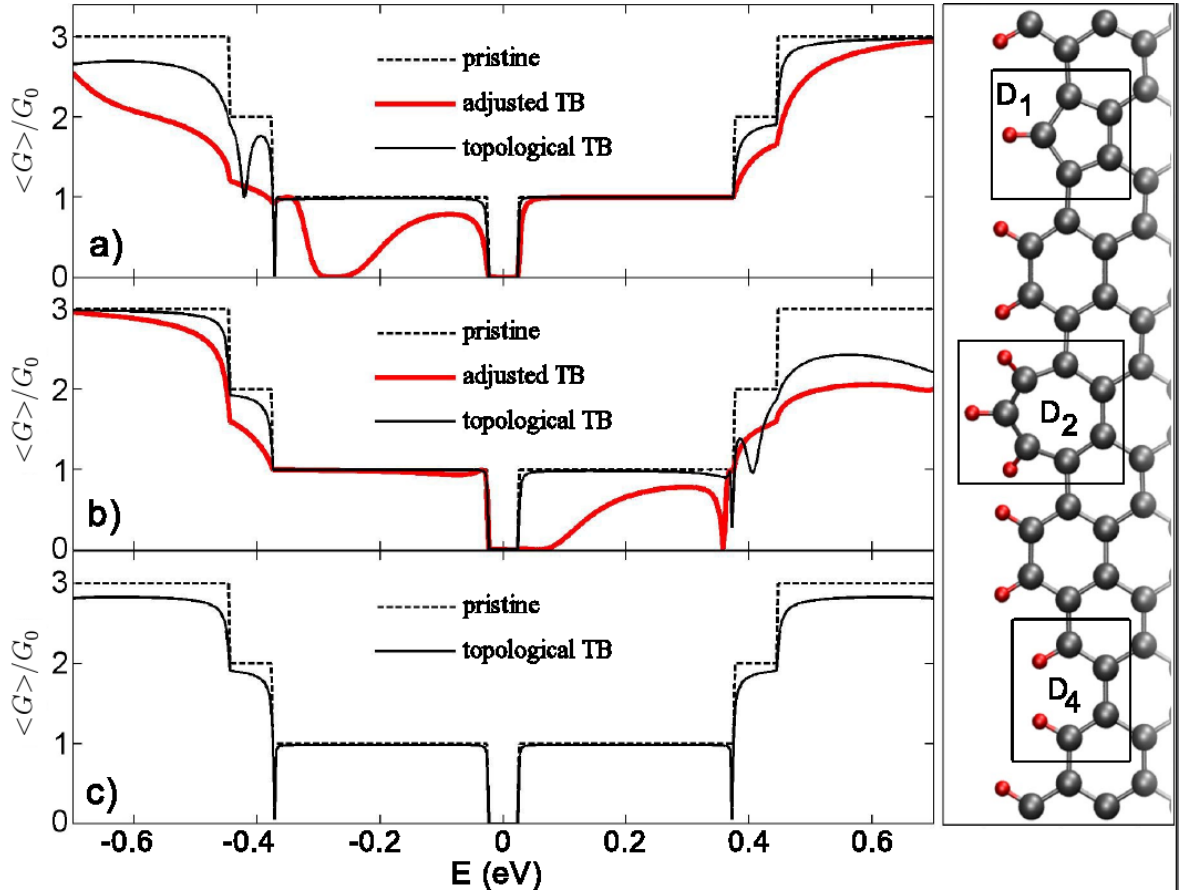


Figure 7.5: Tight-binding model. - Conductance of a single defect obtained by the simple topological TB Hamiltonian (solid line) and by the adjusted TB Hamiltonian (red line) for D1 (top) D2 (middle) and D4 (bottom). Graphical representation of the defects are illustrated in the right panel.

Ab initio transport calculations are highly computationally demanding and the elaboration of an accurate TB model is therefore extremely useful for achieving a complete mesoscopic study. One could use a simple topological n-n TB Hamiltonian, with a limited amount of parameters (one on-site energy per carbon site) and nearest neighbor couplings depending on

7. EDGE CHEMICAL REACTIVITY OF GNRS AND TRANSPORT PROPERTIES

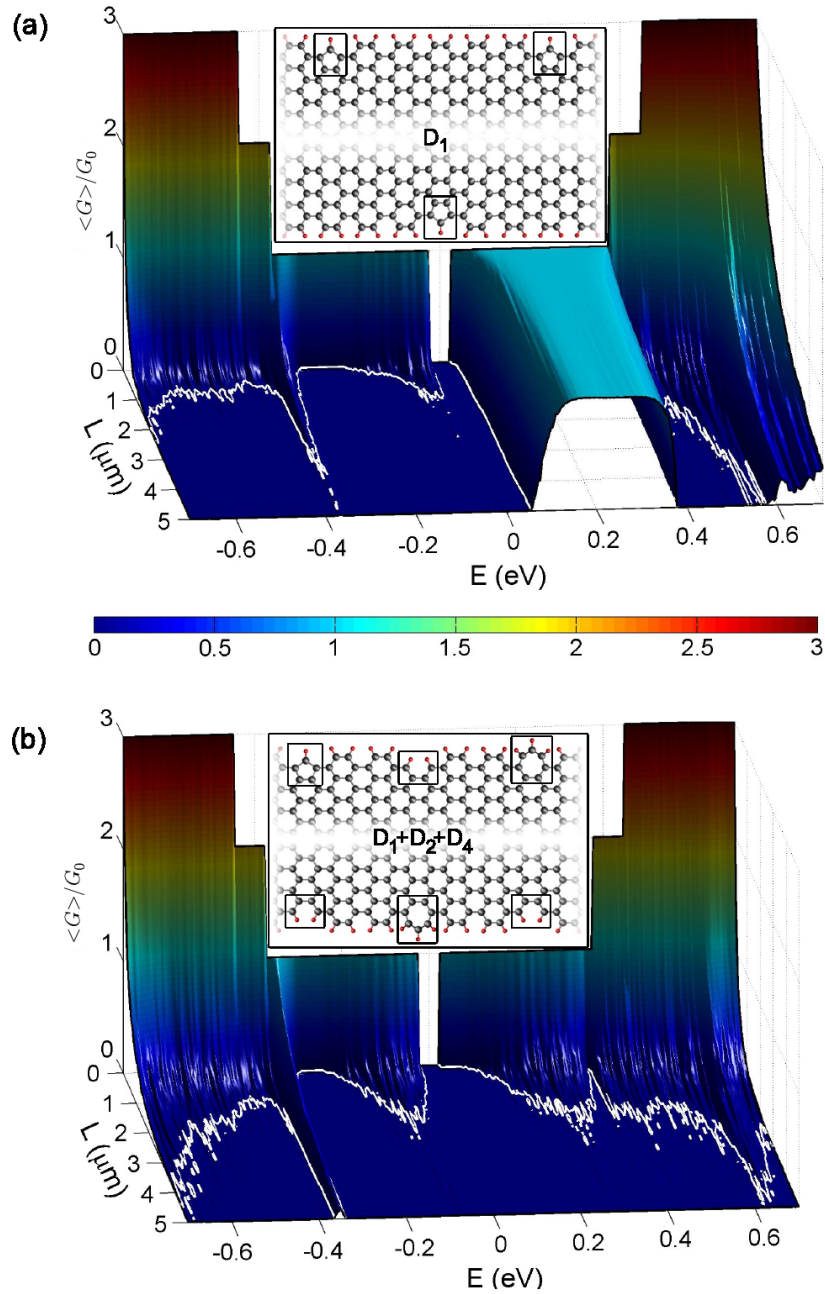


Figure 7.6: Micrometer long GNRs conductance within TB scheme - a) Average conductance $G(L, E)$ as a function of the energy E and the length L of a 35-aGNR with a $6 \times 10^{-2} \text{nm}^{-1}$ density of D1-defects, b) mix of three types of defects (see inset). The white lines delineate the (L, E) regions for which the conductance value $G \leq 0.01 G_0$ (criterion for the experimental conduction gap (202)).

the bond connectivity. However, when compared to *ab initio* results, this turns out to yield a wrong description of transport properties in the case of non-neutral defects. Fig.7.5 shows the conductance profiles for three different defects (D1, D2, and D4) using the topological TB model (black solid lines). If the agreement is good for the D4 defect, a strong discrepancy is found for D1 and D2 defects, when compared to *ab initio* results. In these cases, the topological model leads to a severe underestimation of the backscattering efficiency. However, it is possible to extract renormalized on-site energies from the full *ab initio* Hamiltonian, and to adjust such values in order to reproduce the *ab initio* transport calculation (see Fig.7.6-red lines and Fig.7.3-a) and -b)).

With such an adjusted TB model, the conductance properties of disordered aGNRs are investigated by considering lengths varying up to $L=5\ \mu\text{m}$ and random distribution of defects with a density of $6 \times 10^{-2}\ \text{nm}^{-1}$. Fig.7.6 displays the conductance of long disordered aGNRs (averaged over 100 different configurations), as a function of energy and ribbon length. Two different instructive cases are reported, corresponding to (a) a random distribution of D1 defects, and (b) a mix of three types of defects (D1, D2 and D4) for the same edge defect density. The conductance scaling behavior of a pure D1-defected aGNR is rather striking (Fig.7.6-a)). Indeed, ballistic electron transport is maintained up to length as long as $5\ \mu\text{m}$, whereas a localized regime and vanishingly small hole conductance develops for much shorter ribbon length. Estimated hole localization lengths for energies in the first plateau are of the order of a few tens of nanometers, whereas the electron elastic mean free paths in the same energy window are longer than $5\ \mu\text{m}$. Obviously, such disordered edge defect profiles with a single defect type are rather unlikely. However it shows that spectacular fluctuations of transport length scales occur in some specific situations.

A comparison with a more disordered edge profile with random distribution of D1, D2, and D4 is in that perspective instructive (Fig.7.6-b)). The conductance decay becomes now more homogeneous within the first electron and hole plateaus as well as within higher energy subbands. However, the overall features are reminiscent of the initial marked differences between hole and electron conductance profiles related to single D1 and D2 defects. Indeed, for similar energy shifts (in the range of a few tens of meV) with respect to both band edges, hole conduction dominates over electron conduction, as a result from stronger impact of D2 defect at low energy.

Finally, the conduction gaps (defined experimentally as the energy window for which $G(E) \leq 0.01G_0$) are delineated by white lines in the (L, E) -plane in Fig.7.6-a) and -b). Such conduction gaps are driven by defect-induced localization effects, which will thus not only depend on the defect density and ribbon length but also on the geometry and chemical reactivity of edge imperfections.

We note here that the above analysis has been drawn from physical processes that are general in essence. The scope of the results should therefore extent beyond the specific 35-aGNR considered throughout the study.

7. EDGE CHEMICAL REACTIVITY OF GNRS AND TRANSPORT PROPERTIES

7.5 Technical details

Electronic structures of the edge-reconstructed ribbons are computed by means of the density functional theory within the generalized-gradient approximation as implemented in the SIESTA code (87). Atomic orbital basis set of double- ζ quality and norm-conserving pseudo-potentials are used. The integration of the first Brillouin zone is achieved through a summation over a regular grid of 24 k -points. Ribbon geometries are relaxed such as residual forces on atoms become lesser than 0.01 eV/Å. 12 Å of vacuum between GNRS in neighboring cells is taken.

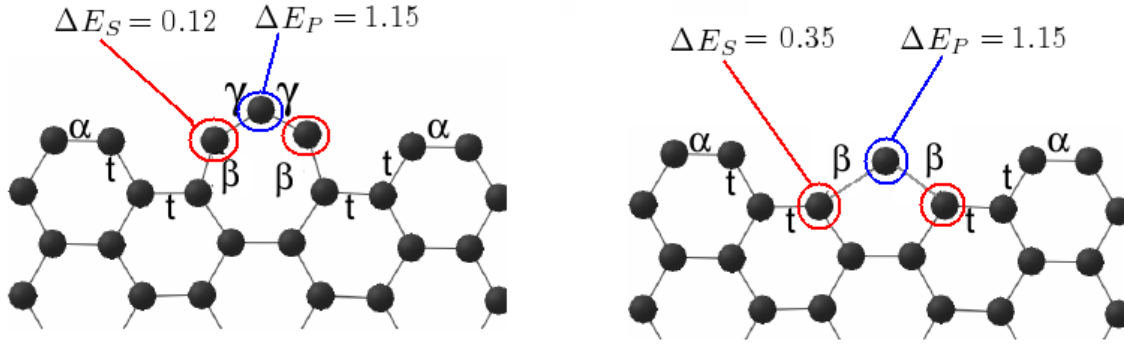


Figure 7.7: Tight-binding parameterization scheme - In this figure the carbon atoms affected by the reparameterization are marked by red and blue lines, depending on the applied on-site energy shift (energies are in eV). The overall coupling term t between nearest neighbouring carbon atoms is modulated by a multiplicative factor in the case of atoms in the edge.

The computation of the mesoscopic electronic conductance of long disordered aGNRs with random distribution of edge defects is performed within the Landauer-Büttiker formalism and implemented at both first principles and tight-binding (TB) levels. In the former case, *ab initio* self-consistent Hamiltonians corresponding to defective supercells are used to build long (≈ 500 nm) aGNRs containing 30 randomly distributed defects. In the latter case, a suited nearest-neighbor (n-n) TB Hamiltonian is derived.

We refer to p_z -orbital as the orbital of a carbon atom which is perpendicular to the flat surface of the GNR. An effective model based on the p_z -orbital on-site energy values of GNR carbon atoms obtained from DFT simulation is suitable for electronic transport properties description of edge defected GNRS. Both pentagon-type and heptagon-type defects can be reparameterized to a simple model in which the p_z -orbital on-site energies of carbon atoms of defected rings are shifted with respect to the rest of carbon atoms in the structure. By $\Delta E_P = 1.15$ eV and $\Delta E_S = 0.12$ eV we denote the shift in energy of the SIESTA-DZ basis p_z -orbital the heptagon-type defect atoms as shown in Fig.7.7, and $\Delta E_S = 0.35$ eV for pentagon-type defect atoms. In addition, coupling terms between pairs of first neighbouring p_z -orbitals obtained from SIESTA calculation need also to be adjusted to reproduce the conductance

curves such as they are calculated from the full *ab initio* Hamiltonian transport calculation. This is done as follows: a homogeneous coupling of $t = -2.7$ is established between nearest neighbouring carbon atoms in the ribbon and, to some of them, a multiplicative factor α, β or γ is applied, as shown in Fig.7.7. For heptagonal ring $\beta = 1$ and $\gamma = 1.1$, and for pentagonal ring $\beta = \gamma = 1$. All t -coupling terms that link carbon atoms along the outter C-C-line parallel to nanoribbon axis are multiplied by $\alpha = 1.12$. This modification with respect to the rest of C-C bonds takes into account the differences between inner and edge carbon atoms of the nanoribbon.

By reducing the computational cost of conductance calculations, this TB technique enables the exploration of conductance scaling properties in disordered ribbons with lengths up to several micrometers.

At zero temperature and in the low bias limit, the conductance is given by $G(E) = G_0 T(E)$, where $T(E)$ denotes the transmission coefficient at a given energy E ($G_0 = 2e^2/h$ is the conductance quantum). Conductance fingerprints of single defects are computed using the SMEAGOL code (211). The defective supercells are connected to perfect aGNR-based leads, and $T(E)$ is evaluated by the approach presented in Chapter 3.

7.6 Conclusions

In conclusion, charge transport properties of edge disordered graphene nanoribbons have been investigated using both fully *ab initio* techniques and accurately parametrized TB models. In this work, we find that the scattering efficiency of the reconstructed defects depends on their topology and degree of hydrogen passivation, and it can range from suppression of hole or electron conduction, to weak backscattering for defects preserving a benzenoid geometry. Single topological defects, such as pentagon-type and heptagon-type defects, are predicted to induce a strong electron-hole transport asymmetry, in contrast to other types of edge reconstructions. Defects conserving the benzenoid structure of the original lattice hardly affect the conduction ability of the ribbon.

Besides, the observed possibility to markedly tune conductance fingerprints of some defects by further hydrogenation could also make a significant step toward overcoming the current limitations of transport in graphene ribbons based devices. For instance, the dihydrogenation of some defects is found to fully restore an otherwise suppressed conductance for the mono-hydrogenated defect cases.

Our results find some resonance with the recent experimental already published (199). In this latter work, the coverage of monoatomic hydrogen grafted on two-dimensional graphene surface was controlled, with the possibility to tune a metal-insulator transition, as deduced from ARPES optical spectroscopy. Similar study on graphene ribbons would bring a better understanding of low dimensional transport.

Our theoretical findings suggest a possible way to circumvent the disadvantages of graphene ribbons, by a controlled passivation of the edges, for achieving unprecedented ballistic transport properties in ribbons with length up to the micron scale. This study is an example of an

7. EDGE CHEMICAL REACTIVITY OF GNRS AND TRANSPORT PROPERTIES

increasing global interest on mixing several scientific knowledge field, since our work unravels fascinating effects stemming from both chemistry and physics complexity at the nanoscale.

Chapter 8

Conclusions

This thesis has explored the transport regimes in chemically functionalized metallic and semiconducting carbon nanotubes by using a fully *ab initio* transport approach. In addition, the same methodology has been applied to the study of edge defects and functional groups in graphene nanoribbons.

By comparing two different and important types of chemical bonding we have assessed the true potential of cycloaddition reactions as a precursor for further enhancement of devices functionalities. For metallic nanotubes, the results evidence good conduction ability in the case of carbene cycloadditions, whereas phenyl addends were found to yield a strongly diffusive regime, with estimated mean free path ranging from a few tens to the nanometer scale, depending on the coverage density and incident electron energy.

In the case of semiconducting CNTs, small diameter functionalized tubes have been shown to preserve good conduction ability, whereas a strongly diffusive regime was obtained for larger diameter tubes, similarly to the effect of a low dihydrogenation density. This effect was explained by the orbital rehybridization of the atoms to which functional groups are attached. Our study quantifies the severe limits of divalent additions in large diameter semiconducting nanotubes, and suggest that smaller diameter sizes nanotubes should be targeted to engineer efficient novel device functionalities.

This demonstrates the non-invasive character of carbene functionalization when compared with phenyl and sp^3 -like functionalization, which preserves good conduction capability of underlying nanotubes, and suggests this type of functionalization as a better option for adding new functionalities to the nanotube-based devices.

Notwithstanding, it must be highlighted the limitations of the study here presented. Typically, scaling analysis are performed with the length of the system L as a variable which is modified. In this way, some useful quantities as the mean free path l_e and localization length ξ can be related to the averaged conductance of a system with a constant impurity rate. Given l_e , ξ different transport regimes can be defined depending on L . In this study, however, the approach has been the opposite: the system length has been fixed to a constant value ($1\mu\text{m}$ for carbene functionalization and $0.3\mu\text{m}$ for phenyl functionalization) and the

8. CONCLUSIONS

impurity rate has been varied. This allows us to extract some useful information about the functionalization possibilities of nanotubes with regard the conservation of their electronic conduction abilities. Although such a system are not completely characterized in terms of relevant quantum transport quantities, these results may be considered of interest interest for a broad scientific community ranging from chemist to engineering.

In the case of graphene nanoribbons, the sensitivity of charge transport with respect to OH-H and phenyl pair defects attached to a graphene nanoribbon surface have been analyzed. The joint attachment of hydroxyl and hydrogen groups induces atomic orbital rearrangement from sp^2 to sp^3 hybridization. The bonding nature of these defects onto graphene gives rise to strongly energy-dependent backscattering phenomena, with conductance pattern that are dependent on the functionalization sites. Results show a rapid decay of the conduction ability of armchair GNRs with increasing defect density and when reducing transport dimensionality. For armchair GNRs with initial large energy gaps, a superimposed functionalization-induced transport gap develops close to the band edges and, at a fixed coverage density, widens with decreasing ribbon width or increasing ribbon length.

Finally, charge transport properties of edge disordered graphene nanoribbons have been investigated using both fully *ab initio* techniques and accurately parametrized TB models. In this work, it has been shown that the scattering efficiency of the reconstructed defects depends on their topology and degree of hydrogen passivation, and it can range from suppression of hole or electron conduction, to weak backscattering for defects preserving a benzenoid geometry. Single topological defects, such as pentagon-type and heptagon-type defects, are predicted to induce a strong electron-hole transport asymmetry, in contrast to other types of edge reconstructions. Defects conserving the benzenoid structure of the original lattice hardly affect the conduction ability of the ribbon.

The possible presence of intrinsic defects on the GNRs such as vacancies, Stone-Wales defects, etc. would also impact on the hydrogenation and functionalization processes with obvious consequences on the transport mechanisms. Futher studies on this field would give a more complete overview of electronic tranport properties in GNRs with defects. As well, an important the incorporation of spin in the numerical simulations should shed light on the electronic transport mechanism of carbon-based systems in the presence of magnetic defects.

Conclusions (French version)

Cette thèse a exploré les régimes de transport dans les nanotubes de carbone métalliques et semi-conducteurs fonctionnalisés, en utilisant une approche de transport complètement *ab initio*. De plus, la même méthodologie a été appliquée pour étudier les défauts de bord et les groupes fonctionnels dans les nanorubans de graphène.

En comparant deux types de liaison chimique différents et importants, nous avons évaluer le véritable potentiel des réactions de cycloaddition comme précurseur pour l'amélioration des fonctionnalités des dispositifs. Pour les nanotubes métalliques, les résultats montrent clairement une bonne conduction dans le cas des cycloadditions de carbène, tandis que les groupes

phényl entraînent un régime fortement diffusif, avec un libre parcours moyen estimé allant de quelques dizaines de nanomètres à l'échelle du nanomètre selon la densité de couverture et l'énergie de l'électron incident.

Dans le cas des nanotubes semi-conducteurs, nous avons montré que les nanotubes fonctionnalisés de petit diamètre conservent une bonne capacité de conduction, tandis qu'un régime fortement diffusif est obtenu pour les nanotubes de grand diamètre, de manière comparable à l'effet d'une dihydrogénation de faible densité. Cet effet a été expliqué par la re-hybridation orbitale des atomes auxquels les groupes fonctionnels sont attachés. Notre étude quantifie les limites sévères des additions divalentes dans les nanotubes semi-conducteurs de grand diamètre, et suggèrent que les nanotubes de plus petit diamètres devraient être envisagés pour concevoir des dispositifs efficaces ayant de nouvelles fonctionnalités.

Cela démontre le caractère non-invasif de la fonctionnalisation carbène par rapport à la fonctionnalisation phényl et de type sp^3 . La première préserve la bonne conduction des nanotubes, ce qui en fait une meilleure option pour ajouter de nouvelles fonctionnalités aux dispositifs à base de nanotubes.

Cependant, les limitations de l'étude présentée ici doivent être soulignées. Habituellement, les analyses de lois d'échelle sont effectuées en considérant la longueur L du système comme une variable. Ainsi, des quantités utiles telles que le libre parcours moyen l_e et la longueur de localisation ξ peuvent être reliés à la conductance moyenne d'un système avec un taux d'impuretés constant. Etant donné l_e et ξ , différents régimes de transport peuvent être définis selon la valeur de L . Dans cette étude, l'approche a été inverse : la longueur du système a été fixée ($1\mu\text{m}$ pour la fonctionnalisation carbène et $0.3\mu\text{m}$ pour la fonctionnalisation phényl) et on a fait varier le taux d'impuretés. Cela nous permet d'extraire des informations utiles sur les possibilités de fonctionnalisation des nanotubes, au regard de la conservation de leurs propriétés de conduction électrique. Bien qu'un tel système ne soit pas entièrement caractérisé en termes des grandeurs pertinentes du transport quantique, ces résultats peuvent intéresser une communauté scientifique large allant des chimistes aux ingénieurs.

Dans le cas des nanorubans de graphène, la sensibilité du transport de charge à des défauts OH-H et bi-phényls attachés à la surface du ruban a été analysée. Le greffage conjoint de groupes hydroxyle et hydrogène induit des réarrangements des orbitales atomiques de l'hybridation sp^2 vers l'hybridation sp^3 . La nature des liaisons de ces défauts sur le graphène induit des phénomènes de rétrodiffusion fortement dépendants de l'énergie, avec des profils de conductance qui dépendent des sites de fonctionnalisation. Les résultats montrent une dégradation rapide de la conductance des rubans armchair quand la densité de défauts augmente et quand la dimensionnalité du transport diminue. Pour les rubans armchair avec de grands gaps d'énergie initiaux, un gap additionnel de mobilité induit par la fonctionnalisation se développe près des bords de bande et s'élargit lorsqu'on diminue la largeur du ruban ou qu'on augmente sa longueur, à densité de greffage fixée.

Enfin, les propriétés de transport de charge des nanorubans de graphène avec des défauts de bord ont été étudiées, en utilisant des techniques complètement *ab initio* et des modèles de liaisons fortes paramétrisés avec précision. Dans ce travail, il a été montré que l'efficacité

8. CONCLUSIONS

de diffusion des défauts reconstruits dépend de leur topologie et du degré de passivation par l'hydrogène, et qu'elle peut aller de la suppression de la conduction des électrons ou des trous jusqu'à une faible rétrodiffusion pour les défauts préservant une géométrie aromatique. Il a été prédit que des défauts topologiques simples tels que des défauts pentagonaux ou heptagonaux induisent une forte asymétrie électron-trou du transport, contrairement à d'autres types de reconstructions des bords. Les défauts conservant la structure aromatique du réseau initial dégradent très peu la capacité de conduction du ruban.

La présence probable de défauts intrinsèques des nanorubans tels que des lacunes ou des défauts de Stone-Wales devraient aussi avoir un impact sur les processus d'hydrogenation et de fonctionnalisation, avec des conséquences certaines sur les mécanismes de transport. D'autres études concernant cet aspect donneraient un panorama plus complet des propriétés de transport électronique des nanorubans avec des défauts. D'autre part, la prise en compte du spin dans les simulations clarifierait les mécanismes de transport des systèmes carbonés en présence de défauts magnétiques.

Bibliography

- [1] L. Picard, F. Lincker, Y. Kervella, M. Zagorska, R. DeBettignies, A. Peigney, E. Flahaut, G. Louarn, S. Lefrant, R. Demadrille, A. Pron, *The Journal of Physical Chemistry C* 2009 113 (40), 17347
- [2] Latil S., Roche S., Mayou D. and Charlier J.-C. (2004) *Phys. Rev. Lett.* 92, 256805
- [3] Latil S., Roche S. and Charlier J.-C. (2005) *Nano Lett.* 5 2216
- [4] Mao Y-L, Yan X-H and Xiao Y 2005 *Nanotechnology* 16 3092
- [5] Chemistry Operations (December 15, 2003). Los Alamos National Laboratory. <http://periodic.lanl.gov/elements/6.html>. Retrieved on 2008-10-09.
- [6] Bowman, S. British Museum Press. ISBN 0-7141-2047-2 (1990).
- [7] Glossary of term used in physical organic chemistry, IUPAC Recommendations 1994
- [8] English Wikipedia
- [9] Nitish Nair, Woo-Jae Kim, Monica L. Usrey, and Michael S. Strano, *JACS*, 129, 13 (2006)
- [10] Michael S. Strano, et al. *Science* 301, 1519 (2003)
- [11] S. Campidelli, B. Ballesteros, A. Filoramo, D. Daz Daz, G. de la Torre, T. Torres, G. M. A. Rahman, C. Ehli, D. Kiessling, F. Werner, V. Sgobba, D. M. Guldi, C. Cioffi, M. Prato, J.-P. Bourgoïn, *J. Am. Chem. Soc.* 2008, 130, 11503.
- [12] A.T. Collins, H. Kanda, J. Isoya, C.A.J. Ammerlaan, J.A. van Wyk *Diam. Relat. Mater.* 7 (1998) 333
- [13] M.I., Ravi, K.V., *Applied Physics Letters* 55, (1989), 975
- [14] S. Koizumi et al., *Science* 292 (2001) 1899
- [15] E. Ekimov et al. *Nature* 428 (2004) 542
- [16] Y. Takano *Sci. Technol. Adv. Mater.* 7 (2006) S1

BIBLIOGRAPHY

- [17] In chemistry, the standard state of a material is a reference point used to calculate its properties under different conditions. The standard state for solids is simply the state of the pure substance subjected to a total pressure of 1 bar. For elements, the reference point of $\Delta_f H = 0$ is defined for the most stable allotrope of the element
- [18] Y. Takano et al. *Diam. Relat. Mat PG Pure Appl. Chem.*, 1995, Vol. 67, No. 3, pp. 473-506
- [19] <http://goldbook.iupac.org/>
- [20] S, Lorette et al. *Nano Letters* 6, 8, (2006) pp 1711-1718
- [21] IUPAC Gold Book
- [22] English Wikipedia
- [23] Cleavage is the tendency of crystalline materials to split along definite crystallographic structural planes
- [24] IUPAC Compendium of Chemical Terminology 2nd Edition (1997)
- [25] <http://www.webelements.com>
- [26] H.W. Kroto, J.R. Heath, S.C. O'Brien, R.F. Curl and R.E. Smalley, *Nature* (1985) 318, 162
- [27] A. Hirsch, Z. Chen, and H. Jiao, *Angew. Chem. Int. Ed.*, 39, 3915 (2000).
- [28] <http://nobelprize.org>
- [29] S. Iijima, *Nature* 354, 56 (1991)
- [30] Single-walled carbon nanotubes may pose health risks, *Medical Science News*, (2007)
- [31] *Fullerenes and Carbon Nanotubes*, J.-P. Bourgoïn, A. Loiseau, J.-F. Nierengarten, Springer Berlin Heidelberg (2007)
- [32] Insights on Interfacial Charge Transfer Across P3HT/Fullerene Photovoltaic Heterojunction from Ab Initio Calculations, Y. Kanai and J.C. Grossman, *Nano Lett*, 2007, 7 1967
- [33] Hebard, A. F. *Annu. ReV. Mater. Sci.* 1993, 23, 159.
- [34] A. G. Nasibulin, P. V. Pikhitsa, H. Jiang, D. P. Brown, A. V. Krasheninnikov, A. S. Anisimov, P. Queipo, A. Moisala, D. Gonzalez, G. Lientschnig, A. Hassanien, S. D. Shandakov, G. Lolli, D. E. Resasco, M. Choi, D. Tománek, and E. I. Kauppinen, (2007) A Novel Hybrid Nanomaterial, *Nature Nanotechnology* 2(3), 156-161.

- [35] J.A. Furst, J. Hashemi, T. Markussen, M. Brandbyge, A.P. Jauho, R.M. Nieminen arXiv:0905.0969v1, (2009)
- [36] Carbon - Naturally occurring isotopes. WebElements Periodic Table. <http://www.webelements.com>. Retrieved on 2008-10-09
- [37] F. A. Kekulé, "Sur la constitution des substances aromatiques". Bulletin de la Societe Chimique de Paris 3 98110 (1865).
- [38] Krichko, A. A., T. A. Titova, B. S. Filippov, and N. E. Dogadkina. "Production of tetralin by the hydrogenation of naphthalene-containing fractions." Chemistry and Technology of Fuels and Oils 5 (1969): 18-22
- [39] Fetzer, J. C. (2000). The Chemistry and Analysis of the Large Polycyclic Aromatic Hydrocarbons. New York, Wiley
- [40] Vazquez de Parga et al., PRL 100, 056807 (2008)
- [41] Arkadiusz Ciesielski, Micha K. Cyraski, Tadeusz M. Krygowski, Patrick W. Fowler, and Mark Lillington J. Org. Chem.; 2006; 71(18), 6840-6845
- [42] M. Orlita, C. Faugeras, P. Plochocka, P. Neugebauer, G. Martinez, D.K. Maude, A.-L. Barra, M. Sprinkle, C. Berger, W.A. de Heer, and M. Potemski, Phys. Rev. Lett. 101, 267601 (2008).
- [43] C. Berger, Z. Song, X. Li, X. Wu, N. Brown, C. Naud, D. Mayou, T. Li, J. Hass, A.N. Marchenkov, E.H. Conrad, P.N. First and W.A. de Heer, Science 312, 1191 (2006).
- [44] M.L. Sadowski, G. Martinez, M. Potemski, C. Berger and W.A. de Heer, Solid State Commun. 143, 123 (2007).
- [45] X. Wu and X. Li and Z. Song and C. Berger and W.A. de Heer, Phys. Rev. Lett. 98, 136801 (2007).
- [46] W.A. de Heer, et al., Sol. State Comm. 143, 92 (2007).
- [47] D.L. Miller, K.D. Kubista, G.M. Rutter, M. Ruan, W.A. de Heer, P.N. First and J.A. Stroscio., Science, 324 924 (2009).
- [48] M. Sprinkle, D. Siegel, Y. Hu, J. Hicks, P. Soukiassian, A. Tejada, A. Taleb-Ibrahimi, P. Le Fèvre, F. Bertran, C. Berger, W.A. de Heer, A. Lanzara, E.H. Conrad, arXiv:0907.5222v1
- [49] C. T. White and J. W. Mintmire, J. Phys. Chem. B, Vol. 109, No. 1, 2005
- [50] Physicsworld, <http://physicsworld.com/cws/article/news/33832>
- [51] Yu-Ming Lin, Vasili Perebeinos, Zhihong Chen, Phaedon Avouris

BIBLIOGRAPHY

- [52] K. Nakada, M. Fujita, G. Dresselhaus and M.S. Dresselhaus, Phys. Rev. B 54, 17954 - 17961 (1996)
- [53] A. Cresti, N. Nemeç, B. Biel, G. Niebler, F. Triozon, G. Cuniberti and S. Roche, Nano Research 1, 361-394 (2008)
- [54] Gopalan, S., Rice, T. M., Sigrist, M. Phys. Rev. B 1994, 49, 8901 8910.
- [55] L. Jiao, L. Zhang, X. Wang ,G. Diankov and H. Dai, Nature 458, 877-880 (2009)
- [56] A. G. Cano-Márquez, F. J. Rodríguez-Macías, J. Campos-Delgado, C. G. Espinosa-González, F. Tristán-López, Daniel Ramírez-González, D. A. Cullen, D. J. Smith, M. Terrones and Y.I. Vega-Cantú, Nano Lett., 2009, 9 (4), pp 15271533
- [57] Y.-W. Son, M.L. Cohen, and S.G. Louie, PRL 97, 216803 (2006)
- [58] Gomer R., Field Emission and Field Ionization, Harvard University Press, Cambridge, MA (1961)
- [59] S.J. Tans, M.H. Devoret, H. Dai, A. Thess, R.E. Smalley ,L.J. Georliga and C. Dekker 1997 Nature 386 4747
- [60] M. Bockrath, D.H. Cobden, P.L. McEuen, N.G. Chopra, A. Zettl, A. Thess and R. Smalley (1997) Science 275 19225
- [61] A.Star, J-C.P. Gabriel, K. Bradley and G. Grüner 2003 Nano Lett. 3 45963
- [62] Fuhrer M S, Kim B M, Chen Y-F, Dürkop T and Brintlinger T 2002 Nano Lett. 2 7559
- [63] S. Datta, Electron Transport in Mesoscopic Systems (Cambridge: Cambridge University Press)
- [64] Kong J, Zhou C, Morpurgo A, Soh H T, Quate C F, Marcus C and Dai H 1999 Appl. Phys. A 69 3058
- [65] White C. T. and Todorov T. N. 1998 Nature 393 2402
- [66] McEuen P L, Bockrath M, Cobden D H, Yoon Y-G and Louie S G 1999 Phys. Rev. Lett. 83 5098101
- [67] Pennington G and Goldsman N 2003 Phys. Rev. B 68 045426
- [68] T Dürkop, B M Kim and M S Fuhrer
- [69] Ch. W. Marquardt, S. Dehm, A. Vijayaraghavan, S. Blatt, F. Henrich and R. Krupke 2008 Nano Lett. 8 2767-2772
- [70] I. Heller, A. M. Janssens, J. Männik, Ethan D. Minot, S. G. Lemay, and C. Dekker Nano Lett., 2008, 8 (2), pp 591595

- [71] Smith, B.W., Monthieux, M. Luzzi, D.E. 1998 Nature 39 6 323
- [72] Derycke V., Martel R, Appenzeller J., Avouris P. Nano Letters 1 (9) 453 (2001)
- [73] Heller, I., Kong, J., Williams, K. A., Dekker, C., Lemay, S. G. J. Am. Chem. Soc. 2006, 128, 7353-7359.
- [74] Alberts, B.; et al. Molecular Biology of The Cell, 3rd ed.; Garland Publishing, Inc.: New York, 1994.
- [75] Allen, B. L., Kichambare, P. D., Star, A. AdV. Mater. 2007, 19, 1439-1451.
- [76] S.G. Lemay, J.W. Janssen, M. van den Hout, M. Mooij, M.J. Bronikowski, P.A. Willis, R.E. Smalley, L.P. Kouwenhoven and C. Dekker Nature 412, 617-620 (2001)
- [77] A. Bachtold, M. S. Fuhrer, S. Plyasunov, M. Forero, Erik H. Anderson, A. Zettl, and Paul L. McEuen, Phys. Rev. Lett. 84, 6082 - 6085 (2000)
- [78] Jauey et al. Phys. Rev. Lett. 92, (1982) 106804
- [79] Triozon, F., S. Roche, A. Rubio, and D. Mayou, 2004, Phys. Rev. B 69, 121410.
- [80] Tan, Y. W.; Zhang, Y.; Bolotin, K.; Zhao, Y.; Adam, S.; Hwang, E. H.; Das Sarma, S.; Stormer, H. L.; Kim, P. , Phys. Rev. Lett. 2007, 99, 246803.
- [81] *Density Functional Theory Of Atoms And Molecules*, Parr, Robert G., Weitao, Yang, Oxford University Press
- [82] Goedecker, S. 1999 Rev. Mod. Phys. 71 1085
- [83] Ordejón, P. 2000 Phys. Status Solidi b 217 335
- [84] Sankey, O.F. and Niklewski, D. J., 1989, Phys. Rev. B 40 3979
- [85] E. Artacho et al, J. Phys.: Condens. Matter, 2008, 20, 064208
- [86] Sánchez-Portal, D., Ordejón, P., Artacho, E. and Soler, J.M. 1997, Int. J. Quantum Chem. 65 453
- [87] Ordejón, P.; Artacho, E.; Soler, J. M. , Phys. Rev. B, 1996, 53, 10441.
- [88] Artacho, E.; Sánchez-Portal, D.; Ordejón, P.; García, A.; Soler, J. M. Phys; Stat; Sol. (b) 1999, 215, 809.
- [89] Pearson, M., Smargiassi, E. and Madden, P.A., J. Phys. Condens. Matter,
- [90] L. Kleinman and D. M. Bylander, Phys. Rev. Lett. 48, (1982) 1425
- [91] J.C. Charlier, X. Blase and S. Roche, Review of Modern Physics 79, 677 (2007)

BIBLIOGRAPHY

- [92] M. Büttiker, Y. Imry, R. Landauer, and S. Pinhas. Phys. Rev. B, 31(10):6207, May 1985.
- [93] http://inac.cea.fr/L_Sim/TB_Sim/index.html
- [94] H. M. Pastawski, E. Medina, arXiv:cond-mat/0103219v1
- [95] M. P. López-Sancho, J. M. Lopez-Sancho, and J. Rubio, (100). J. Phys. F, 141205, (1984)
- [96] G. Grosso, G. Pastori Parravicini, “Solid State Physics”, Elsevier Science & Technology (2000)
- [97] G. Grosso, S. Moroni, G. Pastori Parravicini, Phys. Rev. B 40, 12328 (1989)
- [98] A. R. Williams, P. J. Feibelman, and N. D. Lang, Phys. Rev. B 26, 5433 (1982)
- [99] R.D. Graft, D.J. Lohrmann, G. Pastori Parravicini, L. Resca, Phys. Rev. B 36, 4782 (1987)
- [100] K.S. Thygesen, Quantum Transport Lectures Notes, CAMD Summer School, Copenhagen (2008)
- [101] F. Yndurain, Solid State Physics Lectures Notes at Universidad Autónoma de Madrid, Madrid (2006)
- [102] C. Adessi et al., C. R. Physique 10 (2009)
- [103] Charlier, J.C.; Blase, X.; Roche, S. Rev. Mod. Phys. **2007**, 79, 677.
- [104] X. Guo *et al.*, J. Am. Chem. Soc. **127**, 15045 (2005)
- [105] J.M. Simmons *et al.*, Phys. Rev. Lett. **98**, 086802 (2007); J. Borghetti *et al.*, Adv. Mater. **18** 2535 (2006).
- [106] J. Mannik, B.R. Goldsmith, A. Kane, and P.G. Collins, Phys. Rev. Lett. **97**, 016601 (2006); B.R. Goldsmith *et al.*, Science **315**, 77 (2007); V. Meunier, S.V. Kalinin, B.G. Sumpter, Phys. Rev. Lett. **98**, 056401 (2007).
- [107] J. Bahr and J. Tour, Chem. Mater. **13**, 3823 (2001).
- [108] J. Cabana and R. Martel, J. Am. Chem. Soc. **129**, 2244 (2007); K. Balasubramanian *et al.*, Phys. Status Solidi A **205**, 633 (2008).
- [109] Y.-S. Lee, M. Buongiorno Nardelli, N. Marzari, Phys. Rev. Lett. **95**, 076804 (2005).
- [110] Y. Chen *et al.*, J. Mater. Res. **13**, 2423 (1998); J. Chen *et al.*, Science **282**, 95 (1998); M. Holzinger *et al.*, Angew. Chem., Int. Ed. **40**, 4002 (2001); K.S. Coleman *et al.*, J. Am. Chem. Soc. **125**, 8722 (2003).

-
- [111] Z. Chen *et al.*, *Angew. Chem. Int. Ed.* **43**, 1552 (2004)
- [112] Odom, T.W.; Huang, J.L.; Kim, Ph.; Lieber, C.M. *J. Phys. Chem. B* **2000**, 104, 2794.
- [113] Chen, Z.; Appenzeller, J.; Knoch, J.; Lin, Y.-M.; Avouris, Ph. *Nano Lett.* **2005** 5, 1497.
- [114] Dürkop, T.; Getty, S.A.; Cobas, E.; Fuhrer, M.S. *Nano Letters*, **2004**, 4 35.
- [115] Katz, E.; Willner, I. *Chem. Phys. Chem.* **2004**, 5, 1084.
- [116] Robinson, J.A.; Snow, E.S.; Bdescu, S.C.; Reinecke, T.L.; Perkins, F.K. *Nano Lett.* **2006**, 6 (8), 1747.
- [117] Zhang, Y.B., et al., *Nano Lett.* **2007**, 7 (10), 3086.
- [118] Zheng, G.; Patolsky, F.; Cui, Y.; Wang, W.U.; Lieber, C.M. *Nat. Biotechnol.* **2005**, 23, 1294.
- [119] Allen, B. L.; Kichambare, P. D.; Star, A. *Adv. Mat.* **2007**, 19, 1439.
- [120] Goldsmith, B. et al., *Science* **2007**, 315, 77.
- [121] Balasubramanian, K.; Lee, E.J.H.; Weitz, R.T.; Burghard, M.; Kern, K. *Phys. Stat. Sol. (a)* **2008**, 205, 633.
- [122] Ballesteros, B.; Campidelli, S.; de la Torre, G.; Ehli, C.; Guldi, D.; Prato, M.; Torres, T. *Chem. Commun.*, **2007**, 2950.
- [123] Simmons, J.M.; In, I.; Campbell, V.E.; Mark, T.J.; Léonard, F.; Gopalan, P.; Eriksson, M.A. *Phys. Rev. Lett.* **2007**, 98, 086802.
- [124] Latil, S.; Roche, S.; Charlier, J.-C. *Nano Lett.* **2005**, 5, 2216.
- [125] Tournus, F.; Latil, S.; Heggie, M. I.; Charlier, J.-C. *Phys. Rev. B* **2005**, 72, 075431.
- [126] Zhao, J.; Park, H.; Han, J.; Lu, J. *J. Phys. Chem. B* **2004**, 108, 4227.
- [127] Park, H.; Zhao, Z.; Lu, J. P. *Nanotechnology* **2005**, 16, 635.
- [128] Park, H.; Zhao, Z.; Lu, J. P. *Nano Lett.* **2006**, 5, 916.
- [129] Lee, Y.-S.; Buongiorno Nardelli, M.; Marzari, N. *Phys. Rev. Lett.* **2005**, 95, 076804.
- [130] Lee, Y.-S.; Marzari, N. *Phys. Rev. Lett.* **2006**, 97, 116801.
- [131] Cabana, J.; Martel, R. *J. Am. Chem. Soc.* **2007**, 129, 2244.
- [132] N. Marzari and D. Vanderbilt, *Phys. Rev. B* 56, 12847 **1997**.

BIBLIOGRAPHY

- [133] <http://quasiamore.mit.edu/pmwiki/index.php?n=Pics.Research>
- [134] Biel, B.; García-Vidal, F. J.; Rubio, A.; Flores, Phys. Rev. Lett. **2005**, 95, 266801.
- [135] Biel, B.; García-Vidal, F. J.; Rubio, A.; Flores, F. J. Phys.: Condens. Matter **2008**, 20, 294214.
- [136] Rocha, A. R.; Rossi, M.; Fazzio, A.; da Silva, A. J. R. Phys. Rev. Lett. **2008**, 100, 176803.
- [137] Markussen, T.; Rurali, R.; Brandbyge, M.; Jauho, A. P. Phys. Rev. B **2006**, 74, 245313.
- [138] Fisher, D. S.; Lee, P. A. Phys. Rev. B **1981**, 23, 6851.
- [139] Nardelli, M. B. Phys. Rev. B **1999**, 60, 7828.
- [140] Choi, H. J.; Ihm, J.; Louie, S. G.; Cohen, M. L. Phys. Rev. Lett. **2000**, 84, 2917.
- [141] Perdew, J. P.; Zunger, A. Phys. Rev. B **1981**, 23, 5048.
- [142] Troullier, N.; Martins, J. L. Phys. Rev. B **1991**, 43, 1993.
- [143] Artacho, E.; Sánchez-Portal, D.; Ordejón, P.; García, A.; Soler, J. M. Phys; Stat; Sol. (b) **1999**, 215, 809.
- [144] Blase, X.; Margine E.R., Bocquet M. L. *in press*
- [145] Schmidt et al. (146) have recently performed a kinetic study of the covalent coupling of diazoniums onto single-walled nanotubes in water, providing fine details on the reaction pathway of phenyl molecules to CNT. As a result, it can be concluded that the creation of a paired configuration of phenyls on the nanotube surface is done by means of a free radical chain reaction mechanism.
- [146] Schmidt, G.; Gallon, S.; Esnouf, S.; Bourgoïn, J.-P.; Chenevier, P. *to be published*
- [147] Liang, F.; Alemany, L.; Beach, J.; Billups, W. J. Am. Chem. Soc. **2005**, 127, 13941.
- [148] Avriller, R.; Latil, S.; Triozon, F.; Blase, X.; Roche, S. Phys. Rev. B **2006**, 74, 121406.
- [149] White, C.T.; Todorov, T.N. Nature **1998**, 393, 240.
- [150] Areshkin, D.A.; Gynlycke, D.; White, C.T. Nano Letters **2007**, 7, 204.
- [151] Gómez-Navarro, C.; DePablo, P. J.; Gómez-Herrero, J.; Biel, B.; García-Vidal, F. J.; Rubio, A.; Flores, F. Nat. Mater. **2005**, 4, 534.
- [152] H. Park, J. Zhao, J.P. Lu, Nano Letters **6**, 916 (2006).
- [153] Y.-S. Lee and N. Marzari, J. Phys. Chem. C **112**, 4480 (2008).

BIBLIOGRAPHY

- [154] Small, or secondary, gaps for -n- multiple of three are induced by curvature. See C.L. Kane and E.J. Mele, *Phys. Rev. Lett.* **78**, 1932 (1997).
- [155] R. Avriiler *et al.*, *Mod. Phys. Lett. B* **21**, 1955 (2007).
- [156] J.M. Garcia-Lastra, K.S. Thygesen, M. Strange, A. Rubio, *Phys. Rev. Lett.* **101**, 236806 (2008).
- [157] Echtermeyer, T.J., Lemme, M.C., Braus, M., Szafranek, B.N., Geim, A.K.; Kurz, H., *IEEE Electron Device Letters* 2008, 29, 952
- [158] Geim, A.K.; Novoselov, K.S. *Nature Materials* **2007**, 6, 183.
- [159] Berger, C.; Song, Z.; Li, X.; Wu, X.; Brown, N.; Naud, C.; Mayou, D.; Li, T.; Hass, J.; Marchenkov, A.; Conrad, E.; First, P.; de Heer, W. *Science* **2006**, 312, 1191.
- [160] Cresti, A.; Nemeč, N.; Biel, B.; Niebler, G.; Triozon, F.; Cuniberti, G.; Roche, S. *Nano Research* **2008**, 1, 361.
- [161] Wu, Y. Q.; Ye, P. D.; Capano, M. A.; Xuan, Y.; Sui, Y.; Qi, M.; Cooper, J. A.; Shen, T.; Pandey, D.; Prakash, G.; Reifenger, R. *Appl. Phys. Lett.* **2008**, 92, 092192.
- [162] Novoselov, K. S.; Geim, A. K.; Morozov, S. V.; Jiang, D.; Zhang, Y.; Dubonos, S. V.; Grigorieva, I. V.; Firsov, A. A. *Science* **2004**, 306, 666.
- [163] Morozov, S. V.; Novoselov, K. S.; Katsnelson, M. I.; Schedin, F.; Elias, D. C.; Jaszczak, J. A.; Geim, A. K. *Phys. Rev. Lett.* **2008**, 100, 016602.
- [164] Wakabayashi, K.; Fujita, M.; Ajiki, H.; Sigrist, M. *Phys. Rev. B* **1999**, 59, 8271
- [165] Lemme, M.C.; Echtermeyer, T. J.; Baus, M.; and Kurz, H. *IEEE Electron Device Letters* **2007**, 28, 282.
- [166] Li, X.; Wang, X.; Zhang, Li; Lee, S; Dai, H. *Science* **2008**, 319, 1229.
- [167] Han, M. Y.; Özyilmaz, B.; Zhang, Y.; Kim, Ph. *Phys. Rev. Lett.* **2007**, 98, 206805.
- [168] Wang, X.; Ouyang, Y.; Li, X.; Wang, H.; Guo, J.; Dai, H. *Phys. Rev. Lett.* **2008**, 100, 206803.
- [169] Boukhvalov, D.W.; Katsnelson, M. I. *J. Phys. Cond. Matt. to be published*, arXiv:0809.5257.
- [170] Boukhvalov, D.W.; Katsnelson, M. I. *Nano Lett.* **2008**, 8 (12), 4373.
- [171] Boukhvalov, D.W.; Katsnelson, M. I. *J. Am. Chem. Soc.* **2008**, 130, 10697.
- [172] Barone V.; Hod, O.; Scuseria G.E. *Nano Lett.* **2006**, 6, 2748.

BIBLIOGRAPHY

- [173] Hod O.; Barone V.; Peralta J.E.; Scuseria G.E. *Nano Lett.* **2007**, 7, 2295.
- [174] Bekyarova, E.; Itkis, M.E.; Ramesh, P.; Berger, C.; Sprinkle, M.; de Heer, W.; Haddon, R.C. *J. Am. Chem. Soc.* **2009**, 131, 1336
- [175] Yazyev, O.V. ; Helm, L. *Phys. Rev B* **2007** 75 125408
- [176] J. O. Sofo, A. Chaudhari and G. D. Barber, *Phys. Rev. B* 75, 153401 (2007)
- [177] Roman, T., Dino, W. A., Nakanishi, H., Kasai, H., Sugimoto, T. and Tange, K. 2006 *Japan. J. Appl. Phys.* 45 17657
- [178] Boukhvalov, D.W.; Katsnelson, M. I. 2009 *J. Phys.: Condens. Matter* **21**, 344205
- [179] Boukhvalov, D.W.; Katsnelson, M. I. and Lichtenstein, A.I. *Phys. Rev. B* 78, 085413 (2008)
- [180] Derycke, V.; Martel, R.; Appenzeller, J.; Avouris, Ph. *Nano Lett.* **2001**, 1 (9), 453.
- [181] Farmer, D. B.; Golizadeh-Mojarad, R.; Perebeinos, V.; Lin, Y.-M.; Tulevski, G.S; Tsang, J.C.; Avouris, Ph. *Nano Lett.* **2009**, 9, 388.
- [182] Schedin, F.; Geim, A. K.; Morozov, S. V.; Hill, E. W.; Blake, P.; Katsnelson, M. I.; Novoselov, K. S. *Nature Materials* **2007**, 6, 652.
- [183] Wehling, T. O.; Novoselov, K. S.; Morozov, S. V.; Vdovin, E. E.; Katsnelson, M. I.; Geim, A. K.; Lichtenstein, A. I. *Nano Lett.* **2008**, 8 (1), 173.
- [184] Ito, A.; Nakamura, H.; Takayama, A. *J. Phys. Soc. Jpn.* **2008**, 77, 114602.
- [185] Son, Y.-W.; Cohen, M.L.; Louie, S.G. *Phys. Rev. Lett.* **2006**, 97, 216803.
- [186] White, C.T.; Li, J.; Gunlycke, D.; Mintmire, J.W. *Nano Lett.* **2007**, 7, 825.
- [187] Meyer, J.C; Girit, C.O; Crommie, M.F; Zettl, A. *Nature* **2008**, 454, 319.
- [188] Adessi, Ch.; Roche, S.; Blase, X. *Phys. Rev. B* **2006**, 73, 125414.
- [189] Triozon, F.; Lambin, Ph.; Roche, S. *Nanotechnology* **2005** 16, 230.
- [190] Elias, DC; Nair, RR; Mohiuddin, TMG; Morozov, SV ; Blake, P; Halsall, MP; Ferrari, AC; Boukhvalov, DW; Katsnelson, MI; Geim, AK ; Novoselov, KS *Science* **2009**, 323, 610.
- [191] Jiang, D.E.; Sumpter, B.G.; Dai, S. *J. Phys. Chem. B* **2006**, 110, 23628.
- [192] Areshkin, D. A.; Gunlycke, D.; White, C. T. *Nano Lett.* **2007**, 7, 204.
- [193] Cervantes-Sodi, F.; Csanyi, G.; Piscanec, S.; Ferrari, A. C. *Phys. Rev. B* **2008**, 77, 165427.

-
- [194] Evaldsson M.; Zozoulenko, I.V.; Xu, H.; Heinzl, T. *Phys. Rev. B* **2008**, 78, 161407.
- [195] Mucciolo, E. R.; Castro Neto, A.H.; Lewenkopf, C. H. *Phys. Rev. B* **2009**, 79, 075407.
- [196] Naumis, G. *Phys. Rev. B* **2007**, 76, 153403.
- [197] Z. Liu, K. Suenaga, P.J.F. Harris, S. Iijima, *Phys. Rev. Lett.* 102, 015501 (2009);
- [198] P. Koskinen, S. Malola, H. Hakkinen, *Phys. Rev. Lett.* 101, 115502 (2008). T. Wassmann, Ari P. Seitsonen, A. Marco Saitta, Michele Lazzeri, and Frances , *Phys. Rev. Lett.* 101, 096402 (2008); B. Huang, M. Liu, N. Su, J. Wu, W. Duan, B.-L. Gu, and F. Liu, *Phys. Rev. Lett.* 102, 166404 (2009)
- [199] A. Bostwick, J. L. McChesney, K. V. Emtsev, Th. Seyller, K. Horn, S. D. Kevan, E. Rotenberg, *Phys. Rev. Lett.* 103, 056404 (2009).
- [200] A.K. Geim, *Science* **324**, 1530 (2009); A.H. Castro Neto *et al.*, *Rev. Mod. Phys.* 109 **81** (2009).
- [201] K. Nakada, M. Fujita, G. Dresselhaus, M.S. Dresselhaus, *Phys. Rev. B* **54**, 17954 (1996); K. Wakabayashi, *Phys. Rev. B* **64**, 125428 (2001); K. Sasaki, S. Murakami, R. Saito, *Appl. Phys. Lett.* **88**, 113110 (2006); F. Muñoz-Rojas, D. Jacob, J. Fernández-Rossier, J.J. Palacios, *Phys. Rev. B* **74**, 195417 (2006).
- [202] M.Y. Han, B. Özyilmaz, Y. Zhang, P. Kim, *Phys. Rev. Lett.* **98**, 206805 (2007).
- [203] M.C. Lemme, T.J. Echtermeyer, M. Baus, H.A. Kurz, *IEEE Electron Device Letters* **28**, 282 (2007); X. Wang *et al.*, *Phys. Rev. Lett.* **100**, 206803 (2008). M. Wimmer *et al.*, *Phys. Rev. Lett.* **100**, 177207 (2008). O. V. Yazyev, M.I. Katsnelson, *Phys. Rev. Lett.* **100**, 047209 (2008).
- [204] Y.-W. Son, M.L. Cohen, S.G. Louie, *Phys. Rev. Lett.* **97**, 216803 (2006); V. Barone, O. Hod, G.E. Scuseria, *Nano Lett.* **6**, 2748 (2006); C.T. White, J. Li, D. Gunlycke, J.W. Mintmire, *Nano Lett.* **7**, 825 (2007).
- [205] D.A. Areshkin, D. Gunlycke, C.T. White, *Nano Lett.* **7**, 204 (2007); M. Evaldsson *et al.*, *Phys. Rev. B* **78**, 161407(R) (2008); E.R. Mucciolo, A.H. Castro Neto, C.H. Lewenkopf, *Phys. Rev. B* **79**, 075407 (2009); A. Cresti and S. Roche, *Phys. Rev. B* **79**, 233404 (2009).
- [206] T. Wassmann *et al.*, *Phys. Rev. Lett.* **101**, 096402 (2008); P. Koskinen, S. Malola, H. Häkkinen, *Phys. Rev. Lett.* **101**, 115502 (2008); B. Huang *et al.*, *Phys. Rev. Lett.* **102**, 166404 (2009); P. Koskinen, S. Malola, H. Häkkinen, *Phys. Rev. B* **80**, 073401 (2009).
- [207] X. Li *et al.* *Science* 319, 1229 (2008)
- [208] C.O. Girit *et al.* *Science* 323, 1705 (2009)

BIBLIOGRAPHY

- [209] Y. Kobayashi, K.I. Fukui, T. Enoki, K. Kusakabe, Phys. Rev. B **73**, 125415 (2006); C. Casiraghi *et al.*, Nano Letters **9**, 1433 (2009); Z. Liu, K. Suenaga, P.J.F. Harris, S. Iijima, Phys. Rev. Lett. **102**, 015501 (2009);
- [210] A. Bostwick *et al.*, Phys. Rev. Lett. **103**, 056404 (2009); D.C. Elias *et al.*, Science **323**, 610 (2009).
- [211] A.R. Rocha, V.M. García-Suárez, S. Bailey, C. Lambert, J. Ferrer, S. Sanvito *et al.*, Phys. Rev. B **73**, 085414 (2006).
- [212] J.-C. Charlier, T.W. Ebbesen, Ph. Lambin, Phys. Rev. B **53**, 11108 (1996).
- [213] R. Tamura, M. Tsukada, Phys. Rev. B **49**, 7697 (1994).
- [214] H.-J. Choi, J. Ihm, S.G. Louie, M.L. Cohen, Phys. Rev. Lett. **84**, 2917 (2000).
- [215] E. Clar, *The Aromatic Sextet*, Wiley, London, (1972)
- [216] M. Baldoni, A. Sgamellotti, F. Mercuri, Chem. Phys. Lett. **464**, 202 (2008).